Institut für Strömungsmechanik und
Hydraulische Strömungsmaschinen

Feasibility of Transient Model Tests in a Closed-Loop Test Rig with the Example of a Reversible Pump Turbine

J. Junginger

Universität Stuttgart

Mitteilung Nr. 47 | 2023

Feasibility of Transient Model Tests in a Closed-Loop Test Rig with the Example of a Reversible Pump Turbine

Von der Fakultät Energie-, Verfahrens- und Biotechnik
der Universität Stuttgart zur Erlangung der Würde
eines Doktors der Ingenieurswissenschaften (Dr.-Ing.)
genehmigte Abhandlung

vorgelegt von

Johannes Junginger

aus Freudenstadt

Hauptberichter: Prof. Dr.-Ing. Stefan Riedelbauch
Mitberichter: Prof. M. Hanif Chaudhry, PhD

Tag der mündlichen Prüfung: 10.03.2023

Institut für Strömungsmechanik und Hydraulische
Strömungsmaschinen der Universität Stuttgart

2023

ISBN 978-3-948328-06-1

Universität Stuttgart
Institut für Strömungsmechanik und
Hydraulische Strömungsmaschinen
Pfaffenwaldring 10
D-70550 Stuttgart

Tel.: +49-711-685-63260
Fax: +49-711-685-53255
Email: sekretariat@ihs.uni-stuttgart.de
http://www.ihs.uni-stuttgart.de

D 93 Stuttgart

Druck und Bindung: Druckerei Kormann, Geislingen an der Steige

Es irrt der Mensch so lang er strebt.

Faust - Johann Wolfgang Goethe

Vorwort

Die Veröffentlichung meiner Dissertation ist sogleich der letzte Akt einer großartigen, intensiven und entbehrungsreichen Zeit, in der ich in enger Verbindung zum Institut für Strömungsmechanik und Hydraulische Strömungsmaschinen der Universität Stuttgart stand. Als Student, wissenschaftliche Hilfskraft und anschließend als Mitarbeiter habe ich in dieser langen Phase vieles gelernt, viele Erfahrungen gesammelt und durfte tolle Menschen kennenlernen. Ich möchte allen danken, mit denen ich sowohl beruflich als auch neben der Arbeit Zeit verbracht habe.
Das Ziel zu promovieren, habe ich mir während des vierten Semesters meines Studiums gesetzt und anschließend vehement verfolgt. Ein besonderer Dank gilt daher denjenigen, die durch ihr offenes Ohr und ihren Rat in irgendeiner Weise einen Beitrag zu der Erstellung meiner Dissertation beigetragen haben. Ich möchte es mir nicht nehmen lassen, ein paar ausgewählte Personen bei meiner Danksagung hervorzuheben.

Zunächst geht mein Dank an Professor Stefan Riedelbauch. Durch Ihr Vertrauen und die von Ihnen eröffnete Gelegenheit, dieses Forschungsthema untersuchen zu dürfen, wurde mir die Chance zur Promotion bereitet. Vielen Dank dafür!
I would also like to express a special thanks to Professor Hanif Chaudhry. It was a pleasure to have you as co-rapporteur for my thesis. Thanks for your support, Hanif!

Zur Umsetzung meiner Forschung waren einige Montage-, Umbau- und Fertigungsarbeiten am Versuchsstand notwendig. Ohne die Hilfe und die Fähigkeiten der Mechaniker im Labor wäre das nicht gelungen. Vielen Dank dafür!
Ein besonderer Dank geht auch an Dr. Oliver Kirschner. Ohne Dein Wissen und Deine Erfahrungen, aber auch Dein stets offenes Ohr, wäre diese Forschungsarbeit erheblich schwieriger für mich gewesen.

Auch meinen Bürokollegen Christoph möchte ich nicht unerwähnt lassen. Danke für deine guten Tipps über nützliche Haushaltsgeräte und die Diskussionen über schöne Diagramme. Alex, danke für die nicht immer nützlichen fachlichen Diskussionen, aber der umso wichtigeren Hilfe bei Fragen zum Programmieren. Ein großer Dank geht auch an Dich, Jonas, für Deine Hilfe bei allen Fragen, egal um welches Thema es

sich handelte. Auch Dir, Bernd, möchte ich einen Dank aussprechen. Du hattest stets einen Tipp auf Lager. Für die geniale Zeit während der Konferenz in Kyoto und der anschließenden Reise nach Tokio, geht auch ein großer Dank an Dich, Axel - das war ein klasse Trip! Christa, danke, dass ich durch Dich Hydrostatik, am Beispiel eines Dammbauwerks in Gewässern des Nahen Ostens, noch besser verstehen gelernt habe.

Abschließend möchte ich mich ganz besonders bei meiner Frau Maike bedanken. Die intensive Phase der Bearbeitung meiner Dissertation fiel in dieselbe Zeit, wie die Geburt unserer Zwillinge. Ohne Deine Aufopferung und Rücksichtnahme wäre es mir nicht möglich gewesen, die Wochenenden mit programmieren, auswerten und schreiben zu verbringen. Ich danke Dir unendlich dafür, dass Du mir bei all meinen Zielen zur Seite stehst.

Abstract

The growing share of renewable energies in power generation increases the risk of unintended exceedings of frequency limits in an interconnected grid. To counteract this, a so-called redispatch, a correction of the power balance in the grid, takes place. Due to their flexible operating capability, pumped storage power plants often perform this correction. However, the frequent change of the operating point of these power plants leads to an increase in transient events and thus raises the mechanical stress on the plant components. In addition to the known methods for analyzing fluid machinery, transient model tests are an important element for investigating the increasing demands on mechanical stress capacity and operating behavior.

In this work, a method to implement transient model test in a closed-loop test rig is presented. For this propose, various transient load cases of a real pumped storage power plant with a reversible pump turbine are simulated. The time-dependent quantities of the machine are transferred to the scaled model using suitable laws of similarity. A special feature is the use of the Strouhal number to convert the time scale. These transferred data serve as setpoints for the model machine when simulating the test rig. An iterative optimization procedure is used to adapt the behavior of the test rig actuators until the setpoints are reached with the specified accuracy. With the knowledge about the entire control sequence, the transient experiment is carried out on the laboratory test rig. The use of a bypass increases the spectrum of transient load cases under investigation. This enables, for example, a fast change between pump and turbine operation of the model machine.

In order to examine the developed method for its capability, various influencing factors were considered. By means of a parameter study, the speed of sound of the numerical test rig model was varied. Especially for load cases with modified guide vane opening, different values of the speed of sound have an influence on the simulation results. Therefore, the speed of sound must be modeled as close as possible to the same values as in the real test rig. Furthermore, it is shown that the readout procedure of the characteristic diagram of the hydraulic machines can influence the simulation results. Responsible is the linear interpolation between the grid points used by the simulation software during the transient process, which leads to discontinuities.

The general applicability of the method was investigated with the help of various transient load cases, such as operating point changes and fast transitions. Due to the lack of automated guide vane adjustment on the test rig used, only the fast transitions were carried out experimentally. For this purpose, the model rotational speed was adjusted between pump and turbine operating point at constant guide vane opening. The findings were then transferred to the simulated load cases with active guide vane adjustment. The applied methodology is confirmed by the good agreement between setpoints and measurement results. Limitations of the transient model test are given by the electrical machines. To reduce the differences in dynamic similarity between model and prototype, high rotational speeds of the model are required. For load cases with ambitious speed changes, such as fast transitions or total load rejections, the drives reach their acceleration restrictions.

Another challenge is the measurement of the transient discharge, which influences the results especially at high discharge gradients. It is revealed that the used indirect measurement of the model discharge in the pump branch in conjunction with the bypass branch using two sensors with too high delay times is insufficient. These challenges need to be addressed in future research.

Kurzfassung

Durch den wachsenden Anteil an erneuerbaren Energien an der Stromerzeugung steigt das Risiko von ungewollten Überschreitungen von Frequenzgrenzen in einem Verbundnetz. Um dem entgegenzuwirken, kommt es zu einem sogenannten Redispatch, einer Korrektur der Leistungsbilanz im Netz. Auf Grund ihrer flexiblen Betriebsfähigkeit übernehmen in einigen Fällen Pumpspeicherkraftwerke diese Korrektur. Jedoch führt diese Anpassung des Betriebspunkts zu einem transienten Ereignis, welches bei häufigem Auftreten eine erhöhte mechanische Belastung der Anlagenkomponenten zur Folge hat. Neben den bekannten Methoden zur Analyse von Strömungsmaschinen sind transiente Modellversuche ein wichtiges Element zur Untersuchung der steigenden Anforderungen an die mechanische Belastbarkeit und das Betriebsverhalten.

In dieser Arbeit wird eine Methode vorgestellt, wie diese Modellversuche in einem geschlossenen Versuchskreislauf umgesetzt werden. Hierzu werden diverse transiente Vorgänge eines realen Pumpspeicherkraftwerks mit reversibler Pumpturbine simuliert. Die zeitabhängigen Größen der Maschinen werden mit geeigneten Ähnlichkeitsgesetzen auf das skalierte Modell übertragen. Eine Besonderheit stellt hier die Verwendung der Strouhalzahl dar, um den Zeitmaßstab auf das Modell zu skalieren. Diese übertragenen Daten dienen als Sollwerte, welche in der Simulation eines geschlossenen Versuchskreislaufs an der Modellmaschine erzielt werden sollen. Um dies zu erreichen wird das Verhalten der Betriebspumpen des Versuchskreislaufs über ein iteratives Optimierungsverfahren so lange adaptiert, bis die Zielgrößen mit vorgegebener Genauigkeit erfüllt werden. Das ermittelte Verhalten der simulierten Komponenten wird dann auf den realen Versuchskreislauf übertragen und das transiente Experiment durchgeführt. Die Verwendung eines Bypasses erhöht das Spektrum zu untersuchender transienten Lastfälle. So ist beispielsweise ein schneller Wechsel zwischen Pump- und Turbinenbetrieb der Modellmaschine möglich.

Um die entwickelte Methode auf ihre Fähigkeiten zu untersuchen, wurden verschiedene Einflussfaktoren betrachtet. Unter anderem wurde über eine Parameterstudie die Wellenlaufgeschwindigkeit des numerischen Kreislaufmodells variiert. Es zeigt sich, dass verschiedene Werte der Wellenlaufgeschwindigkeit, im Besonderen bei

Fällen mit Verstellung der Leitschaufeln, einen Einfluss auf die Ergebnisse haben. Bei der Modellierung sollten diese Werte möglichst genau den Werten des realen Veruchsstands entsprechen. Des weiteren zeigt sich, dass das Ausleseverfahren der Kennfelder der hydraulischen Maschinen die Simulationsergebnisse beeinflussen können. Verantwortlich ist das von der Strömungssimulationssoftware verwendete lineare Interpolieren zwischen den Stützstellen, während des transienten Prozesses, welches zu Unstetigkeiten führt.

Die allgemeine Anwendbarkeit der Methode wurde mit Hilfe verschiedener transienter Lastfälle, wie Betriebspunktänderungen und Schnellübergänge, untersucht. Auf Grund der fehlenden automatisierten Leitapparatverstellung am verwendeten Versuchsstand, wurden nur die Schnellübergänge experimentell durchgeführt. Hierfür wurde bei konstanter Leitschaufelöffnung die Modelldrehzahl zwischen Pump- und Turbinenbetriebspunkt angepasst. Anschließend wurde die Erkenntnisse auf die simulierten Lastfälle, mit aktiver Leitapparatverstellung, übertragen.

Die angewandte Methode wird durch die gute Übereinstimmung zwischen Sollwerten und Messergebnissen bestätigt. Die Grenzen der transienten Modellversuche sind durch die elektrischen Maschinen gegeben. Um die Unterschiede in der dynamischen Ähnlichkeit zwischen Modell und Prototyp zu verringern, sind hohe Modelldrehzahlen erforderlich. Bei Lastfällen mit anspruchsvoller Drehzahländerung, wie zum Beispiel Schnellübergängen oder Lastabwürfen, geraten die Antriebe an ihre Beschleunigungsbeschränkungen.

Eine weitere Herausforderung stellt die Messung des transienten Durchflusses dar, welche die Ergebnisse insbesondere bei hohen Durchflussänderungen beeinflusst. Es zeigt sich, dass die verwendete indirekte Messung des Modelldurchflusses, im Pumpen- und Bypassstrang, unter Verwendung zwei Messsensoren mit zu hohen Verzögerungszeiten, unzureichend ist. Diese Herausforderungen müssen in künftigen Forschungsarbeiten bewältigt werden.

Contents

List of Variables

Acronyms

1D	one dimensional
3D	three dimensional
ASME	American Society of Mechanical Engineering
BEP	best efficiency point
CFD	computational fluid dynamics
DFIM	double-fed induction asynchronous motor generator
FSI	fluid-structure-interaction simulations
FT	fast transition (change of operating mode)
HYPERBOLE	HYdropower plants PERformance and flexiBle Operation towards Lean integration of new renewable Energies - project funded by the European Union [47]
IEC60193	international standard for model acceptance tests in the field of hydro power
IHS	Institute of Fluid Mechanics and Hydraulic Machines
MG	motor generator
MoC	method of characteristics

PU	pump mode
PUB	pump brake mode
RES	renewable energy source
RPU	reverse pump mode
SIPROHS	SImulation PROgram for Hydraulic Systems. Software tool for simlulating transient flow based on the method of characteristics.
SMFC	synchronous motor generator with full power converter
SVC	static volt-ampere reactive compensator. Devices for providing reactive power on high-voltage electricity transmission networks
TSO	transmission system operator
TU	turbine mode
XFLEX-HYDRO	Hydropower Extending Power System Flexibility - project funded by the European Union [141]

Indices

0	high pressure reference section machine
2	low pressure reference section machine
1’	high pressure reference section runner
1”	low pressure reference section guide vanes
2’	low pressure reference section runner
abs	absolute
bypass	bypass branch
elec	electric
FL	fluid
gross	gross head
HWV	head water vessel
hyd	hydraulic
ini	initial value
max	maximum
meas	measurement
mech	mechanic
m	meridional component
min	minimum
model	model machine
nom	nominal value
opt	optimizer or optimization

perm	permitted
PP	power plant
proto	prototype machine
PS	pressure side
pumps	service pumps or pumps branch
r	radial component
rated	rated operating point
rel	relative
ref	reference
RO	rotor shaft
RU	runner
set	setpoint
sim	simulation
SS	suction side
steady	steady-state conditions
TR	test rig
trans	transient corrected value according to [2]
TWV	tail water vessel
u	circumferential component
unsteady	unsteady conditions
z	component of the axis of rotation

Latin Letters

Symbol	Description	Unit
a	guide vane opening	m
a	speed of sound	$\mathrm{m\,s^{-1}}$
A	area	$\mathrm{m^2}$
I	pipeline characteristic impedance	$\mathrm{s\,m^2}$
$\vec{c}$	vector of velocity or absolut velocity	$\mathrm{m\,s^{-1}}$
c	velocity or absolut velocity	$\mathrm{m\,s^{-1}}$
C	constant value	*unit*
C	compressive modulus	$\mathrm{kg\,s^{-2}\,m}$
C^+	C^+ characteristic line for MoC	$\mathrm{m\,s^{-1}}$
C^-	C^- characteristic line for MoC	$\mathrm{m\,s^{-1}}$
D	diameter	m
e	error value	m
E	specific hydraulic energy of machine	$\mathrm{J\,kg^{-1}}$
f	frequency	Hz
Fr	Froude number	–
g	acceleration due to gravity	$\mathrm{m\,s^{-2}}$
H	turbine or pump head	m
h_y	transformed output value of the controller structure of the optimizer	m
i	iteration step of optimization	–
$\vec{i}$	unit vector	–

Symbol	Description	Unit
k	sampling factor to adjust the optimizer time step	–
K_{hn}	head correction factor for transient rotational speed	m^2
K_{hQ}	head correction factor for transient discharge	m^{-1}
K_{TQ}	torque correction factor for transient discharge	$\mathrm{kg\,s}^{-2}$
K_P	propotional value of optimizer	–
$\vec{L}$	angular momentum vector	$\mathrm{N\,m}$
L	length	m
$\dot{m}$	mass flow	$\mathrm{kg\,s}^{-1}$
n_{ed}	speed coefficient	–
n	speed of rotation	min^{-1}
p	pressure	Pa
p_{vap}	vapor pressure $f(\theta)$	Pa
P	power	kW *or* MW
Q_{ed}	discharge coefficient	–
Q	discharge	$\mathrm{m}^3\,\mathrm{s}^{-1}$
r	radius	m
R	pipeline resistance coefficient	$\mathrm{s}^2\,\mathrm{m}^{-3}$
R	fixed radius	m
Re	Reynolds number	–

Symbol	Description	Unit
s	length	m
Sr	Strouhal number	–
t	time	s
t_0	start of fast transition PU to TU mode	s
t_1	end of fast transition PU to TU mode	s
t_2	start of fast transition TU to PU mode	s
t_3	end of fast transition TU to PU mode	s
$\tilde{t}$	time sequence of setpoint values	s
$\hat{t}$	shifted time for service pump performance sequence	s
T_a	period for shifting the time sequence of the service pump performance	s
T	torque	N m
T_{ed}	torque coefficient	–
T	time of oscillation or specified time period	s
$\vec{T}$	torque vector	N m
u	circumferential velocity	$\mathrm{m\,s^{-1}}$
$\vec{u}$	vector circumferential velocity	$\mathrm{m\,s^{-1}}$
$\vec{w}$	relative velocity vector	$\mathrm{m\,s^{-1}}$
x_{t-Fr}	time scaling factor for Froude similarity	–
x_{t-Sr}	time scaling factor for Strouhal similarity	–
y	variable as dummy for different machine parameters	*unit*
z	reference level	m

Greek Letters

Symbol	Description	Unit
α	absolut flow angle	$^\circ$
γ	relativ guide vane opening angle	$^\circ$
β	relative flow angle	$^\circ$
β^*	blade angle	$^\circ$
Γ	circulation	$\mathrm{m^2\,s^{-1}}$
ϕ	blade tilt angle	$^\circ$
η	efficiency	$-$
Θ	rotating inertia	$\mathrm{kg\,m^2}$
λ	friction coefficient	$-$
ν	kinetic viscosity	$\mathrm{m^2\,s^{-1}}$
Ω	angular acceleration	$\mathrm{s^{-2}}$
ω	angular velocity	$\mathrm{s^{-1}}$
$\vec{\omega}$	angular velocity vector	$\mathrm{s^{-1}}$
Φ	time span	s
ρ	density	$\mathrm{kg\,m^{-3}}$
σ	cavitation number	$-$
θ	temperature	°C

Symbol	Description	Unit
Υ	integral of absolute value of error	$\mathrm{s} \cdot unit$
Υ_t	time-related integral of absolute value of error	$unit$
Υ_{norm}	normalsized error value	$-$

1 Introduction

In 2019, the emissions of CO_2 (carbon dioxide) resulting from the burning of oil, gas, and coal reached their all-time high and was briefly reduced by the Corona virus Pandemic until today [51]. The effect of this greenhouse gas on the climate is an undisputed fact according to the current state of science [19]. In order to mitigate the consequences of the resulting climate change, governments around the globe are trying to turn the tide with political programs [33, 53, 114]. One basis is the Paris Climate Agreement. With this convention the league of nations decided to limit average global warming to 2 °C compared to pre-industrial times [136].
One key to achieve this goal is the expansion of emission-free energy sources, such as solar and wind power. However, the increasing share of these volatile renewable energies in total electricity generation creates new challenges [52, 65].

Due to its specific characteristic, hydropower is moving into a new focus as part of the solution. In contrast to wind and solar power plants, hydropower plants are particularly controllable. In addition, pumped storage power plants can eliminate the temporal discrepancy between generation and demand with sufficient flexibility and high efficiency [21].
As a consequence hydropower plants are used more often in off-design operating points. In addition to loads such as pressure fluctuations in part-load [24] or full-load [75] operation, the number of load changes from control interventions to stabilize the electrical grid is also increasing [25]. Frequent changes of operating points, as well as fast transitions, lead to further stresses on all components involved. All these unsteady and transient load cases have an influence on the lifetime and service intervals of a power plant. In order to reduce fluctuations and increase operational flexibility, energy companies are focusing more and more on variable speed machine technology for the renovation or new construction of pumped storage power plants [17, 36, 62, 63, 107].

For the development of these hydraulic machines, 3D-CFD simulations and model tests on laboratory test rigs are used to investigate the properties of the machine. Especially in the experiments, but also in many CFD simulations, steady-state boundary conditions are considered. This means that the guide vane opening, the rotational speed as well as the inflow conditions remain constant. The transient

behavior of the prototype, e.g. the interaction with the piping system during start up, shut down, increase or decrease of power, and others is explored and evaluated by means of 1D simulations.
Contrary to the model acceptance tests, standardized in IEC60193 [50], there is no established procedure for transient investigations in test rigs. However, the interest in reproducing transient load conditions physically is gaining momentum.
With the approach of the present work, a methodology for performing transient model tests is given. Factors influencing the results, both numerically and experimentally, are presented and the limitations of this methodology are identified. The findings serve as a basis to establish a uniform procedure for the investigation of transient load conditions in the development of hydraulic machines.

1.1 Research on Hydraulic Transients

The phenomena of transient flow is known to humans for many centuries. Since then, various scientists have established more and more precise equations to describe their effects mathematically. Growing industrialization, increasing energy requirements, and new technologies gave a significant boost to research efforts in the field of transient flows at the beginning of the 20th century.

Basic Experimental Investigations

In 1937, Knapp describes a procedure for creating a map of the characteristic of a hydraulic machine [61]. With this map, he was able to record the entire machine characteristic from pump operation over pump brake operation to turbine operation and pumping in the direction of turbine rotation. Further, he discussed the possibility of predicting the behavior of the machine during the occurrence of transient conditions and described an analytical model for calculation. In this model, he also addressed the interaction with the connected piping system. He confirmed his assumptions with a series of experiments.

Several decades later, in 1962, Otashi established an analytical model to describe pressure increases in axial turbopumps due to fluctuating discharge [85]. His calculations based on the determination of the deflection angle in a linear two-dimensional blade cascade due to periodically oscillating inflow conditions.

In experiments with turbopumps, he was able to show a reliable approximation to the analytical model.

Safwat investigated the transient behavior of piping systems during the opening and closing of valves and published the results in his dissertation in 1972 [104]. His findings from the analytical and experimental investigations on cooling pipeline systems for thermal power plants are subsequently applied to general piping systems.

Like Safwat, Eichinger also investigated transient flow through piping systems in 1992 [29]. The individually and periodically applied pressure surges were caused by specially designed pressure surge generators. His focus was particularly on the investigation of the frictional behavior during transient flow processes.

These investigations are followed by a series of different publications by Tsukamoto et al., Barrand and Picavet, Saito, and Schneider, who combined some of the previous works. For example, the behavior of centrifugal pumps during start up from standstill to nominal operation [6, 105, 135] or shut down from nominal operation to standstill [133] were investigated in detail. The behavior of a centrifugal pump, when opening or closing valves in the connected upstream and downstream pipe [134] or when single pressure waves occur at a constant rotational speed [109], was also examined more intensively. All authors used experiments to substantiate their analytical calculation approaches to describe the transient behavior of the machines.

A whole series of the above-mentioned works point out the deviations between the actually measured results of the transient experiments and the analytically calculated results. An indication is found in the characteristic diagrams, which are classically determined from steady-state measured conditions.
In his dissertation from 1990, Acosta Del Carpio describes that a significant influence on the transient behavior is given by the inertia of the fluid masses in all parts of the hydraulic machine [2]. If a rapid change in rotational speed occurs, these masses must be taken into account in the analytical calculation. With his approach, an improvement of the previously established analytical models are possible.

A second reason for the discrepancies between experimental and analytical results is the cavitation phenomena, which is not adequately captured in some studies. Therefore, in 1999 Tanake published a series of papers with the results of the repeated experiments of Tsukamoto et al. [133–135] and included the occurrence of cavitation in the analytical models [123–125]. There is also a particular focus on the analysis of cavitation during the start up of turbopumps for rocket engines in the work of Duplaa et al. published in 2010 [28].

With the increasing development of measurement technology, the possibilities for measuring details of the flow in pipes and machine parts were improved. This led to a more precise analysis of the flow fields, away from the averaged flow quantities of a one-dimensional observation, towards the possibility of a three-dimensional recording. Thus, it is possible to detect unsteady or transient flow conditions using PIV (Particle Image Velocimetry) and LDV (Laser Doppler Velocimetry) measurements [9, 59, 90]. Furthermore, it became possible to measure mechanical loads on the surfaces of machine components which are in direct contact with the fluid, even in the rotating system of the runner. For this purpose, small piezoresistive pressure transducers and strain gauges are attached to the relevant locations on the component to determine the stresses induced by the interaction between the fluid and the structure [35, 70].

In the use of new measurement techniques, one of the interests is to get a better estimation of the loads on the entire turbomachine during its service life. This information is important for power plant operators and equipment suppliers. The resulting parameters such as lifetime, downtimes, and maintenance intervals are key decision factors for new installations or refurbishment of existing plants. Experimental results to determine such lifetime loads caused by pressure fluctuations at the blades of a propeller turbine are published in 2010 by Houde et al. [45, 46].

A whole series of experiments with the same objective is published by Trivedi et al. The investigations determined the mechanical load on various components of a high-head Francis model turbine. The model was put into different states, which corresponded to a certain operation mode of the prototype. Thus, the loads of a start up and shut down [130], load acceptance and rejection (increase and decrease of power output) [127], emergency shut down and total load rejection (generator loses connection to the power grid) [129], speed-no-load [128] and runaway [126] operating conditions are imitated. In all experiments, a wide variety of measurements are carried out, such as pressure fluctuations on the rotor blades, the guide vanes, and in the blade-less area. These works are also used as validation cases for CFD simulations.

Investigations of transient flow with 1D simulations and 1D-3D simulation coupling

Parallel to the developments in experimental research, powerful computer solutions for the calculation of one-dimensional plant dynamics simulations and three-dimensional flow simulations are developed.

For example, the Institute of Fluid Mechanics and Hydraulic Machines (IHS) at the University of Stuttgart developed a real-time capable 1D simulation software called SIPROHS (Simulation Program for Hydraulic Systems). With this software tool, simulations of entire hydropower plants with all relevant hydraulic components, the electrical machines, and the interaction with the electrical grid [40] are possible. The solver of this software is based on the method of characteristics (MoC) to determine the values of transient flow. Comparable programs are developed at various other institutes, such as the Hydraulic Machines Laboratory of the Ecole Polytechnique Fédérale de Lausanne (EPFL) [117].

This offers the possibility to simulate and analyze thousands of different variants of a given load case under different boundary conditions in a relatively short time. Among others, these studies include the investigation of the behavior of delayed load rejection in combination with other machines [34], the optimization of the shut down behavior of a power plant in case of emergency [58], the combination of many simultaneously operating machines in hydraulic short-circuit operation [54, 55] investigation of geometry variations such as surge tanks, pipelines, etc. [13], the stability analysis in case of runaway [80, 81], the stability analysis of power plant controllers [4], or the recovery of power grids with hydropower plants after a blackout [12].

This wide range of possible applications requires the prediction of the flow behavior and pressure surges close to reality. Therefore, these 1D software tools are constantly being improved and expanded. Examples are the implementation of cavitation models or models of unsteady friction.
One of the earlier models of cavitation in 1D simulations are set up by Brennen and Acosta [11] or Ghahremani [37]. They extended the original conservation equations by the parameters cavitation compliance and the mass flow gain factor, which are necessary for the mass conservation equation of cavitating flow. These approaches are refined by Dörfler [23] and Chen [16] for different operating points of Francis turbines. Furthermore, Pezzinga developed an additional viscosity term [91] in order to consider an additional dissipation in the momentum equation [3, 43]. In 2020, Decaix et al. published another approach to determine these parameters. His approach is not based on measurements but on the comparison of 3D-CFD to 1D results [20].

In addition to these findings, a realistic reproduction of pressure wave propagation in 1D simulations is also of great importance. In 2012, Landry et al. presented an extension of the conservation equations to take into account the effects of unsteady

friction and viscoelastic damping in the simulation. Using these extensions and comparing the results to a series of measurements, they demonstrated a more accurate prediction of the behavior of pressure waves in pipelines. [66].

Another challenge in the modeling of 1D simulation is the steady-state measured characteristic diagram. As described before, in some transient load cases deviations between the actual behavior of the machine and the determined simulation results can occur.
Up to a certain accuracy, this problem can be solved with the help of 3D-CFD simulations. The simulation of a 3D flow field allows a detailed resolution of the flow in the machine. Time-resolved pressure and flow variations caused by partial load operation [64], full load operation [137, 138], or the rapid change of rotational speed [118] are detected with 3D simulations.
However, these simulations are resource- and time-intensive. For this reason, it is not practicable to analyze entire power plants with this method. In most cases, the simulation domain is limited to the hydraulic machine or specific parts of it. Thus, the boundary conditions at the inlet and outlet must be specified in the simulation setup.

The combination of both software solutions, 1D and 3D simulations, enables an even more accurate reproduction of the transient behavior of a power plant. The complex three-dimensional flow in the machine is simulated by CFD and the interaction with the adjacent piping system is calculated with the 1D plant dynamics software. The exchange of the information of the averaged flow parameters with the 1D software takes place in every time step at the inlet and outlet boundaries of the CFD grid.

This approach to analyze complex flow systems was used by various authors from different scientific disciplines, such as investigations of cooling water systems in nuclear power plants [89], simulation of blood flow in the human body [7], engine simulations [8], and more.

One of the earliest works in the field of hydro power is published by Ruprecht et al. [102]. He coupled the CFD simulation of a Francis turbine at part load with the water passages of a representative power plant. The flow behavior in the pipelines was simulated by a 1D solver. His results show a discharge variation of about 1 % which seems small compared to real power plants at the same load conditions. An overload case on a Francis turbine was investigated by Mössinger et al. using two-phase CFD coupled with a 1D simulation [73]. His results also show deviations from measurement

results. According to Mössinger, a reduction of these deviations are possible by improving the cavitation and turbulence models [74].

In 2019, Yin et al. published a study of transient load cases using 1D-3D coupling [143]. The authors simulated simultaneous load rejection scenarios of two pump turbines and compared their results with pure 1D simulation and experiments. Assuming symmetrical upstream pipelines and downstream pipelines respectively, the CFD simulation was performed with only one pump turbine and connected to both pipelines. They explained this approach with the reduction of the computational effort.

Finally, it should not be underestimated that also with 1D-3D coupling, the investigation of thousands of different load cases - as usual for 1D simulations - is not possible, even today. The reason for this remains the time-intensive transient CFD simulation.

Investigations of Grid Support based on Variable Speed Pump Turbines

The steady growth in the share of fluctuating renewable energy sources in the European interconnected grid leads to an increasingly fluctuating grid frequency. Since generation and consumption cannot be guaranteed at the same time, security of supply requires efficient storage technologies [48, 87]. It is well known, that pumped storage power plants play an important role in energy transition due to their special advantages [98, 111].

In order to fulfill this role and contribute to grid stability, it will be necessary that storage power plants operate more flexibly in the future. There will be significant more and faster changes of operating points. In addition, a wide operating range will be required in order to provide differentiated power input or output. To extend the limits of performance and to get a better prediction of the mechanical loads on the machine and other power plant components resulting from extended operation, various research projects have been initiated in recent years. Of particular importance was the research into variable speed machine sets.

In 1998, Schafer described the advantages of a variable speed unit for hydropower plants [106], as was already realized in the planning of the new construction of the Goldisthal hydropower plant in 1997 [31]. From an economical point of view, he saw no possibility of equipping a synchronous machine with a full power converter (SMFC) at that time.

However, he points out that a double-fed induction asynchronous motor generator (DFIM) in combination with a cyclo-converter in the rotor circuit, allows a speed range of up to ±10 % around the nominal speed - in pump and turbine rotation direction. This corresponds to a power control range of about ±30 % and allows active power control also in pump mode.
Further advantages are reactive power controls at the interconnection point of the grid, immediate electricity feed into the grid by using the energy stored in the rotating mass, and higher efficiency in part load. The latter was confirmed by Iliev et al. [49] in model tests on a Francis turbine and a pump turbine. Schafer demonstrates some of the other advantages of using 1D simulations.

A few years after Schafer's publication, Hildinger and Ködding went into detail about the differences and characteristics of DFIM and SMFC units [42]. They describe the design differences of the rotors, the operating modes of both concepts, and the connection to the grid via different converters. Because of further developments and lower costs, they saw an increasing potential for SMFC units.
The authors particularly emphasize the advantages for the operation of the power plant. Using SMFC-technology includes maximum flexibility in the choice of rotational speed, fast start up and rapid change of the operating point, acceleration with almost nominal torque from standstill to operating speed, and fast transition from pump to turbine operation or vice versa without disconnection from the grid.
They also point out that hydroelectric power plants are usually equipped with synchronous generators. Thus, it is possible to convert existing equipment to variable speed operation using an SMFC-bypass-concept. An advantage that makes a complete re-equipment unnecessary.

Since grid stability and security of supply is an issue of the entire European interconnected grid, the research project HYPERBOLE (HYdropower plants PERformance and flexiBle Operation towards Lean integration of new renewable Energies) of the European Union was launched in 2013 [47]. The aim of this project is to make more intensive use of the properties of hydropower to meet the challenges of integrating renewable energy sources. Thus, with the help of leading European research institutions and companies, the hydraulic, mechanical, and electrical dynamics of hydropower plants under future operating conditions were investigated.

In the context of the HYPERBOLE project, Hell [41] describes the differently fed power grids of selected European countries and analyzes their flexibility according

to the methods described by Yasuda et al [142]. Using the example of Great Britain - which has a high proportion of RES (renewable energy source) - he shows the different effects of pumped storage power plants with different technologies on the grid frequency and thus the stability. For these simulations, he uses a pumped storage power plant with a reversible pump turbine which operates in one case at fixed speed and at another case at variable speed. According to his study, the high requirements of the TSO (Transmission System Operator), especially in pump operation, can only be met with variable speed units.

Using the SMFC-technology as an example, Claude gives a deeper look at the structure of the electrical components of such a variable speed unit. In his publication, he also discusses the case of a fast change of operation from pump to turbine mode from the perspective of the electrical components [18].

Fast transitions from pump to turbine mode and vice versa were carried out in scaled physical model tests by Ruchonnet and Braun [100]. For these tests, the change of rotational speed was specified as linear. The necessary model head was generated by the variable speed service pump of the test rig. The tests were repeated for different guide vane openings and different durations of the fast transition.

With the help of these measurements, 1D simulations of the test rig were carried out and the results have been compared [101]. In a further step, 1D plant dynamic simulations of the prototype power plant were carried out, which was fictitiously equipped with an SMFC [83, 84]. While the behavior of variable speed power plants were already investigated in earlier studies, e.g. [82, 88], special emphasis was placed on transferring the transient process between model and prototype. In addition to the typical laws of similarity, the authors used the Froude similarity to convert the time scale between model and prototype.

Furthermore, transient CFD simulations of the entire pump turbine model were carried out [97, 119–122]. The boundary conditions were defined by laboratory measurements and 1D plant dynamic simulations. These results are used as basis for further experimental investigations of the mechanical loads on the machine.
In addition, to avoid using independent boundary conditions from pure 1D simulation, Stens coupled 1D with CFD simulation to obtain an even better analysis of machine behavior during the fast transition simulation. With this approach, it is possible to evaluate both the model on the test rig and the prototype in the power plant under the direct interactions with the connected piping system. Stens published the results of these investigations in 2018 in her dissertation [118].

Besides the European Union research project XFLEX-HYDRO [141], to further investigate the flexible operation of hydropower plants in combination with renewable energies, there are also new investments in modern test rigs. One of these was built by the IHS at the University of Stuttgart in 2020 [60, 96]. During its design, special attention was paid to the investigation of transient processes, which is reflected in its construction.

1.2 Scope of this Work

The previous section shows the high interest in researching flexible operating modes of hydro power plants. Questions about increased structural stresses on certain machine components, additional revision cycles, and the impact on lifetime, due to additional dynamic loads, are increasingly coming into focus [26, 27]. Decisive factors are which types of load, at what level, and how frequently they occur [67]. These loads have different effects depending on the power plant and its mode of operation.

In addition to time-intensive numerical approaches (e.g., 3D-CFD or fluid-structure interaction simulations (FSI) [108]), model tests are necessary to validate numerical results and support hydraulic machinery investigations. In the case of transient model tests, no standardized procedure is established yet, as it exists for model acceptance tests [50].

The objective of this work is to provide a methodology for the investigation of transient prototype load cases in a physical closed-loop test rig. In this methodology, the characteristic behavior of a prototype during a transient process is replicated at the associated model machine. The machine parameters, which describe the behavior of the prototype, are obtained from 1D power plant simulations. By the help of appropriate similarity laws, these parameters are transferred between the prototype and the scaled model. The results of this parameter transition are used as the setpoint values for the model experiment.
The behavior of various actuators of the test rig, such as valve positions, rotational speeds of the service pumps, and others, influence the quality of replication of the load case. To achieve the setpoint values at the model, 1D simulations of the test rig are used to determine the suitable behavior of these actuators. An iterative optimization procedure analyzes the results and adjusts actuators behavior accordingly. Once the suitable behavior of each actuator is determined, the experiment is carried out at the real test rig.

This methodology is independent of the power plant or the load case under investigation. For the implementation and validation of this methodology, the following issues need to be addressed.
In contrast to steady-state model tests, transient tests require the transfer of the time-dependent machine parameters. This causes an adjustment of the time scale. The choice of appropriate similarity laws and the investigation of their influence on the feasibility is a main task.
Another task concerns the design and equipment of the test rig to implement transient load cases. This is directly related to the determination of the actuators behavior, to enable a sufficient quality of replication. Thus, the design of the test rig and the programming of an optimization procedure are tasks, which need to be handled together.
Once the experiment is carried out at the real test rig, the appropriate measurement technology and data acquisition is necessary to verify the replication of the load case. Therefore, it must be determined, which sensors are needed at which points of the test rig to record meaningful data.
In all these tasks, the limitations of the transient model test according to this methodology and all influencing factors must be investigated.

The findings of this work will provide a starting point for experimental investigations of transient load cases and all related issues, which are generally applicable and not only for the investigated test rig.

2 Fundamentals

The present work is based on two fundamental areas. The first area deals with the physical properties of a hydraulic machine and their transfer between similar machines. The necessary tools to calculate transient flow processes by means of 1D simulation are explained in the second part.

2.1 Physical Background

2.1.1 Basic Physical Quantities of Hydraulic Machines

Hydraulic machinery convert energy which is removed from or added to a fluid. To determine the performance of a machine and to compare it with others, uniform boundaries (reference sections) and calculation methods are used. The International Standard IEC60193 for model acceptance tests [50], which is frequently used in the further description, is suitable for this purpose.

Figure 2.1 shows the design of a reversible pump turbine and its reference sections (blue surfaces) at the spiral inlet (0) and draft tube outlet (2). The specific hydraulic energy E of the machine is determined from the energy differences of the pressures p, the velocities $\vec{c}$ and the geodetic height z (Eqn. 2.1).

$$E = g \cdot H = \frac{p_{abs,0} - p_{abs,2}}{\rho} + \frac{\vec{c_0}^2 - \vec{c_2}^2}{2} + (z_0 - z_2) \cdot g, \left[\frac{m^2}{s^2}\right] \tag{2.1}$$

In addition, the efficiency η of the machine for turbine or pump operation is calculated (Eqn. 2.2) using the torque T and angular velocity ω at the rotor shaft and the relationship between density ρ, discharge Q, and specific hydraulic energy E.

$$\eta_{TU} = \frac{P_{mech}}{P_{hyd}} = \frac{T \cdot \omega}{\rho \cdot Q \cdot E} \quad \text{or} \quad \eta_{PU} = \frac{P_{hyd}}{P_{mech}} = \frac{\rho \cdot Q \cdot E}{T \cdot \omega}, [-] \tag{2.2}$$

Due to various sources of loss not all of the available energy is converted. On the one hand, friction losses occur when the water flows through the individual components

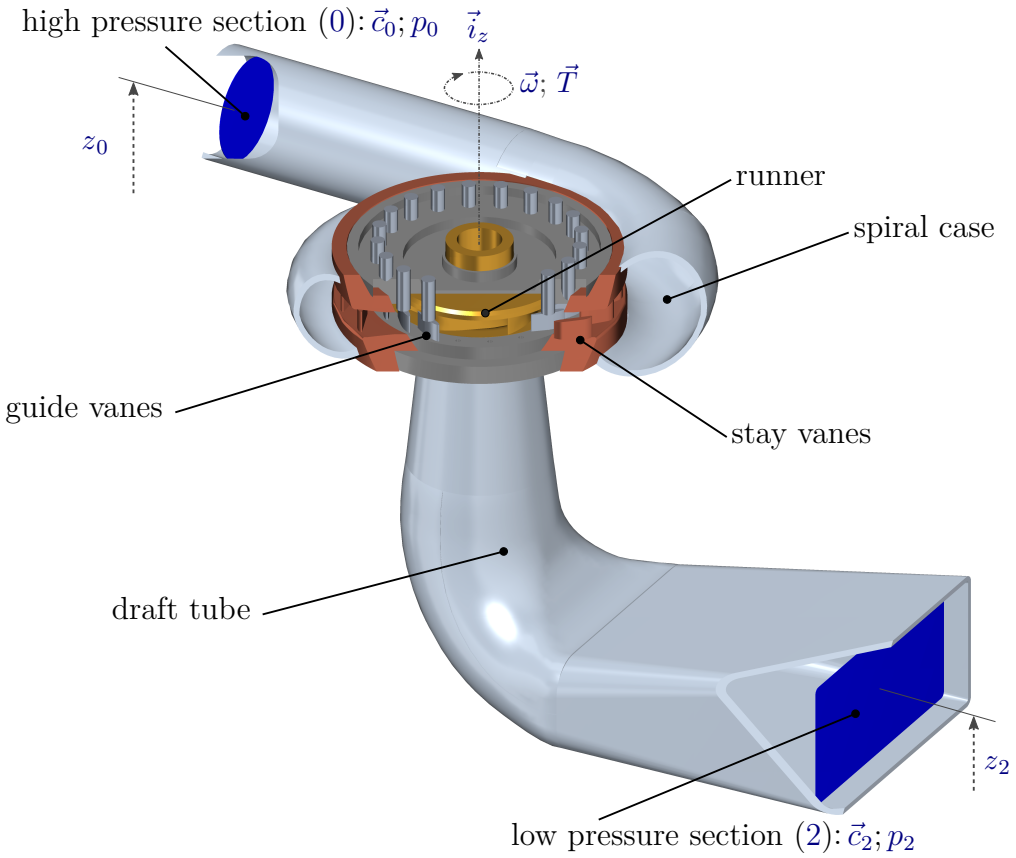

Figure 2.1: Isometric view of a reversible pump turbine.

of the machine. On the other hand, the gaps between rotating and fixed components cannot be infinitely small. This means not all of the volume flow passes the runner. In addition, these gaps are filled with fluid which generates additional friction between fixed and rotating components. Also, the bearing of the rotor is a source of loss [94].

In addition to the sources of loss mentioned above, the flow conditions at the runner inlet and outlet play a special role in the degree of energy conversion. Some damaging or unsteady behavior, such as cavitation at the leading edge, various forms of flow separation, or also full-load or part-load vortices in the draft tube, are caused by this conditions.
For the turbine operation of a reversible pump turbine, the flow conditions at the high pressure and low pressure side of the runner are shown in Figure 2.2 and 2.3.

The adjustable guide vanes (gray and transparent-gray) impose an angle γ to the flow and also adjust the discharge Q through the machine. In the blade-less space between the guide vanes outlet (1") and the leading edge of the runner (1') the conservation of

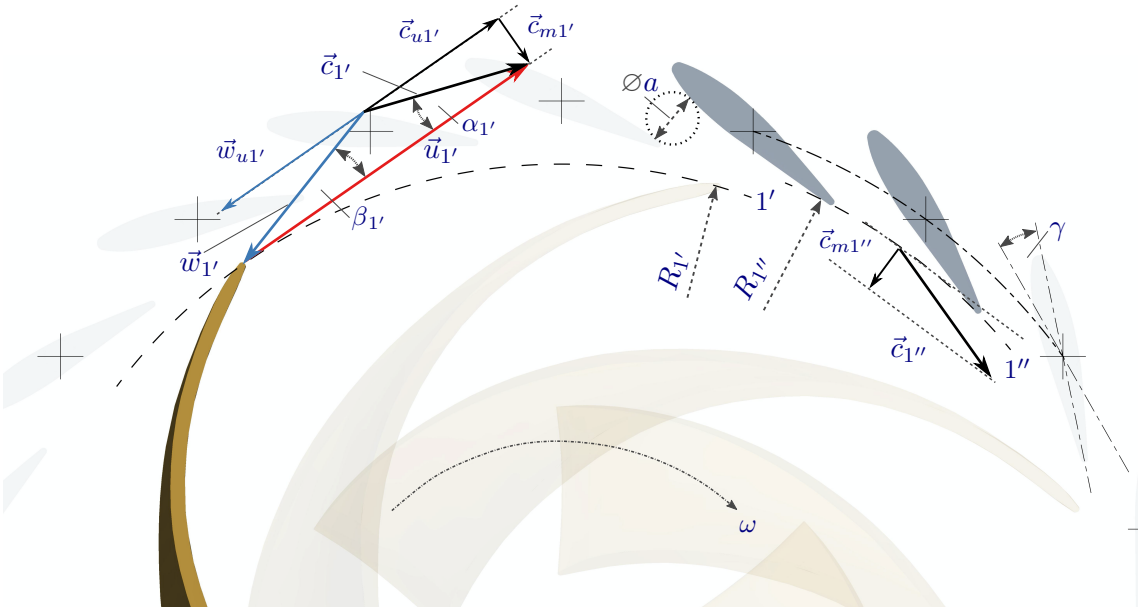

Figure 2.2: Velocity triangle of turbine operation on the high pressure side of the runner (1'). Sectional view normal to the axis of rotation.

the massflow ($\dot{m} = \rho c A = const.$) and the circulation ($\Gamma = r c_u = const.$) is valid [132]. This results in the absolute velocity $\vec{c}_{1'}$ at the inlet of the runner.
Absolute velocity $\vec{c}$ and relative velocity $\vec{w}$ of the fluid in connection with the circumferential velocity $\vec{u}$ of the runner form a velocity triangle [93] which is described mathematically as:

$$\vec{c} = \vec{u} + \vec{w}, \; [\mathrm{m\,s^{-1}}] \tag{2.3}$$

The rotor blades of this example pump turbine are not extended strictly radial. Therefore, the velocity triangles on the low pressure side vary with the radius r (Fig. 2.3).

Even if the absolute and relative velocities have components in axial ($\vec{c}(r)_{z2'}$) and radial ($\vec{c}(r)_{r2'}$) direction, only the circumferential components are relevant for the angular momentum balance and thus for the torque generated by the fluid on the runner (Eqn. 2.4).

$$\vec{T}_{RU} = \vec{L}_{1'} - \vec{L}_{2'} = \rho \cdot Q(r_{1'} c_{u1'} - r_{2'} c_{u2'}), \; [\mathrm{N\,m}] \tag{2.4}$$

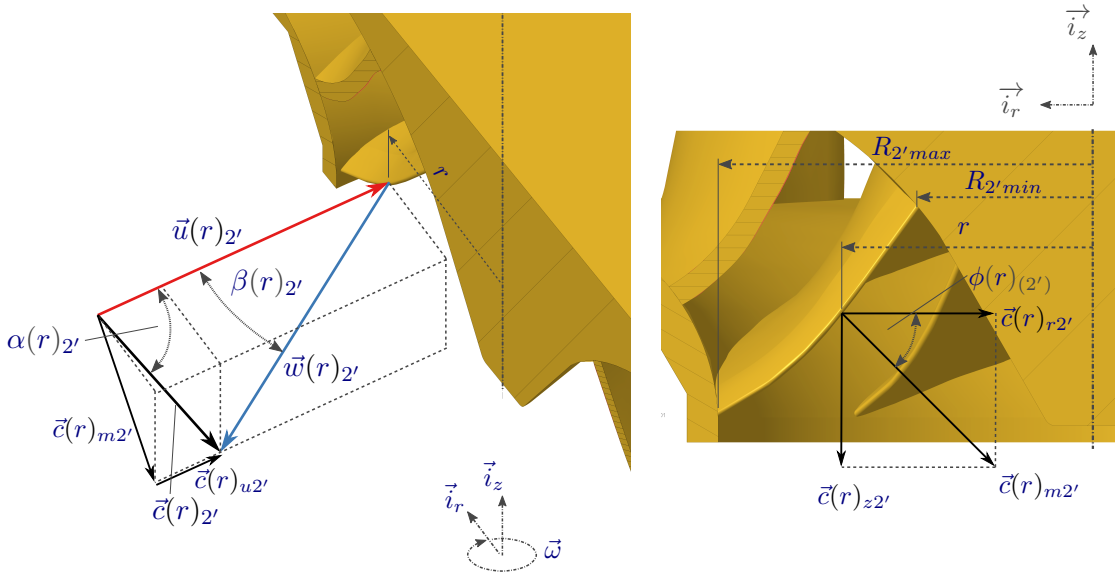

(a) Isometric view. **(b)** Meridional cut.

Figure 2.3: Velocity triangle of turbine operation on the low pressure side of the runner (2') depending on the radius r.

These illustrations explain the occurrence of cavitation and flow separation at the leading edge if flow angle (γ) and blade angle ($\beta_{1'}$) deviate too much [110]. Phenomena which also apply to pump operation.
Also the full-load or part-load vortex in the draft tube are comprehensible on the basis of the velocity triangles (Fig. 2.3(a)). If $\vec{c}(r)_{u2'} \neq 0$ the relative flow $\vec{w}(r)_{2'}$ at the outlet of the runner contains a tangential velocity component, which is not equal to the circumferential velocity $\vec{u}(r)_{2'}$ of the runner. Thus the flow has a spin which creates a vortex in the draft tube. This vortex rotates either in the same direction (part-load vortex: $\vec{c}(r)_{u2'} < 0$) or against (full-load vortex: $\vec{c}(r)_{u2'} > 0$) the direction of rotation of the runner.

As mentioned all these phenomena lead to an unsteady operating behavior and in worst case damage parts of the machine. Besides the steady-state operation of the power plant, some of these effects are also triggered by transient events. Regarding these phenomena, the prototype as well as the model have the same properties which are transferred to the two different sized machines by using the laws of similarity.

2.1.2 Laws of Similarity

When transferring machine properties between prototype and model under steady-state conditions, several basic laws of similarity are applied. In the case of a transient process, an adaption of the time scale, using an additional similarity law, is necessary.

Similarity Laws of Steady-State Operating Behavior

The basic similarity laws of model tests are geometric similarity, kinematic similarity and dynamic similarity [32].
The geometric similarity is based on compliance with the length scaling of the hydraulic components. The kinematic similarity describes the proportionality of the velocity vectors at the runner for a certain operating point, independent of the geometrical size. In conjunction with the geometric similarity, dimensionless numbers of a machine are derived (Eqn. 2.5). These normalized parameters describe the characteristics of a machine and enable a comparison of the operating behavior between model and prototype.

$$n_{ed} = \frac{n \cdot D_{ref}}{\sqrt{g \cdot H}}, Q_{ed} = \frac{Q}{{D_{ref}}^2 \cdot \sqrt{g \cdot H}} \text{ and } T_{ed} = \frac{T}{\rho \cdot {D_{ref}}^3 \cdot g \cdot H}, [-] \tag{2.5}$$

Using the Reynolds number, dynamic similarity is quantified as the ratio of inertial to viscous forces (Eqn. 2.6). Usually, dynamic similarity between model and prototype is almost impossible to achieve. Since the size of the model turbine is limited (D_{ref}) and it is very difficult to change the viscosity of the fluid (ν), model tests are usually carried out at higher rotational speed than the prototype speed. Thus, the deviation in dynamic similarity can, at least, be reduced. The International Standard IEC60193 specifies minimum values for the Reynolds number to limit the deviation in dynamic similarity [50].

$$Re = \frac{u_{ref} \cdot D_{ref}}{\nu}, [-] \tag{2.6}$$

Similarity Laws of Transient Processes

If a time-dependent process is to be compared between model and prototype, the time scale which determines the duration of a process has to be adapted. In literature,

two different approaches are described. According to these approaches, the initial rotational speed of the runner at the beginning of a model test is either freely selectable or has a linear dependence on the process duration.

One of the first publications tries to establish this time scale adjustment by using the Froude similitude [83]. The Froude number Fr is mainly used for free-surface flows and gives a ratio between convective inertia forces to gravity forces (Eqn. 2.7). In their approach, the authors inserted appropriate machine parameters into the Froude equation. Therefore, the relationships of ${c_{ref}}^2 \sim g \cdot H \sim \frac{u^2}{2}$ and $u = r \cdot \omega$ are assumed and the reference length L_{ref} is replaced by the reference diameter of the runner D_{ref}.

$$Fr = \frac{c_{ref}}{\sqrt{g \cdot L_{ref}}} = \sqrt{\frac{g \cdot H}{g \cdot D_{ref}}} = \frac{\omega}{2}\sqrt{\frac{D_{ref}}{2 \cdot g}}, \; [-] \tag{2.7}$$

With $\omega = \frac{1}{\Delta t}$ the Froude similarity obtains a relationship between the duration of prototype and model process, which depends only on the geometric scaling (Eqn. 2.8). This time scaling factor is named x_{t-Fr}.

$$\begin{aligned} Fr_{model} &= Fr_{proto} \\ \Rightarrow \frac{\Delta t_{proto}}{\Delta t_{model}} &= \sqrt{\frac{D_{proto}}{D_{model}}} = x_{t-Fr} \\ \Rightarrow \Delta t_{model} &= \Delta t_{proto} \cdot \sqrt{\frac{D_{model}}{D_{proto}}} = \Delta t_{proto} \cdot \frac{1}{x_{t-Fr}} \end{aligned} \tag{2.8}$$

With this approach, the initial rotational speed of the model test is freely selectable. As a result, the sum of the revolutions of the runner over the duration of the process is different at each initial speed. This means runner blades and guide vanes pass each other with different incidences. In addition, this can lead to different characteristic loads acting on the machine components depending on the chosen speed. It is suspected, that the model test of the transient process does not represent the prototype process. However, this requires further investigation.

Using the Strouhal number Sr to transform the time scale provides a different approach which avoids this problem (Eqn. 2.9) [57, 118]. The Strouhal number is often used to evaluate unsteady flow phenomena and is generated from the inertia forces. This number gives a relationship between frequency f and characteristic length L_{ref} to fluid velocity c_{ref}. By converting the frequency to $1/\Delta t$, replacing the reference length

with the reference diameter of the runner D_{ref} and assuming that u is proportional to c_{ref}, a useful equation for transferring the time scale is given.

$$Sr = \frac{f \cdot L_{ref}}{c_{ref}} = \frac{D_{ref}}{\Delta t \cdot u} = \frac{D_{ref}}{\Delta t \cdot R \cdot \omega} = \frac{1}{\Delta t \cdot \pi \cdot n}, [-] \tag{2.9}$$

Under the assumption of a Strouhal similarity between prototype and model, the duration of the process depends on the initially selected rotational speed of the model (Eqn. 2.10). In short, a higher rotational speed leads to a faster process. This time scaling factor is named x_{t-Sr}.

$$\begin{aligned} Sr_{model} &= Sr_{proto} \\ &\Rightarrow \frac{\Delta t_{proto}}{\Delta t_{model}} = \frac{n_{model}}{n_{proto}} = x_{t-Sr} \\ &\Rightarrow \Delta t_{model} = \Delta t_{proto} \cdot \frac{1}{x_{t-Sr}} \end{aligned} \tag{2.10}$$

A special claim of the realization of the Strouhal similarity in the model test becomes clear when considering the acceleration of the rotor (2.11). A change of rotational speed of the prototype rotor acts to the square of the time scaling factor x_{t-Sr} in the model test.

$$\left.\frac{dn}{dt}\right|_{model} = {x_{t-Sr}}^2 \cdot \left.\frac{dn}{dt}\right|_{proto}, [\mathrm{s}^{-2}] \tag{2.11}$$

Under similitude in Froude, the factor of x_{t-Fr} acts only linearly. Figure 2.4 illustrates the relationship between model speed and test duration for a Froude-similar (left) and Strouhal-similar (right) transient process.

Considering the pending issue on Froude similarity and the aim to investigate the limits of the feasibility of transient model tests, the subsequent steps focus on the similarity in Strouhal.

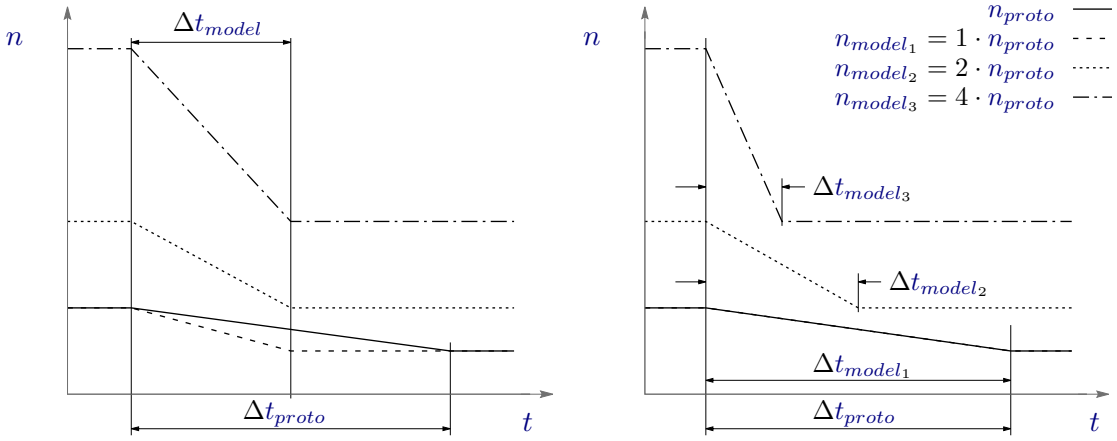

(a) Similitude in Froude. **(b)** Similitude in Strouhal.

Figure 2.4: Comparison of similarity methods for adjusting the time scale using the example of the ratio of rotational speed to duration.

2.1.3 Head and Torque under Transient Conditions

The operation behavior of a machine, which is represented by the n_{ed}–Q_{ed} and n_{ed}–T_{ed} curves in the four quadrant characteristic, is obtained from steady-state measured operating points. A change in discharge or rotational speed, for example, due to a load rejection or acceptance, results in deviations of the actual head and torque compared to the steady-state values. There are two responsible phenomena. First, water cannot be considered as an incompressible fluid in case of transient changes in discharge. Second, during acceleration processes, additional unsteady inertial forces of the rotor and water masses have an influence on the transient behavior of the head and the torque [2, 86].

By imagining a control volume with an abrupt change in fluid velocity at its end, the basic equation of transient flow is derived with the help of mass and momentum conservation (Eqn. 2.12). This equation represents a relationship between the change in pressure to a change of fluid velocity Δc via the speed of sound a, as the compressibility of the fluid. This phenomenon is called water hammer and calculated precisely for all flow-through components of the power plant. But in most cases, this phenomenon is not considered for the hydraulic machine itself.

$$\Delta H = \pm \frac{a}{g} \Delta c, \text{ [m]} \tag{2.12}$$

The speed of sound has a special meaning for the phenomenon of water hammer. It is defined as the ratio between the compressive modulus and the density (Eqn. 2.13). Assuming an isothermal water hammer, which is valid for water as the fluid under consideration, it is also described as the ratio between the pressure change to the density change [95].
Depending on the dissolved gas content in the fluid as well as the absolute pressure, the speed of sound can reach values of up to 1500 $\mathrm{m\,s^{-1}}$. Thus, even small changes in velocity result in high pressure surges, which propagate through the pipelines at the speed of sound.

$$a = \sqrt{\frac{C}{\rho}} = \sqrt{\frac{dp}{d\rho}}, \; [\mathrm{m\,s^{-1}}] \tag{2.13}$$

In his work on the dynamic behavior of centrifugal pumps, Acosta Del Carpio derives equations to determine the unsteady head (Eqn. 2.14) and the unsteady torque (Eqn. 2.15) during the acceleration processes of the runner [2]. He uses the unsteady energy and momentum equation at entire machine, with reference to the geometrical properties. Furthermore, the assumption is made that the steady and unsteady losses in the machine are the same and that the relative velocity in the runner channels is blade congruent.

Both equations consist of three terms. One for steady-state values of head or torque and the others for the correction of changes in rotational speed and discharge versus time. In contrast to the unsteady head, the change of rotational speed in equation 2.15 generates an additional torque from the rotational inertia of the fluid mass Θ_{FL} and the rotor mass Θ_{RO}. The correction factors are derived from the geometry of the runner, the spiral with stay vanes and guide vanes and the draft tube.

$$H_{unsteady} = K_{hn} \cdot \frac{dn}{dt} + K_{hQ} \cdot \frac{dQ}{dt} + H_{steady}(n, Q), \; [\mathrm{m}] \tag{2.14}$$

$$T_{unsteady} = \frac{\pi}{30} \cdot (\Theta_{FL} + \Theta_{RO}) \cdot \frac{dn}{dt} + K_{TQ} \cdot \frac{dQ}{dt} + T_{steady}(n, Q), \; [\mathrm{N\,m}] \tag{2.15}$$

By scaling the constants in Equations 2.14 and 2.15 to model size, the comparison of the transient behavior between model and prototype is possible. However, due to the different bearing constructions, the rotational inertia of the rotor Θ_{RO} is not exactly scalable.

2.2 Numerical Calculation of One-Dimensional Flow

In this work, the calculation of the unsteady pressure wave propagation for pipelines is carried out using the method of characteristics (MoC). With this method large pipe systems with many complex hydraulic components can be calculated. Since a detailed description would exceed the scope of this thesis, only the basic properties are discussed here and reference are made to the following sources for further information [15, 95].

The MoC is based on the partial differential equations for mass and momentum conservation of a compressible fluid. These consist of independent variables s for the distance and t for the time. Using certain simplifications and rearrangements (derivation described in [15] and [140]), a pair of equations of total differentials are obtained (Eqn. 2.16 and Eqn. 2.17). These differential equations are called compatibility conditions and are valid along their characteristics defined by the C^+ and C^- equations.

$$\frac{dQ}{dt} + \frac{gA}{a}\frac{dH}{dt} + \frac{\lambda}{2DA}Q|Q| = 0 \quad \text{for} \quad \frac{ds}{dt} = a \ (C^+ \text{ equation}) \tag{2.16}$$

$$\frac{dQ}{dt} - \frac{gA}{a}\frac{dH}{dt} + \frac{\lambda}{2DA}Q|Q| = 0 \quad \text{for} \quad \frac{ds}{dt} = -a \ (C^- \text{ equation}) \tag{2.17}$$

These characteristics are illustrated in a two dimensional diagram with distance and time axis (Fig. 2.5). Assuming a constant speed of sound, the characteristics are straight lines with positive or negative gradients, respectively.

By integrating the equations along the characteristic between points A and P or B and P, an algebraic relationship is obtained for the hydraulic head H and the discharge Q. These contain the pipeline characteristic impedance $I = a/(gA)$ and the pipeline resistance coefficient $R = (\lambda \Delta s)/(2gDA^2)$. If H_A, Q_A, H_B and Q_B are known from a steady-state calculation, the values for H_P (Eqn. 2.18) and Q_P (Eqn. 2.19) of a transient flow are calculated for the next time step $t + \Delta t$.

$$H_P = \frac{(H_B - IQ_B) \cdot (I + R|Q_A|) + (H_A + IQ_A) \cdot (I + R|Q_B|)}{(I + R|Q_A|) + (I + R|Q_B|)} \tag{2.18}$$

$$Q_P = \frac{(H_A + IQ_A) - (H_B - IQ_B)}{(I + R|Q_A|) + (I + R|Q_B|)} \tag{2.19}$$

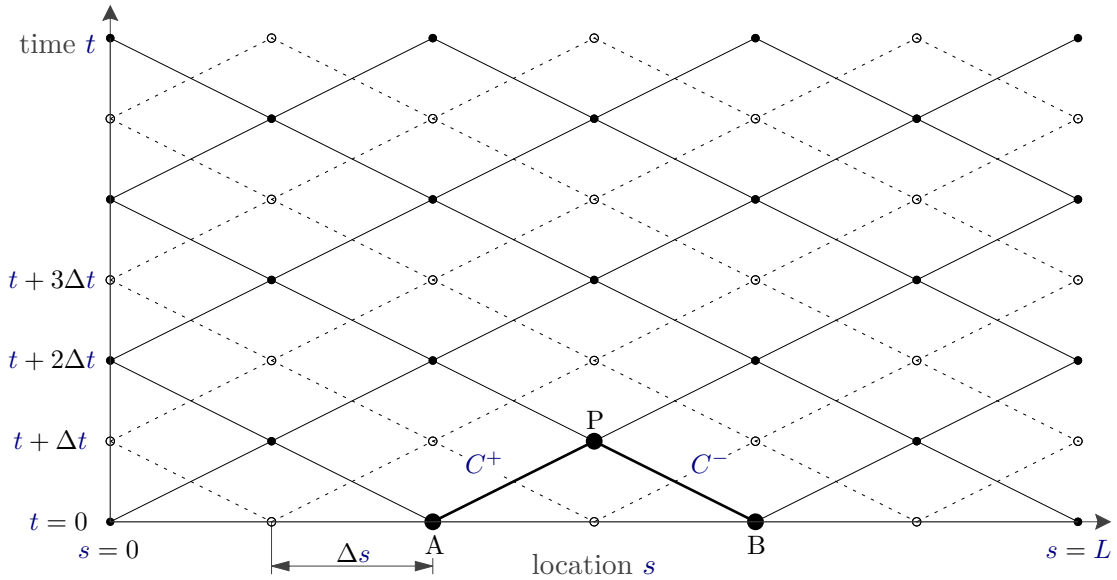

Figure 2.5: Grid of the method of characteristics to determine the condition in the next time step from the previous and locally surrounding conditions.

At the right and the left end of the grid, one of the equations H or Q is coupled with the boundary condition. If this method is extended by a second independent grid, which is shifted by Δs, a solution of the transient flow is obtained for each time step at each grid point. The use of the MoC requires the division of the entire length L into integer intervals of Δs.

3 Power Plant Under Transient Conditions

Hydroelectric power plants are subject to various controlled transient processes during operation, but also to sudden transient events. During these processes and events, a power plant must be operated safely or, if necessary, shut down safely. Conventional power plants have guide vanes and shut-off valves for control. In modern pumped storage power plants, variable speed electrical equipment is often a further control device (detailed explanation in appendix A). In this chapter, a selection of controlled transient processes is presented and discussed which are suitable for transient model tests.

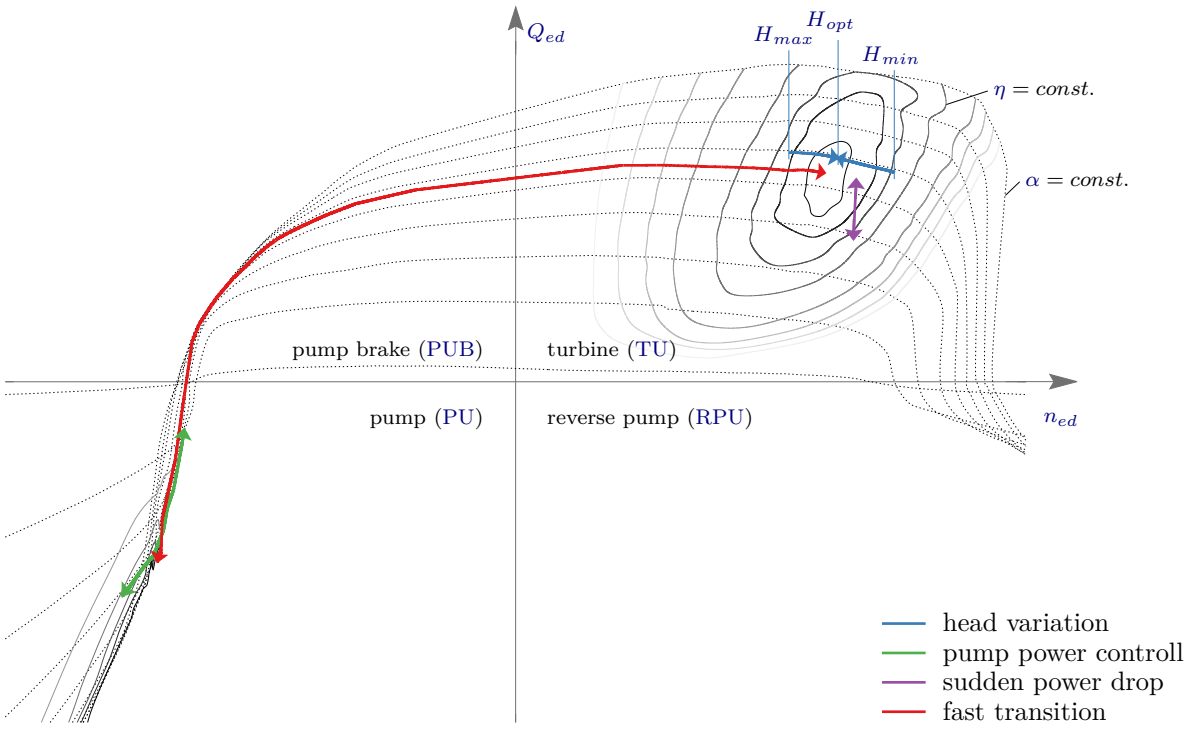

Figure 3.1: Paths of operating points for a variable speed reversible pump turbine in the four quadrant characteristic diagram.

Besides the start up and shut down processes, there are four main controlled operating modes. In the following, these are described from a hydraulic point of view and the

advantages of speed variability are explained. The behavior of a reversible pump turbine under these operating modes is shown by four examples in the normalized n_{ed}-Q_{ed} characteristic diagram (Fig. 3.1).

The blue arrows visualize the deviations of the operating point from the region of higher efficiency due to the deviating head relative to the optimum head. In the pump quadrant, the power control in pump operation by adjusting the rotation speed is illustrated with the green arrows. The purple arrows illustrate the opening and closing of the guide vanes for load acceptance or rejection. Finally, a fast transition from pump and turbine operation or vice versa is depicted with the red arrows.

3.1 Gross Head Variation

The deviation in gross head compared to the optimum head has an influence on the operating behavior of the hydraulic machine. Equation 2.5 describes the behavior of the operating point along a guide vane opening towards smaller or higher n_{ed}-values when head increases or decreases (Fig. 3.1). This leads an increase or decrease of discharge through the machine (compare Q_{ed} of Eqn. 2.5) and thus influences the velocity triangle at the runner (dashed arrows in Fig. 3.2). Misaligned flow at the leading edge could cause cavitation on the pressure side at lower head or on the suction side at higher head, respectively. Consequences are lower efficiency shown in the characteristic diagram and rising pressure fluctuations [49]. Therefore, a continuous operation outside the optimal range can produce damage to the runner.

By adjusting the rotational speed n and thus the circumferential speed $\vec{u}$, the velocity triangle (solid arrows in Fig. 3.2) changes. The relative velocity $\vec{w}$ is again blade congruent (parallel to the blade angle β^*). Because of the changing discharge Q during these processes, also the meridional component of the absolute velocity c_m does not remain constant.

As the variation of the head moves very slowly, this process is quasi steady-state and is not considered as transient. Nevertheless, it is a controlled process for which variable speed equipment is necessary.

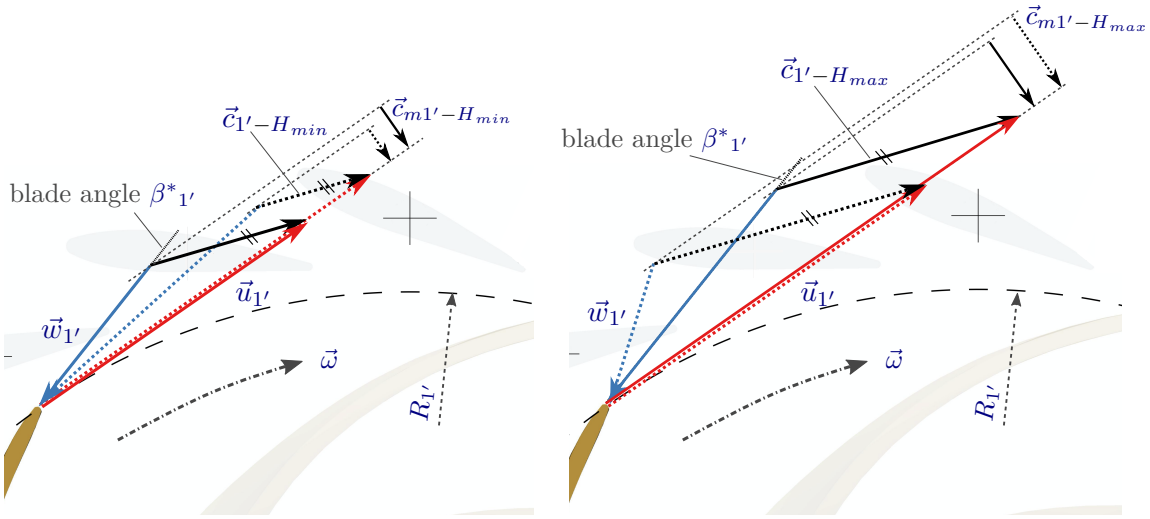

(a) $H < H_{BEP}$. **(b)** $H > H_{BEP}$

Figure 3.2: Comparison of the velocity triangles in turbine operation at the runner inlet of a fixed speed (dashed) and variable speed (solid) reversible pump turbine.

3.2 Controlled Load Acceptance and Rejection

Assuming a request for a controlled power rejection, e.g. by the transmission system operator, a closing process of the guide vanes begins. The opening a is reduced which leads to a change of absolute velocity $\Delta\vec{c}$. This change produces pressure waves which propagate downstream (as low pressure wave) and upstream (as high pressure wave) of the guide vanes at the speed of sound (Eqn. 2.12). Thus the head of the machine increases.
At the first moment of this transient event, the discharge does not decrease in the same relation as head increases. The physical properties of water (inertia and weak compressibility) lead to a short-term increase in power output, although a reduction is requested (Fig. 3.3(a)) [68]. This effect of "wrong control" is particular for hydroelectric power plants. It also occurs the other way around when an increase in power is required and the guide vanes begin to open.

If a hydropower plant is equipped with a variable speed machine, this negative control effect can be avoided (Fig. 3.3(b)). By rapidly changing the rotor speed, the power increase is counteracted by the flywheel effect [41]. The reduction of the braking torque

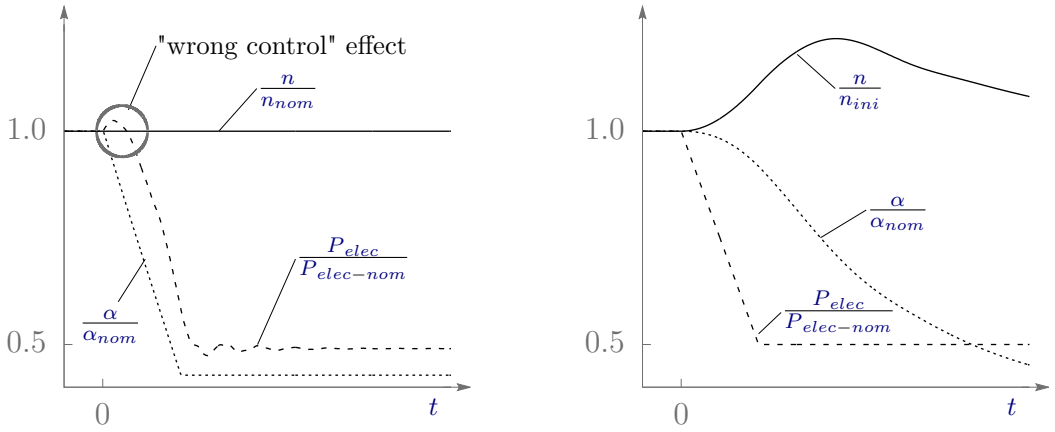

(a) Without variable speed technology the increasing head leads to an increase of power.

(b) With variable speed technology.

Figure 3.3: Normalized values for illustration of power reduction control process in turbine mode.

at the motor generator T_{MG} causes an imbalance, which leads to an acceleration depending on the moment of inertia Θ_{RO} (Eqn. 3.1). The increase in hydraulic power caused by the closing process is stored as rotational energy in the rotor and is not released to the grid as electrical power. In reverse, this energy is released again by decelerating the rotor. A requirement for this operating behavior is a coordinated control between the guide vane adjustment and the change of rotational speed to achieve the demanded electrical power output.

$$\Theta_{RO} \cdot \frac{dn}{dt} = T_{RU} - T_{MG}, \text{ [N m]} \tag{3.1}$$

This operating behavior is important if the grid frequency has reached a critical limit and further stimulation would cause the grid to collapse.

3.3 Power Control in Pump Mode

One of the biggest advantages of variable speed machines is the power control in pump mode. With fixed speed machines, the influence on the discharge and thus the power output is very limited (Fig. 3.4(a)). Under certain circumstances, an adjustment of the guide vanes opening leads to a misaligned flow to the guide vanes and subsequently

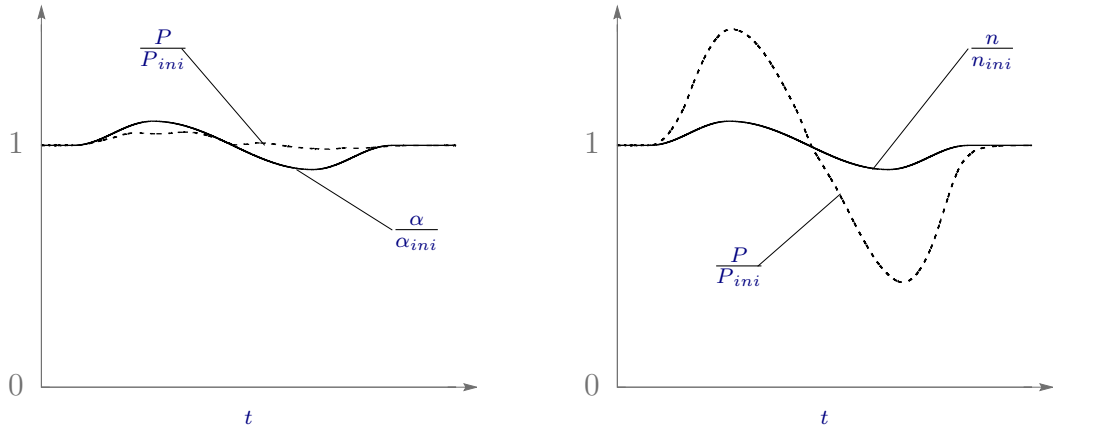

(a) ±10 % of guide vanes opening variation.

(b) ±10 % of rotational speed variation.

Figure 3.4: Normalized values for illustration of power control in pump mode.

to flow separation [39]. By varying the rotational speed and thus the discharge, the power output to the electrical network is determined precisely (Fig. 3.4(b)).

3.4 Change of Operation Mode

A fast transition of a fixed speed machine from pump to turbine mode includes the disconnection from the grid and the closing of the guide vanes to the so-called synchronization position. The rotation in pump direction is decelerated by the acting forces until the rotor speed reverses and accelerates in the direction of turbine rotation. Once the synchronous speed is reached, the electrical machine is reconnected to the grid.
The transition from turbine to pump mode requires complete closure of the guide vanes and blowing-out of the water in the runner section. Subsequently, the rotor must be accelerated until the synchronous pump speed is reached. This is often enabled by an additional small Pelton turbine [38, 103].

For power plants equipped with a double-fed induction asynchronous machine (DFIM-technology, appendix A), the fast transition from pump to turbine mode is similar to the transition with a fixed speed machine. But the more flexible rotational speed range makes it easier to synchronize with the electrical grid. Other advantages are that the reverse process does not require the blow-out of the runner and no additional Pelton turbine is needed to accelerate the rotor in the direction of pump

rotation.

Nevertheless, the procedures described are relatively time-consuming in relation to the demands of stabilizing the electrical grid. This is due to the technology of this machines. Fixed speed machines or machines with DFIM technology always require a wide adjustment of the guide vanes to perform fast transitions. To avoid unnecessarily strong pressure surges, this process cannot be carried out at every adjusting speed.

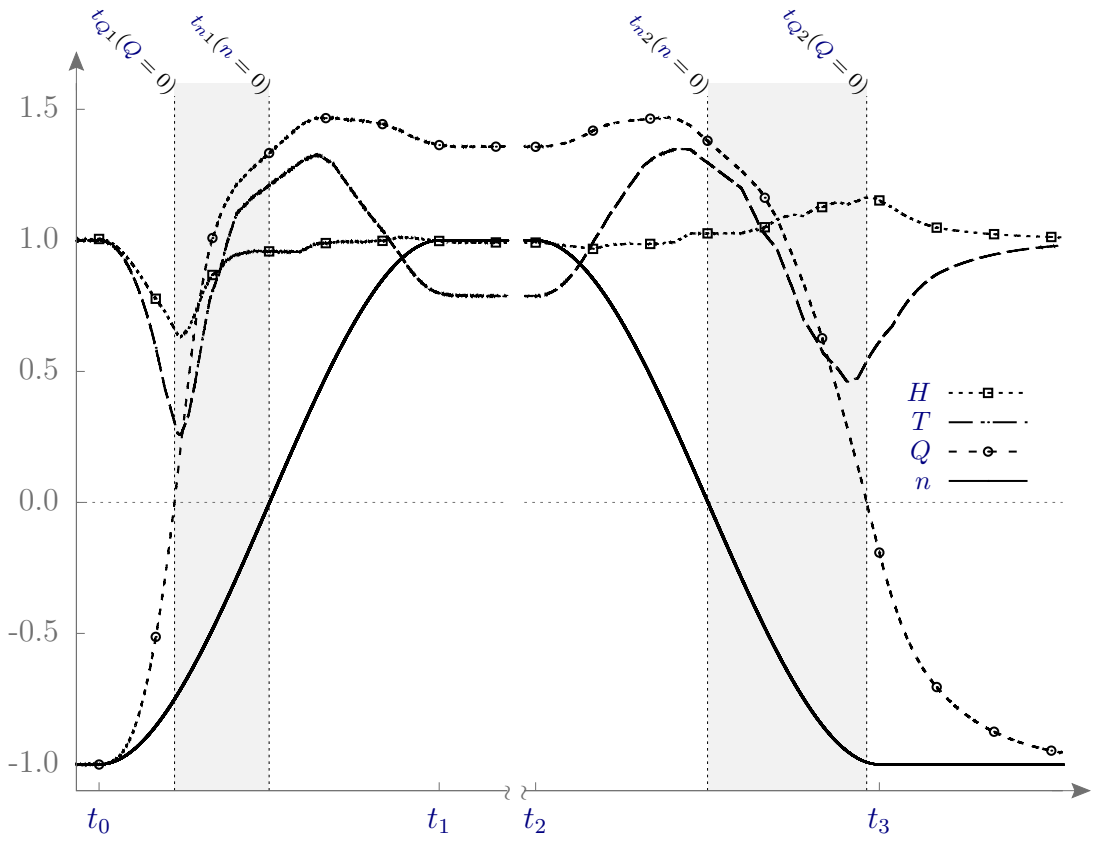

Figure 3.5: Illustration of normalized values of head H, torque T, discharge Q and rotational speed n during a fast transition from pump to turbine mode and vice versa with SMFC technology.

Fast transitions from pump to turbine mode and vice versa of much shorter duration are possible with power plants equipped with synchronous machines in conjunction with full power converters (SMFC-technology, appendix A). With this technology, there is no need to disconnect from the grid, close the guide vanes, and blow-out the runner.

The simulation results of an exemplary transition at a power plant with

SMFC-technology are shown in Figure 3.5. Starting from pump mode at time t_0, the power plant reaches turbine mode at time t_1. The reverse process takes place between the points in time t_2 and t_3.
The guide vane opening remains constant during the entire process. The controlled variable is exclusively the rotational speed. Its sequence is defined as a cubic function between the steady-state operating points. In this illustration, the rotational speed is normalized to the synchronous speed. Head, torque, and discharge are normalized to the initial values in pump mode.

When observing these global values, considerable variations are visible, especially in the progress of the torque. This indicates the occurrence of additional stresses in the machine shaft. Assuming an increasing number of fast transitions, these loads must be evaluated with regard to fatigue strength.
Furthermore, during such a transition, local loads can occur inside the machine. Depending on the initial operating point in the four quadrant characteristic diagram (red curve Fig. 3.1), a variety of flow separation phenomena and cavitation effects occur [118]. This results in particularly high stresses at the runner, which have an influence on the maintenance intervals of a power plant equipment and its overall life-time.

Due to the increasing demand for grid frequency stabilization and the rising use of variable speed machine sets, challenging transient processes can occur in hydropower plants. For this reason, the focus of the present work is on the investigation for replication of such processes in a model test environment.

4 Object of Research

The object of research is presented in this chapter. At first, information about the power plant is given. Then, the closed-loop test rig with the model machine is described which also includes the measurement technology used. Finally, a short explanation of the control of the test rig for the transient model tests is given.

4.1 Power Plant

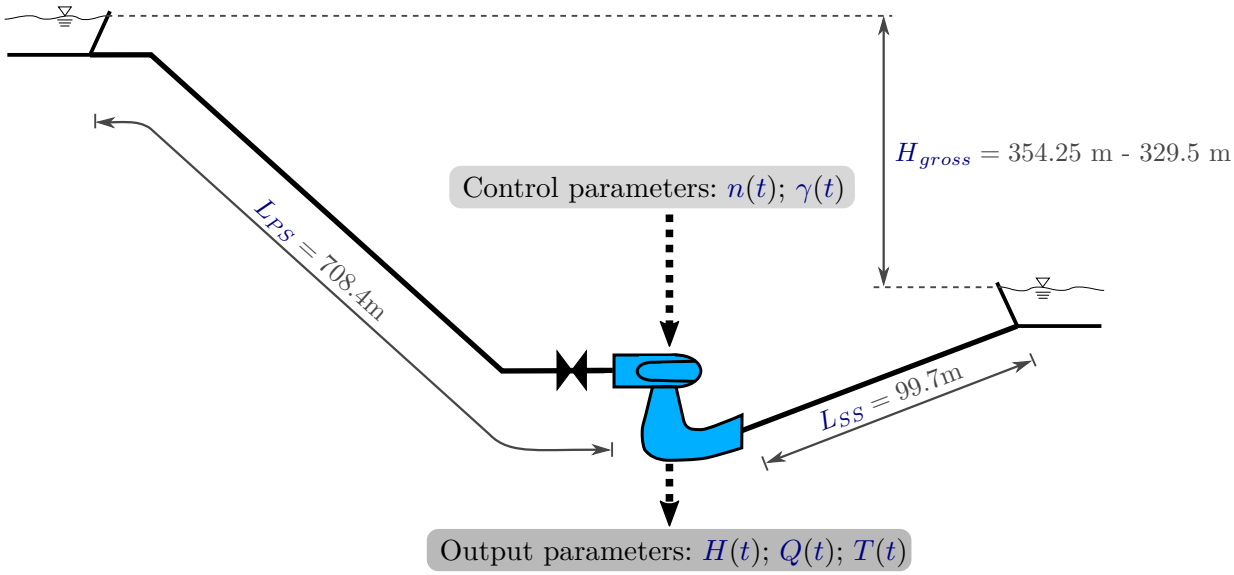

Figure 4.1: Schematic of the power plant with characteristic dimensions.

The object of research is an existing power plant with a reversible pump turbine in the Austrian Alps, schematically shown in Figure 4.1. The nominal power output in turbine mode is about 280 MW. This power plant serves as base for the transient processes, which are replicated in the model test.
The original power plant has a fixed speed synchronous motor generator, which is adapted to a SMFC in the numerical model by specifying the stator frequency. The control variables of the 1D simulations are the rotational speed $n(t)$ and the opening

angle $\gamma(t)$ of the guide vanes. The gross head remains constant during a simulation. The hydraulic behavior of the power plant is obtained as characteristic quantities of discharge $Q(t)$, head $H(t)$, and torque $T(t)$ or the corresponding coefficient $n_{ed}(t)$, $Q_{ed}(t)$, and $T_{ed}(t)$.
Details of the numerical model as well as results of the validation, using measurement data from closing and opening processes during commissioning, are presented in Appendix B.

4.2 Closed-Loop Test Rig

4.2.1 Composition

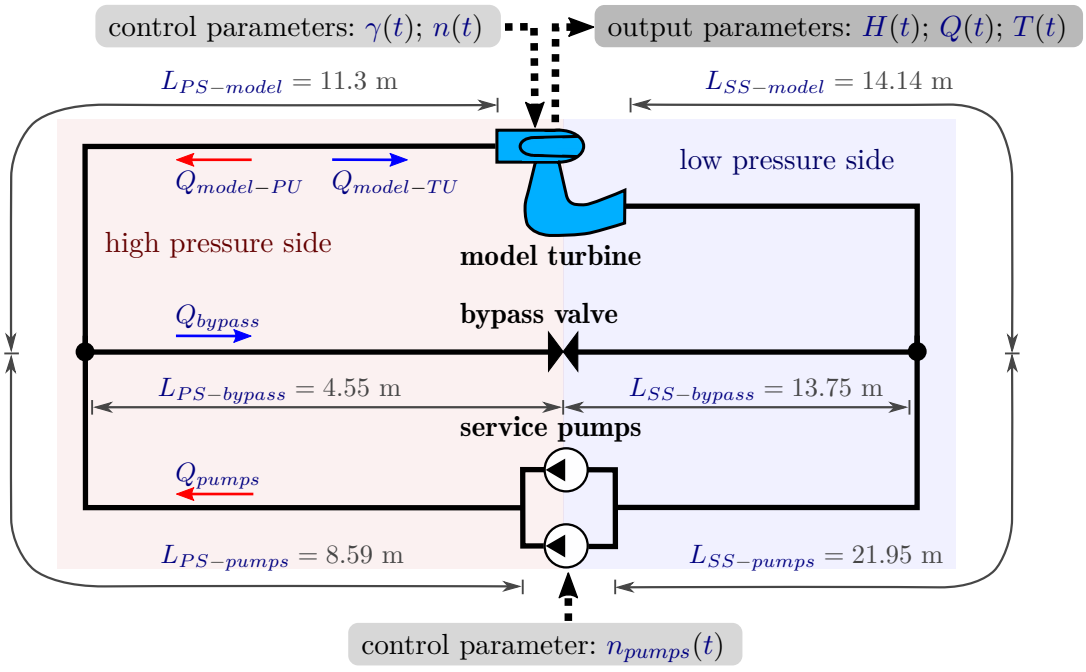

Figure 4.2: Schematic of the test rig with characteristic dimensions of the branches.

The laboratory test rig with the scaled model of D_{model}:D_{proto} = 1:13.358 has three branches, divided into high and low pressure sides. In the lower part of the schematic illustration (Fig. 4.2), the parallel arranged service pumps are shown. These pumps provide the corresponding energy difference in the system. Since the pumps share the same drive motor, they always have the same speed.
The branch with the model is located in the upper part. To enable a dynamic operation

behavior of the model up to a reversal of discharge, the test rig is equipped with a bypass branch. The partially closed valve in-between ensures a flow through the bypass while preserving the pressure difference between the high and low pressure side.

For guide vanes opening of $\gamma/\gamma_{max} = 0.6$ the best efficiency point (BEP) values in turbine mode between model and prototype are compared in Table 4.1. The values for the model machine are listed at single, double, and triple rotational speed of the prototype speed.

Table 4.1: BEP values in turbine operation for $\gamma/\gamma_{max} = 0.6$.

		proto	model		
$D_{1'}$	[m]	4.328		0.324	
n_{model}/n_{proto}	[−]	−	1	2	3
n	[min^{-1}]	375	375	750	1125
H_{nom}	[m]	347.6	1.95	7.79	17.53
Q_{nom}	[$\mathrm{m}^3\,\mathrm{s}^{-1}$]	64.6	0.027	0.054	0.081
T_{nom}	[N m]	4.4×10^6	10.3	41.1	92.4
$P_{mech\|nom}$	[kW]	172×10^3	0.4	3.2	10.9
Re	[−]	33.6×10^6	1.3×10^6	2.4×10^6	3.5×10^6

4.2.2 Measurement Technology

The test rig is equipped with various instruments to comprehensively analyze the course and result of a transient experiment (Fig. 4.3). On the one hand, these techniques are used to check how precisely the transient processes of the prototype can be replicated in the experiment. On the other hand, the entire dynamic behavior of the test rig, during a transient event, is monitored, its physical limits are detected and its characteristic response are captured.

The measurement data acquisition is done with the help of the software LabView™ [76]. In conjunction with the appropriate hardware, it is ensured that a sufficient resolution in time is possible for the acquisition and storage of the data. Further information can be found in [77–79].

The processing and evaluation of the measurement data are carried out according to the standardized specifications of American Society of Mechanical Engineering (ASME) [1, 99] and IEC60193 [50]. In the following, the sensors used and their purpose are described in detail.

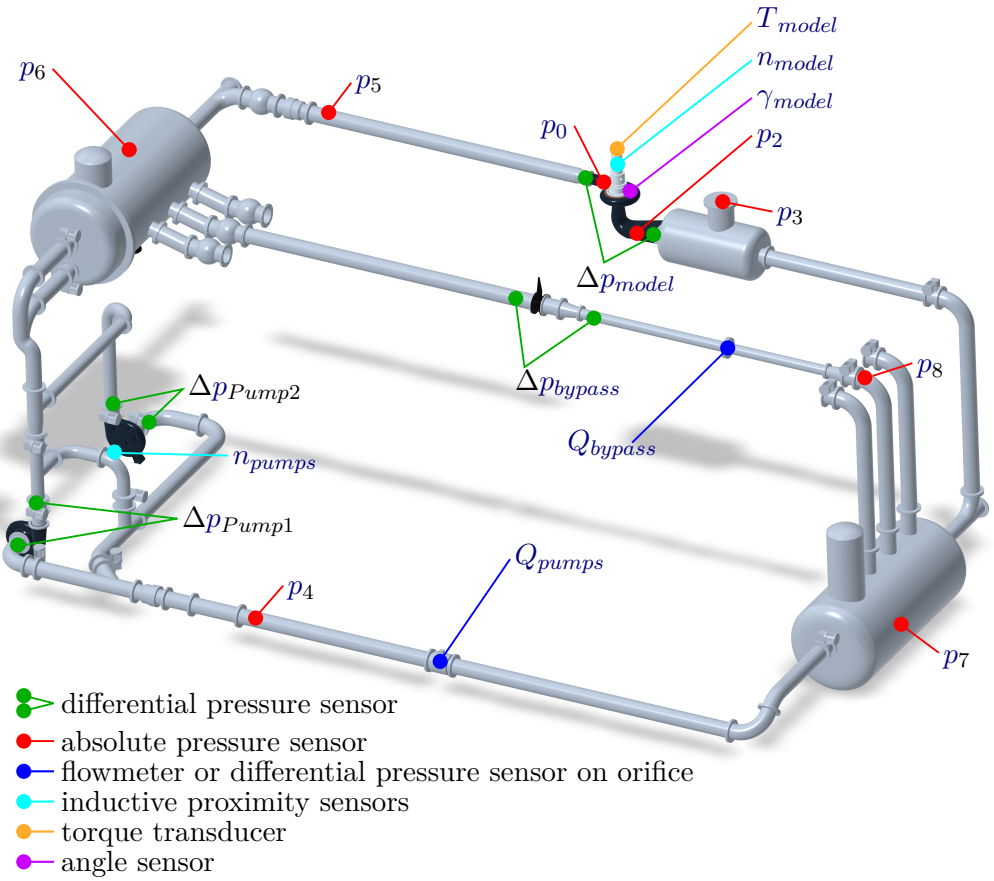

Figure 4.3: Isometric representation of the closed-loop test rig with installed measuring sensors.

Pressure Measurement

Four differential pressure sensors are mounted on the model (Δp_{model}), the bypass valve (Δp_{bypass}) and the two pumps (Δp_{pumps1} and Δp_{pumps2}) to determine the pressure differences. These sensors are characterized by high accuracy.
Three of the eight absolute pressure sensors are located directly on the model machine, more precisely in the spiral (p_0), in the draft tube (p_2), and on the tail water vessel (p_3) of the model turbine. They are intended to record the pressure fluctuations on the model machine during a transient process. The remaining absolute pressure sensors (p_4-p_8) are installed in the piping system. These sensors are intended to detect the propagation of pressure waves in the other branches. All absolute pressure sensors will also be used to determine energy balances in the piping system (Table 4.2).

Table 4.2: Sensors for pressure measurement. Response time is the sum of the dead time and the time constant.

Sensor	Response Time	Sampling Rate	Measuring Range	Uncertainty
$p_0 - p_8$	–	1.0 kHz	0.0 – 6.0 bar	0.1% [139]
Δp_{model}	45 + 100 ms	22.0 Hz	0.0 – 2.48 bar	0.04% [30]
Δp_{Pump1}	45 + 100 ms	22.0 Hz	0.0 – 20.7 bar	0.04% [30]
Δp_{Pump2}	45 + 100 ms	22.0 Hz	0.0 – 2.48 bar	0.04% [30]
Δp_{bypass}	45 + 100 ms	22.0 Hz	0.0 – 138.0 bar	0.065% [30]

Discharge Measurement

The discharge is measured in two branches only. A flowmeter is installed in the pump branch upstream of the service pumps. Contrary to all other specifications on measurement uncertainties, the flowmeter uncertainty refers to the measured value and not the measuring range. The measurement in the bypass is carried out by measuring the pressure difference at an orifice. Calibration is done with the help of the flowmeter. For this reason, the uncertainty is the same (Table 4.3). The discharge of the model turbine is calculated by the difference between the two measurements (Eqn. 4.1).

$$Q_{model}(t) = Q_{pumps}(t) - Q_{bypass}(t) \tag{4.1}$$

Table 4.3: Sensors for discharge measurement.

Sensor	Response Time	Sampling Rate	Measuring Range	Uncertainty
Q_{pumps}	0 + 100 ms	3.75 Hz	0 – 10.0 $\mathrm{m\,s^{-1}}$	0.2% [115, 116]
Q_{bypass}	45 + 100 ms	22.0 Hz	0.0 – 0.62 bar	0.2% [30]

Rotational Speed, Torque and Guide Vane Opening Measurement

To check the rotational speeds of the pumps and the model machine, inductive proximity sensors are installed next to the shafts of each machine (n_{model} and n_{pumps}). Eight shaft markings per revolution guarantee a high resolution, even with rapid speed changes.

The torque of the model machine (T_{model}) is measured by a torque transducer in the shaft. In this experimental setup the torque transducer is located behind the bearing of the rotor. When determining the mechanical power, it must be taken into account that the whole shaft bearing is designed with ball and roller bearings which generate additional friction.
Finally, an angle sensor indicates the opening of the guide vanes (γ_{model}). An overview of sensors used is shown in Table 4.4.

Table 4.4: Overview of the sensors for rotational speed, torque, and guide vane opening measuring.

Sensor	Time constant	Sampling Rate	Measuring Range	Uncertainty
n_{pumps}	$\leq$ 60 ms	$\leq$ 2.5 kHz	–	– [69]
n_{model}	$\leq$ 60 ms	$\leq$ 2.5 kHz	–	– [69]
T_{model}	0.4 ms	1.0 kHz	$\pm$0.5 kN	0.05% [44]
γ_{model}	–	1.0 kHz	0.0 – 60.0 °	0.5% [5]

4.2.3 Test Rig Control System

The test rig is controlled by the operating software. If the opening of the guide vanes and all valves are correctly adjusted, a transient test can start and runs automatically. During such a test, the electrical machines of the model turbine and the service pumps are speed-controlled by the internal feedback controller. This means that the speeds of the machines are specified via separate files of setpoints versus time. The test rig speed controller allows a time discretization up to $\Delta t_{TR} = 0.1$ s.
Since the speed behavior of the model machine is transferred from the prototype via the above mentioned law of similarity, these setpoint values are defined. However, the corresponding behavior of the service pumps is unknown. The procedure for determining the behavior of the service pumps to achieve the setpoints on the model is explained in the following chapter.

5 Procedure for Determining the Test Rig Control Sequence

5.1 General Procedure

In order to reproduce the results of a transient power plant simulation in the physical model test rig, all degrees of freedom must be identified and the modifiable variables must be known and defined. Due to various possibilities and largely non-linear correlations of the acting components, it is almost impossible to find a suitable behavior for these components with analytical approaches. For this reason, the entire test rig is simulated as a 1D-model and the operation behavior of the actuators are adapted via an optimizer.

The process flow diagram gives an overview of the entire procedure (Fig. 5.1). In order to reproduce a transient event in a model experiment, it must be known how the power plant behaves under this load case. This information is gained from a 1D power plant simulation. Subsequently, the result is transferred to the model size according to the laws of similarity described above (Section 2.1.2). These transferred data are used as setpoints for further steps. Additionally, this data is utilized to determine an initial solution for the performance of the test rig service pumps.
With these initial conditions, the 1D simulation of test rig is carried out. Setpoint values and test rig simulation result are compared by an optimizer over the entire simulation time. The aim of the optimization is to determine the appropriate behavior of the entire test rig actuators to ensure a replication of the prototype process at the model with a conformity as high as possible. Based on this comparison, the updated performance curve of the service pumps and, if necessary, an adjustment of the certain valve positions is determined for the next iteration. Afterwards, the test rig is simulated again with the adapted data.
If the iteration limit or a convergence criterion is reached, the optimization loop stops. A file of the pump rotational speed is created, which serves as setpoint data for the

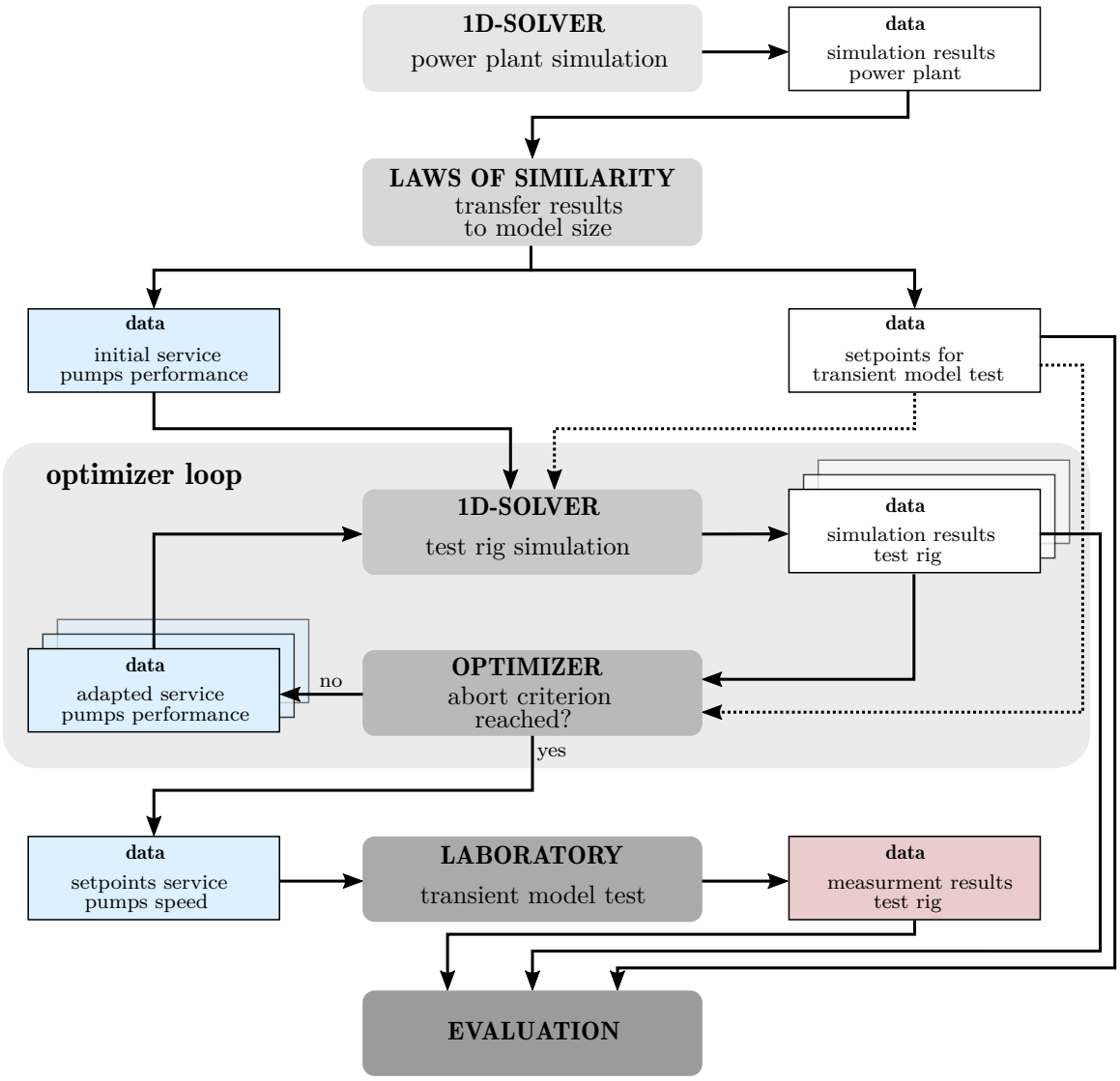

Figure 5.1: Procedure for performing transient model tests.

controller of the physical model test rig. Once this model test is carried out, all data of the setpoint values, simulation results, and measurement results are evaluated.

5.2 Numerical Model of Test Rig

Similar to the simulation model of the power plant, the test rig with all its components and properties is modeled on basis of the original test rig of the laboratory. Physical dimensions of the pipes, valves, and vessels are obtained mainly from drawings. The hydraulic properties of these components are gained from steady-state measurements

of several operating points. Further, characteristic diagrams are used to implement the hydraulic machines. Nevertheless, there are some special features which need to be explained in more detail.

Simulation of a Closed Loop Test Rig

Basically, simulations of any kind have boundary conditions which are essential for the numerical solution. In the example of power plant simulations, these are the energy differences resulting from head water and tail water reservoirs. Based on these energy differences, an initial solution is determined and then the transient process is calculated.

To define the initial conditions for the test rig simulation, the test rig is separated into two pressure zones via closed valves inside each branch before the transient process starts. The pressure in each zones is specified via additional water reservoirs with defined water levels. Immediately at the beginning of the simulation, these reservoirs are separated from the actual test rig by closed valves. The subsequent start up of the machines and the opening of the valves inside the branches follow a fixed sequence until steady-state conditions are reached.
This specification of the initial pressure level has no influence on the behavior of the simulation result. On the one hand, the solver does not take cavitation into account. Values of the absolute pressure below a level of $p_{abs} < 0$ m are numerically possible. On the other hand, the pressure difference between the high and low pressure side is only determined by the hydraulic machines and the bypass valve during the transient simulation. For a further comparison of the measurement and simulation results, all absolute pressure values of the simulation are adjusted by a uniform value in the evaluation step. This value is determined individually for each experiment from a steady-state measurement before the start of the transient process.

Control of Electrical Machines

The rotational speed behavior of the model machine is known from the power plant simulation. It will be implemented via the grid frequency fed to the motor generator of the model machine. Since the applied 1D-solver can only simulate one electrical grid, a fictitious frequency converter is used to control the drive motor of the service pump. In contrast to the real test rig, in the simulation, the two pumps are not connected to one motor via one shaft each, but modeled as two separate pump-motor units with

their own converter. As a result, minimal different rotational speeds can occur at the pumps due to different hydraulic connection. For the setpoints of the physical test rig, the average value of the two pump speeds is used.

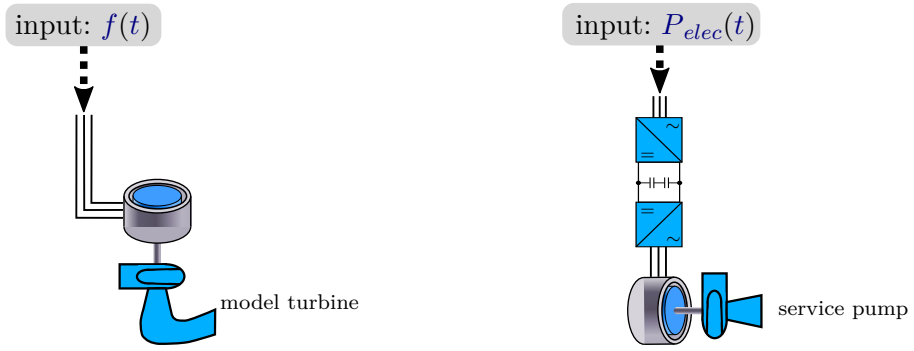

(a) Model machine controlled via given frequency.

(b) Service pumps controlled via electrical power.

Figure 5.2: Rotation speed control of electric machines in test rig simulation.

To achieve appropriate hydraulic conditions on the model machine, the optimizer adjusts the electrical power at the converter of service pumps in each time step over the entire simulation. Thus, an exact n_{ed}–Q_{ed} pump characteristic curve and the exact modeling of the piping system are decisive for detecting the correct speed behavior of the pumps. Since the control of the physical test rig in the laboratory is carried out via rotational speed setpoints, for the simulation, it is not necessary to know the properties of the electrical components.

In any case, the moment of inertia of the service pumps and the drive motor is important. Deceleration and acceleration occur at this intersection with the acting torques (Eqn. 3.1) and are influenced by the moment of inertia. Differences to the original should be kept as small as possible. If the moments of inertia differ significantly from the real components, this could unnecessarily extend the optimization process. A major disadvantage would be that the optimization results exhibit a behavior of the service pumps that cannot be realized in the physical model test.

Adjustment of Loss Coefficients for Volume Flow Reversal

At the model machine branch, different loss coefficients for turbine and pump flow direction must be taken into account. This difference arises from the installation direction of an annular piston valve on the pressure side of the model machine, which

generates different losses depending on the flow direction.
Since the loss coefficients of pipelines cannot be changed within a simulation, this issue is solved by using different openings of this valve in the simulation. If there is a volume flow reversal, this valve abruptly changes its opening position exactly at the moment of $t(Q = 0)$ and thus creates an adapted loss, depending on the flow direction. The optimizer detects these points in time and creates the appropriate control file for this valve for the next iteration. Pressure surges caused by an abrupt change in opening disappear after a few iterations.
Details on the numerical model of the test rig and validation results are presented in chapter B in the appendix.

5.3 Optimizer Loop

To understand the principles of the optimizer, a closer look at the logic and the mathematical definitions is necessary.
As already mentioned, after each completed test rig simulation, the optimizer has the function of comparing simulation results with setpoints and adjusting the performance of the service pumps accordingly. The head of the model machine is defined as the target value of the optimization. This parameter proves to be suitable for optimization, as the control of the pressure difference in the test rig via the service pumps can be easily implemented. Using the specified rotational speed and the guide vane opening of the model machine, the corresponding discharge results from the characteristic diagram according to the available head. The same applies to the torque of the model machine. Thus, all relevant machine parameters are achieved by providing only the correct energy difference. A more detailed view of the optimization structure is shown in Figure 5.3.

5.3.1 Handling of Different Time Steps

To obtain the highest possible resolution in a given time, the simulation time step should be as small as necessary. For this reason, the time step for both the power plant simulation as well as the test rig simulation is set to $\Delta t_{sim-PP} = \Delta t_{sim-TR} = 10^{-4}$ s. With regard to the time resolution of the optimizer, it might make sense to choose a larger time step ($\Delta \tilde{t}_{opt} \geq \Delta t_{sim-TR}$). This can reduce computational effort and leads to a faster achievement of the convergence criterion (e.g. achieving the setpoint with

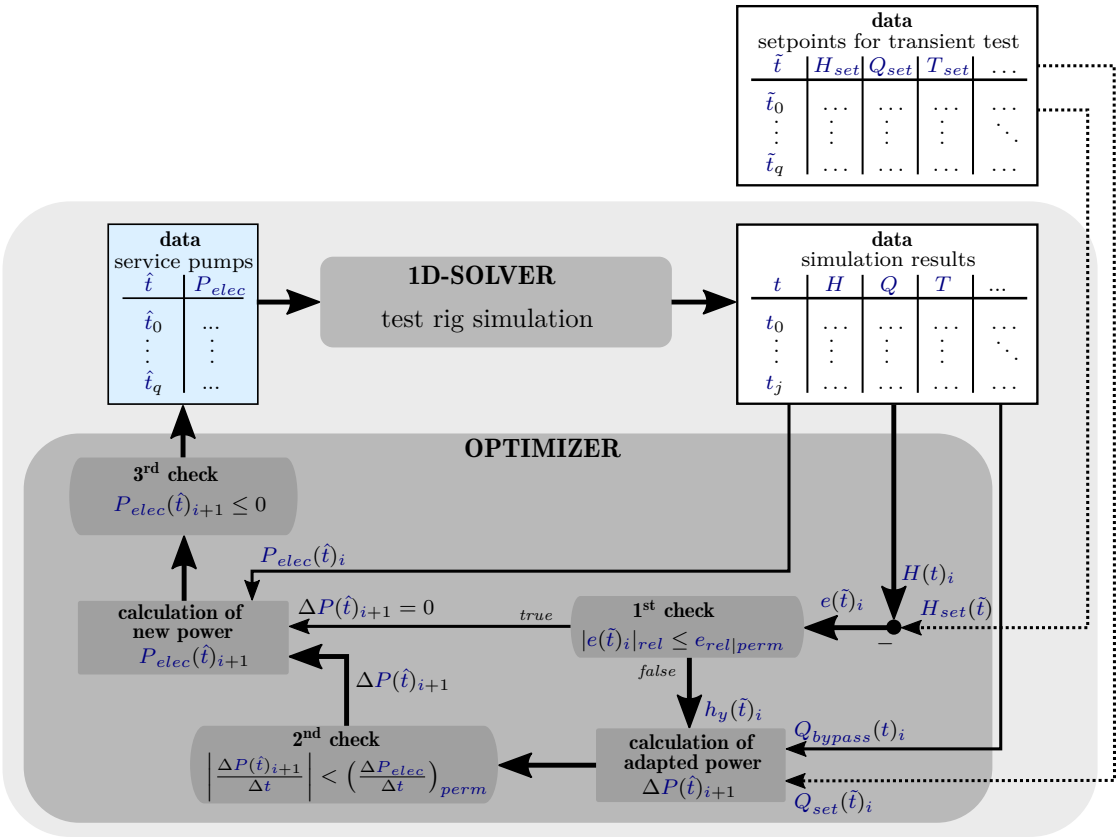

Figure 5.3: Structure to determine service pump behavior.

a permissible error) without losing the overall quality of the results.
The optimization time step depends on the time step of the power plant simulation (Δt_{sim-PP}) and the time scale factor x_{t-Sr}. Via the sampling factor k ($k \in \mathbb{N}$) this time step is varied to a higher value (Eqn. 5.1). Thus, the optimizer does not compare test rig results and setpoints at each available time step but covers the same period of time ($[\tilde{t}_0 - \tilde{t}_q]_{opt} = [t_0 - t_j]_{sim-TR}$). The influence of k on the optimization result and the duration of an iteration loop has to be investigated to find the appropriate value.

$$\Delta \tilde{t}_{opt} = \Delta t_{sim-PP} \cdot \frac{k}{x_{t-Sr}}, \text{ [s]} \tag{5.1}$$

For the input performance file of the service pumps, a further physical relationship, which has an influence on the time sequence, must be taken into account. This relationship is explained with an example. If a certain head $H(t_0)$ at the model

machine should be achieved at a certain time t_0, the necessary energy difference must have been generated by the service pumps at a certain time $\hat{t}$ in the past (Eqn. 5.2).

$$\hat{t} = t_0 - T_a, \text{ [s]} \tag{5.2}$$

A major influence on T_a results from the fact that the simulation model includes inertias of the pumps and the water mass. A change of the electrical power at the drive of the pumps does not immediately lead to a changed energy difference at the model machine. This takes into account that the fluid is assumed to be weakly compressible and thus the wave propagation in the pipelines is time-dependent.
In the test rig, the service pumps, the bypass valve, and the model machine are installed asymmetrically (not with the same distance to each other) in their three branches. These three branches are connected to each other on the high pressure and low pressure side via two vessels, modeled as large diameter pipes. Thus, an analytical determination of the time offset T_a is not exactly possible. Suitable values should be identified via a parameter study.

5.3.2 Pump Performance Calculation and Optimizer Parameter

The calculation of a new pump performance at a certain point in time only takes place if the deviation $e(\tilde{t})$ from the setpoint value is exceeded or undercut (Eqn. 5.3).

$$e(\tilde{t})_i = H(t)_{i|sim} - H(\tilde{t})_{set}, \text{ [m]} \tag{5.3}$$

To make this procedure uniform for different load cases, it is necessary to choose a relative value as the permitted error $e_{rel|perm}$, e.g. related to the initial head ($e_{rel|perm} \geq |e(\tilde{t})_{rel}| = |e(\tilde{t})|/H_{ini}$). The **1st check** verifies whether this value is exceeded or undercut and thus decides whether an adaption of the power $\Delta P(\tilde{t})_{i+1}$ is necessary for this time step. This adjustment is added to the performance of the pumps in the same time step of the previous iteration (Eqn. 5.4).

$$P_{elec}(\hat{t})_{i+1} = P_{elec}(\hat{t})_i + \Delta P(\tilde{t})_{i+1}, \text{ [W]} \tag{5.4}$$

Before the adjusted power is calculated, the error is multiplied by a constant factor. This procedure is known in the field of control engineering [71]. Here, the error $e(\tilde{t})$

as the input variable is transformed via a proportional element K_P to a new output variable $h_y(\tilde{t})$ (Eqn. 5.5).

$$h_y(\tilde{t})_i = K_P \cdot e_i(\tilde{t}),\ [\mathrm{m}] \tag{5.5}$$

Subsequently, the adapted power $\Delta P(\tilde{t})_{i+1}$ is calculated as a hydraulic power of a turbo machine. The output variable $h_y(\tilde{t})$ serves as head. Depending on the operating mode of the model machine, this value is multiplied by the sum or subtraction of the bypass discharge of the previous iteration $Q(t)_{i|bypass}$ and the discharge setpoints of the model machine $Q(\tilde{t})_{set|model}$ (Eqns. 5.6, 5.7).

$$\Delta P(\tilde{t})_{i+1} = \rho \cdot g \cdot [Q(t)_{i|bypass} + Q(\tilde{t})_{set|model}] \cdot h_y(\tilde{t})_i,\ [\mathrm{W}] \text{ for TU-mode} \tag{5.6}$$

$$\Delta P(\tilde{t})_{i+1} = \rho \cdot g \cdot [Q(t)_{i|bypass} - Q(\tilde{t})_{set|model}] \cdot h_y(\tilde{t})_i,\ [\mathrm{W}] \text{ for PU-mode} \tag{5.7}$$

This formulation includes the assumption that the pressure difference at the bypass valve and at the model machine is the same. A closer look indicates that this is not correct. However, as the optimization progresses, the error $e(\tilde{t})_i$ decreases and thus the influence of this incorrect assumption also decreases.

The optimization loop consists of further logical checks. A **2nd check** ensures that a change of electrical power per time step does not exceed. This prevents the optimization from getting unstable due to unrealistically high performance jumps.
Before the merged values of adjusted power and electrical power are written into the new file, a **3rd check** ensures that no values above 0 W occur. This is necessary because the drives of the service pumps are not able to consume power from the test rig. Consequently, positive values are not permitted. The decelerations of a rotors results from the torque balance between the drive motor and the acting forces on the pump impeller.

Depending on the **2nd check** and the values K_P and T_a the optimization can take a long time or become unstable. Suitable values must be determined separately for each test rig by means of parameter studies. Once these are known, it is possible to determine the appropriate rotational speed of the service pumps for the transient model experiment.

5.4 Evaluation

An exact match of setpoints, test rig simulation results, and measurement results cannot be expected. In order to evaluate the deviations from these results, a suitable tool is needed to compare two or more curves to each other. In addition to the evaluation of e.g. the maximum deviation (e_{max}), the error area offers an evaluation of entire processes [72].
Mathematically, the error area corresponds to the sum of all deviations in a time interval over a defined period (Eqn. 5.8). The graphical relationships are illustrated in Figure 5.4.

$$\begin{aligned} \Upsilon &= \int_{t_{start}}^{t_{end}} |y(t) - y_{set}(t)|\, dt \\ &= \sum_{t_{start}}^{t_{end}} |y(t_m) - y_{set}(t_m)| \Delta t \\ &= \sum_{t_{start}}^{t_{end}} |e(t_m)| \Delta t, \text{ [s·unit of } y\text{]} \end{aligned} \tag{5.8}$$

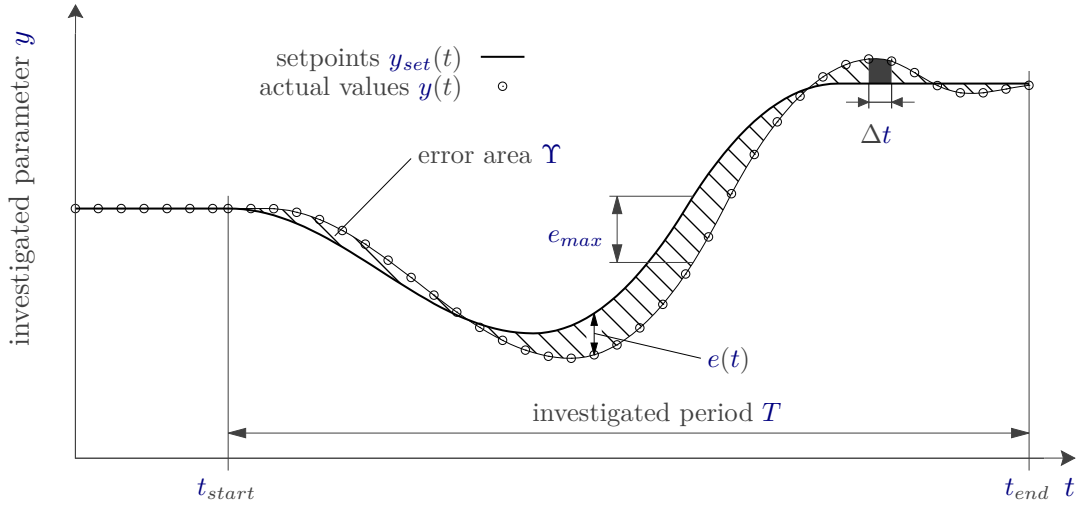

Figure 5.4: Example for evaluation of two curves via the error area and maximum deviation.

However, a single value of Υ has limited information about the quality and can be evaluated only in comparison to other values of error areas.
But since Υ is not dimensionless, comparability with other cases is difficult. In this procedure, it must be taken into account that when investigating a certain load case, the x_{t-Sr} factor has an influence not only on the duration but also on the amount of the parameters under consideration. To solve this, the time influence is corrected by dividing Υ by the duration of the investigated transient processes (Eqn. 5.9).

$$\Upsilon_t = \frac{\Upsilon}{(t_{end} - t_{start})}, \text{ [unit of } y\text{]} \tag{5.9}$$

By normalizing Υ_t to a uniform value (e.g. to the initial setpoint value of the investigated parameter $y_{set-ini} = f(x_{t-Sr})$) a comparison of all cases independently of time scale factor x_{t-Sr} is possible (Eqn. 5.10).

$$\Upsilon_{norm} = \frac{\Upsilon_t}{y_{set-ini}}, \text{ [-]} \tag{5.10}$$

6 Test Case

In this chapter, the capability of the optimization procedure is examined using a test case as an example. Among other things, the influences of all control parameters and limit values are investigated. Subsequently, the simulation results of the test rig are compared to the corresponding measurement results.

6.1 Transfer of Prototype Test Case Results to Model Size

A fast transition from pump mode to turbine mode and vice versa is used as a test case. In this case, only the rotational speed of the machine is varied, the guide vanes remain constant at an opening of $\gamma/\gamma_{max} = 0.6$. This corresponds to the opening at the BEP in turbine mode. The maximum water level difference of the reservoirs is taken as boundary conditions.
In the power plant simulation, a spline function (Eqn. 6.1, valid for $0 \leq t \leq \Phi$) of the rotational speed is given as a transition form. The time span Φ of the speed change per fast transition is 30 seconds.
This speed profile is characterized by starting as a horizontal asymptote in the transient and ending as such. Moreover, it is a continuously differentiable function, which has no kink in its course, neither in the root function nor in the derivative. Immediate jumps of acceleration which are difficult to reproduce in the physical experiment are not present in this speed form. These properties make this function suitable for testing the optimizer and finding appropriate control parameters.

$$n_{proto}(t) = |n_{proto-rated}| \begin{cases} (-\frac{1}{2}(\frac{t}{\Phi/2} - 1)^3 + \frac{3}{2}(\frac{t}{\Phi/2} - 1)), & PU \rightarrow TU \\ (+\frac{1}{2}(\frac{t}{\Phi/2} - 1)^3 - \frac{3}{2}(\frac{t}{\Phi/2} - 1)), & TU \rightarrow PU \end{cases} \tag{6.1}$$

The test case results in transient behavior for the physical quantities H, Q, and T versus time or the machine coefficients n_{ed}, Q_{ed}, and T_{ed}, respectively. These curves are specific for this power plant, the selected speed form, and the duration of the

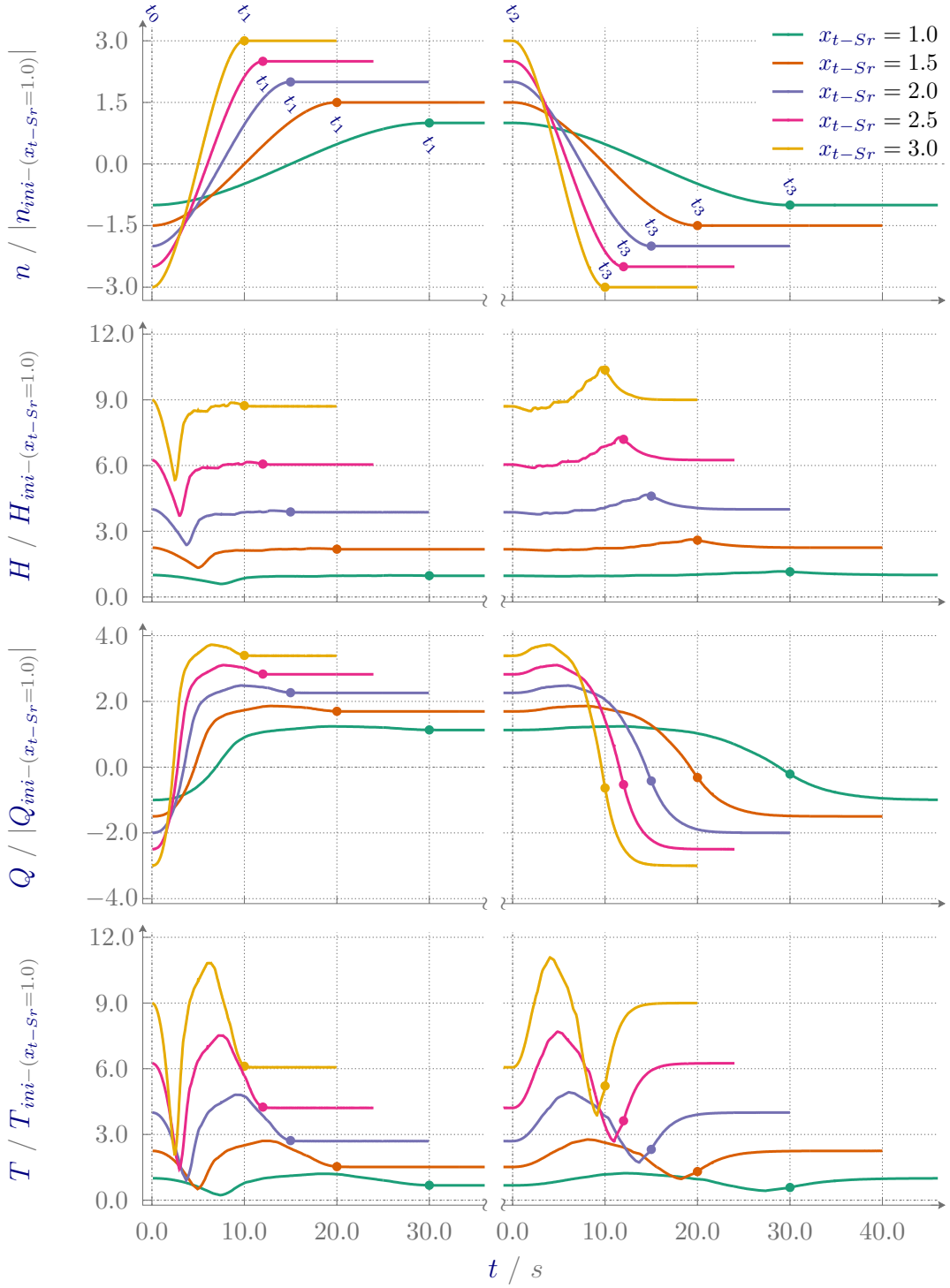

Figure 6.1: Transferred test case prototype results to model size via the Strouhal similarity.

transition. By transferring these curves to the model size, different x_{t-Sr}-values can be selected.
In Figure 6.1 the parameters n, H, Q, and T for different x_{t-Sr} values are shown normalized to the initial values of the transformation for $x_{t-Sr} = 1$. The left diagrams represent the transition from pump to turbine mode, the right diagrams the vice versa process. At all curves, the end of the transient change of rotational speed is marked with a dot. Especially during the transition from turbine to pump operation (right diagrams), it is evident that the end of the whole transient process occurs significantly later than the end of the transient rotational speed change. Therefore, it is necessary to consider this extended time range in the evaluation procedure.
Comparing the curves of the different x_{t-Sr} to each other, the influence on time-dependent courses, which is described in Eqn. 2.11, is clearly visible. As x_{t-Sr} increases, the slopes become steeper and the extreme values are more pronounced.

In order to determine the optimizer parameters and to verify the applied method, the transformation with $x_{t-Sr} = 2$ is used as the test case.

6.2 Optimization and Numerical Results

6.2.1 Influence of Optimizer Control Parameters

As described in Section 5.3, the optimizer has three control parameters (proportional factor K_P, time shifting T_a and sampling factor k) to adapt its behavior. Additionally, there are the three limit values (1st-3rd check). In order to define these for the test rig used, several parameter studies are carried out and the results are evaluated according to the criteria defined in Section 5.4.

Influence of K_P and T_a

The studies indicate that the parameters K_P and T_a, as well as the number of optimizer iterations have a mutual influence on the results. Figure 6.2 presents the behavior of Υ_t (top) and e_{max} (bottom) for head over 800 iteration loops. Here K_P is varied from 0.1 to 2.2, and T_a from 0.0 s to 1.5 s in gross steps.
First of all, it is visible that the worst results are achieved with $T_a = 0.0$ s, when $K_P \geq 0.8$. Further, high K_P values in combination with high T_a values initially lead to rapidly decreasing error values, but diverge again as the number of iterations

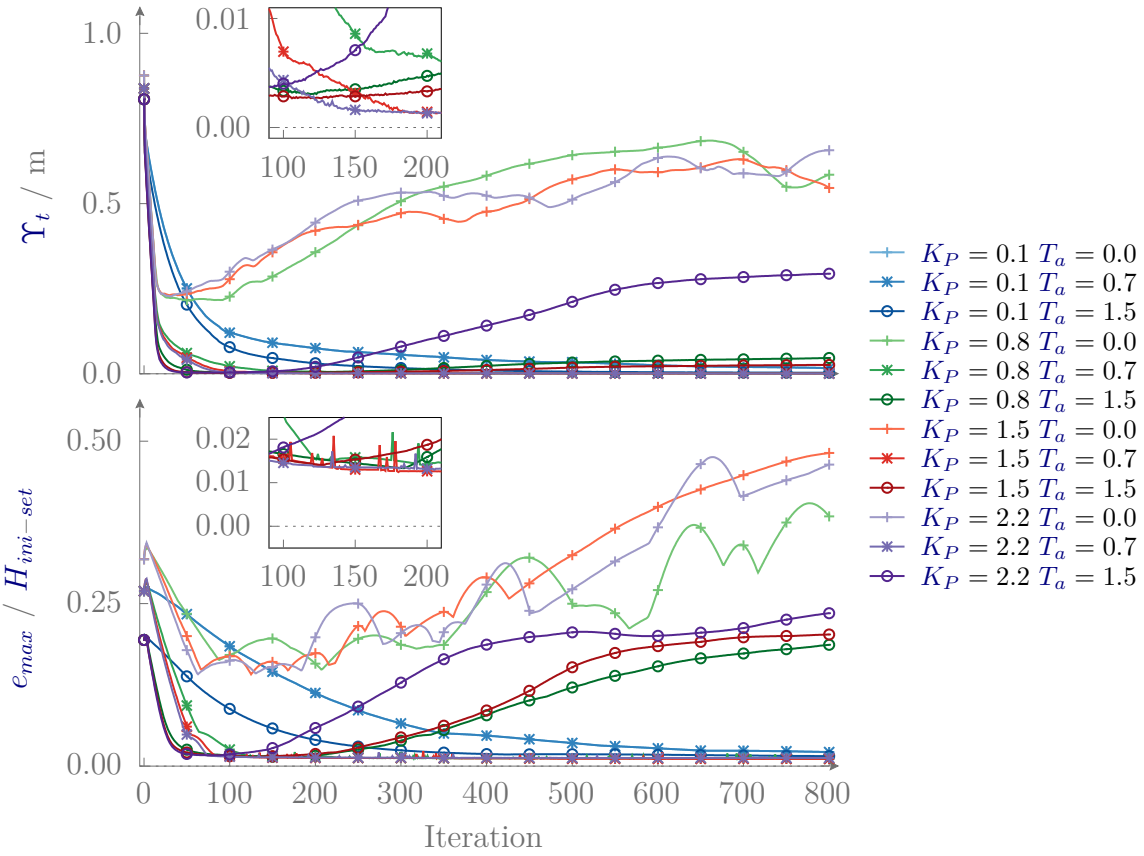

Figure 6.2: Behavior of Υ_t and e_{max} over 800 iteration loops of the optimization for different combinations of T_a and K_P.

increases. The detailed diagrams indicate that further improvement of the results above 200 iteration loops is hardly possible. For almost all parameter combinations the optimization stagnates. This can be explained by the permissible error per time step which is almost reached over a wide range of the transient process (1st check). In this study the permissible error is set to $e_{perm} \leq 0.25\ \% \cdot H(t)$.

In the following, the results for 200 iteration loops are considered in finer increments of the control parameters. The minimum of Υ_t ($\Upsilon_{t|min} = 0.00087$ m) is reached at the combination of $T_a = 1.0$ s and $K_P = 1.8$ (Fig. 6.3). In the three-dimensional bar chart, the K_P values at $T_a = 1.0$ s are sorted in descending order of Υ_t.
Over a certain time span (approx. $0.7 - 1.0$ s) T_a has a significant influence on Υ_t. In this time span, K_P plays a subordinate role to minimize Υ_t. Outside of this range, K_P becomes more important. For low values of T_a (e.g. $T_a \leq 0.5$ s), higher K_P values

are beneficial, whereas for high T_a values (e.g. $T_a \geq 1.2$ s), low K_P values produce better results.

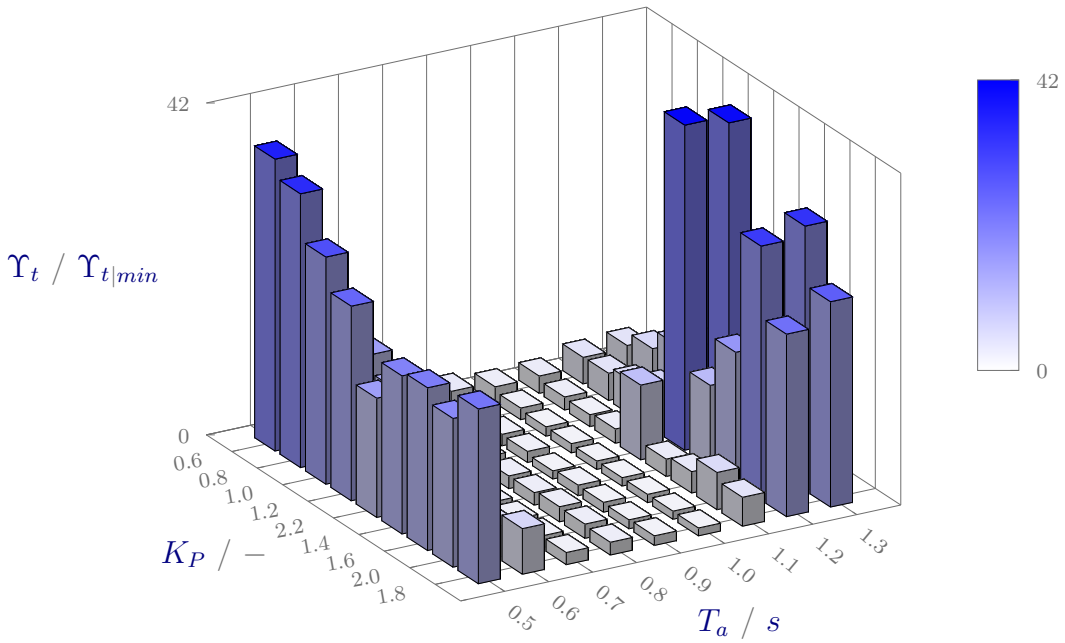

Figure 6.3: Influence of the optimizer parameters T_a and K_P for 200 iteration loops on the time-related error area Υ_t.

Subsequently, the values $T_a = 1.0$ s and $K_P = 1.8$ are set for further investigations. Moreover, in most cases the optimization process is limited to $i = 200$ iterations, as this value is proven to be sufficient.

Influence of k

With the knowledge gained from the parameter studies of T_a and K_P, it is useful to investigate the influence of the sampling factor k. The parameter studies about T_a and K_P are carried out with a sampling factor of $k = 20$ Hz.
Sampling rates of 1 Hz, 10 Hz, 20 Hz, 40 Hz, 100 Hz, and 250 Hz are investigated. A low sampling rate corresponds to a less frequent intervention in the performance of

the service pumps.

Despite the different sampling rates, which are associated with different computational efforts, the time required for one iteration hardly differs from each other (approx. 5 seconds per iteration). This can be explained by the effort of reading the result file and writing the new service pump performance file. These processes are more time-consuming than the calculations themselves. The solver needs about 1:30 min per iteration to simulate the test case and thus needs significantly more operating time than the optimization process. Hence, the varying sampling rate is evaluated only at the simulation result, regardless of the required computation time.

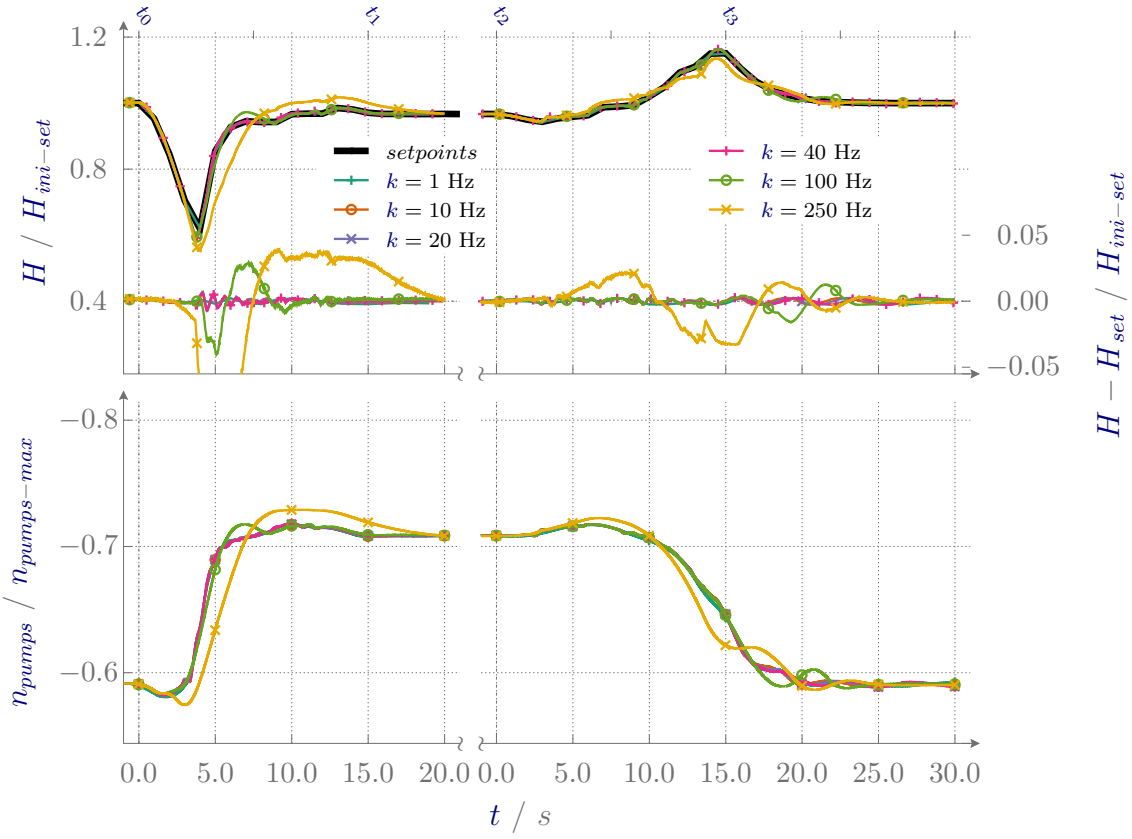

Figure 6.4: Influence of the optimizer sampling factor k to the head at the model machine and rotational speed of the service pumps.

The parameter study demonstrates that high sampling rates do not lead automatically to good optimization outcomes. The comparison between setpoints and optimized head curves views particularly high deviations at sampling rates of 100 Hz and higher (Fig. 6.4 top). While the cases with sampling rates of 40 Hz and lower do not show any differences in the course of the rotational speed of the service pumps (Fig. 6.4

bottom), the results of the high sampling rates show clear deviations from the other cases.

The quantitative differences between the optimization runs are listed in Table 6.1. Here, the time-related error areas Υ_t is normalized to the smallest value in this investigation. A further evaluation parameter is the maximum error, normalized by the same scheme. The best over all result is achieved with a sampling rate of 40 Hz ($\Upsilon_{tmin} = 0.0099$ m) while the smallest local deviation $e_{max|min}$ (= 0.0224 m) occurs at 1 Hz.

Table 6.1: Error values for different sampling rates k of the optimization.

k / Hz	1	10	20	40	100	250
$\Upsilon_t/\Upsilon_{t\|min}$	1.134	1.132	1.092	1.000	2.840	13.188
$e_{max}/e_{max\|min}$	1.000	2.433	2.576	2.571	14.893	58.004

Influence of limit values

In the test case, the 3rd check ($P_{elec} \leq 0$ W) does not intervene because the power curve is too far away from this limit. Only at very low time scale factors (e.g. at $x_{t-Sr} = 1$) this check is relevant.

As expected, the setting of $e_{perm} = 0.0$ % (1st check) leads to the best result as far as the error area is concerned. However, considering the stability of the rotational speed of the service pumps, the disadvantage of this setting becomes clear (Fig. 6.5). Approximately 8 seconds before ($t < t_1$) and after ($t > t_2$) the steady-state turbine operation, both, the power input and the pump speed fluctuate. This fluctuation is not visible in the other cases shown with a higher error tolerance of 0.25 % and more. Moreover, the 0.0 % permission does not result in the lowest local error e_{max} (Table 6.2).

Table 6.2: Error area and maximum deviation after 200 iteration loops. The results are listed for different permitted values of electrical power changes per time step and different permitted maximum deviations as optimizer input.

$dP_{elec}/dt\|_{perm}$ / W s^{-1}	1000	5000	5000	5000	25000	12500
e_{perm} / %	0.25	0.0	0.25	0.5	0.25	0.25
$\Upsilon_t/\Upsilon_{t\|min}$	6.071	1.000	2.327	5.241	2.639	2.647
$e_{max}/e_{max\|min}$	5.792	1.024	1.000	1.002	1.016	1.016

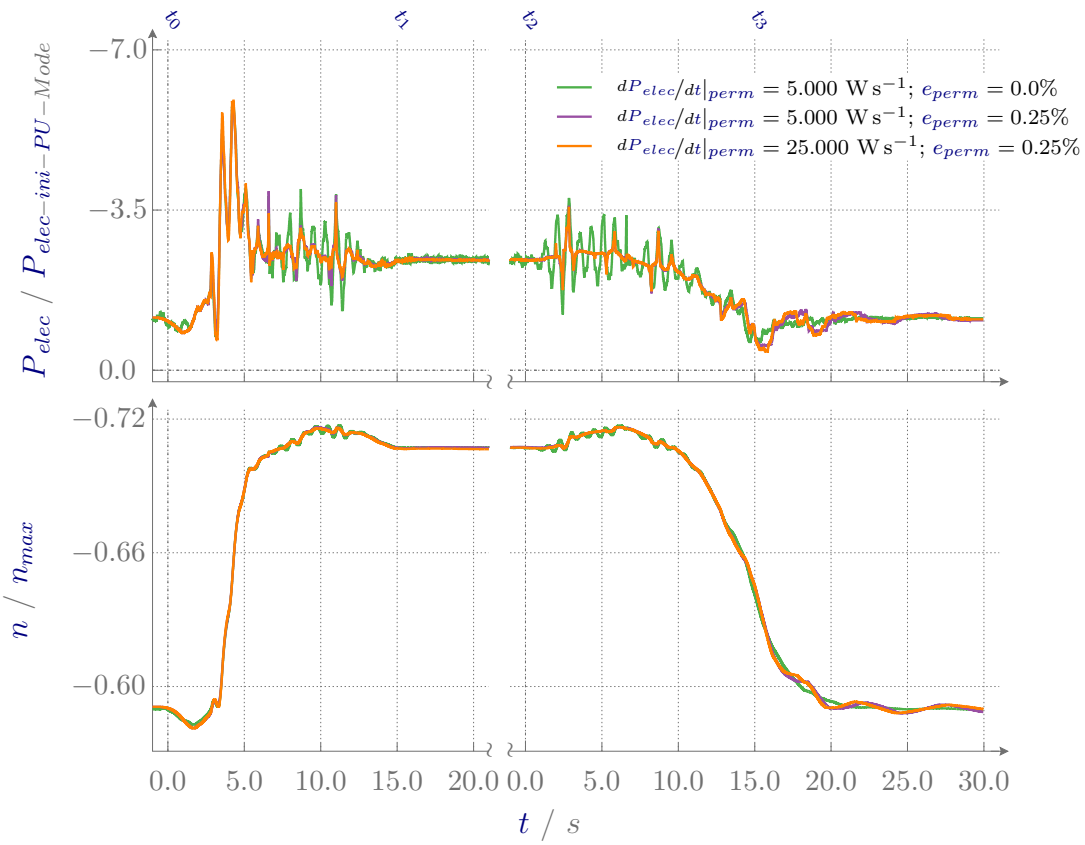

Figure 6.5: Electrical power and rotational speed of the service pumps versus time for different optimizer settings (permitted electrical power per time step and maximum permitted error).

It should be emphasized that when returning to steady-state pump mode (right diagram $t > 15$ s), the green curve (0.0 %) is smoother than those with greater error tolerance. Here, the narrow margin of error has a positive effect on the course.

All combinations investigated are listed in Table 6.2. It is noticeable that in the first case with a power limit of 1000 W s^{-1}, 200 iteration loops are not sufficient to obtain a convergent solution. Both the error area and the maximum error are about six times higher as the best results from the cases with the 5000 W s^{-1} limit.
Thus, the goal of a stable pump speed with the smallest possible error area and the lowest possible deviation to the setpoints are achieved with the settings ${}^{dP_{elec}}/_{dt}|_{perm}$ = 5000 W s^{-1} and $e_{max}|_{perm} = 0.25\%$.

6.2.2 Influencing Factors on Simulation Results

As discussed above, the speed of sound has an influence on the pressure wave propagation in weakly compressible fluids. Therefore, its influence on the simulation results is investigated in the following. In addition, the influence of the characteristic diagram quality of the model machine on the simulation is examined.

Speed of Sound Setting for Test Rig Simulation

For the setup of the test rig simulation, it is necessary to specify the speed of sound in the different pipe sections. However, the actual value of the speed of sound in the real test rig is not known. Since the speed of sound in the piping systems not only depends on the dissolved gas but also on the pressure [95], it may vary according to different usage of the test rig. For this reason, an exact determination is omitted.
A parameter study is used to investigate the influence of this unknown quantity on the optimization result. In four steps, the speed of sound is varied from very low values ($a_{PS} = 400\ \mathrm{m\,s^{-1}}$ and $a_{SS} = 300\ \mathrm{m\,s^{-1}}$) to very high values ($a_{PS} = 1200\ \mathrm{m\,s^{-1}}$ and $a_{SS} = 800\ \mathrm{m\,s^{-1}}$), considering different levels between the pressure and suction sides.

Using the example of the pressure wave at the positions of p_0 (spiral case) and p_2 (draft tube), which are initiated by the fast transitions of the model machine, hardly any differences on the optimization result are noticeable despite varying speed of sound (Fig. 6.6 top).
Compared to the measured results (lower left diagram), the pressure increase in the draft tube is clearly more pronounced in the simulations independent of the speed of sound. Further, the pressure in the spiral case decreases less in the simulations than in the measurement. Both behavior occur in reverse during the transition from turbine operation to pump operation (lower right diagram). Since the fluid behavior does not differ at the different speeds of sounds, it is not surprising that the optimizations of the service pump speeds also do not show significant variance to each other.

The change in head and thus the pressure curves in the spiral and draft tube are results of the interaction between the piping system and the behavior of the operating point in the characteristic diagram. Changes of the guide vane opening, the rotational speed, or incoming pressure waves at the machine shift the operating point. This movement of the operating point can in turn cause a change in flow rate.
Equation 2.12 indicates that the change in flow velocity causes a proportional change in pressure, which also depends on the speed of sound. Since the simulations do not

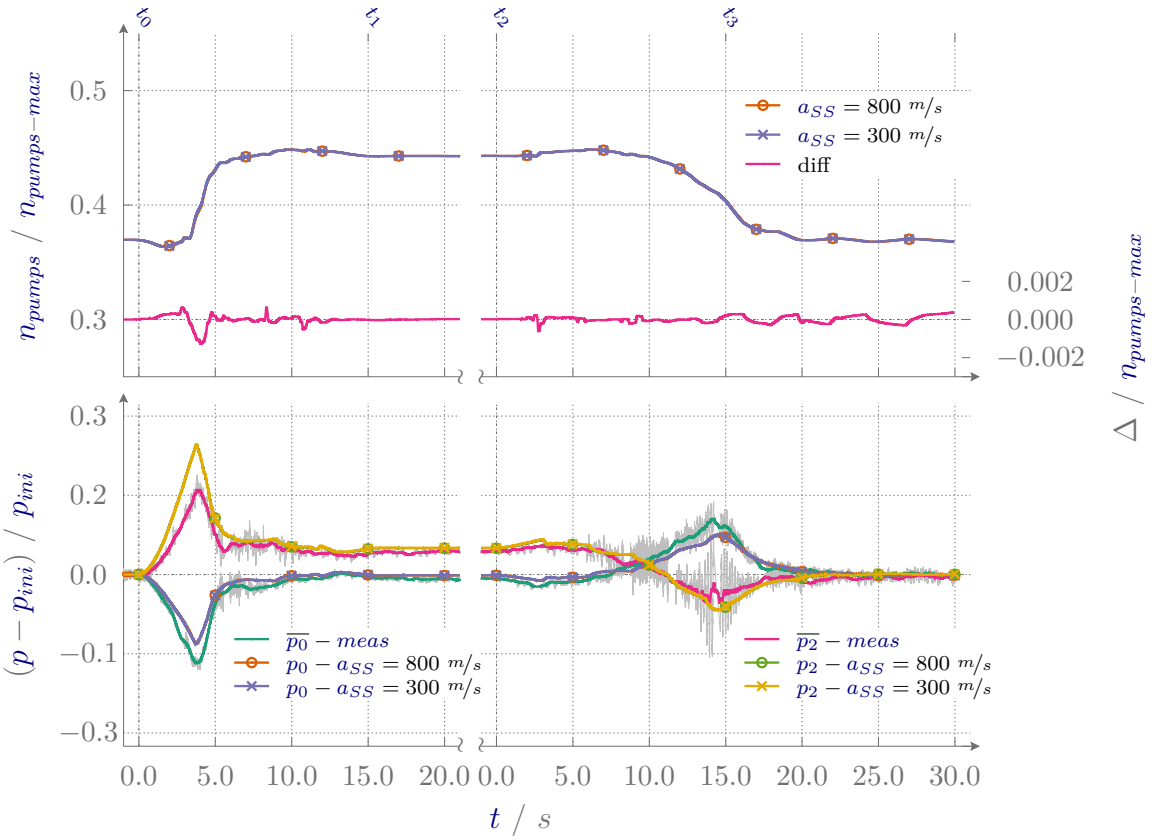

Figure 6.6: Influence of speed of sound on the optimization result. Behavior of rotational speed of the service pumps (top) and pressure p_0 resp. p_2 at model machine (bottom).

show a different pressure behavior despite different speed of sound (Fig. 6.6), it is assumed that the change in flow velocity is too small. This assumption is confirmed by means of three further simulation series.

Starting from the test case with the transition from pump to turbine operation on the closed test rig, this transition was simulated on an open-loop test rig model in a further configuration (illustrated in Fig. B.2 in the appendix B). This configuration is intended to rule out the possibility that modeling as a closed-loop is the reason for the absence of different pressure curves at different speeds of sound. For this purpose, fictitious basins with a constant level are modeled as energy sources close to the intersection points where the three branches of the test rig meet. The bypass and the service pumps branch are removed.
The second change relates to the test itself. To force a larger change in fluid velocity,

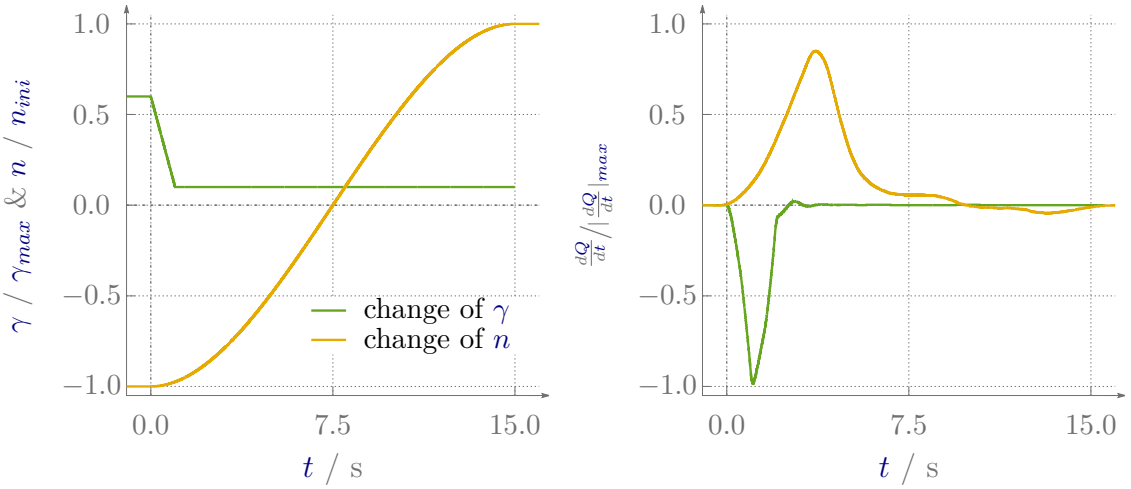

(a) Control mechanisms to trigger transient process on the test rig.

(b) Change in flow rate due to transient process.

Figure 6.7: Setting to study the influence of the speed of sound for simulations on the test rig. Initiation of transient processes via change of rotational speed (yellow) or guide vane opening (green) and effect on the change in flow rate (Fig. b).

a fast closing of guide vanes in turbine mode is simulated (Fig. 6.7 green curve). This load case is simulated with the open-loop as well as the closed-loop test rig model.

The results show that the absolute change in head is smaller for the open-loop than for the closed-loop model (compare Fig. 6.8(a) and 6.8(c) with 6.8(b) and 6.8(d)). In both test rig configurations, the speed of sound plays no role in the results when simulating the transition from pump to turbine mode (Fig. 6.8(a) and 6.8(b)). For the cases with the fast closing of the guide vanes, differences in the head are visible for the different values of speed of sound. Further, it is noticeable that qualitative differences of head profiles only appear in the closed-loop rig configuration. This is due to the longer pipes.

These investigations underline the assumption that consistent results of the fast transition simulations are not related to the configuration of the closed-loop. Despite the varying speed of sound, the results are almost identical. This is caused by the insufficient change of the flow velocity, which appears in this type of simulation.
If the flow velocity is subject to stronger changes, as in the case of the guide vane adjustment, the speed of sound becomes more important. But even in this case, the test rig configuration is not decisive. For these types of transient model tests, a

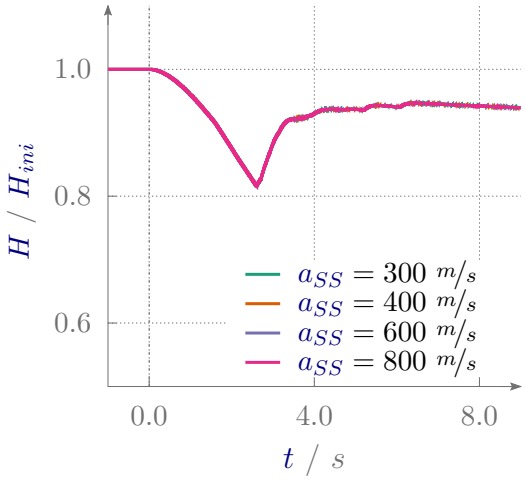

(a) Transient head initiated by fast transition from pump to turbine operation with open-loop test rig configuration.

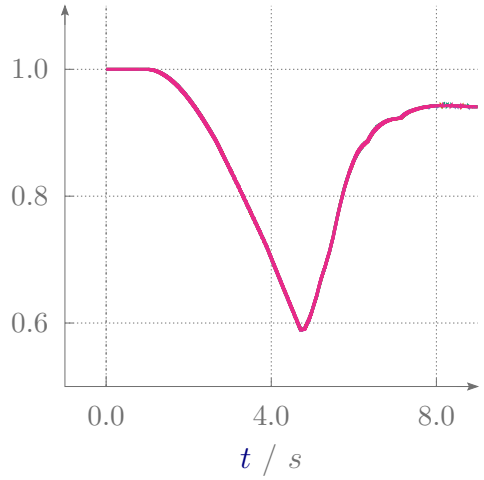

(b) Transient head initiated by fast transition from pump to turbine operation with closed-loop test rig configuration

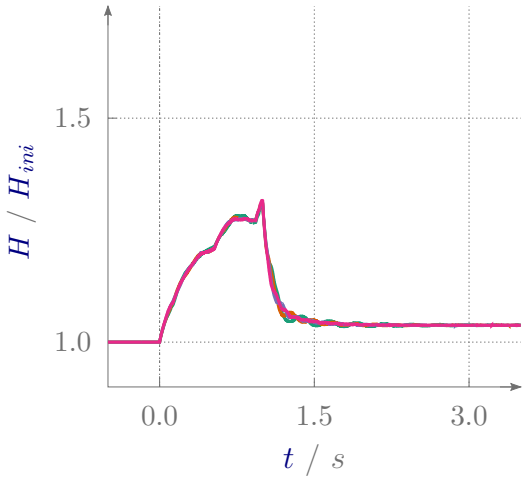

(c) Transient head initiated by fast closing of guide vanes in turbine mode with open-loop test rig configuration.

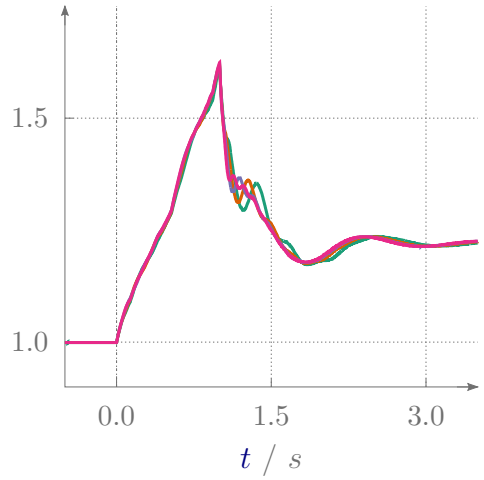

(d) Transient head initiated by fast closing of guide vanes in turbine mode with closed-loop test rigs configuration.

Figure 6.8: Investigation of the influence of the speed of sound on the head under different test rig configurations and different triggers of a transient events.

parameter study of the speed of sound must be performed with subsequent comparison to the measured results.

Influence of the Characteristic Diagram

Section 6.2.1 explains that the optimization method used can deliver reliable results even if the permissible error e_{perm} of the head is set to a very low value. Narrow limits can cause the optimization to react sensitively to abrupt changes.
In a concrete example, two remarkable kinks in the setpoint curve of the head, at the transition from turbine to pump operation, are responsible for the optimizer generating a conspicuous speed curve of the service pumps. The kinks in head are visible in the pink curve at about $t = 18$ s and $t = 21$ s in the upper diagram of Figure 6.9(a). The diagram below illustrates the rotational speeds of the service pumps measured at the test rig. The curve profiles correspond to the results generated by the optimizer. In comparison, it is noticeable that the yellow curve presents a significantly more discontinuous behavior. The reason why the speed curve already shows a conspicuous behavior at the time of approx. $t = 17$ s is related to the time shift T_a described in Chapter 5.3.1.

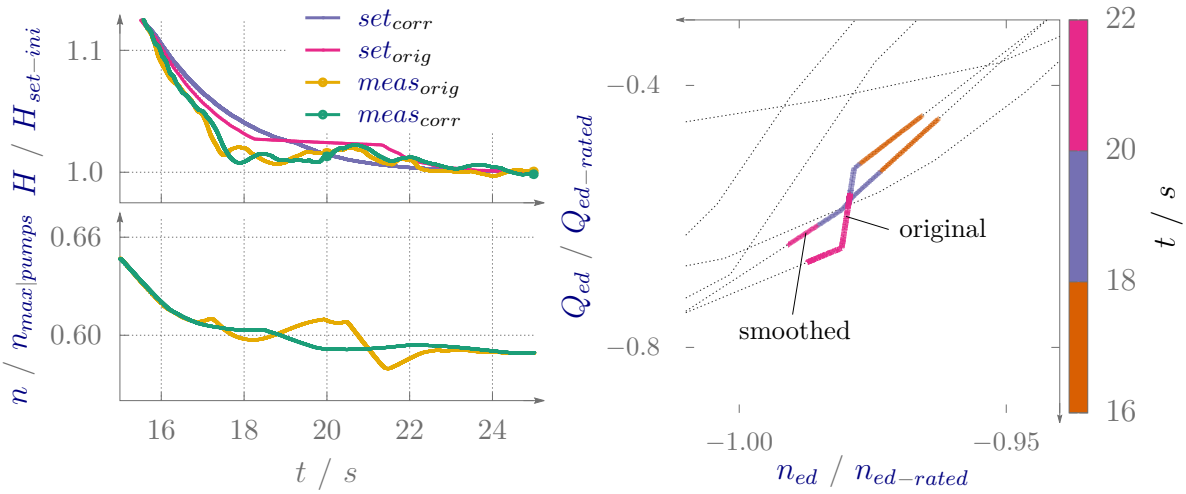

(a) Setpoints and measurement results of head (top) and optimized rotational speed of service pumps (bottom).

(b) Pump quadrant of the model machine characteristic diagram with highlighted opening $\gamma/\gamma_{max} = 0.6$.

Figure 6.9: Influence of kinked map lines of model machine to solver results and measurement results of head.

A look at the characteristic diagram of the model machine (Fig. 6.9(b)) reveals the reason for these phenomena. In this diagram, the operating point moves on a curve of constant guide vane opening from top right to bottom left. The colored segmentation refers to the point in time in the simulation. Following the curve labeled "original", two remarkable kinks are visible.
In the same diagram, a corrected form of this opening curve is plotted with the label “smoothed”. If this corrected curve is used for optimization, the result of the service pump speed is fluctuating less (green curve Fig. 6.9(a) bottom).
Looking at the measurements of the head (yellow and green curves in Figure 6.9(a) top), it is noticeable that the differences are minor. For this example, it is concluded that the two service pump speeds do not produce qualitatively different results at first glance. Nevertheless, these discontinuities in the characteristic diagram can have negative consequences, such as the optimization do not achieve a convergent solution. However, both curves (”original” and ”smoothed”) are not acceptable solutions. The so-called “original” is based on the original measurements of the characteristic diagram. Depending on the degree of discretization and stability of the measured operating point, jumps can lead to more or less pronounced discontinuous curves of the constant guide vane opening, as in this example.
In the corrected curve, the kinks have simply been removed to stabilize the optimizer. It would be better to prepare the characteristic diagram using continuously differentiable spline functions and more interpolation points. Then the setpoint curve would have no kinks, the solver would not have to work with abrupt changes, and the measured values would be closer to the setpoints (compare the distance between measurement and set_{orig}).

Since there is no established procedure for the preparation of a characteristic diagram so far, in the further course of this work the original measurement data of the diagram are used as far as possible. Adjustments are only made in individual cases.

6.3 Comparison of Simulation and Measurement Results

With the course of the pump speed determined by the optimizer, it is possible to generate measured data, which is compared with the numerical results in the following paragraphs.

6.3.1 Model Machine Results

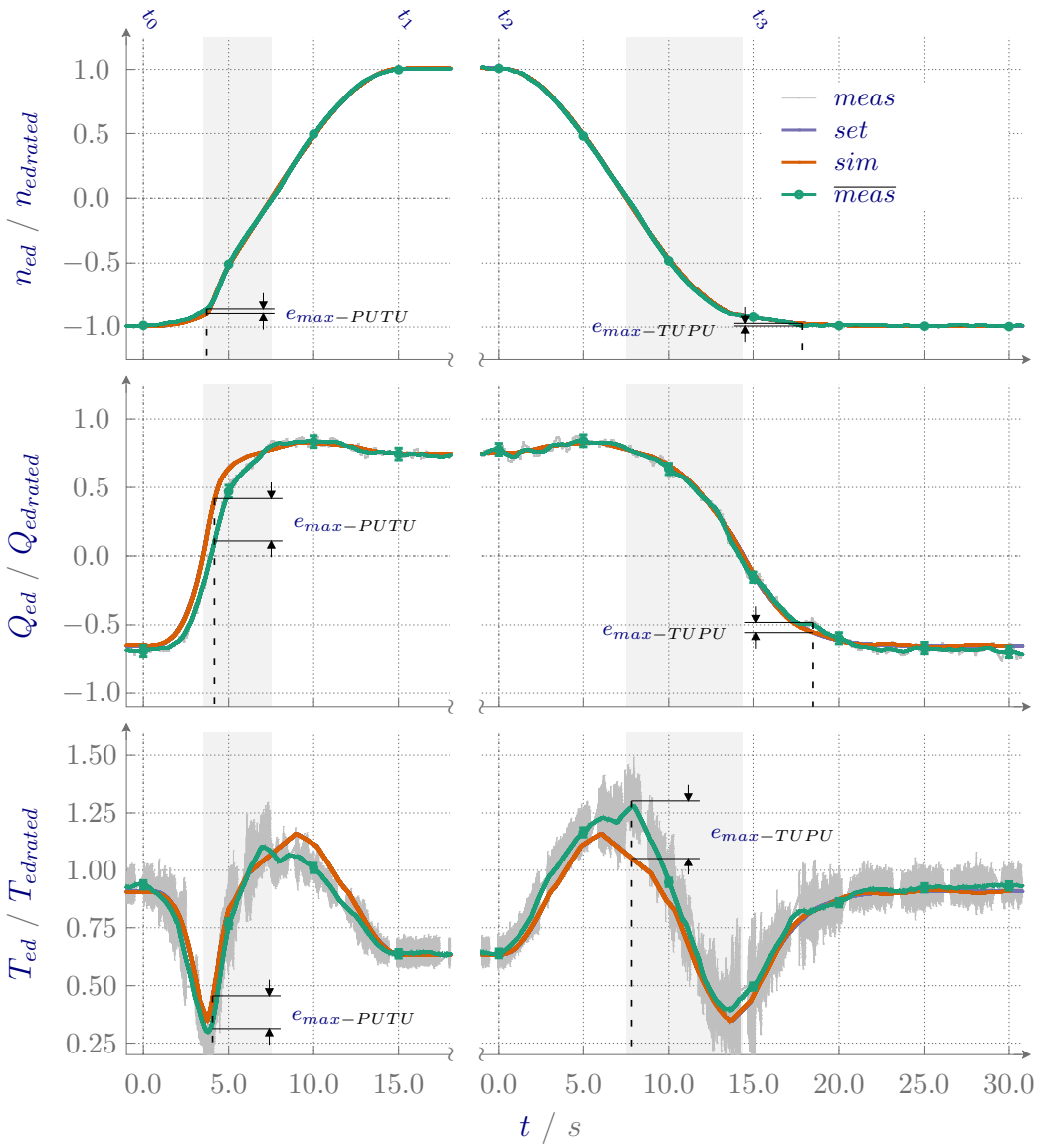

Figure 6.10: Behavior of the model machine during the test case using the machine coefficients versus time.

The machine coefficients provide a good overview of the similarity of the processes between setpoints, simulation, and measurement results (Fig. 6.10). The setpoints are represented by the blue curves, the simulation results of the test rig are shown in orange, and moving average of the measured signals are plotted as green curves.

The unprocessed measurement signal is plotted in a darker gray in the background of these curves. Since the differential pressure measurement consist of a higher accuracy compared to the absolute pressure sensors, this signal is used to calculate the coefficients. All curves are normalized to the rated values of the model machine in turbine mode. As in previous plots, the left diagrams represent the fast transition from pump to turbine operation (t_0-t_1) and the right diagrams represent the reverse process (t_2-t_3). Moreover, as in all further diagrams, the pump brake mode is visualized as a gray area in the background. This gives some orientation about the operating point of the machine in the characteristic diagram.

The curves of the speed coefficients show excellent agreement (top). Not only the simulation values, but also the measured values are almost identical to the setpoints versus time. A small deviation of the measured values are noticeable in the first few seconds in the left diagram, which reaches a maximum approximately at the entry into the pump braking mode ($t = 3.7$ s). A similar behavior does not occur in the reverse process.

The discharge coefficient (center) presents a different picture. The clear offset of the measured results from the setpoint curve is noticeable, especially in the region of the high gradients in the transition from pump to turbine operation. In the reverse transition (right diagram), this deviation is not visible. The maximum deviation is even more pronounced than for the speed coefficient. In addition, the measured values in steady-state pump operation are slightly higher (more negative) than the setpoint values indicate.

This is also evident in the slightly higher torque coefficient in this operating region (bottom). It is also remarkable, that the measured values in the transition from pump to turbine operation are predominantly below the setpoint values and in the reverse process, predominantly above them.

In the section of the reversal of the direction of rotation ($t = 7.5$ s), first a peak and then a local minimum occurs (left diagram). The same characteristic behavior is visible in mirrored form in the reverse process. This behavior does not appear in the setpoints. Furthermore, the maximum deviation occurs at this peak in the transition to pump mode. The original signal of the measurement (gray) also indicates a high degree of fluctuation, especially during the transitions. The repeating interruptions in the signal is explained by the storage process of the measurement data acquisition. Hence, these interruptions are also visible in further diagrams.

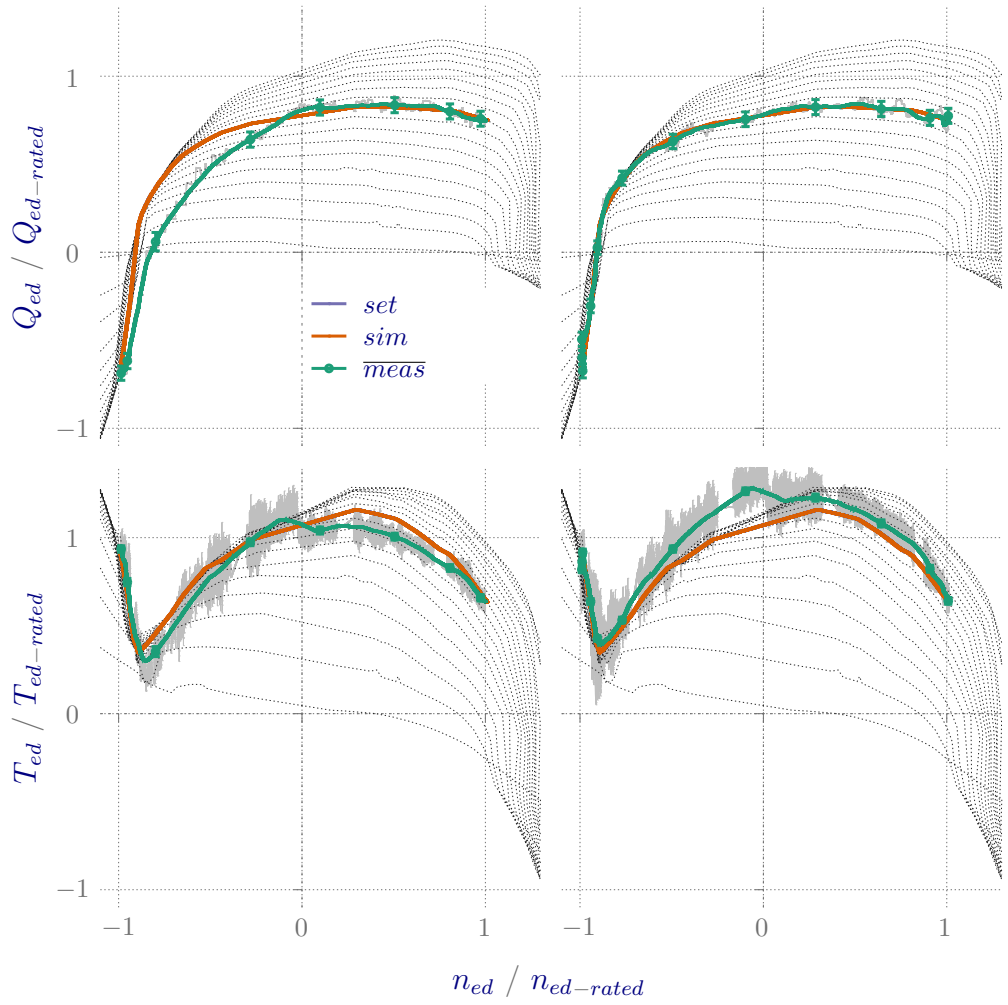

Figure 6.11: Transient paths of operating points of the model machine in the characteristic diagram during the test case. Discharge coefficient in the top diagrams and torque coefficient below. Pump to turbine mode is shown in the left diagrams and the reverse process on the right.

The difference in the quality of the replication of the two fast transitions is also evident when looking at the curves of the machine coefficients in the characteristic diagram (Fig. 6.11). Setpoints and test rig simulation results lie exactly on top of each other for both the discharge coefficient (top) and the torque coefficient. In the simulation, these are tied to the guide vane opening and thus do not deviate from this curve. Also in the measurement, guide vane position is constant during the process. However, due to the time offset, the time related behavior of n_{ed} and Q_{ed} do not match (left). It gives the impression that the opening of the guide vanes change in the course of

the transition. During the reverse process from turbine to pump mode, all curves lie largely on top of each other (right).
Considering the torque coefficient (bottom), setpoints and measured values fit slightly better together in the left diagram than in the transition to pump mode on the right diagram. In fact, the normalized error area is similar in both cases ($\Upsilon_{norm|PUTU}$ and $\Upsilon_{norm|TUPU}$).
On one hand the characteristic diagram presents the coupling of n_{ed} with Q_{ed} and n_{ed} with T_{ed}, respectively. On the other hand, this diagram is not suitable for the investigation into the causes of the deviations. The time related behavior can only be estimated by the distances of the points on the curves. Thus, characteristic diagrams are unsuitable for the evaluation of transient behavior.

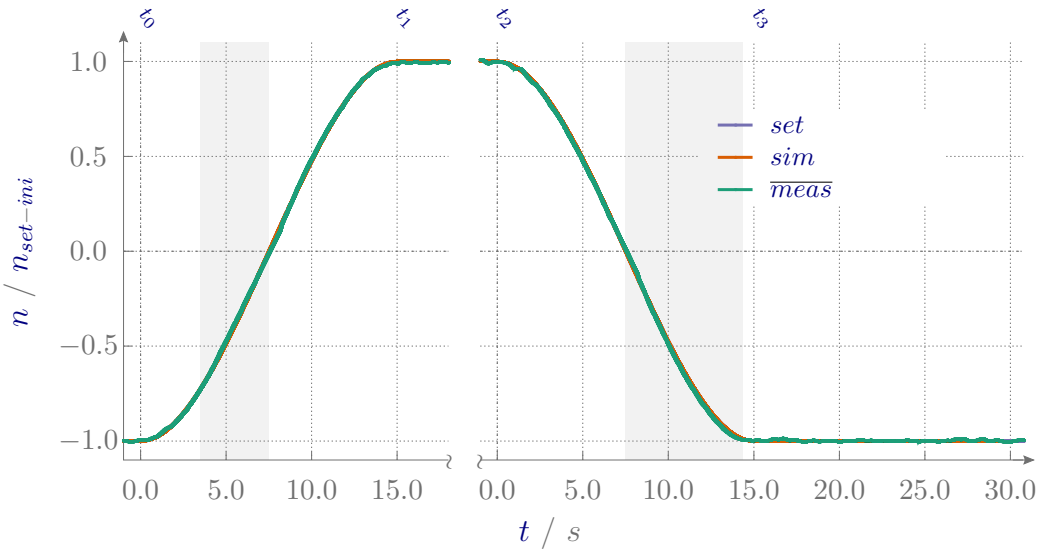

Figure 6.12: Specified rotational speed at the model turbine for the test case scenario.

Because the coefficients are functions of various parameters, the causes of the deviations can only be clarified on the basis of the individual parameter. Considering the speed curve of the model machine, it is not surprising that this follows the setpoints almost ideally, as these values are fed to the test rig speed control (Fig. 6.12). In order to recognize deviations, deep zoomed views would be necessary. Consequently, the speed curve is excluded as the cause of the deviations of the speed coefficient and the focus is directed to the energy curve.

The pressure at the model machine is measured on the one hand via the differential pressure measurement (green curve) and on the other hand via the two absolute pressure measurements in the spiral and in the draft tube (red curve in Fig. 6.13).

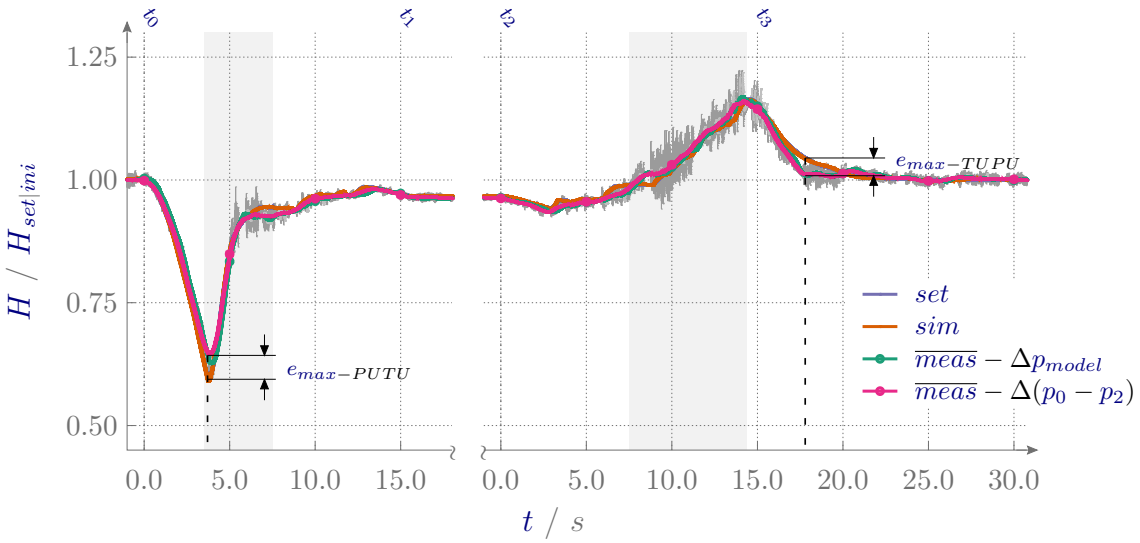

Figure 6.13: Evolution of head versus time during the test case.

Using these pressure measurements in combination with the kinetic energy, the head of the machine is determined. By comparing the two energy curves, hardly any differences are visible. This leads to the conclusion, that both sensor variants deliver similarly fast and similarly accurate results for the test case.

As expected from the observation of the speed coefficient, measured values and simulation values show good agreement with the setpoint curve. This diagram is used to explain the deviations from n_{ed} at the transition from pump to turbine operation (at approx. 4 seconds after start). The measured signals do not capture the pressure minimum to the same extent as predicted by the setpoint or the test rig simulation. The largest deviation also occurs at that point in time.

In the reverse process, the maximum deviation occurs at about 18 seconds. The measured values show, that the head drops back to the value of steady-state pump operation more quickly than setpoints and simulation predict. This also explains the maximum deviation of the speed coefficient at this point.

Furthermore, both transitions have minor deviations in the regions around the rotational speed reversal (about 7.5 seconds). Flow effects that occur when the rotor is close to standstill may be the reason for these deviations. Such effects cannot be predicted by the solver used. Further investigations are necessary to confirm this assumption, but they are not addressed in this work.

To understand the pronounced deviations of the discharge coefficient, it is necessary to look at the discharge of the model machine (Fig. 6.14). But as mentioned earlier, this value is calculated based on the discharge measurements of the bypass branch (middle)

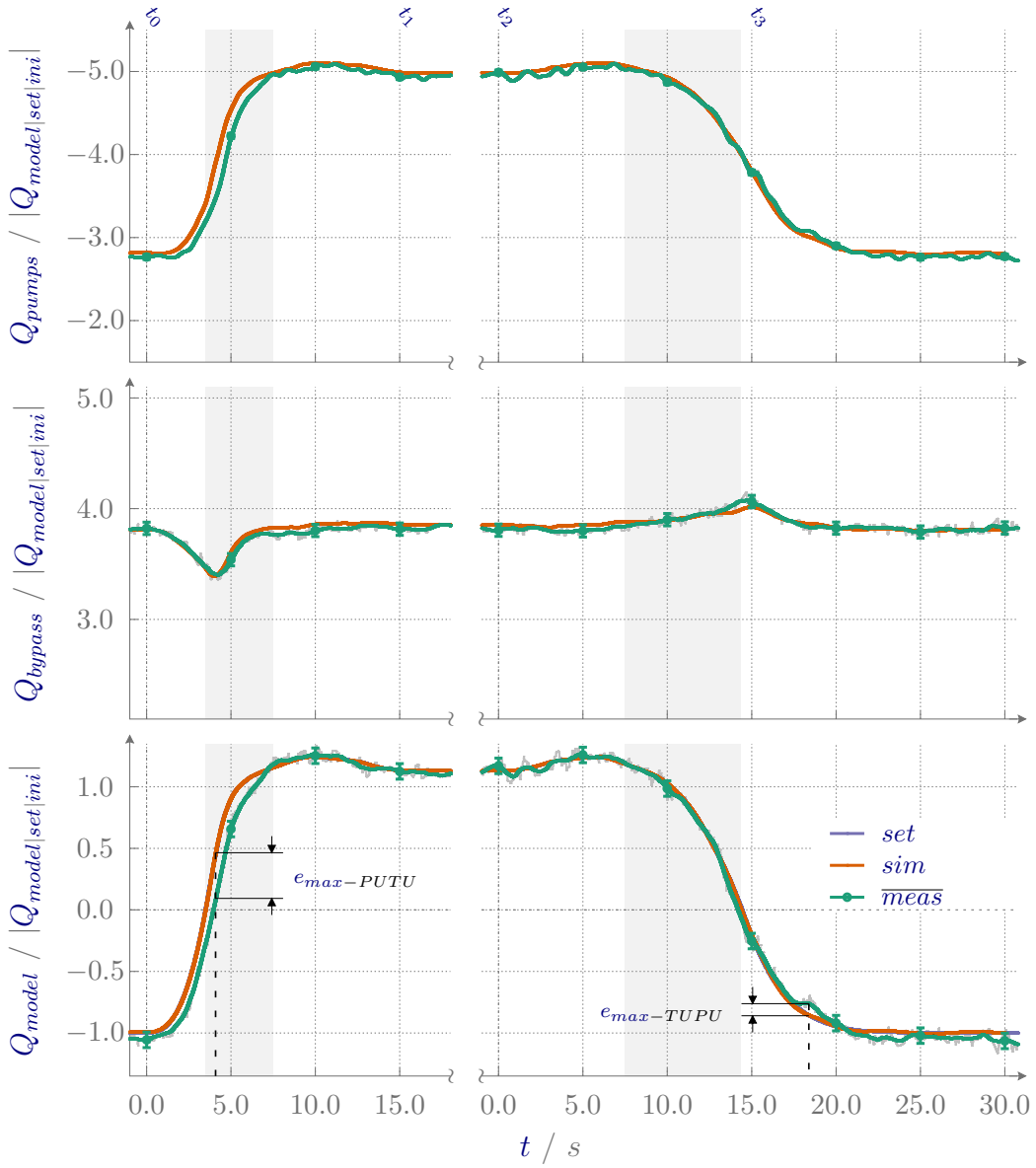

Figure 6.14: Discharges in the individual branches for the test case scenario versus time.

and the service pump branch (top). Thus, these parameters cannot be omitted from the evaluation. All curves are normalized to the setpoints of the model machine in pump mode.
The measured values of the bypass show a good agreement with the results of the test rig simulation, especially in pump mode. Even at high gradients (in pump braking mode, left diagram), no excessive deviations occur, although the curve loses agreement. This small deviation remain over the entire turbine operation.
However, when considering the service pump discharge, it becomes clear that the measurement follows the simulation values only with a noticeable time offset in the area of high gradients (fast transition from pump to turbine operation). In the reverse transition from turbine to pump operation, this offset is less pronounced. Obviously, the sensor used in the branch of the service pumps is not fast enough. Damping and dead time seem to be too high for the dynamic process. This results in a significant maximum deviation of the model discharge at about $t = 4$ s. The maximum deviation in the right diagram seems to result from fluctuations in discharge in the service pump branch and may not occur to this extent on the model machine.

Under these conditions, it is not surprising that there are pronounced deviations in the discharge coefficient of the model machine. However, it is questionable whether these deviations actually occur at the model. In theory, for a given guide vane opening, a given rotational speed, and a given head, there is a fixed value for the discharge. Without taking Reynolds effects into account, this theory is stored in the machine's characteristic diagram. However, the influence of the boundary layer as a cause for deviations is negligible. Both the map generation as well as the transient model tests are carried out at similar speed orders.
Since the measurement results of speed and head do not show significant deviations from the setpoints and, in addition, the guide vane opening is specified with a high degree of accuracy, it may be assumed that the discharge does not deviate significantly from the setpoints either. This indicates that the power plant discharge is replicated more accurately in the transient model test than the deviations in the flow coefficient suggest.
Further investigations are necessary to confirm this assumption. It must be excluded that inertial forces do not influence the course of discharge significantly. This would require a fast measurement technique in the branch of the model machine.

To evaluate the torque coefficient, the results of torque itself are examined (Fig. 6.15). In their characteristic T_{ed} and T hardly differ from each other. Only the point in time

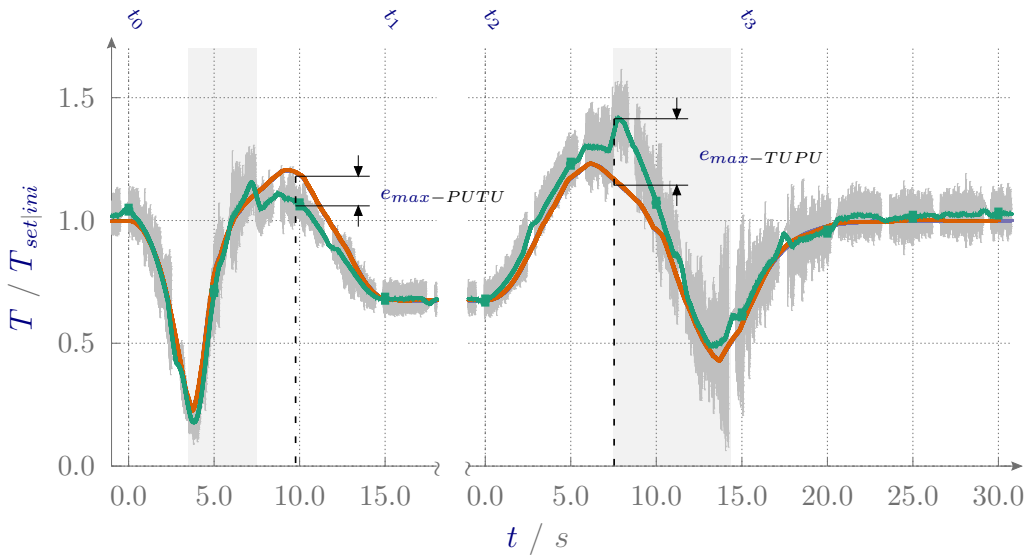

Figure 6.15: Behavior of torque versus time during transients of the test case.

of the maximum deviation, during the transition from pump to turbine operation, is not the same.

The detected sequence of the peak with the following local minimum (or vice versa respectively) arises from the measured torque signal. It occurs exactly at the time of the reversal of the direction of rotation ($t = 7.5$ s) and is explained by this event. Up to the peak, torque vector and direction of rotation are contrary. This leads to the highest torque of this transition, exactly at the time when the motor generator of the model machine forces the rotor to standstill. The runner continues to generate torque due to the remaining flow (compare T_{ed} in Fig. 6.11 at $n_{ed} = 0$). Subsequently, the direction of rotation reverses and has the same sense of rotation as the torque vector. The forces acting on the runner blades now accelerate the rotor in the direction of turbine rotation. This acceleration leads to a brief drop in torque. In return, now the motor generator takes over the task of braking the rotor, because the test rig speed controller fulfills its fixed setpoints. Thus, the torque increases again.

The same happens in reverse in the transition from turbine to pump operation. Since the motor generator must accelerate the rotor against the flow, the absolute highest torque of both fast transitions occurs at this operating point. The average value rises up to 40 % above the rated value in pump mode, the fluctuations even reach values up to 60 %.

Table 6.3 lists the deviations during steady-state operation, as well as the maximum error, and the error area during the transients for all mentioned parameters.

Table 6.3: Investigated deviations of the model machine parameters of the test case.

Mode	**PU**	**PU→TU**		**TU**	**TU→PU**	
Parameter	$(meas-set)/set$	e_{max}/set_{ini}	Υ_{norm}	$(meas-set)/set$	e_{max}/set_{ini}	Υ_{norm}
n	0.001	-0.015	-0.010	-0.005	-0.013	-0.010
H	0.001	0.039	0.012	-0.007	0.029	0.006
Q	0.052	0.274	0.066	-0.019	0.073	0.023
T	0.024	0.107	0.051	-0.001	0.240	0.049
n_{ed}	0.000	0.039	8.620	-0.002	0.023	8.253
Q_{ed}	0.052	0.394	56.48	-0.019	0.094	54.03
T_{ed}	0.023	0.176	173.1	0.008	0.310	165.6

6.3.2 Test Rig Results

In the following diagram, the curves of the eight absolute pressure sensors are normalized to the initial measured value in pump mode (Fig. 6.16). With exception of the pressure measuring position p_4, simulation and measurement results demonstrate a good agreement in the steady-state pump and turbine operation.

In combination with the results of the discharge rates, it is concluded that the simulation model of the test rig can replicate the conditions of the steady-state operating points with sufficient precision. Table C.1 (Chapter C.1) underscores this assessment. In this table, the deviations of the measurement results, with respect to a reference pressure for the steady-state pump or turbine operation, are listed. For the measuring positions p_0 and p_2, the reference pressures are the setpoints, which are known from the transferred power plant data. For the remaining positions, the results of the test rig simulation are used as references.
As in the analysis of the influence of the speed of sound, deviations between simulation and measurement are noticeable in the transient regions. In these regions the courses of the simulated pressures are overestimated on the low-pressure side (p_2, p_3, p_4, p_7, and p_8) and pressure drops are underestimated on the high-pressure side. Since the values are normalized to different pressure levels, no absolute errors can be compared between the measuring positions. From the analysis of head, it is known that simulation and

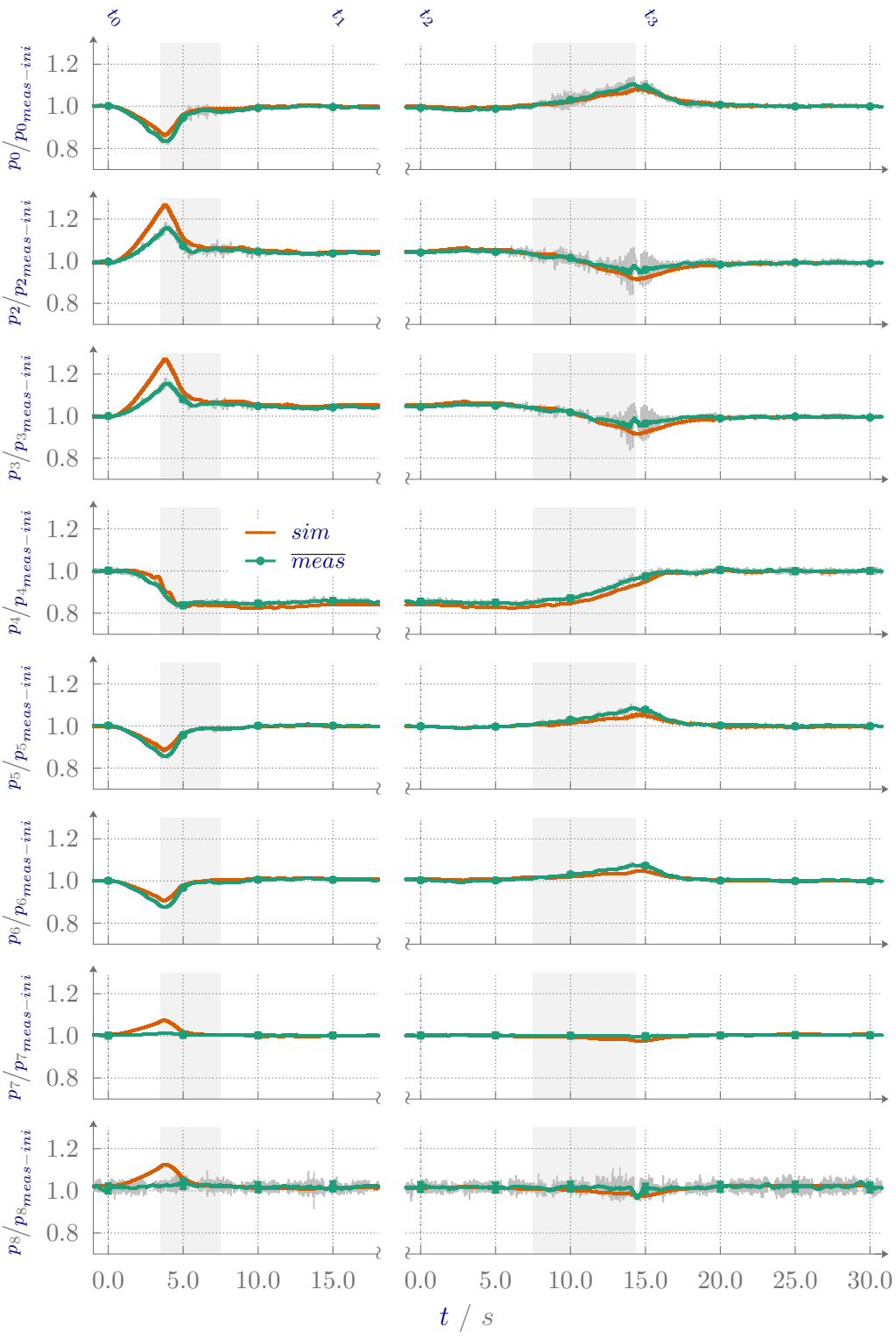

Figure 6.16: Test case results of absolute pressure at sensor locations (Fig. 4.3).

measurement results of energy differences show good agreement. If head corresponds but the individual pressures show deviations, it is concluded that these deviations occur at almost the same amount on the low-pressure and high-pressure side.
As already indicated, p_4 shows a permanent deviation during steady-state turbine operation. This sensor is installed in the branch of the service pump. In this branch, the highest change in discharge occurs between pump ($\approx 3 \cdot Q_{model}$) and turbine operation ($\approx 5 \cdot Q_{model}$) of the model machine (compare Fig. 6.14). This corresponds to the range of the Reynolds number starting from $Re = 5.7 \cdot 10^5$ to $Re = 1.0 \cdot 10^6$ at the different modes.
Depending on the roughness, changes in the pipe friction coefficient occur in this zone of the Moody diagram [131]. The higher velocity would lead to a decrease in friction coefficient. The actual energy loss differs from the prediction of the simulation, thus the curves do not match. However, an adjustment of the pipe friction coefficient in a pipe element is not possible during the simulation. In the other branches, the difference in the Reynolds number between pump and turbine operation is not that noticeable and thus the friction coefficient hardly changes.

Considering the scale of the axis of ordinate, simulation and measurement results of the service pumps reveal a reasonable agreement over a wide section. This applies to both the speed and the discharge coefficients (Fig. 6.17). The course of the measurement of n_{ed} from *pump*1 shows two outliers. One after entering pump braking mode (top-left diagram) and another right after t_3. It cannot be ruled out that the first outlier is related to the pressure drop at the model machine that occurred shortly before. However, this would raise the question why the measured value at *pump*2 does not show this effect. The same could be valid for the second outlier.
The slight offset in the discharge coefficient curves may be attributed to two reasons. On the one hand, the already discussed discharge measurement in the pump branch is of relevance. The delayed course of the measurement, which is particularly pronounced at the transition from pump to turbine operation, is visible in this diagram (bottom-left diagram at approx. $t = 2$ .. 6 s). On the other hand, due to the mounting position of the flowmeter, the actual distribution of flow between the two pumps is not known. Nevertheless, when calculating the discharge coefficients, a uniform distribution of the volume flow is assumed. Taking into account the different heads, this results in an over- or undervaluation, respectively. Thus, small deviations between simulation and measurement results occur. The quantitative evaluation of the behavior of the service pumps are listed in Table C.2 in Chapter C.1.

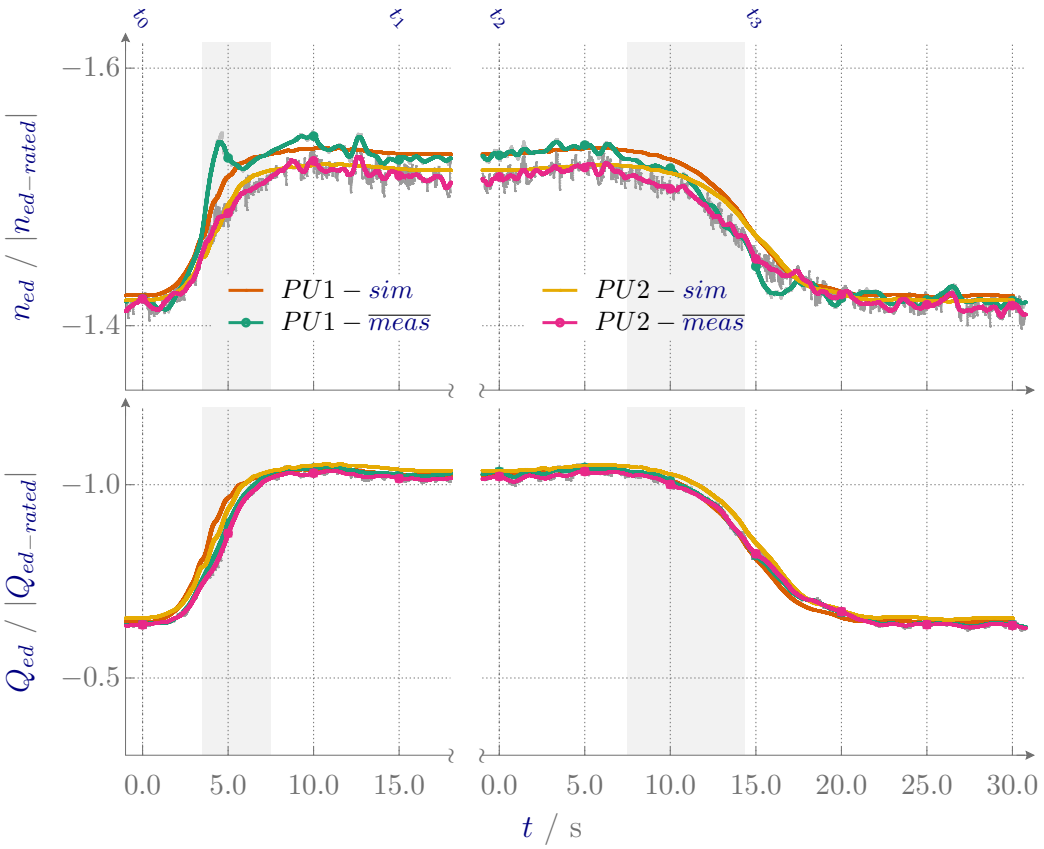

Figure 6.17: Machine coefficients of the service pumps during the test case fast transient of the model machine.

The differential pressure measurement at the bypass valve obtain very reasonable results (Fig. 6.18). The presented characteristic of the valve corresponds to a normalized ratio between flow and energy difference over the scale of 0 to 1. Only minor deviations are visible during the transitions, which are not predicted by the simulation. This is attributed to pressure fluctuations, as the flow in the bypass shows agreement with the simulation values (Fig. 6.14).

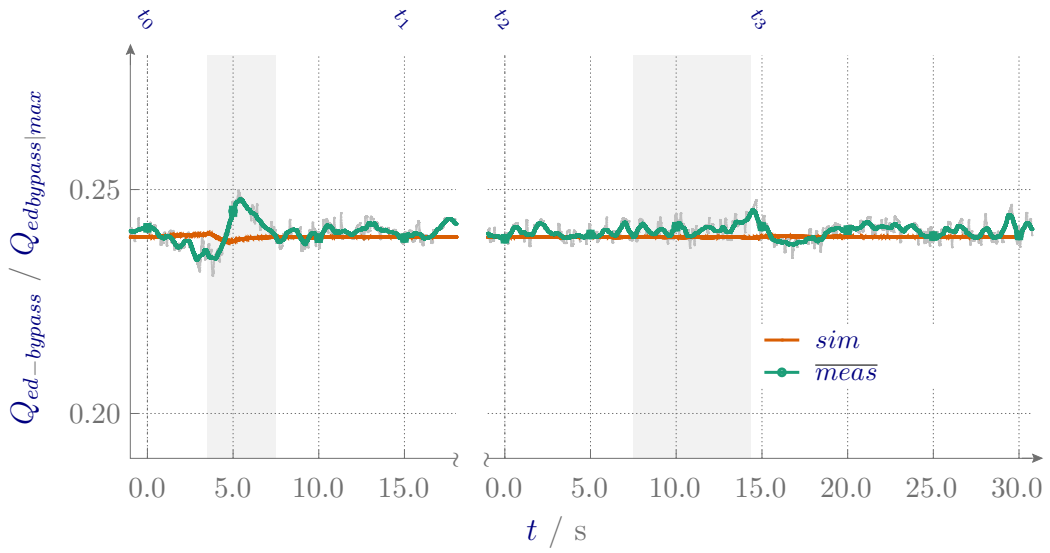

Figure 6.18: Characteristics of the bypass valve during the test case of fast transient of the model machine (0 corresponds to completely closed and 1 to completely opened valve).

6.3.3 Influencing Factors on Quality Assessment

All diagrams and tables of the test case results provide an impression of the model-scale replication of the transient power plant process. In general, most results show good agreement with the setpoints. Nevertheless, depending on the parameter, different pronounced deviations are visible. The following investigation demonstrates whether these deviations between measurement and simulation have systematic causes that influence the quality assessment.

Correction of Transient Simulation Results of Head and Torque

As discussed in Section 2.1.3, in the 1D simulation hydraulic machines are represented by their characteristic diagram. However, this diagram does not take into account the different inertial forces within the machine. The method developed by Carpio [2] to correct simulation results of head and torque to the transient characteristics is intended to reduce deviations between measurement and simulation. Time-dependent quantities are the behavior of rotational speed and discharge derived by time ($^{dn}/_{dt}$ and $^{dQ}/_{dt}$ in Eqns. 6.2 and 6.3). The geometry properties of the machine are reflected in the calculated factors of these equations. For the correction of the transient torque, the inertial masses of the rotor and the water masses inside the machine are also relevant.

$$
\begin{aligned}
&H_{unsteady} - H_{steady} \\
&\qquad = 1.502 \cdot 10^{-2} \cdot \frac{dn}{dt} \\
&\qquad + (11.0598 + 19.2922 + 2.3427) \cdot \frac{dQ}{dt}, \text{ [m]}
\end{aligned}
\tag{6.2}
$$

$$
\begin{aligned}
&T_{unsteady} - T_{steady} \\
&\qquad = \frac{\pi}{30} \cdot (4.53 \cdot 10^{-2} + 3.5 \cdot 10^{-1}) \cdot \frac{dn}{dt} \\
&\qquad + 1.502 \cdot 10^{-2} \cdot g \cdot \rho \cdot \frac{dQ}{dt}, \text{ [N m]}
\end{aligned}
\tag{6.3}
$$

In the following, the setpoints of head and torque, which are transferred from the power plant simulation, are corrected to the dynamics of the test case and compared with the measurement results. With the factors calculated according to A. Carpio [2], the correction of the setpoint values of head leads to a higher deviation from the measured values (blue dashed curve Fig. 6.19) than the uncorrected setpoints. This is particularly noticeable in the much lower drop in head during the transition from pump to turbine operation. In the reverse process, the head is expected to reach a more pronounced maximum. Error area and maximum error are increased considerably (Tab. 6.4).

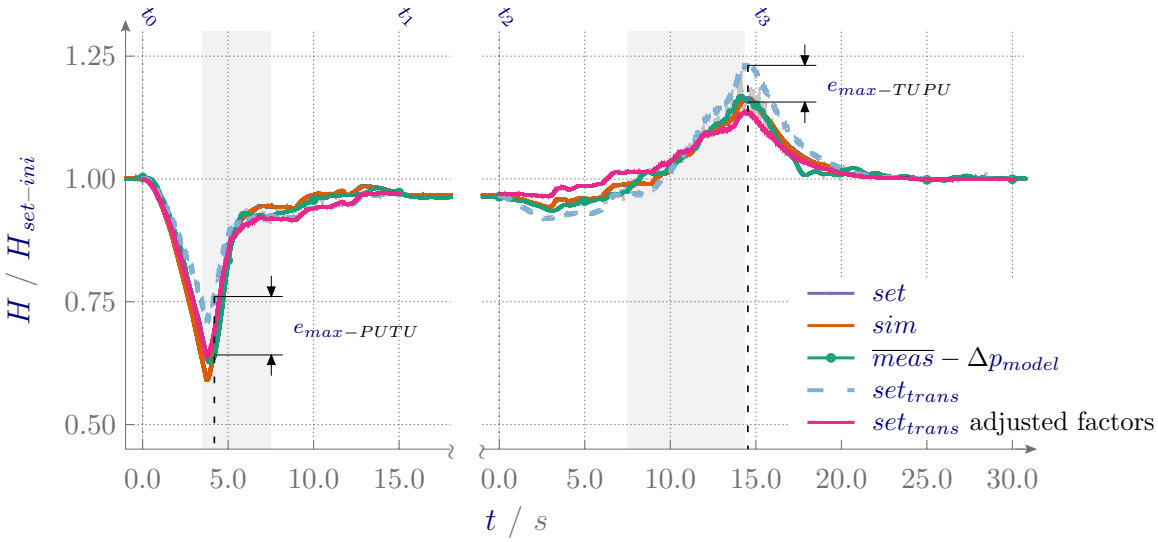

Figure 6.19: Corrected setpoints of head (blue dashed) to consider transient effects according to A. Carpio [2]. Adjusted transient factors result in better setpoint correction (red).

In the previous sections, the agreement between measured values and setpoints, related to the head, is already pointed out. Since the measured values reflect the reality of the transient process, the correction with these factors does not provide a practicable procedure.
In the region of the largest deviation (compare lowest points of the curves) the $^{dQ}/_{dt}$ term has the dominating influence on the correction. If the setpoint correction should have a minimum deviation to the measured head (green curve), the factors of Eqn. 6.2 of this term are approximately 2.5 times too high. By adjusting the factors (red curve), setpoints and measurements match better, at least in the region of the head drop during the transition from pump to turbine operation.

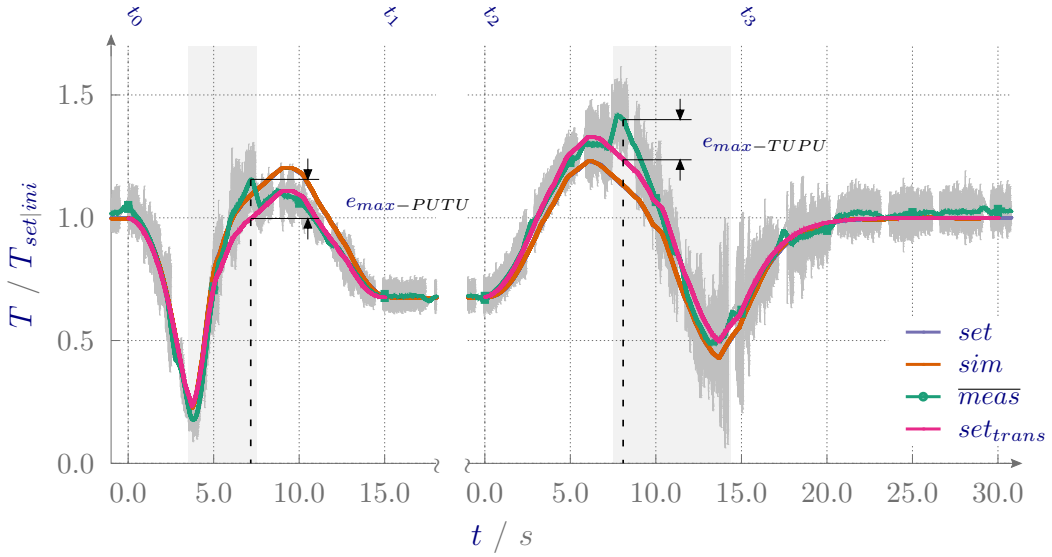

Figure 6.20: Corrected setpoint of torque (pink) to consider transient effects according to A. Carpio [2].

A different result is obtained by the correction of torque setpoints (Fig. 6.20). Here, the measured values (green) and transient setpoints (red) move much closer together. Both error area and maximum error are significantly reduced (Tab. 6.4).
For this parameter, the correction procedure is evaluated as a positive contribution and should be considered when comparing simulation and measurement results. This method is also supportive when predicting actual torques based on simulations, whether from the power plant or the test rig. However, the interaction between the direction of rotor rotation and the torque vector must be taken into account to achieve reasonable results.

Neither with adjusted nor with original factors this method leads to meaningful reductions of the deviations of head. For this reason, the method is not applied to

head in the further investigations.
With regard to the optimization process, this correction also does not need to be applied when comparing setpoints with the results of the test rig simulation. As mentioned, the optimization target value is the head at the model machine and thus only Equation 6.2 would be relevant. The geometry factors as well as $^{dn}/_{dt}$ values are exactly the same for the setpoints and the test rig simulation. Since the power plant and test rig simulations are based on the same characteristic diagram and during optimization procedure H will be brought as close as possible to its setpoint, also $^{dQ}/_{dt}$ behaves more and more similarly to its transferred setpoints. Thus, it is not relevant whether H_{steady} or $H_{unsteady}$ is used as a comparison to the optimization (shown in Fig. 5.3).

Table 6.4: Comparison of maximum deviation and error area for corrected setpoints relative to uncorrected setpoints of head and torque.

Mode	**PU→TU**		**TU→PU**	
	$e_{max\|trans}/e_{max}$	$\Upsilon_{t\|trans}/\Upsilon_t$	$e_{max\|trans}/e_{max}$	$\Upsilon_{t\|trans}/\Upsilon_t$
H adjusted factors	1.277	0.982	1.270	1.859
T	1.323	0.658	0.604	0.543

Influence of Test Rig Pressure Level on the Measurement Results

The conditions in the test rig can also cause systematic deviations between measurement and simulation. A remaining degree of freedom of the model experiment is the absolute pressure level in the test rig. More precisely, this concerns the pressure on the suction side of the model machine, which has an influence on the occurrence of cavitation and thus on the operating behavior. A quantity for this is the cavitation number sigma (Eqn. 6.4), which represents a normalized energy level available until cavitation occurs at the trailing edge of the rotor blade (or leading edge in pump mode).

$$\sigma = \frac{\frac{(p_2 - p_{vap})}{\rho \cdot g} + (z_2 - z_{2'}) + \frac{1}{2 \cdot g} \cdot (Q_{model}/A_2)^2}{H} \tag{6.4}$$

The course of sigma during the execution of the test case for different pressure levels is shown in Figure 6.21. In addition, the behavior of sigma in the test rig simulation as well as the power plant simulation is shown. In order to present the power plant data in the same diagram, the time axis is normalized to the duration of the transition Φ. For each case the corresponding pressures in the draft tube versus ambient pressure are listed in Table 6.5.

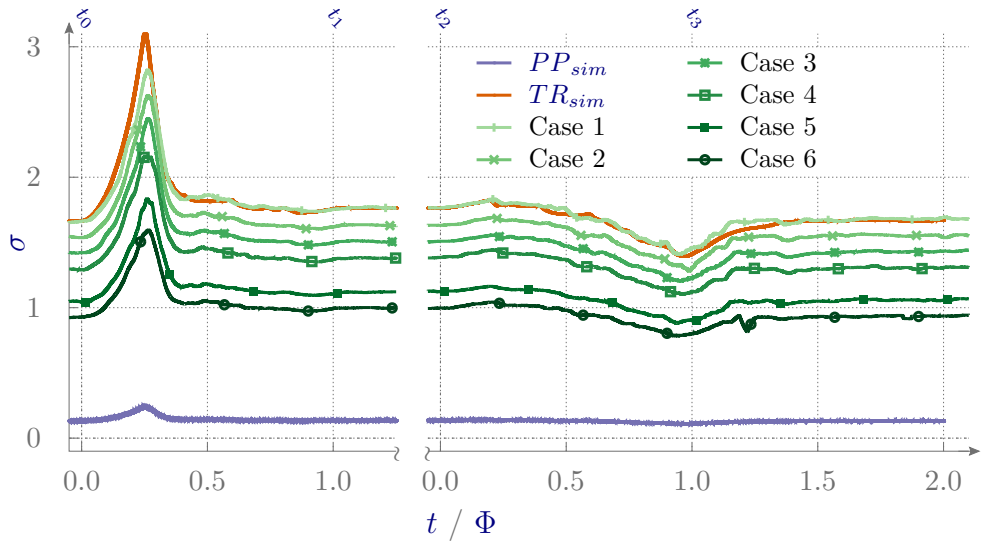

Figure 6.21: Measurement results of different cavitation numbers σ compared with the results of power plant and test rig simulation.

The significantly lower level of the power plant result is noticeable. As described before, the power plant simulation is carried out with the maximum difference in head of the reservoirs. Thus, the tail water reservoir has the lowest water level, which corresponds to a low pressure level on the suction side of the machine. If the pressure in the draft tube of the model machine is calculated from the sigma value in the steady-state pump mode of the power plant, this results in a pressure of $p_2 = -8.52$ m below ambient pressure.

It should be mentioned that cavitation is not considered in the 1D power plant simulation. But, if cavitation occurs in reality, it has an influence on the discharge and thus also on the pressure. If a similar cavitation behavior of the power plant should be considered in the model test, the 1D power plant simulation can only provide an approximation for the pressure on the suction side. To obtain more reliable results, CFD simulations might be helpful.

Nevertheless, to achieve such a low pressure level, modifications to the test rig are necessary which could not be implemented within the scope of this work.

Table 6.5: Results to evaluate the influence of the pressure level on the transient model test.

Mode	PU		PU→TU		TU		TU→PU	
	p_2 [m]	σ	$\Upsilon_t(H)$	$\Upsilon_t(Q)$	p_2 [m]	σ	$\Upsilon_t(H)$	$\Upsilon_t(Q)$
TR_{sim}	3.882	1.667	0.002	0.002	4.167	1.762	0.002	0.004
Case 1	3.913	1.656	0.016	0.092	4.174	1.765	0.009	0.037
Case 2	2.908	1.542	0.015	0.096	3.170	1.631	0.008	0.040
Case 3	1.900	1.422	0.015	0.094	2.159	1.506	0.008	0.035
Case 4	0.897	1.293	0.015	0.100	1.165	1.383	0.010	0.044
Case 5	-1.078	1.049	0.016	0.096	-0.825	1.125	0.008	0.031
Case 6	-2.062	0.926	0.014	0.092	-1.818	0.995	0.011	0.037

When comparing the different cases, no clear trend of degradation are visible for error areas of head. Nevertheless, the table shows that the transition from turbine to pump operation is worst in case 6 ($\Upsilon_t(H) = 0.011$). Since the cavitation number is proportional to $^{p_2}/_{H}$, one explanation for the poor result is an outlier that occurs at approx. $^{t}/_{\Phi} = 1.25$. However, these experiments were not repeated several times for each case to prove this assumption beyond doubt.

Further investigations of the influence of the pressure level are observed with the help of fluctuations of the absolute pressure measurement in the draft tube. Figure 6.22 illustrates the amplitudes of the pressure signal in the draft tube versus frequency, normalized to the initial rotational frequency of the model machine. The course in time is plotted on the axis of ordinate. In addition, the measured rotational speed of the model machine is plotted (red curve). The horizontal, white, rhythmically occurring stripes represent the storage intervals of the measurement data acquisition.
In all cases, the largest fluctuations occur mainly in the range $^{f}/_{f_{n_{ini}}} < 0.5$, during the transitions and after re-entry into pump mode ($t > t_3$). These fluctuations seem to become weaker with decreasing draft tube pressure. A different picture arises for the period around the reversal of the rotation speed (midway between t_0 and t_1 or t_2 and t_3). In these phases, the fluctuations increase with decreasing pressure level in several frequency ranges. A similar behavior was detected by Ruchonnet et al. [100] on the suction side of the runner blades. This is particularly evident at two points

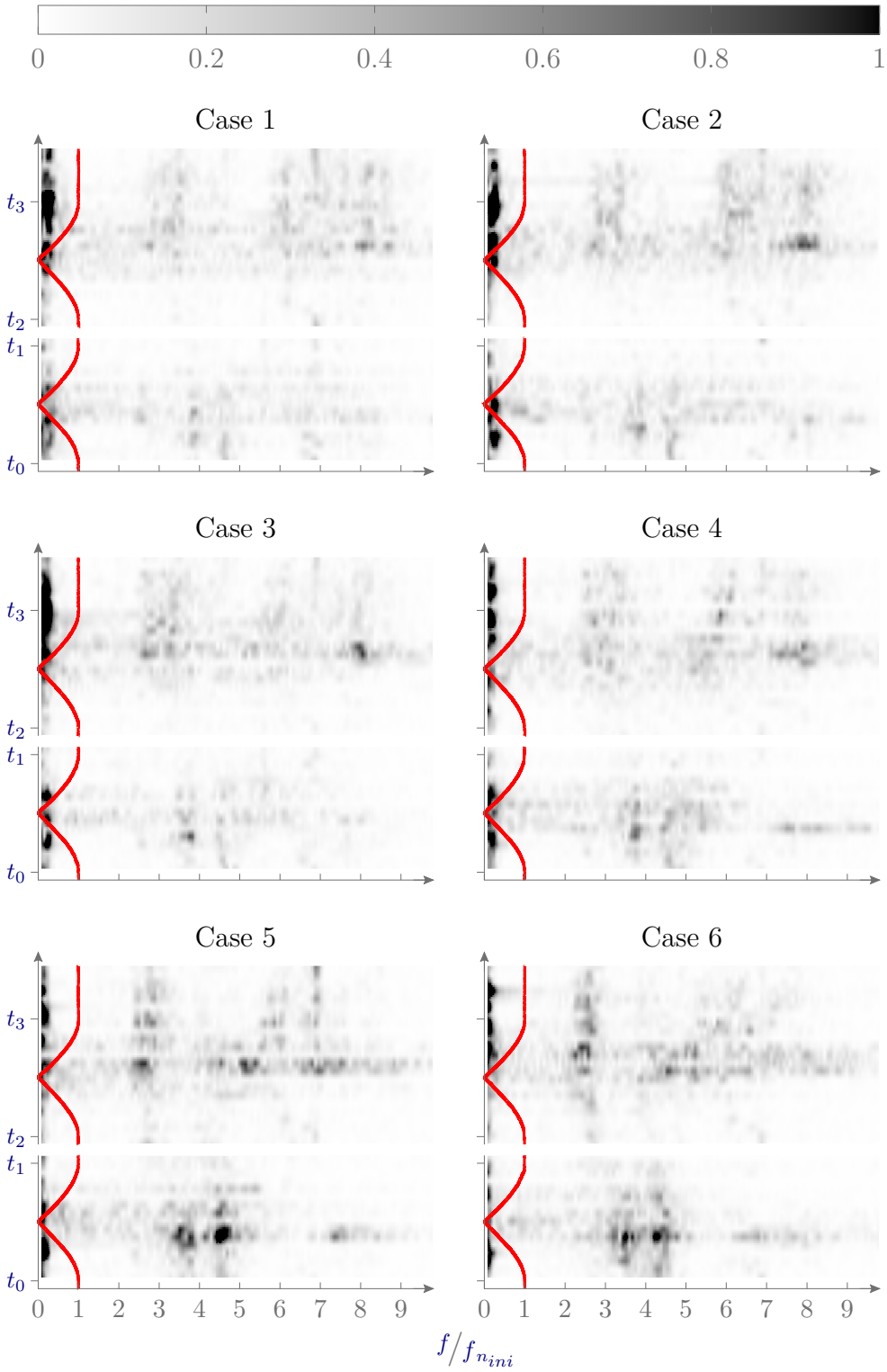

Figure 6.22: Frequency analysis by means of the normalized amplitude spectrum of draft tube pressure for different pressure levels in the test rig. Axis of ordinate refers to the course in time. The rotational speed of the model machine is shown as red curve. An overview of integral values are listed in Table 6.5.

with their centers at $f/f_{n_{ini}} \approx 3.75$ and ≈ 4.5, just before the reversal of rotation direction to turbine operation (t_0 to t_1). Especially in these operating regions, there are strong misaligned flow at the blades (see also Section 2.1.1) and swirling outflows in the draft tube. In addition, a decreasing pressure level encourages the occurrence of cavitation. All these effects lead to a pronounced unsteady flow behavior and cause the observed pressure fluctuations. The different flow phenomena in these operating regions and their causes have been studied, for example, by Braun [10] and specifically for a fast transition by Stens [118].

The results from the frequency analysis indicate that some of the findings from the steady-state investigations on certain operating ranges, which are described by Braun [10], also occur during the transient experiment. With regard to the initial question whether systematic influences are responsible for deviations between measurement and simulation results, the following is identified. For the investigated range of the pressure level in the test rig, the error values hardly differ from each other despite of increasing cavitation. Thus, the pressure level is excluded as the cause for the remaining deviations. Moreover, two findings should be noted. On the one hand, the influences on the quality of the test rig measurement results are hardly recognizable without technically supported lowering of the suction-side pressure (e.g. with a vacuum pump). This is especially necessary if sigma values comparable to those of the power plant should be achieved. On the other hand, if the interest is directed to the cavitation phenomena within the machine, further measurement equipment is needed.

6.4 Investigation of Methodology Based on Test Case

Based on the test case, the applied methodology is evaluated for its capability to reproduce transient processes in a real test rig. Furthermore, the reliability of the methodology in terms of repeatability of a given load case is also of interest.

6.4.1 Capability Investigations

One of the first experiments of fast transitions in a closed-loop test rig are carried out by Ruchonnet et al. [100]. In this investigation, the rotational speed of the service pumps is changed linearly and without optimization, in the transient zone between pump and turbine operation of the model machine. By comparing the different

approaches of Ruchonnet with the optimization of the service pump behavior used in this work, the capability of the latter approach is investigated. For this purpose, two further experiments are carried out. In these experiments (linear case 1 and 2) the speed of the service pumps follow a given linear change (Fig. 6.23).

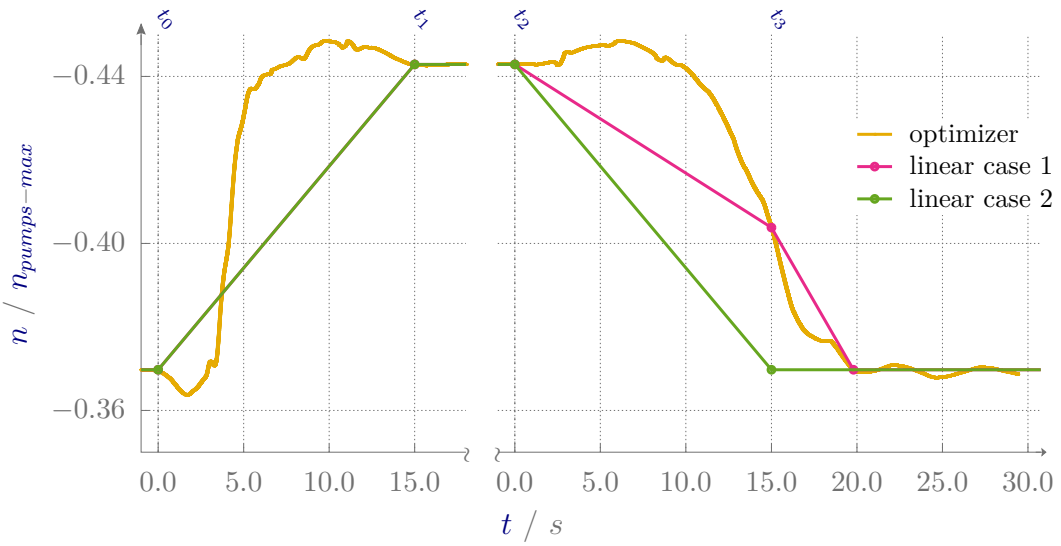

Figure 6.23: Comparison of optimized rotational speed with two cases of linear speed change of service pumps.

During the transition from pump to turbine operation (t_0 to t_1), the speed profiles of the service pumps are equal in both cases. In the reverse process, linear case 1 (red) has an additional breakpoint extracted from the optimized course. This considers the longer duration of the transition back to steady-state pump operation.

The comparison of the measured head of these three cases with the setpoints (blue) illustrates the clear differences (Fig. 6.24). The optimized process reveals a better agreement with the setpoints than the other two cases. Only in a short section during the transition from turbine to pump operation, in the period from approx. $t = 16$ .. 20 s, the red colored course of the linear case 1 is closer to the setpoints than the optimized course.

These results lead to the conclusion that the two linear cases do not replicate the power plant process at all or only in very small sections. In both linear cases, the replication is significantly worse than in the presented method with optimized pump speed. This is evident when looking at the quantitative results listed in Table 6.6. If the head has such large deviations from the setpoints as in these examples, all three machine coefficients will also have large deviations. The transient processes at the power plant and at the test rig are no longer consistent.

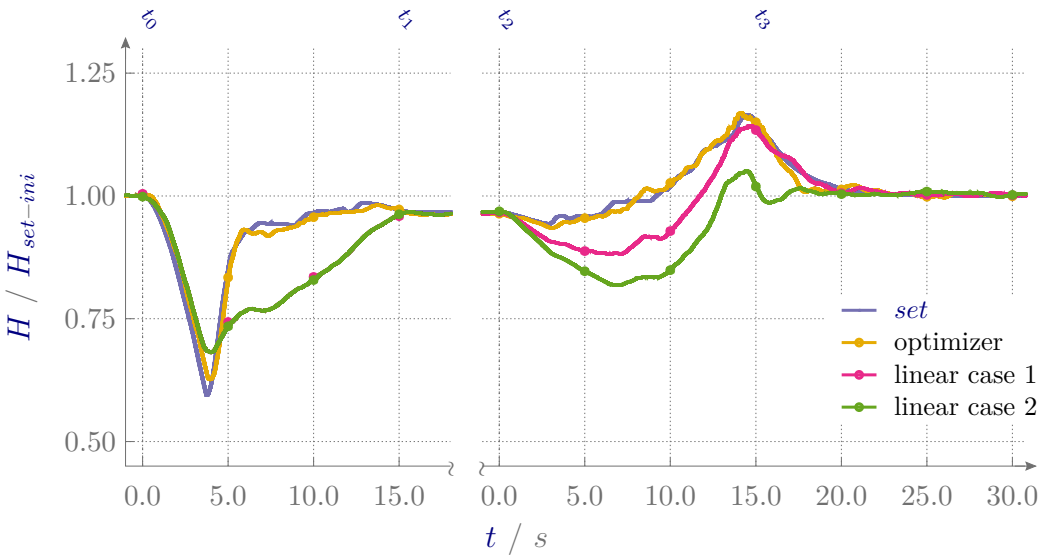

Figure 6.24: Behavior of head versus time during the transition from pump to turbine operation (left) and vice versa (right) for different speed behavior of the service pumps.

The approach of linear speed profiles of the service pumps is not a practicable option to perform model scale replications as accurately as possible. The effort to determine the appropriate service pump speed via the optimization process is therefore not only justified, but an essential step to generate results with the necessary quality.

Table 6.6: Evaluated head for comparison of optimized speed change and linearly assumed speed change of the service pumps.

Mode	**PU→TU**		**TU→PU**	
	$e_{max}/H_{set_{ini}}$	Υ_{norm}	$e_{max}/H_{set_{ini}}$	Υ_{norm}
solver	0.0399	0.0153	0.027	0.008
linear case 1	0.1425	123.06	0.088	162.25
linear case 2	0.1465	97.34	0.146	128.45

6.4.2 Repeatability Investigations

Classical experiments with hydraulic machines have the characteristic that the measurement results of an examined operating point are averaged over a certain period of time. This procedure is intended to reduce the influence of the random error and sudden outliers in the measurement.
In the case of the transient model test, the measured quantities are time-dependent, which makes this averaging method unable. However, it is possible to perform an experiment several times and then average the results versus time (Eqn. 6.5). In the following averaging processes of the individual cases i, the parameter under consideration has already been processed with a moving average.

$$\overline{H}(t) = \frac{1}{z} \sum_{i=1}^{z} H_i(t) \tag{6.5}$$

In Figure 6.25, the error areas of the head of ten experiments of the test case executed in a series (transition from pump to turbine operation and vice versa) are presented as blue bars. The results are normalized to the smallest error area (case 5) of the ten measurement series. The additionally shown error bars appear to cover a large range compared to the measured values. This is correct, because the error area only represents the deviation between measured values and setpoints. Related to this difference, the measurement uncertainty is significantly larger than in the diagrams of the absolute parameters (e.g. Fig. 6.13). Furthermore, the maximum error related to the smallest value of all ten cases (case 10) is plotted in this diagram.

By averaging the measured head of two or more cases and subsequent recalculating the error area, the orange cases 11 to 19 are obtained. With this method, the error area of the worst case (case 7) is reduced by 8.3 percentage points. Compared to the best case (case 5), the averaging over ten cases is still 2.7 percentage points worse.
Continuing this method with even more cases, the averaged result stagnates above the best individual case. Regardless of how many experiments are necessary until stagnation, this does not result in the best replication of the prototype process.

If the individual cases are not considered equally when calculating the average, this leads to a better overall result. This method corresponds to a weighted arithmetic mean [22]. In this approach, the cases are sorted in descending order according to the error area. Then the first two cases (cases 7 and 2) are averaged and a new case (case 11) is formed (Fig. 6.25). This new case is then averaged with the next case (case 3)

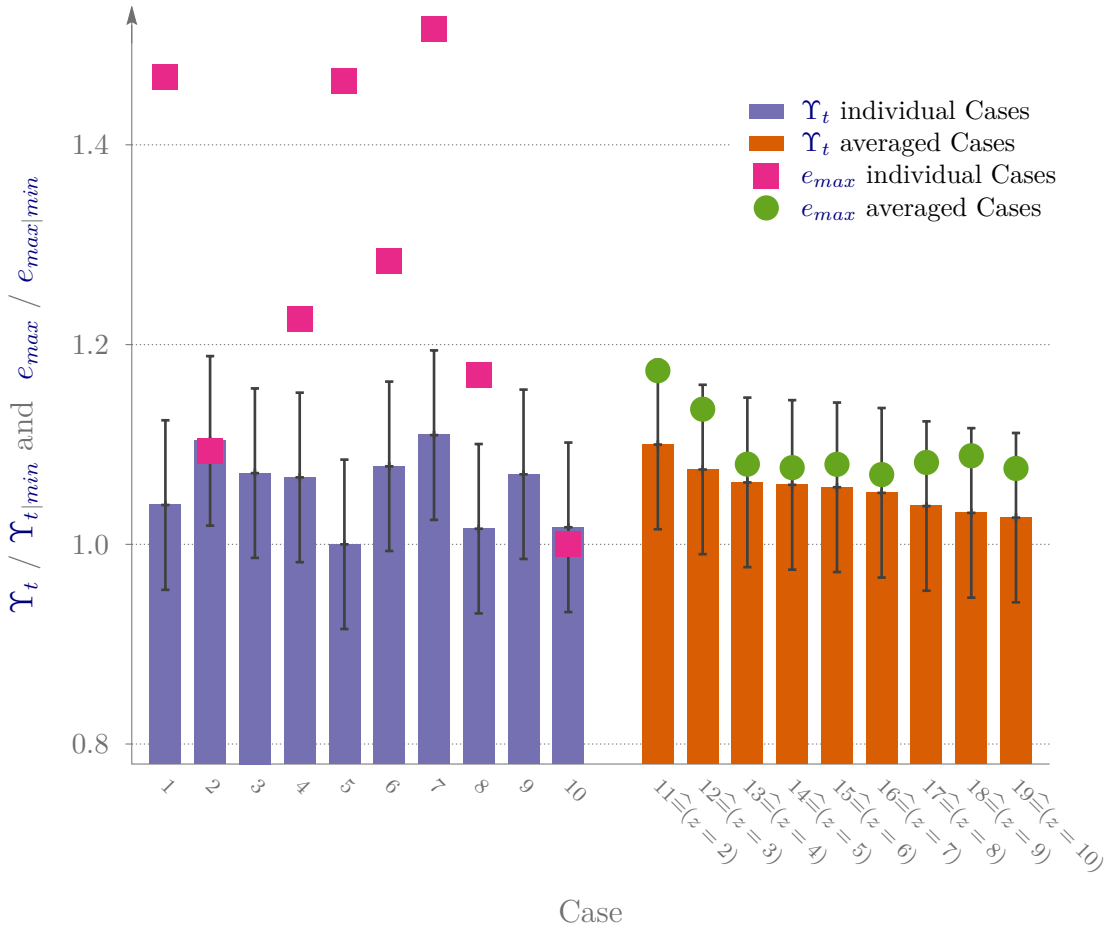

Figure 6.25: Repeatability study: error area and maximum deviation over ten executions of the test case (blue bars and pink squares) and results of the averaged cases (orange and green). Values are normalized to case 5 (minimum of error area). Maximum deviation of case 3 and 9 outside the range.

and so on.

Thus, the better individual results are weighted higher, which is expressed in the result of the last case (case 19). The error area is about 1 % better than in the best measured case and thus represents the transient power plant case best in relation to the head.

However, this procedure does not automatically lead to an improvement of all parameters. Table 6.7 demonstrates that weighting via the head leads to a degradation of other parameters such as discharge or torque. In the example of the discharge, the weighting via the head even leads to a worsening of the result. The weighting of the cases must therefore be done independently for each relevant parameter.

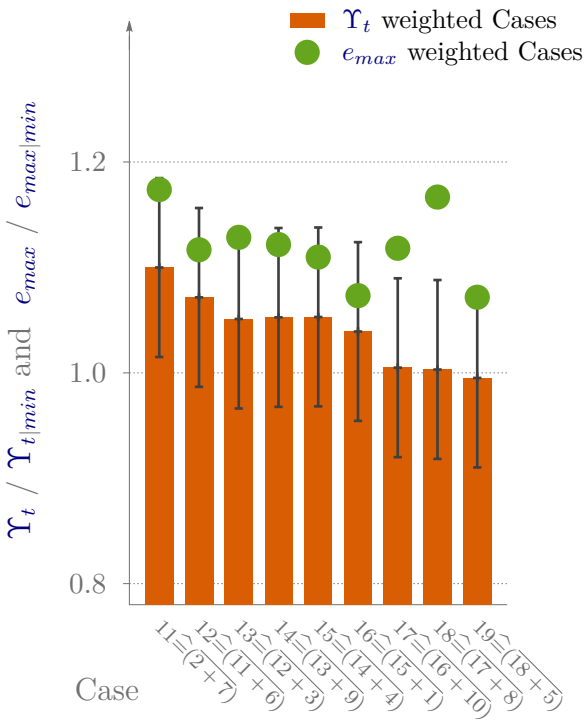

Figure 6.26: Weighted evaluation of the executed test cases.

This study reveals two findings. The results of individual experiments can differ significantly. Thus, a single result is not sufficient to make precise statements about the quality of the replication. For this reason, the experiments must be repeated several times. Nevertheless, the necessary number of experiments can be reduced by using appropriate mathematical methods.

Table 6.7: Error areas of head, discharge and torque in the repeatability study. For case 19 (weighted), the weighting parameter is the head.

Parameter	$\Upsilon_t(H)$	$\Upsilon_t(Q)$	$\Upsilon_t(T)$
min	0.1839	0.0050	6.374
max	0.2040	0.0057	7.427
Case 19	0.1888	0.0057	6.555
Case 19 (weighted)	0.1830	0.0060	6.687

6.5 Summary and Discussion

The test case investigations reveal that the established methodology by simulating the test rig in conjunction with optimization delivers results which replicate the power plant load case with good consistency. It is demonstrated that a rotational speed specification for the service pumps derived from the optimization achieves better results than the non-optimized cases. However, before these investigations are performed, a handful of parameter studies and further investigations are carried out, e.g. to define the appropriate parameters and limit values for the optimizer. It turns out that, especially with the appropriate time shift T_a, converging results are achievable with a reasonable amount of iterations.

Furthermore, it is shown that multiple repetitions and subsequent averaging of the measurement results are essential to obtain reliable results via transient model tests. In this context, the selected averaging procedure can also contribute to the improvement of the measurement quantities. Also the differences in torque between simulation and measurement could be successfully reduced via the correction of transient dynamics according to Carpio [2]. Both methods should be considered in future investigations.

Attention must also be paid to the definition of the speed of sound for the test rig simulations. The parameter study demonstrates that the choice of speed of sound has a minor influence on the simulation results for moderate changes in discharge. However, if a certain rate of $^{dQ}/_{dt}$ exceeds during the transient process, the influence increases. A parameter study with subsequent comparison of measurement results can provide a solution.

An influence on the quality of the results, which comes from the adjustable pressure level of the test rig, could not be determined. However, since one of the goals of these model tests are to predict the load on the power plant, it is necessary to replicate the same conditions. The necessary cavitation number σ, which is derived from the prototype simulation, could not be achieved in these investigations. This would require a further reduction of the pressure level, e.g. via a vacuum pump.

In summary, the chosen setup of the test rig, the optimization method and the evaluation procedures of the results are suitable for a successful execution of the transient model test.

7 Results of Various Transient Load Cases

In Chapter 3 some transient load cases are described; these are examined in the following for their feasibility in a transient model experiment. These include the fast transition already discussed in Chapter 6, as well as load acceptance and rejection by guide vane adjustment. Power control in pump mode is not discussed because it challenges the established methodology for transient model tests in a similar manner to a fast transition.
As mentioned above, the real test rig does not have a controlled guide vane adjustment. Thus only tests with simple speed control are verified with measured values. Nevertheless, the investigations of the test case in Chapter 6 show that a lot of knowledge can be gained from the test rig simulations.

7.1 Investigations of Fast Transitions via Changes in Rotational Speed

From a power plant's point of view, a transition from one mode to another will be carried out due to a change in power demand from the electrical grid. If the electric machine remains connected to the grid during the transition, the power output depends, among other conditions, on the rotational speed profile. In the following, the implementation of model experiments at different speed profiles of fast transition is investigated.

7.1.1 Description of Fast Transition Tests

In addition to the spline speed profile, discussed in Chapter 6, additional profiles for a fast transition are considered. These profiles generate different mechanical power output curves of the power plant. The given speed profiles and power output results at maximum gross head and a guide vane opening of $\gamma/\gamma_{max} = 0.6$ are illustrated in Fig. 7.1. Besides the spline profile, the transition is assumed to be linear or different variants of a tangent hyperbolic function (Eqns. C.1, C.2, C.3, and C.4). On the left,

the transition from pump to turbine mode (t_0 and t_1) and on the right, the reverse process (t_2 to t_3) is represented.

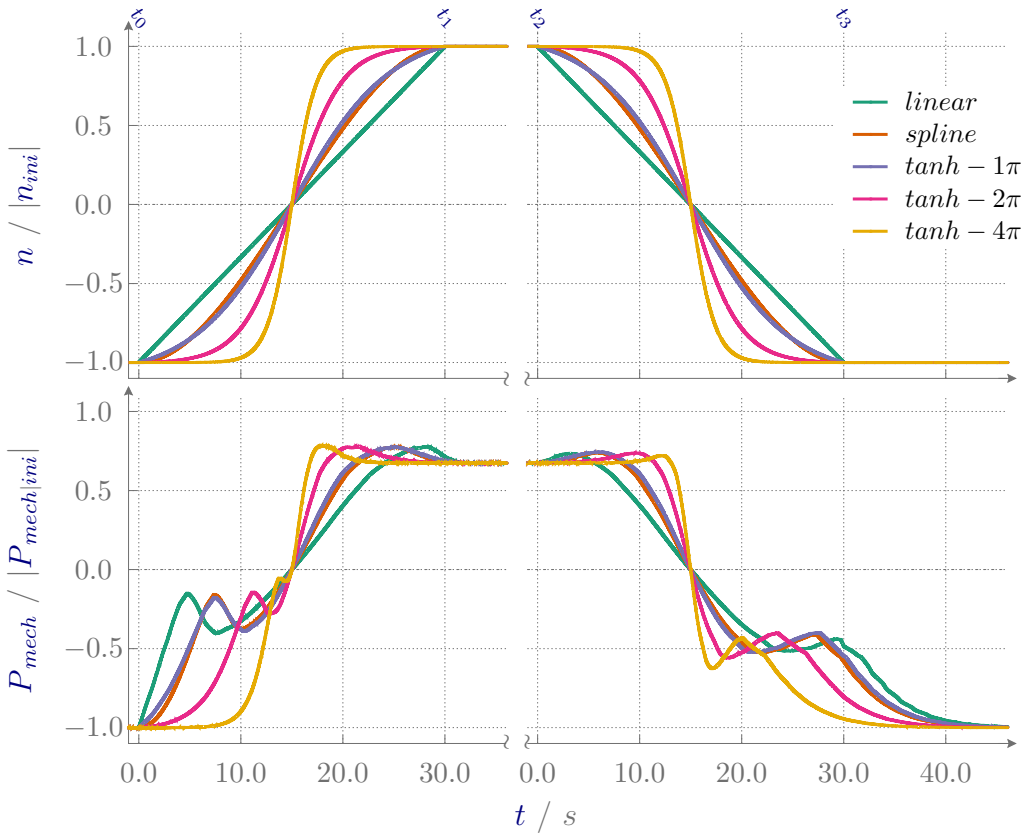

Figure 7.1: Various profiles of rotational speed changes of a fast transition (top) and the resulting mechanical power at the power plant (bottom) with a maximum gross head and a guide vane angle of $\gamma/\gamma_{max} = 0.6$.

Each of these profiles has its own characteristic. It is noticeable that the case of linear speed change takes the longest time to reach a steady-state operating point. This is valid for both transitions. In all cases, the power exhibits a local minimum in pump mode, before and after the rotational speed reversal. This is related to the torque minimum that occurs at the point of flow reversal (Fig. 7.2 middle and bottom). Moreover, when entering or leaving the turbine operation, the mechanical power exceeds the steady-state value of this mode.

Figure 7.2 indicates that the different speed profiles have different requirements with regard to replication in the model test. This applies to both the optimization process of the service pumps behavior and the measurement technology for verifying the results.

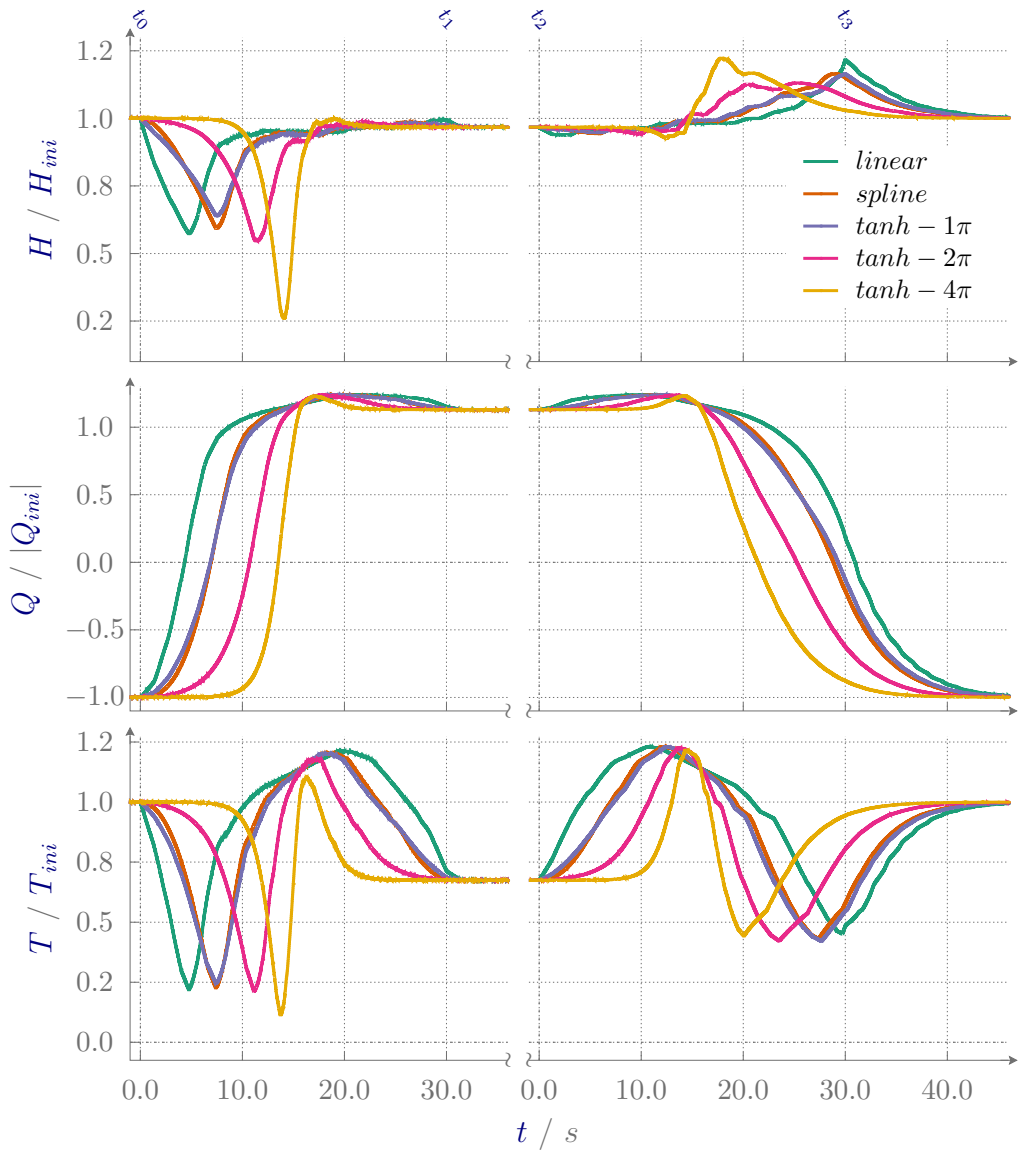

Figure 7.2: Behavior of head (top), discharge (middle), and torque (bottom) of the power plant load cases normalized to their initial values.

The duration of an experiment, based on the time scale factor x_{t-Sr}, has a decisive influence on the feasibility of these model tests.

When transferring the speed profiles to the model size, the time scale factor is an independent variable. However, this variable defines the $^{dn}/_{dt}$ behavior of the hydraulic machines. But this values cannot be chosen arbitrarily, because in the experiment the accelerations of the hydraulic machines depend on the drive motors. To determine limits of x_{t-Sr} according to the different speed profiles, experiments of defined speed jumps are carried out on the test rig (Fig. 7.3). The acceleration and deceleration limits of the electrical machines are derived from these measurements (orange curves).
If all valves of the closed circuit are open, the influence of the inertia of water masses on the acceleration or deceleration is taken into account. Such an influence is visible for the service pumps in the deceleration section (Fig. 7.3(a) right diagram at $t > 4$ s). The one-quadrant operation of this electric drive allows only power output. Consequently, the motor is powerless during deceleration. Only frictional forces and forces on the runner decelerate the rotor. If the flow in the pipes slows down, the deceleration also decreases.

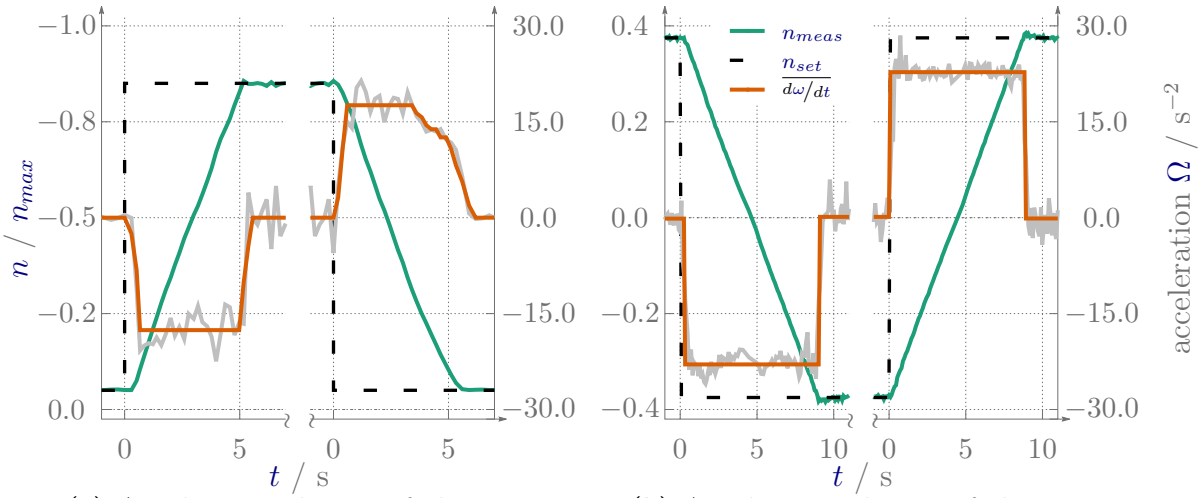

(a) Acceleration limits of the motor of the service pumps.

(b) Acceleration limits of the motor generator of the model machine.

Figure 7.3: Measured acceleration limits of the electric machines of the test rig by triggering a sudden increase and decrease in setpoint of rotational speed.

Comparing the speed profiles transferred to the model size with the maximum possible acceleration rates of the motor generator, the limit for the time scale factors x_{t-Sr} are determined. Figure 7.4 shows acceleration of the model speed profiles for the transition from pump to turbine mode (left) and vice versa (right). The cases are discretized in

0.5 steps of time scale factor to indicate the fastest possible and the next case which exceeds this limit. For a better visualization, the curves are shifted against each other on the abscissa axis.

This study demonstrates the limitation of the applied similarity law to adjust the time scale through the physical limits of the test rig. In addition, this restricts the approximation of the dynamic similarity between model and prototype, as the duration of the transient power plant process and the acceleration limits of the machines have a direct influence on the maximum initial speed of the model experiment. According to these results, the fast transition with the $tanh(4\pi)$ profile, for example, cannot be performed faster and thus not with a higher initial speed compared to the prototype ($x_{t-Sr} = 1.0$). Whereas the *linear* profile with $x_{t-Sr} = 2.5$ achieves the highest possible initial speed and enables the fastest model test.

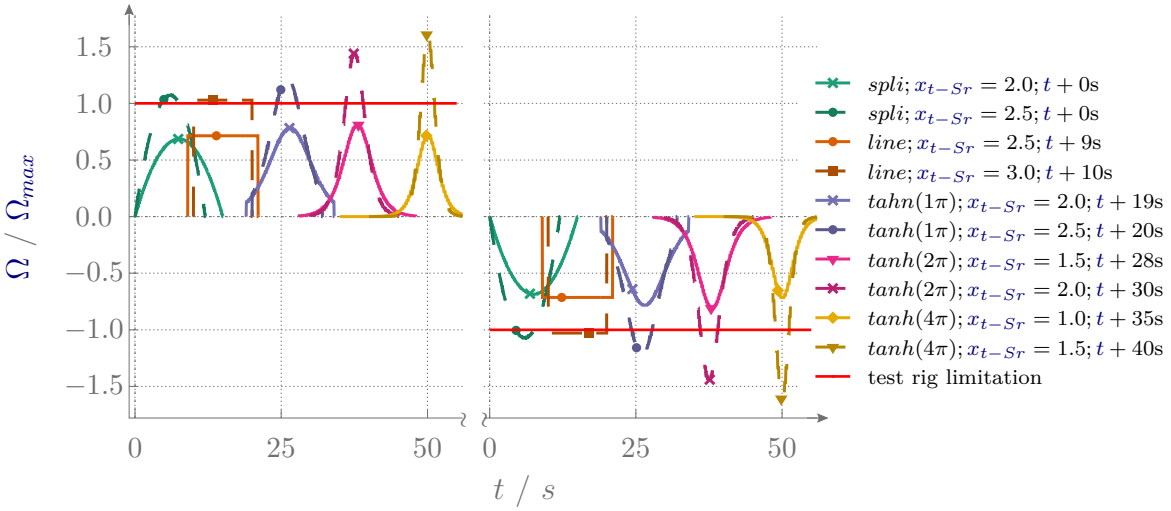

Figure 7.4: Angular acceleration limits of various speed profiles for fast transitions.

7.1.2 Result of Fast Transition Tests

In addition to the variation of the speed profiles and the time scale factor, the tests are also carried out for different guide vane openings ($\gamma/\gamma_{max} = 0.4$, 0.6, and 0.8). This results in numerous findings, which are presented on the basis of representative cases. Preliminary results with spline speed profile at $x_{t-Sr} = 1.5$ are already published in [56].

First, the results of the spline profile at $\gamma/\gamma_{max} = 0.6$, which served as the test case for $x_{t-Sr} = 2.0$, are presented. Since the duration of an experiment differs over the

variation of the x_{t-Sr} values, the time axis is normalized for the duration of the corresponding process $\Phi(x_{t-Sr})$. Furthermore, the limits of the pump braking mode, which is shown as the gray area in the background, are related to the setpoints of the model discharge.

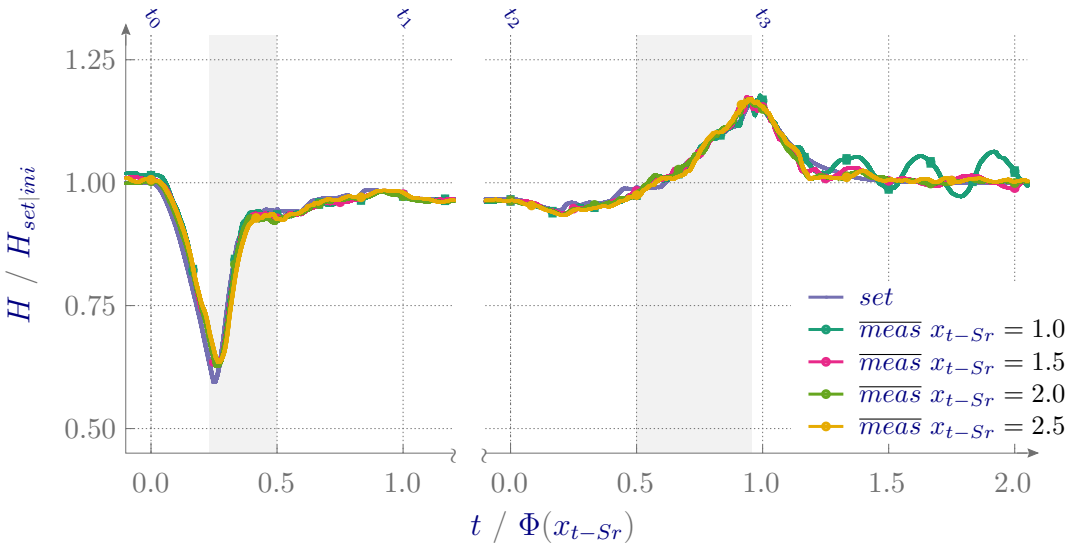

Figure 7.5: Comparison of the head between setpoints and measurement results for different time scale factors of speed controlled fast transitions from pump to turbine mode (left) and vice versa (right) with spline profile and a guide vane opening of $\gamma/\gamma_{max} = 0.6$.

Except the case of $x_{t-Sr} = 1.0$, variation of head hardly differ from each other (Fig. 7.5). The extreme values and gradients lie almost identically on top of each other. This also applies to the $x_{t-Sr} = 2.5$ case, which actually cannot be realized exactly according to the evaluation of the motor generator acceleration limit.
On the basis of the measured rotational speed at the model machine, it is noticeable that at moment before the rotational speed reversal, the course no longer follows the setpoint (Fig. 7.6(a)). An influence of this rotational speed deviation on head or discharge (Fig. 7.7) is not indicated.

However, the $x_{t-Sr} = 1.0$ case is remarkable, because a fluctuation of almost ± 10 % around the setpoints, after re-entry into pump mode is visible. These fluctuations are also observed in discharge. The origin of these fluctuations are identified in the optimization process of the speed of the service pumps. The combination of a small allowable error and a low actual head results in a sensitive system. In this case, a slight adjustment of the speed of the service pumps tends to exceed the target value which results in an unstable behavior.

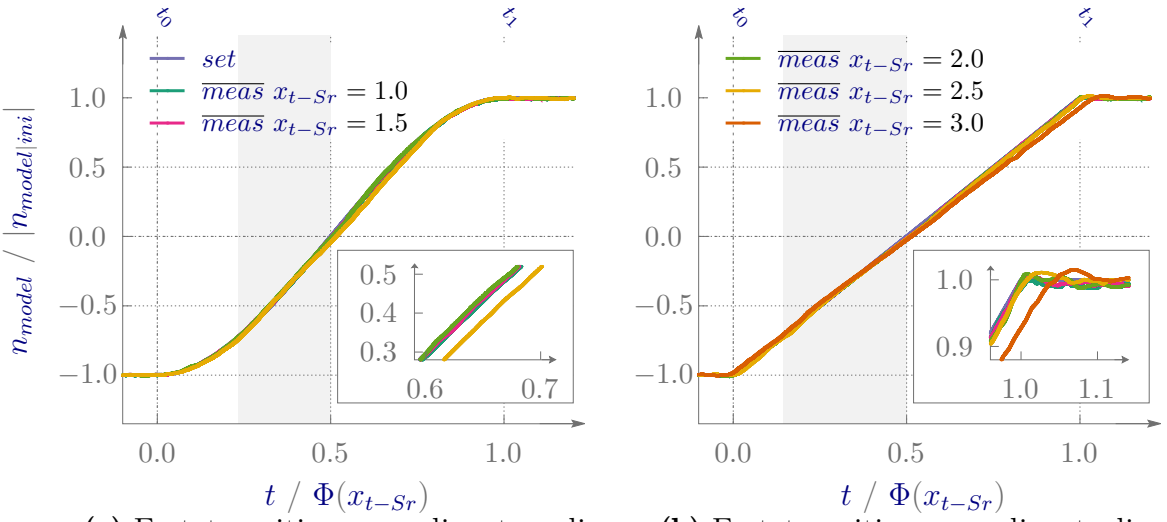

(a) Fast transition according to spline profile. Noticeable deviation for time scale factor of $x_{t-Sr} = 2.5$.

(b) Fast transition according to linear profile. Noticeable deviation for time scale factor of $x_{t-Sr} = 3.0$.

Figure 7.6: Comparison of the rotational speed at the model machine between setpoints and measurement results for different time scale factors of a speed controlled fast transition from pump to turbine mode. The zoom shows the region with the larges deviations. The legend belongs to both diagrams.

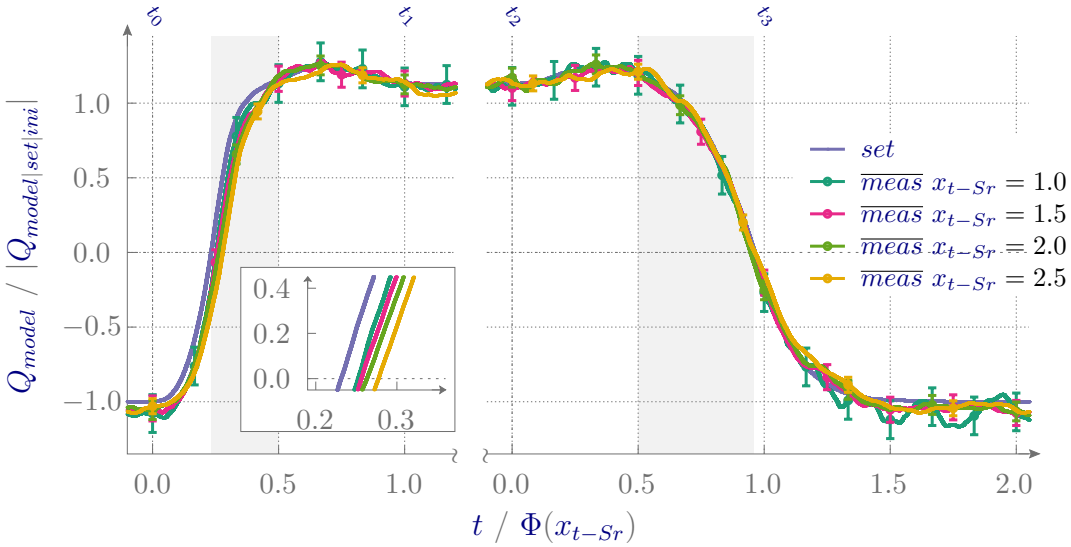

Figure 7.7: Comparison of the discharge between setpoints and measurement results for different time scale factors of speed controlled fast transitions from pump to turbine mode (left) and vice versa (right) with spline profile and a guide vane opening of $\gamma/\gamma_{max} = 0.6$.

Concerning the discharge, especially the deviations from the setpoints in the area of the large gradients during the transition from pump to turbine mode are noticeable (Fig. 7.7). The greater the $^{dQ}/_{dt}$ values, the greater the deviation from the setpoints (zoom diagram). Except for the already mentioned fluctuations at the time scale factor $x_{t-Sr} = 1.0$, only marginal differences are recognizable for the further course.

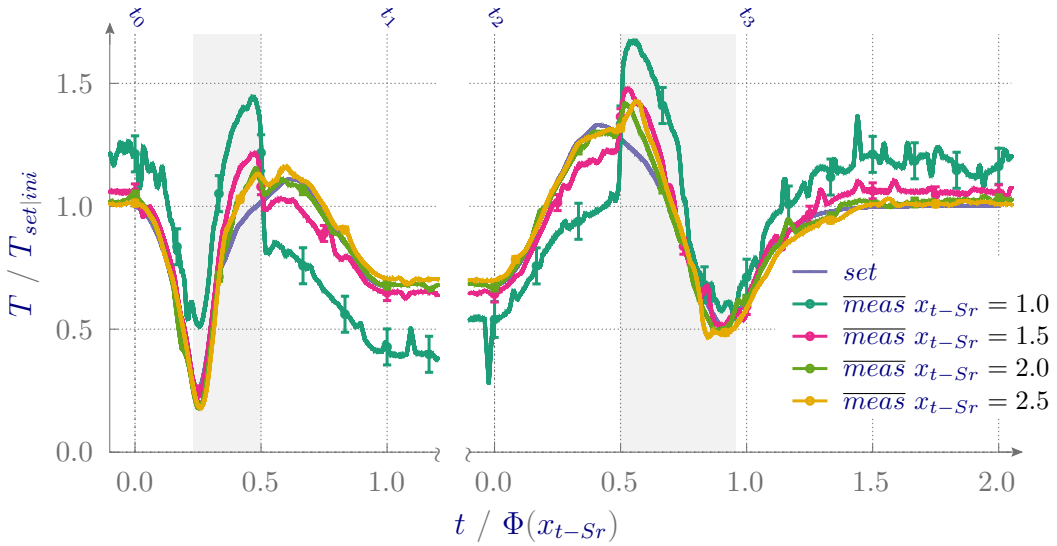

Figure 7.8: Comparison of the torque between setpoints and measurement results for different time scale factors of speed controlled fast transitions from pump to turbine mode (left) and vice versa (right) with spline profile and a guide vane opening of $\gamma/\gamma_{max} = 0.6$.

The significant influence of the time scale factor on the results becomes clear when considering the torque measurements (Fig. 7.8). The higher the time scale factor, the better the measurement result. Only for values of $x_{t-Sr} = 2.0$ or greater the measurements are considered to be replications of the prototype behavior. Below them, the curves show remarkable deviations of up to ±40% over the entire process. Even at the steady-state operating points, the deviations are around 20% of the setpoints ($x_{t-Sr} = 1.0$).

The error areas for evaluating the quality of the replication are summarized for head, discharge, and torque in Table 7.1, subdivided into the two transitions. These values are normalized to the lowest result of a parameter over the time scale factor cases.
The results for discharge agree with the qualitative findings from the associated diagrams. The fact that the lowest x_{t-Sr} case does not present the best result during the transition from turbine to pump mode is due to the persistent fluctuations during re-entry into pump mode.
Head and torque reveal the best results for $x_{t-Sr} = 2.0$. In the faster case, significant

deviations are observed, especially during the transition from pump to turbine mode. This finding is difficult to obtain from the diagrams.

The other cases of different guide vane openings and other speed profiles for the fast transition show the same findings. All diagrams and tables of the transient model experiments carried out are available in appendix C. Among others, the results of the machine coefficients and parameters related to the test rig are also be found there.

Table 7.1: Comparison of error area for different time scale factors of speed controlled fast transitions from pump to turbine mode and vice versa with spline speed profile and a guide vane opening of $\gamma/\gamma_{max} = 0.6$. Values are normalized to the minimum value of all cases of a transition.

Mode	**PU→TU**			**TU→PU**		
$\Upsilon_{norm}/\Upsilon_{norm\,\vert min}$	H	Q	T	H	Q	T
x_{t-Sr}=1.0	1.216	1.000	8.623	1.866	1.363	7.166
x_{t-Sr}=1.5	1.065	1.111	2.145	1.037	1.000	2.276
x_{t-Sr}=2.0	1.000	1.195	1.000	1.000	1.020	1.000
x_{t-Sr}=2.5	1.229	1.556	1.416	1.073	1.252	1.080

7.1.3 Discussion of Fast Transition Tests

Transfer of Time-Depending Parameters

The conversion of the time scale via the initial speed ratio between prototype and model represents a practicable solution. The time scale of the transient model test is thus a function of the speed of the model machine at the beginning of the transient process. The results reveal that with an increasing time scale factor x_{t-Sr} the reproductions in the model test gain a better quality. A time scale factor of at least 2 is recommended. If the required acceleration of the electrical machines exceeds their limit, the results deteriorate. In the simulation model, the loss coefficients of the pipes are adjusted to the case $x_{t-Sr} = 2.0$. Thus, for lower and higher time scale factors, deviations may occur due to non-matching pipe friction. The fact that an increase of the time scale factor is not reflected in the improvement of the error area of discharge is explained by the chosen measurement method, the position and the

selected sensors.

For this work, the time span of the transient power plant process was chosen ambitiously on purpose in order to determine the limits of this methodology during the transient model test. This leads to a conflict of objectives. A short power plant process with rapid speed change runs faster in the model test by the selected time scale factor. In the model test, high rotational speeds are desired to approximate dynamic similarity. Conversely, a high time scale factor requires the electrical machines to generate high acceleration rates on the model. These acceleration rates prove to be one of the main limitations of transient model tests. If the accelerations of the rotor in the power plant are moderate, e.g. because the speed change takes place over a longer period of time, higher time scale factors (of $x_{t-Sr} = 3$ or greater) are feasible. Consequently, these acceleration limitations are also the reason why experiments on total load rejections in a scaled model experiment are difficult to realize with this approach. The behavior of the prototype's rotational speed caused by a total load rejection might not be reproduced by the model's electric machine.

An advantage of the transfer of the time scale via the Strouhal number is the conservation of the number of revolutions between model and prototype. This may be important for certain investigations in the context of frequency analyzes. An overview of the mentioned properties is listed in Figure 7.9 on the right.

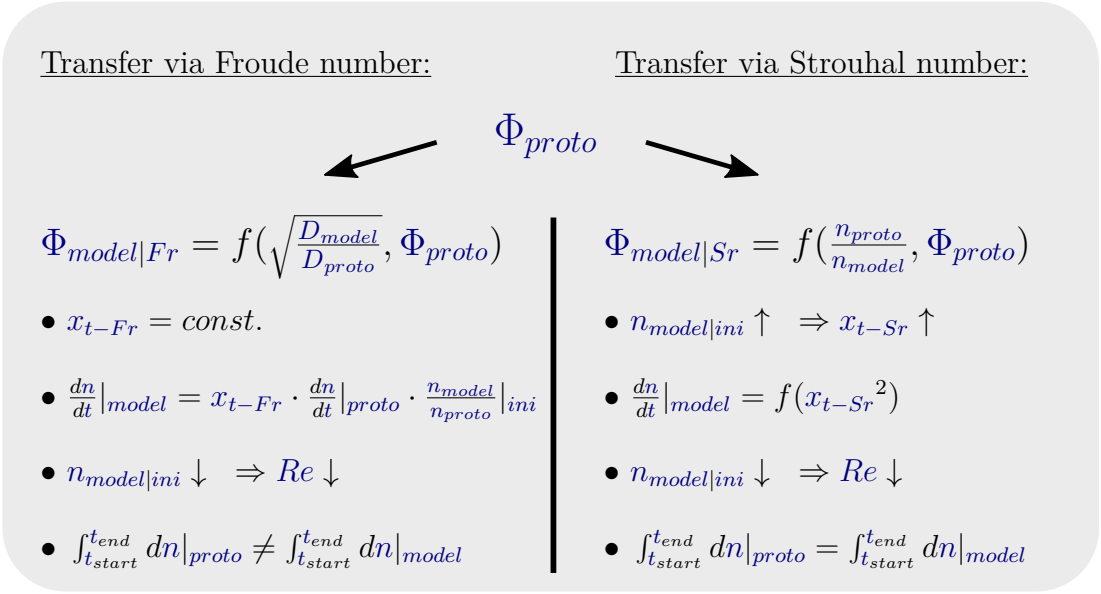

Figure 7.9: Overview of the properties of the transfer of the time scale between prototype and model. On the left with the help of the Froude number, on the right with the help of the Strouhal number.

When using the Froude number to adjust the time scale of the model test, the conservation of revolution between prototype and model is given only for a certain initial speed. Since with this approach the time scale of the model depends on the geometric scaling, the duration of the transient process of the model is small ($\Phi_{model|Fr} \approx 8.2$ s $= const.$). To preserve the number of revolutions, a very high initial model speed and the associated high accelerations are necessary (Fig. 7.9 left). The realization of these requirements will hardly be possible, neither on the test rig used nor on others.

With the determined acceleration limitations of the test rig, the reproduction of the prototype process is only possible with a maximum initial speed of approx. $n_{model|ini} = 100$ min^{-1}. This corresponds to a time scale factor according to Strouhal of less than 0.25. Only for prototype processes with a duration of at least 240 s, it is possible to double the initial speed as recommended. It can be assumed that the geometric scaling between model and prototype is similar for other hydraulic machines. Thus, this conflict of using the Froude number to adjust the time scale applies to most hydraulic machines.

Selected Measuring Technique

The evaluation of the measurement technology used in terms of its ability to quickly and accurately record the transient processes in the test rig varies. The differential pressure sensors used show good results, which are in agreement with both the test rig simulations and the setpoints. This applies to the steady-state operation as well as during the transient process. The differences between simulation and measured values of the absolute pressure sensors, which occur during the transient process, are mainly due to the numerics of the solver (Chapter 6.3.3). Related to the pressure in the spiral case, the difference during the transient process is up to approx. 5% and in the draft tube approx. 15% (compare Fig. 6.16 in Chapter 6.3.2).

In contrast, the results of head, when calculated from the measurements via the absolute pressure sensors in the spiral and draft tube, are significantly better. In relation to the uncorrected setpoints, the error area of the absolute pressure sensors is approx. 70% larger than with the differential pressure measurements (Tab. 7.2). However, these error areas are small in absolute terms.

Table 7.2: Comparison of the measurement technique between normalized error areas with differential pressure sensor and absolute pressure sensor related to uncorrected setpoints. Evaluation of fast transition with linear speed profile at a guide vane opening of $\gamma/\gamma_{max} = 0.6$.

Mode	**PU→TU**		
Υ_{norm}	$H(\Delta p_{model})$	$H(\Delta(p_{0-2}))$	Diff_{rel} / %
x_{t-Sr}=1.0	0.0272	0.0463	+70.2
x_{t-Sr}=1.5	0.0179	0.0282	+57.5
x_{t-Sr}=2.0	0.0197	0.0321	+62.9
x_{t-Sr}=2.5	0.0223	0.0373	+67.2

The noticeable deviations and pronounced fluctuations of the torque at the time scale factor of $x_{t-Sr} = 1.0$ are caused by the low values in relation to the measuring range of the sensor. During the fast transitions, this measuring range was only used up to approximately 4%. With increasing time scale factor the signal shifts to higher values and reaches in the fastest case approx. 25% of the actual measuring range. Thus, the relative share of the measurement error to the measured value decreases.

The measurement of discharge presents a particular challenge. The results reveal that the addition of the measurement of pump discharge and bypass discharge already leads to noticeable deviations at low time scale factors during the transition from pump to turbine mode. These increase with increasing time scale factor. The reason is that the measurement error and the delaying properties of the sensors accumulate. As mentioned for the test case, it is likely that the actual discharge rates are closer to the setpoints and test rig simulation values, respectively. The good agreement of rotational speed and head with the setpoints was mentioned as the reason for this assumption. Nevertheless, the proof of the flows' agreement with the numerical results cannot be omitted, only because of the lack in the measuring technique. This applies on the one hand to the validation of the simulation model of the test rig and on the other hand to the verifications of model machines when investigating their properties under transient conditions.

For the evaluation of the individual sensors, the maximum error of a fast transition versus the time delay ($\Delta t = t(Q_{meas}(e_{max})) - t(Q_{sim} = Q_{meas}(e_{max}))$) to the simulation

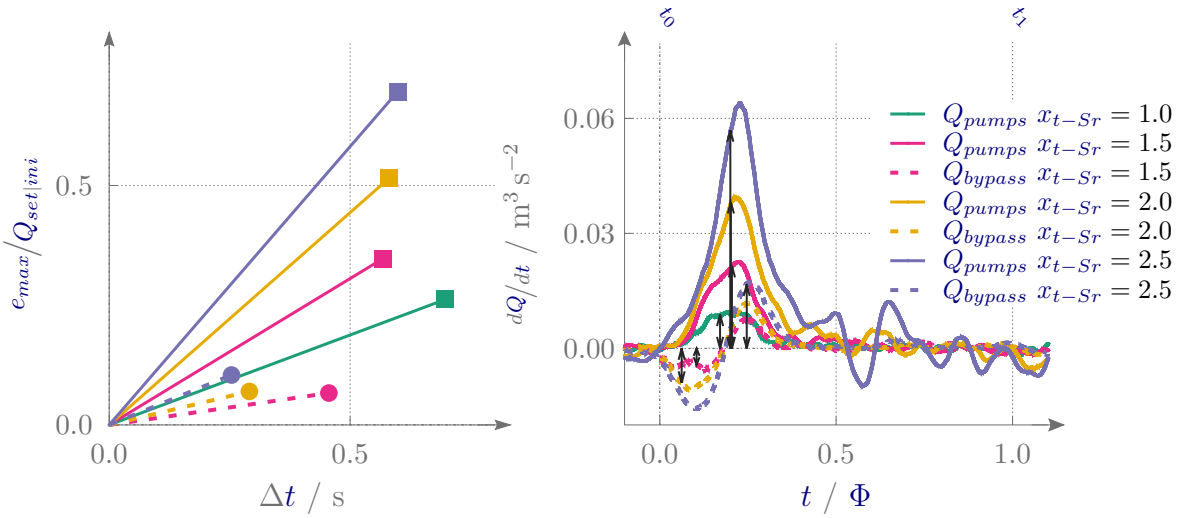

(a) Normalized maximum deviation at the transition from pump to turbine mode with linear speed profile for different x_{t-Sr} values versus the delay in time related to the simulation values.

(b) Measured acceleration of flow. Arrows indicate points in time at which the maximum error occurs during the fast transition.

Figure 7.10: Comparison of discharge measurement sensors at different time scale factors - flowmeter (solid) in pump branch and differential pressure at orifice (dashed) in bypass.

value is considered (Fig. 7.10(a)). This method assumes that the simulated value reflects reality, although this is not known. Therefore, an evaluation of the absolute values is not possible. However, since this assumption applies to both sensors and is based on the same simulation model, the qualitative evaluation is correct. For this investigation, the transition from pump to turbine operation is used, since the greatest accelerations and deviations occur during this transition.
The resulting diagram contains straight lines with different gradients. The steeper these lines are, the faster the sensor detects a deviation. Comparing these results with the accelerations at these points in time, it is evident that the measurement of the flowmeter gives better results than the used differential pressure measurement at the orifice (Fig. 7.10(b)). In all x_{t-Sr} cases the error-delay curves are steeper, although significantly higher accelerations of the flow occur.

To solve this problem, two absolute pressure sensors could be used at the orifice measurement in the bypass, instead of one differential pressure sensor. First, with their high sampling rate and a relative error of 0.1% [139], the flow will be recorded

faster and without much loss of quality (compare Fig. D.1 and Fig. D.5). Second, the flow measurement, whether via flowmeter or pressure difference at an orifice, should be carried out in the branch of the model machine. This makes the mentioned addition of errors obsolete and reduces the time delay to one sensor.

Influence of the Bypass Opening

The opening of the bypass valve plays a key role in the flexibility of the tests, but also in the quality of the results. This influence on the flexibility is presented by the example of the results for the linear fast transition at the time scale factor of $x_{t-Sr} = 3.0$. Head (Fig. 7.11(a) and C.4) as well as discharge (Fig. C.5) and torque (Fig. C.6) illustrate a considerable deviation in turbine mode independent of the selected guide vane opening.

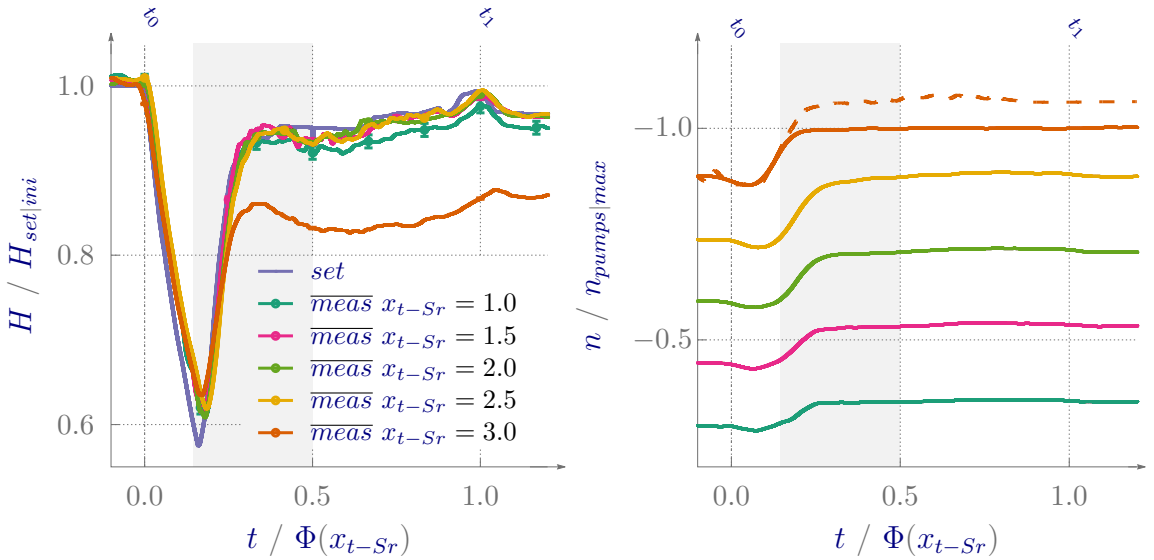

(a) Comparison of head between setpoints and measurement results. The course of $x_{t-Sr} = 3.0$ does not reach the setpoints in turbine mode.

(b) Measured rotational speed of the service pumps. The $x_{t-Sr} = 3.0$ case reaches the maximum rotational speed. The dashed line corresponds to the test rig simulation result generated by the optimizer.

Figure 7.11: Results for different time scale factors of speed controlled fast transitions from pump to turbine mode with linear profile and a guide vane opening of $\gamma/\gamma_{max} = 0.6$.

Regardless of exceeding the acceleration limits of the motor generator of the model machine (Fig. 7.6(b)), the cause of this deviation is due to the rotational speed

limitation of the service pumps (Fig. 7.11(b)). To a certain degree, such a problem may be solved with the help of the bypass opening.

In Figure 7.12, the measured rotational speed of the service pump, in steady-state pump (circle) and turbine (triangle) mode of the model machine, is plotted against the energy difference at bypass valve. This energy difference is normalized to head at the model machine at the associated operation mode. The line between the steady-state points does not represent the course of the speed, but the relationship between the two operating points. The different line types indicate the corresponding time scale factor. The colors blue, green and red refer to the bypass openings 40%, 50% and 60%. The shades within a color provide a differentiation of the guide vane opening of the model machine. If only two shades are present, the openings are $\gamma/\gamma_{max} = 0.4$ and $\gamma/\gamma_{max} = 0.6$.

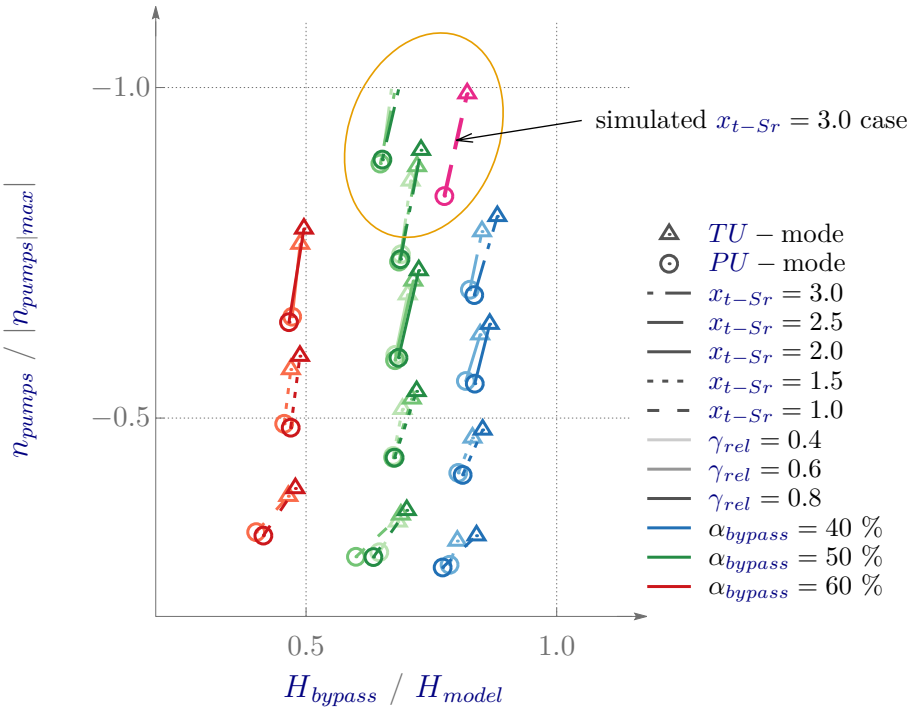

Figure 7.12: Influence of bypass valve opening on rotational speed of service pumps in steady-state turbine and pump mode of the model machine.

Using the bypass opening of 50% (green) as an example, both the average pump speed as well as the difference of speed between the steady-state operating points increase with increasing time scale factor. In the case of $x_{t-Sr} = 3.0$, only the steady-state pump mode is visible. Turbine mode is not achieved due to the limitation of the

maximum pump speed ($n_{pumps}/|n_{pumps|max}| = 1$).
By closing the bypass valve to 40% the bypass discharge is reduced. Thus, a lower speed level of the service pumps is required to achieve the steady-state operating points of the model machine. The simulation results of this finding is illustrated in pink color. This example demonstrates that the range of investigation possibilities is extended by adjusting the valve opening.

Furthermore, the spread of the speed range of the service pumps is also influenced by the bypass opening. With larger valve openings, a wider speed range is realized between pump and turbine operation of the model. The optimization results of the service pump speed demonstrate that the speed behavior turns out to be very detailed. The more precisely the speed behaviour is determined, the more accurately a load case is replicated in the model test. Therefore, a wide speed range and thus a high degree of differentiation is beneficial. Consequently, the bypass opening should be selected as large as possible while achieving the steady-state operating points of the model.

7.2 Investigations of Controlled Load Rejection

In this last section, load cases for power control with guide vane adjustment are considered. For these investigating no measurement results are available. The purpose of the evaluation is to determine which requirements are imposed on the measurement technology and on the conditions of the test rig.

7.2.1 Load Case Description and Simulation Results

A load rejection of 50 % of nominal power is assumed, starting from a relative guide vane opening of $\gamma_{rel} = 0.6$ at maximum gross head of the reservoirs. This load case is investigated in two scenarios. In the first scenario, the power is only controlled by the guide vane opening. In the second scenario, a variable speed machine is used in addition to the guide vane adjustment. The qualitative behavior of the actuators as well as the electrical power output have already been presented in Section 3.2 in the Figures 3.3(a) and 3.3(b). In the following diagrams, this differentiation into **(a)** and **(b)** is kept for the two scenarios.

For both scenarios head versus time indicate good agreement between setpoints and test rig simulation results (Fig. 7.13). This reveals that the optimization procedure also works well for these types of load cases. In the double regulation scenario, the

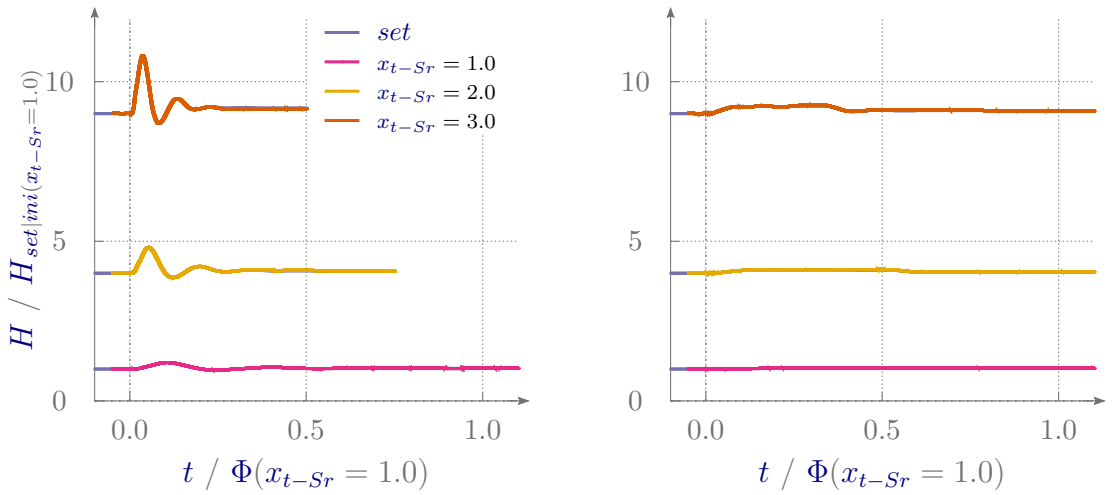

(a) Power control via guide vane opening (single regulated load rejection).

(b) Power control via a combination of guide vane opening and rotational speed change (double regulated load rejection).

Figure 7.13: Course of head versus time for a load rejection of 50 % starting from nominal power at a guide vane opening of $\gamma_{rel} = 0.6$.

head in the transient region shows only minor changes compared to the steady-state value. Consequently, the optimizer is not challenged much.
In the single regulated scenario, the requirements to the optimizer are higher. Good agreements are achieved only by redetermining the optimizer parameters, to these kinds of load cases (Fig. C.39 in the appendix C).

7.2.2 Discussion of Simulation Results

Since the replications of the prototype load case in the test rig show good results, the actuators which are active for power adjustment are considered in the following.
In the first scenario, only the guide vane adjustment has to be considered (Fig. 7.14(a)). The rotational speed of the model machine remains constant. In the second scenario, the accelerations of the guide vane are significantly lower compared to the first scenario (compare Figures 3.3(a) and 3.3(b)). Therefore, in this load case, mainly the dynamic behavior of the rotational speed of the model machine is investigated (Fig. 7.14(b)).

In both diagrams, the time axis is normalized to the respective time span of the x_{t-Sr} case. In addition, in Figure 7.14(b) the acceleration is normalized to the maximum

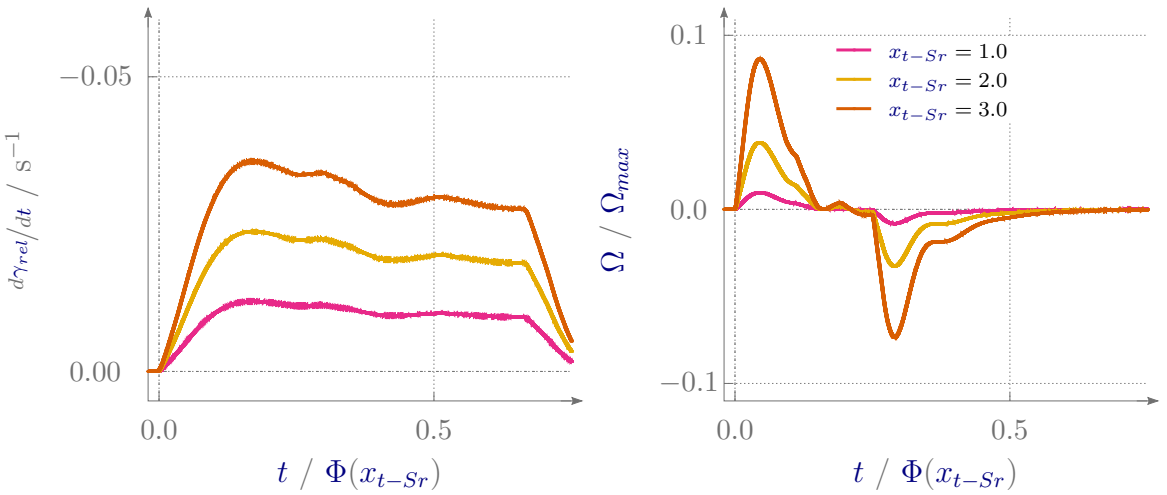

(a) Normalized change of the guide vane opening for the case of single regulated load rejection.

(b) Normalized rotational speed change for the case of double regulated load rejection.

Figure 7.14: Behavior of actuators of power control load case for different x_{t-Sr} cases.

acceleration of the motor generator. It is evident that the accelerations are far from the limits. Thus, the load cases of power control in model experiments are not limited by the properties of the motor generator of the model machine.

The time derivative of the guide vane position shows that the angular change increases linearly with the increasing time scale factor. For this load case, the maximum value for a three times faster process than in the prototype is about $^{d\gamma_{rel}}/_{dt_{min}} = -0.04\ \mathrm{s}^{-1}$ (for $x_{t-Sr} = 3.0$).

However, for the servomotor which has to convert this motion, the decisive factor is not the angle of the guide vane. In most cases, this adjustment is performed by a linear motor. This motor is characterized by the linear traverse speed and the traverse range. Both variables are connected to the guide vane opening via the kinematics of the actuator. With the kinematics of the model machine used, this load case results in a linear velocity of approx. 3.1 mm s^{-1} and a traverse range of approx. 10 mm. Common linear motors, which are used on test rigs for hydraulic machines, can usually implement these and higher requirements [113]. Thus, this actuator also does not represent a limit for the implementation of transient model tests with power control.

The experiments of fast transitions show that especially the behavior of the service pumps has a strong impact on the quality of the replication. In the previous chapter, the influence of the maximum rotational speed of the service pumps as well as the

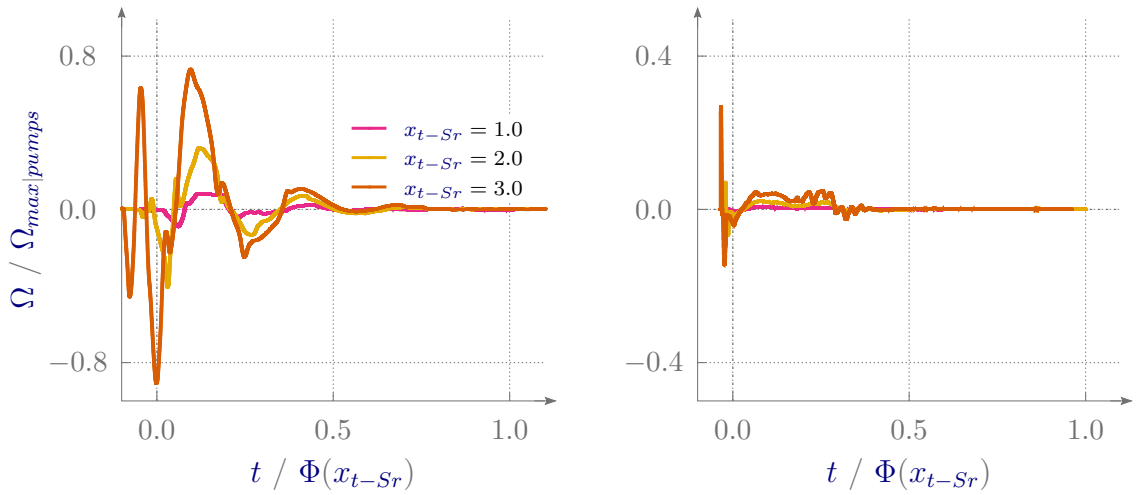

(a) Case of single regulated power rejection.

(b) Case of double regulated power rejection.

Figure 7.15: Rotational speed of the service pumps for different time scale factors for controlled load rejection of 50 %.

connection with other variables (steady-state operating point of the model machine, bypass opening and the time scale factor) are discussed. Therefore, only the transient speed behavior is evaluated for these load cases. For the quantitative evaluation, the maximum acceleration of the service pumps is used.
While the accelerations of the service pumps in the second scenario are very moderate (Fig. 7.15(b)) and far from the maximum limits, the first scenario presents a different situation (Fig. 7.15(a)). On the one hand, the predicted accelerations are also within the limits. On the other hand, the replications of these load cases require frequent acceleration and deceleration in a very short time. Moreover, these processes also run without any visible pattern between the different time scale factor cases.
Since the pumps are not actively controlled for deceleration and their deceleration results from friction, only the experiment can demonstrate whether this behavior is replicable in the model test. A final conclusion on the feasibility is not possible without performing the experiment.

The experiments of fast transitions indicate that especially the flow measurement at the model machine has the largest measurement deviation. This applies in particular to high changes in flow velocity. Acceptable results are obtained only for the transition from turbine to pump operation (Fig. 7.7). For this reason, these results are used as reference values for the evaluation of the discharge in the load cases with power control.

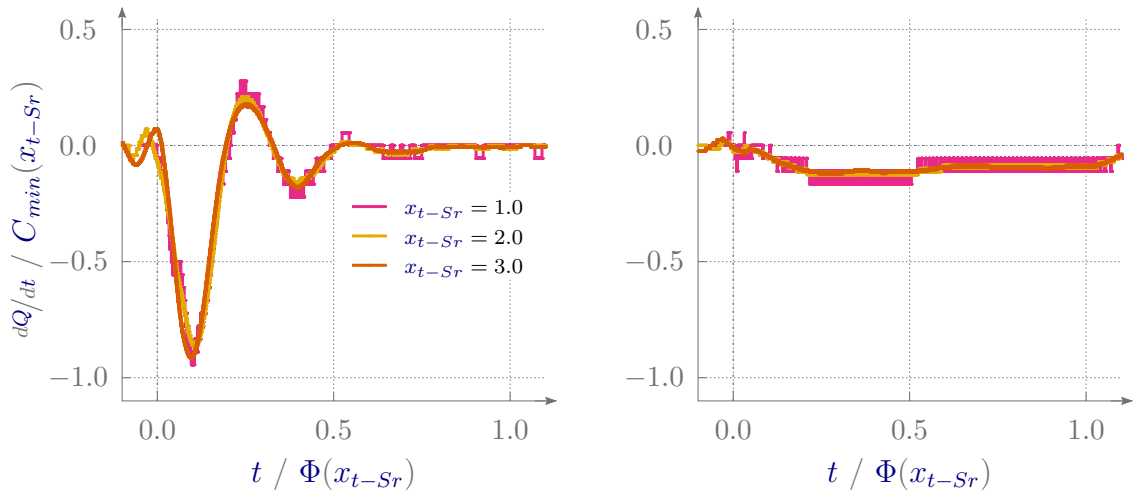

(a) Case of single regulated load rejection.

(b) Case of double regulated load rejection.

Figure 7.16: Time derived discharge normalized to maximum value in case of fast transition from turbine to pump mode with spline speed profile and a guide vane opening of $\gamma_{rel} = 0.6$.

For both scenarios the time derivative of discharge of the model machine is illustrated in Figure 7.16. The simulation results are normalized, depending on the x_{t-Sr} case, to the largest value of the deceleration of discharge from the fast transition simulations with spline speed profile and a relative guide vane opening of $\gamma_{rel} = 0.6$, (Eqn. 7.1).

$$C_{min}(x_{t-Sr}) = min\left[{}^{dQ}/_{dt}(x_{t-Sr})_{FT|spline|\gamma/\gamma_{max}=0.6}\right], \ [\mathrm{m^3\,s^{-1}}] \tag{7.1}$$

In both scenarios, the results are not greater than the accelerations of the fast transitions. Especially in the second scenario, the maximum values are significantly smaller than ±1 (Fig. 7.16(b)). In conclusion, with the measurement technology used, flow measurement is feasible with comparable quality as for the transition from turbine to pump operation.

8 Conclusions

The objective of this work to develop a methodology for transient model tests is successfully realized. For this methodology, it does not matter whether the transient process is triggered by only one controlling actuator (guide vane adjustment or rotational speed change) or several actuators simultaneously. Both, the results of the test rig simulation and those of the measurement series show reasonable agreement with the derived setpoints from the power plant simulation.
Especially in the case of the experimental results, the quality of the replication depends on the applied time scale factor, as well as on the quality of the simulation model of the test rig and the optimizer setting. It is evident that the modeling of the piping of the simulation model, in more detail the parameters speed of sound and loss coefficient, influences the numerical results. Incorrect definitions of these parameters lead to deviating simulation results and thus might be a cause for differences between measurement and setpoints. The same applies to the control parameters of the optimizer. If the proportional value and time shift do not have the appropriate values for the case under investigation, this will influence the numerical results and thus also the experiment.

In the test rig used, the implementation of even higher time scale factors were limited by the acceleration capability of the electric machines and maximum speed of the service pumps. However, the bypass offers an influencing factor to achieve the requirements for the drives of the service pumps. By reducing the opening of the bypass valve, the rotational speed level and the required acceleration values are lowered. The opposite behavior occurs when the valve is opened further. This can be realized without compromising quality of the replication of the prototype process, even at higher time scale factors.

In contrast, the agreement between the measurement results and setpoints of discharge at the model machine worsened with increasing time scale factor in the range of high discharge gradients. Reasons are the type of sensors used and their arrangement in the test rig. Since this contradicts the results of head and torque and considering the known inertia of the sensors, it is assumed that the actual discharge has a better agreement with the setpoint than determined.

In order to replicate the actual loads on the machine in the model test, it is also necessary to induce comparable cavitation behavior. However, the necessary suction-side pressure level could not be achieved with the test rig used due to the lack of a vacuum pump. The evaluation of pressure measurements in the draft tube of different load cases, which vary by a continuous reduction of the σ value, confirms that the pressure level influences both the frequency and the amplitude of the pressure fluctuations. It is known that the mechanical loads of the machine depend on the cavitation behavior. Thus, creating conditions similar to those in the prototype is essential for a complete stress analysis.

Quantitative evaluation variables that would allow comparability of different transient processes of different hydraulic machines are difficult to define due to the diversity of cases. The normalized error area and the normalized maximum error, used in this work, provide a basis for future discussions of the quality requirements for transient model tests. These also include the definition of a minimum Reynolds number or specific energy requirements, which are defined in the IEC60193 for steady-state measurements for model acceptance tests [50].
Related to the investigated fast transitions at high time scale factors, both values were not reached at the test rig used. This was due to the limitation in the choice of the time scale factor. If an orientation towards these limits has to take place in the future, a test rig must be equipped with the appropriate electrical machines and suitable discharge measurement technology.

Finally, it must be mentioned that the dynamics of the model test depend on the dynamics of the power plant process. For this work, purposely high requirements are set in order to expose limits of the methodology and the measurement technology. If the future requirements for the dynamic properties of new hydraulic machines change, this will have a direct impact on the requirements of the model tests.

Based on the promising findings of this work, the next steps in the research on transient model tests can be initiated. A comprehensive list of remaining tasks is included in the Outlook.

9 Outlook

The results and methods of this work are still at the beginning of a research field, which will become more and more important in the future. Consequently, the list of further tasks for the implementation and research of transient model tests is long. With this concluding chapter, subdivided into the individual disciplines numerics, measurement technology, and methodology, the next steps in the field of transient model tests are addressed.

Tasks for Simulation Method

One of the most important tasks is to improve the simulation models of the test rigs. This applies in particular to the most accurate simulation of the losses in the pipes. In this work, the loss coefficients in the individual pipe sections are determined only for the reference case (test case Chapter 6). A better approach is to use a flexible loss model, which is applied for different discharges in the individual branches. Since the loss coefficient for a pipe cannot be adjusted during a simulation, it should, at least, be approximated to the flow velocities at the steady-state operating points at the beginning and end of a transient process of a certain load case.
The discharges of the branches depend on the operating point of the model machine, the selected time scale factor x_{t-Sr}, and the opening of the valve in the bypass. It would be necessary to adapt the simulation model to the conditions in the real test rig before the optimization runs through a transient process. This should be done with an effort as small as possible. An iterative procedure based on the Newton-Raphson method could be used [14]. The prerequisite for this approach are the steady-state measurement results of the desired operating point at the desired x_{t-Sr}-value.
For the iteration procedure to determine the correct pressure losses, only one loss coefficient per branch is initially defined in the simulation of the test rig. In each iteration, these coefficients will then be varied. Target variables are the measured pressure differences at the model machine, bypass valve and service pumps.
The Jacobi matrix, required in this procedure, can then be formed from the three target variables and three variables (one loss coefficient per branch). The measured

rotational speeds of the machines used in the experiment are specified as fixed boundary conditions for the simulation.
This method provides a fast and automated determination of the loss coefficients per branch for the corresponding flow rates. Subsequently, these total losses can be distributed within the branches. For a correct distribution the absolute pressure measuring points can be used.

A further adjustment, which applies especially to the solver used in this work, is the correction of the different rotational speeds of the service pumps. In the real test rig, the pumps are connected to one motor and thus both pumps always have the same speed. The power control with a frequency converter, used in the simulation, leads to different speeds of the pumps when the same set value is given.
The obvious solution would be to use lossless pipes in the simulation, starting at the node of distribution to the pumps until the downstream connection node. However, this would lead to equal pressure differences at both pumps, which does not occur in the real test rig, due to the different pipe routing. Here, three options are possible. On the one hand, the solver could be programmed in such a way that more than one machine can process a time-dependent speed course. This could be done e.g. by assigning parallel electrical grids. As a result, the optimizer would have to be reprogrammed to adapt the speed course instead of a power course.
Another possibility is to apply a correction factor to the power curve of one pump. This factor would depend on the operating point of the pump and first has to be determined for different operating points. It would also be possible to determine this correction factor via an internal iteration within a time step of the optimization. However, the entire optimization procedure would then become computationally intensive. For this approach several steady-state simulations are necessary in each time step investigated to determine the correction factor.
A final solution could be to switch the solver which does not have this limitation.

Another task is to examine the characteristic diagrams of the machines for possible kinks and correct these with suitable procedures (discontinuities in Section 6.2.2). A possible approach is to use more discrete points and appropriate mathematical methods to achieve some smoothing. This would not only lead to more accurate results for the test rig simulations, but also to a better quality of the setpoint values, which are derived from the power plant simulations.

Tasks in the Area of Measurement and Test Rig Technology

On the measurement technology side, there are also points that contribute to the improvement of the presented methodology.

First and foremost, sensors must be found that can measure the flow rates with higher dynamics and lower damping or dead times. Further, the flow should be measured directly in the branch of the model machine. This would increase the accuracy of the measurement and reduce the dead times, since only one instead of two measuring devices are needed.

It would also be helpful, to use additional absolute pressure sensors in the direct area of the service pumps and at the bypass valve. With the help of these measuring points, it would be possible to calibrate the simulation model more precisely to the properties of the real test rig.

Since the methodology presented produce promising results, further measurement technology can be implemented to investigate the mechanical loads. This includes, among others, the attachment of strain gauges to stressed components or the installation of additional pressure sensors on the model machine. These would provide a more detailed view of the processes within the object under investigation.

In addition, a method for simple measurement of the speed of sound on a real test rig should be elaborated. In principle, it would be helpful if, at least, an order of magnitude about this value is known. The parameter study on the test case (Section 6.2.2) demonstrates, that the influence of the speed of sound varies depending on the type of transient process. An influence is particularly evident for processes that are accompanied by a change in the guide vane opening. This must be taken into account in the simulation model.

Attention should be paid to the acceleration limitation of the electrical machines, which is defined in the internal test rig controller. It is revealed that especially the acceleration values of the model machine represent an unintended limit of the transient model tests. If these limits can be extended without safety risks, this will allow higher x_{t-Sr}-values and thus improve the dynamic similarity.

Furthermore, the test rig should be equipped with a controllable guide vane adjustment. This leads to a considerable expansion of the possibilities of experiments. Investigations of start up and shut down processes, or load acceptance and rejection would be possible. It could also be used to investigate double regulated processes

with guide vane adjustment and simultaneous rotational speed change. This implementation is one of the most important next steps and should be prioritized.

Tasks in Methodology

The power plant investigated in this work has only one set of machines. From previous investigations it is known, that especially power plants with several reversible pump turbines, sharing the main piping, are vulnerable to interactions between the machines in case of transient events. Such an interaction could be induced with a fictitious extension of the power plant model. This could be used to investigate, whether the presented methodology can be applied to power plants with multiple sets of machines.

In the introduction of this work, the possibilities of 3D-CFD-simulations and FSI-simulations are described. With the help of the obtained measurement results from this work and possible further values by the extensions of further sensors, e.g. strain gauges etc., such simulations can be validated. If there is a consistency between measurement and CFD-simulation or FSI-simulation at the investigated locations, these tools can also give a view on other locations in-between the model machine, where no instrumentation of sensors are possible. For this reason, it is useful to address these simulations and thus extend the whole methodology of transient model testing.

While there are certainly many more challenges in this field of research, one central task will be mentioned at the end of this work. In order to prove the generality of the presented method, it is essential to repeat it on further test rigs with other model machines. The consolidation of these findings will improve the methodology and, if necessary, extend it with new ideas. Thus, step by step the basic and generally valid requirements for transient model tests can be defined.

Bibliography

[1] Abernethy, R.B.; Benedict, R.P.; Dowdell, R.B.: ASME Measurement Uncertainty, *ASME Journal of Fluids Engineering*, 107(2):161-164. doi: 10.1115/1.3242450, 1985 35

[2] Acosta Del Carpio, H.: *Das dynamische Verhalten von Kreiselpumpen niedriger spezifischer Drehzahl bei raschen Drehzahländerungen*, Ph.D. thesis, University of Stuttgart, ISBN 3-9802130-4-8, 1990 xviii, 3, 20, 21, 75, 76, 77, 88

[3] Alligne, S.; Nicolet, C.; Tsujimoto, Y.; Avellan, F.: Cavitation surge modelling in Francis turbine draft tube, *Journal of Hydraulic Research*, 52(3):399–411, 2014 5

[4] Anz, R.: *Systemidentifikation und Reglerselbsteinstellung in Wasserkraftanlagen*, Ph.D. thesis, University of Stuttgart, ISBN 3-9807322-4-X, 2002 5

[5] ASM GmbH: *Datenblatt POSIROT® PRAS27 Magnetischer Winkelsensor mit Analogausgang*, 2011, KAT-PR/PT-D-11 38

[6] Barrand, J.P.; Picavet, A.: Qualitative Flow Visualizations during Fast Start-up of Centrifugal Pumps, in: *Hydraulic Machinery and Cavitation*, pp. pp. 671-680, Springer Netherlands, Dordrecht, ISBN 978-94-010-9385-9, 1996 3

[7] Blanco, P.; Pivello, M.; Urquiza, S.; Feijóo, R.: On the potentialities of 3D-1D coupled models in hemodynamics simulations, *Journal of biomechanics*, 42:pp. 919-930. doi: 10.1016/j.jbiomech.2009.01.034, 2009 6

[8] Bohbot, J.; Miche, M.; Pacaud, P.; Benkenida, A.: Multiscale Engine Simulations using a Coupling of 0-D/1-DModel with a 3-D Combustion Code, *Oil & Gas Science and Technology - Revue de l'IFP*, 64. doi: 10.2516/ogst/2009007, 2009 6

[9] Bolpaire, S.; Barrand, J.; Caignaert, G.: Experimental Study of the Flow in the Suction Pipe of A Centrifugal Impeller: Steady Conditions Compared with Fast Start-Up, *International Journal of Rotating Machinery*, 8. doi: 10.1080/1023620291910842, 2002 4

[10] Braun, O.: Part load flow in radial centrifugal pumps, p. 197. doi: 10.5075/epfl-thesis-4422, 2009 82

[11] Brennen, C.; Acosta, A.: Theoretical, quasi-static analysis of cavitation compliance in turbopumps., *Journal of Spacecraft and Rockets*, 10(3):175–180, 1973 5

[12] Brost, V.: *Wiederaufbau des Stromnetzes mit einem Inselverbund aus Wasserkraftanlagen*, Ph.D. thesis, University of Stuttgart, ISBN 978-3-9812054-9-7, 2019 5

[13] Brost, V.; Reinhardt, H.; Ruprecht, A.; Kolb, S.; Wiesemann, J.U.: Dimensioning Of The Tailwater System Of The Pumped-Storage Plant Atdorf, in: *16th International Seminar on Hydropower Plants 2010, Vienna, Austria*, 2010 5

[14] Chapra, S.C.; Canale, R.P.: *Numerical Methods for Engineers*, 7th edn., McGraw-Hill Education, ISBN 978-0-07-339792-4, 2015 111

[15] Chaudhry, M.H.: *Applied Hydraulic Transients*, 3rd edn., Springer-Verlag New York. doi: 10.1007/978-1-4614-8538-4, 2014 22

[16] Chen, C.; Nicolet, C.; Yonezawa, K.; Farhat, M.; Avellan, F.; Tsujimoto, Y.: One-dimensional analysis of full load draft tube surge, *Journal of Fluids Engineering*, 130(4), 2008 5

[17] Ciocan, G.; Teller, O.; Czerwinski, F.: Variable speed pump-turbines technology, *UPB Scientific Bulletin, Series D: Mechanical Engineering*, 74:33-42, Jan 2012 1

[18] Claude, J.M.: Performances achieved to the Grid by a Full Power Converter Used in a Variable Speed Pumped Storage Plant, *Journal of Physics: Conference Series*, 813:012008. doi: 10.1088/1742-6596/813/1/012008, 2017 9

[19] Darkwah, W.K.; Odum, B.; Addae, M.; Koomson, D.; Kwakye Danso, B.; Oti-Mensah, E.; Asenso, T.; Buanya, B.: Greenhouse Effect: Greenhouse Gases and Their Impact on Global Warming, *Journal of Scientific Research and Reports*, 17:1-9. doi: 10.9734/JSRR/2017/39630, Feb 2018 1

[20] Decaix, J.; Alligne, S.; Müller, A.; Nicolet, C.; Münch, C.; Avellan, F.: Identification of 1-D cavitation model parameters by means of computational fluid dynamics, *Journal of Hydraulic Research*, 0(0):1-12. doi: 10.1080/00221686.2021.1944922, 2021 5

[21] Deutsche Energie-Agentur GmbH: *Ergebnispapier: Der Beitrag von Pumpspeicherwerken zur Netzstabilität und damit zur Versorgungssicherheit.*, last checked 05/10/2022. URL https://www.dena.de/fileadmin/

dena/Dokumente/Meldungen/Archiv/150716_dena_Ergebnispapier_Pumpspeicherwerke.pdf 1

[22] Dodge, Y.: Weighted Arithmetic Mean, in: *The Concise Encyclopedia of Statistics*, pp. 565–566, Springer New York, New York, NY, ISBN 978-0-387-33828-6. doi: 10.1007/978-0-387-32833-1, 2008 85

[23] Dörfler, P.: System dynamics of the Francis turbine half load surge, in: *Proceedings of the 11th IAHR Symposium on Operating Problem of Pump Stations and Powerplants*, Amsterdam, The Netherlands, 1982 5

[24] Dörfler, P.; Sick, M.; Coutu, A.: *Flow-Induced Pulsation and Vibration in Hydroelectric Machinery: Engineer's Guidebook for Planning, Design and Troubleshooting*, Springer London, ISBN 9781447157953, 2014 1

[25] Doujak, E.: Effects of increased solar and wind energy on hydro plant operation, in: *Hydro Review Worldwide*, pp. 2:28-31, Seville, Spain, 2014 1

[26] Doujak, E.; Stadler, S.; Fillinger, G.; Haller, F.; Maier, M.; Nocker, A.; Gaßner, J.; Unterluggauer, J.: Fatigue Strength Analysis of a Prototype Francis Turbine in a Multilevel Lifetime Assessment Procedure Part I: Background, Theory and Assessment Procedure Development, *Energies*, 15(3). doi: 10.3390/en15031148, 2022 10

[27] Doujak, E.; Unterluggauer, J.; Fillinger, G.; Nocker, A.; Haller, F.; Maier, M.; Stadler, S.: Fatigue Strength Analysis of a Prototype Francis Turbine in a Multilevel Lifetime Assessment Procedure Part II: Method Application and Numerical Investigation, *Energies*, 15(3). doi: 10.3390/en15031165, 2022 10

[28] Duplaa, S.; Coutier-Delgosha, O.; Dazin, A.; Roussette, O.; Bois, G.; Caignaert, G.: Experimental Study of a Cavitating Centrifugal Pump During Fast Startups, *Journal of Fluids Engineering*, 132(2), 021301. doi: 10.1115/1.4000845, 2010 3

[29] Eichinger, P.: *Untersuchung des Reibungsverhaltens bei instationären Strömungsvorängen in Rohrleitungen*, Ph.D. thesis, University of Stuttgart, ISBN 3-9802130-6-4, 1992 3

[30] Emerson Electric Co.: *Produktdatenblatt Rosemount™ 3051 Druckmessumformer*, Apr 2021, rev. WB 37

[31] Erlich, I.; Bachmann, U.: Dynamic Behavior of Variable Speed Pump Storage Units in the German Electric Power System, *IFAC Proceedings Volumes*, 35(1):251-256, 15th IFAC World Congress. doi: 10.3182/20020721-6-ES-1901.01193, 2002 7

[32] Ettema, R.; Arndt, R.; Environmental; (U.S.), W.R.I.; Roberts, P.; Wahl, T.: *Hydraulic Modeling: Concepts and Practice*, ASCE manuals and reports on engineering practice, ASCE, ISBN 9780784404157, 2000 17

[33] EUROPEAN COMMISSION: The European Green Deal, COM(2019) 640 final, Dec 2019 1

[34] Fang, Y.J.; Koutnik, J.: The numerical simulation of the delayed load rejection of a pump-turbine powerplant, *IOP Conference Series: Earth and Environmental Science*, 15(2):022018. doi: 10.1088/1755-1315/15/2/022018, nov 2012 5

[35] Farhat, M.; Natal, S.; Avellan, F.; Paquet, F.; Lowys, P.Y.; Couston, M.: Onboard Measurements of Pressure and Strain Fluctuations in a Model of low Head Francis Turbine. Part 1 : Instrumentation, *Proceedings of the 21st IAHR Symposium on Hydraulic Machinery and Systems, Lausanne, Switzerland*, 1:pp. 865-872, 2002 4

[36] GE Renewable Energy: *GE Renewable Energy Awarded Contract for New Build Tauernmoos Pumped Hydro Storage Power Plant*, last checked 05/10/2022. URL https://www.ge.com/news/press-releases/ge-renewable-energy-awarded-contract-for-new-build-tauernmoos-pumped-hydro-storage-power-austria 1

[37] Ghahremani, F.: Pump cavitation compliance, in: *Cavitation Forum*, vol. 971, pp. 1–3, 1971 5

[38] Giesecke, J.; Heimerl, S.; Mosonyi, E.: *Wasserkraftanlagen*, 6th edn., Springer Vieweg, ISBN 978-3-642-53870-4. doi: 10.1007/978-3-642-53871-1, 2014 29

[39] Gülich, J.F.: *Kreiselpumpen: Handbuch für Entwicklung, Anlagenplanung und Betrieb*, 4th edn., Springer Vieweg, Berlin, Heidelberg, ISBN 978-364-24003-2-2. doi: 10.1007/978-3-642-40032-2, 2013 29

[40] Harbort, T.: *Entwicklung eines echtzeitfähigen Simulationsprogramms zur Untersuchung instationärer Vorgänge in Wasserkraftwerken*, Ph.D. thesis, University of Stuttgart, ISBN 3-9804376-4-7, 1999 5

[41] Hell, J.: High flexible Hydropower Generation concepts for future grids, *Journal of Physics: Conference Series*, 813:012007. doi: 10.1088/1742-6596/813/1/012007, 2017 8, 27

[42] Hildinger, T.; Ködding, L.: Modern Design for Variable Speed Motor-Generators - Asynchronous (DFIM) and Synchronous (SMFI) Electric Machinery - Options

for Pumped Storage Power Plants, in: *Proceedings of Hydro2013*, Innsbruck, Austria, 2013 8, 129, 130

[43] Himr, D.; Habán, V.; Štefan, D.: Inner Damping of Water in Conduit of Hydraulic Power Plant, *Sustainability*, 13(13):7125. doi: 10.3390/su13137125, Jun 2021 5

[44] Hottinger Baldwin Messtechnik GmbH: *Montage Anleitung Drehmoment Messflansch T40*, 2017, a2463 5.0 en/de 38

[45] Houde, S.; Fraser, R.; Ciocan, G.; Deschenes, C.: Experimental study of the pressure fluctuations on propeller turbine runner blades: part 2, transient conditions, *IOP Conference Series: Earth and Environmental Science*, 15(6):062061. doi: 10.1088/1755-1315/15/6/062061, 2012 4

[46] Houde, S.; Fraser, R.; Ciocan, G.D.; Deschenes, C.: Part 1 - Experimental study of the pressure fluctuations on propeller turbine runner blades during steady-state operation, *IOP Conference Series: Earth and Environmental Science*, 15(2):022004. doi: 10.1088/1755-1315/15/2/022004, 2012 4

[47] HYPERBOLE: *official Webpage*, last checked 05/10/2022. URL https://cordis.europa.eu/project/id/608532 xv, 8

[48] Ibrahim, H.; Ilinca, A.; Perron, J.: Energy storage systems - Characteristics and comparisons, *Renewable and Sustainable Energy Reviews*, 12(5):pp. 1221-1250. doi: 10.1016/j.rser.2007.01.023, 2008 7

[49] Iliev, I.; Trivedi, C.; Agnalt, E.; Dahlhaug, O.G.: Variable-speed operation and pressure pulsations in a Francis turbine and a pump-turbine, *IOP Conference Series: Earth and Environmental Science*, p. 240:072034. doi: 10.1088/1755-1315/240/7/072034, 2019 8, 26

[50] International Electrotechnical Commission: *INTERNATIONAL STANDARD IEC60193 - Hydraulic turbines, storage pumps and pump turbines - Model acceptance tests.*, Tech. Rep. 60193:1999, 3, rue de Varembé Geneva, Switzerland, 11 1999 2, 10, 13, 17, 35, 110

[51] INTERNATIONAL ENERGY AGENCY: *Global Energy Review 2021 - Assessing the effects of economic recoveries on global energy demand and CO2 emissions in 2021*, last checked 05/10/2022. URL https://www.iea.org/reports/global-energy-review-2021 1

[52] Jacobson, M.Z.: The cost of grid stability with 100 % clean, renewable energy for all purposes when countries are isolated versus interconnected, *Renewable Energy*, 179:1065-1075. doi: 10.1016/j.renene.2021.07.115, 2021 1

[53] Jacobsson, S.; Lauber, V.: The politics and policy of energy system transformation-explaining the German diffusion of renewable energy technology, *Energy Policy*, 34(3):pp. 256-276, renewable Energy Policies in the European Union. doi: 10.1080/0953732032000199061, 2006 1

[54] Junginger, J.; Junginger, B.; Riedelbauch, S.: Hydraulischer Kurzschluss im Kraftwerk Vianden - Anlagendynamik und CFD-Simulationen der Abzweiger, *WasserWirtschaft*, 109(9):pp. 48-51. doi: 10.1007/s35147-019-0223-3, 2019 5

[55] Junginger, J.; Kirschner, O.; Riedelbauch, S.: Method to Transfer Transient Prototype Conditions to Closed Loop Model Test Rig, *International Journal of Fluid Machinery and Systems*, 13(1):pp. 1-11. doi: 10.5293/IJFMS.2020.13.1.001, 2020 5, 134

[56] Junginger, J.; Kirschner, O.; Riedelbauch, S.: Measurements of Fast Transitions at a Reversible Pump Turbine Model in Closed Loop Test Rig, *Journal of Physics: Conference Series*, 1909(1):012087. doi: 10.1088/1742-6596/1909/1/012087, May 2021 93

[57] Junginger, J.; Riedelbauch, S.; Kirschner, O.: Transfer of Transient Conditions from Prototype to Closed-Loop Model Test Rig, *IOP Conference Series: Earth and Environmental Science*, 240:082010. doi: 10.1088/1755-1315/240/8/082010, 2019 18

[58] Junginger, J.; Ruprecht, A.; Riedelbauch, S.; Kolb, S.: Investigation of the special behaviour of delayed load rejections on a 3x150MW pumped-storage plant, in: *Proceedings of Hydro2017*, Seville, Spain, 2017 5

[59] Kirschner, O.: *Experimentelle Untersuchung des Wirbelzopfes im geraden Saugrohr einer Modell-Pumpturbine*, Ph.D. thesis, University of Stuttgart, ISBN 978-3-9812054-1-1, 2011 4

[60] Kirschner, O.; Junginger, J.; Riedelbauch, S.: Test facility for transient operation point changes of hydraulic machinery, *IOP Conference Series: Earth and Environmental Science*, 774(1):012117. doi: 10.1088/1755-1315/774/1/012117, jun 2021 10

[61] Knapp, R.T.: Complete Characteristics of Centrifugal the Prediction Pumps and Their Use in of Transient Behavior, *Trans ASME*, Vol. 59:pp. 683-689, 1937 2

[62] Kolb, S.; Adler, K.; Vogel, S.: Nant de Drance: a 900 MW variable speed pumped-storage plant: transient and equipment challenges, in: *Proceedings of Hydro2016*, Montreux, Switzerland, 2016 1, 130

[63] Koutnik, J.: Frades II -variable speed pumped storage project and its benefit to the electrical grid, in: *Renewable Energy Conference*, Orlando, FL, USA. doi: 10.13140/2.1.3249.2809, Jan 2012 1

[64] Krappel, T.: *Turbulenzauflösende Strömungssimulation einer Francisturbine in Teillast*, Ph.D. thesis, University of Stuttgart, ISBN 978-3-9812054-6-6, 2018 6

[65] Kroner, N.; Bérubé, R.; Kroner, B.; et al.: Maintaining power grid reliability through individual unit stability, *Hydro Vision*, pp. 1–10, 2008 1

[66] Landry, C.; Nicolet, C.; Bergant, A.; Müller, A.; Avellan, F.: Modeling of unsteady friction and viscoelastic damping in piping systems, 15(5):052030. doi: 10.1088/1755-1315/15/5/052030, nov 2012 6

[67] Läpple, V.: *Einführung in die Festigkeitslehre: Lehr- und Übungsbuch*, Viewegs Fachbücher der Technik, Vieweg+Teubner Verlag, ISBN 9783834891198, 2008 10

[68] Lens, H.: Regelung von Kraftwerken und Netzen, *Lecture notes, IFK Universitiy of Stuttgart*, 2017 27

[69] Leuze electronic GmbH + Co. KG: *Technisches Datenblatt Induktiver Sensor ISS 212MM/4NO-4E0-S12*, 12 2020, deu - 2020-12-15 / 50109685 38

[70] Lowys, P.Y.; Paquet, F.; Couston, M.; Farhat, M.; Natal, S.; Avellan, F.: Onboard Measurements of Pressure and Strain Fluctuations in a Model of low Head Francis Turbine. Part 2 : Measurements and Preliminary Analysis Results, *Proceedings of the 21st IAHR Symposium on Hydraulic Machinery and Systems, Lausanne, Switzerland*, 1:pp. 873-880, 2002 4

[71] Lunze, J.: *Regelungstechnik 1*, vol. 11 of *Springer-Lehrbuch*, Springer Vieweg. doi: 10.1007/978-3-662-52678-1, 2016 45

[72] Lutz, H.; Wendt, W.: *Taschenbuch der Regelungstechnik: mit MATLAB und Simulink*, 11th edn., Europa-Lehrmittel, ISBN 978-3-8085-5869-0, 2019 47

[73] Mössinger, P.; Conrad, P.; Jung, A.: Transient two-phase CFD simulation of overload pressure pulsation in a prototype sized Francis turbine considering the waterway dynamics, *IOP Conference Series: Earth and Environmental Science*, 22(3):032033. doi: 10.1088/1755-1315/22/3/032033, 2014 6

[74] Mössinger, P.; Jung, A.: Transient two-phase CFD simulation of overload operating conditions and load rejection in a prototype sized Francis turbine, *IOP Conference Series: Earth and Environmental Science*, 49:092003. doi: 10.1088/1755-1315/49/9/092003, 2016 7

[75] Müller, A.: *Physical Mechanisms governing Self-Excited Pressure Oscillations in Francis Turbines*, Ph.D. thesis, École Polytechnique Fédérale de Lausanne, Lausanne, Switzerland, 2014 1

[76] National Instruments Co.: *LabVIEW™ User Manual*, 11 2001, 320999D-01 35

[77] National Instruments Co.: *Operating Instructions and Specifications NI 9229/9239*, Jul 2008, 374184E-01 35

[78] National Instruments Co.: *Operating Instructions and Specifications NI 9401*, Jun 2008, 374068D-01

[79] National Instruments Co.: *User Guide and Specifications NI cDAQ-9172*, 6 2008, 371747F-01 35

[80] Nicolet, C.; Alligné, S.; Kawkabani, B.; Koutnik, J.; Simond, J.J.; Avellan, F.: Stability Study of Francis Pump-Turbine at Runaway, in: *Proceedings of 3rd IAHR International Meeting of the Working Group on Cavitation and Dynamic Problems in Hydraulic Machinery and Systems*, pp. pp. 371-384, IAHR, Brno, Czech Republic, 2009 5

[81] Nicolet, C.; Alligné, S.; Kawkabani, B.; Simond, J.J.; Avellan, F.: Unstable Operation of Francis Pump-Turbine at Runaway: Rigid and Elastic Water Column Oscillation Modes, *International Journal of Fluid Machinery and Systems*, 2(4):pp. 324-333. doi: 10.5293/IJFMS.2009.2.4.324, 2009 5

[82] Nicolet, C.; Beguin, A.; Kawkabani, B.; Pannatier, Y.; Schwery, A.; Avellan, F.: Variable Speed and Ternary Units to Mitigate Wind and Solar Intermittent Production, in: *Proceedings of Hydrovision Conference 2014*, Nashville, TN, USA, 2014 9, 130

[83] Nicolet, C.; Braun, O.; Ruchonnet, N.; Beguin, A.; Avellan, F.: Full Size Frequency Converter for Fast Francis Pump-Turbine Operating Mode Transition, in: *Proceedings of Hydrovision Conference 2016*, Minneapolis, MN, USA, 2016 9, 18, 130

[84] Nicolet, C.; Braun, O.; Ruchonnet, N.; Hell, J.; Béguin, A.; Avellan, F.: Simulation of pump-turbine prototype fast mode transition for grid stability

support, *Journal of Physics: Conference Series*, 813:012040. doi: 10.1088/1742-6596/813/1/012040, Apr 2017 9

[85] Ohashi, H.: *Analytical and experimental study of dynamic characteristics of turbopumps*, Tech. Rep., NASA Marshall Space Flight Center; Huntsville, AL, United States, 1968 2

[86] Olimstad, G.; Nielsen, T.; Børresen, B.: Stability Limits of Reversible-Pump Turbines in Turbine Mode of Operation and Measurements of Unstable Characteristics, *Journal of Fluids Engineering*, 134. doi: 10.1115/1.4007589, Nov 2012 20

[87] Padrón, S.; Medina, J.; Rodríguez, A.: Analysis of a pumped storage system to increase the penetration level of renewable energy in isolated power systems. Gran Canaria: A case study, *Fuel and Energy Abstracts*, 36. doi: 10.1016/j.energy.2011.10.029, 2011 7

[88] Pannatier, Y.; Nicolet, C.; Kawkabani, B.; Deniau, J.L.; Schwery, A.; Avellan, F.; Simond, J.J.: Transient Behavior of Variable Speed Pump-Turbine Units, in: *Proceedings of 24th IAHR Symposium on Hydraulic Machinery ans Systems*, Foz Do Iguassu, Brasil, Jan 2008 9

[89] Papukchiev, A.; Lerchl, G.: Extension and Application of the Coupled 1D-3D Thermal-Hydraulic Code ATHLET-ANSYS CFX for the Simulation of Liquid Metal Coolant Flows in Advanced Reactor Concepts, *International Conference on Nuclear Engineering, Proceedings, ICONE*, 4. doi: 10.1115/ICONE20-POWER2012-54872, 2012 6

[90] Pedersen, N.; Larsen, P.; Jacobsen, C.: Flow in a Centrifugal Pump Impeller at Design and Off-Design Conditions-Part I: Particle Image Velocimetry (PIV) and Laser Doppler Velocimetry (LDV) Measurements, *Journal of Fluids Engineering-transactions of The Asme - J FLUID ENG*, 125. doi: 10.1115/1.1524585, 2003 4

[91] Pezzinga, G.: Second viscosity in transient cavitating pipe flows, *Journal of Hydraulic Research*, 41(6):656–665, 2003 5

[92] Pfeiffer, A.: PSW Goldisthal ausgestattet mit drehzahlgeregelten Motor/Generatoren, in: *Tagungsband 10. Internationales Seminar Wasserkraftanlagen*, pp. pp. 227-238, Technische Universität Wien, Technische Universität Wien, Karlsplatz 13, A-1040 Wien, Nov 1998 130

[93] Pfleiderer, C.; Petermann, H.: *Strömungsmaschinen*, vol. 7., Springer-Verlag Berlin Heidelberg. doi: 10.1007/b138287, 2005 15

[94] Riedelbauch, S.: Hydraulische Strömungsmaschinen in der Wasserkraft, *Lecture notes, IHS Universitiy of Stuttgart*, 2015 14

[95] Riedelbauch, S.: Transiente Vorgänge und Regelungsaspekte in der Wasserkraft - Transiente Vorgänge in Rohrleitungssystemen, *Lecture notes, IHS Universitiy of Stuttgart*, 2017 21, 22, 57

[96] Riedelbauch, S.; Junginger, J.; Kirschner, O.: Betriebsübergänge von hydraulischen Strömungsmaschinen - ein neuer Versuchsstand, *WasserWirtschaft*, 109(9):pp. 12-15. doi: 10.1007/s35147-019-0217-1, 2019 10

[97] Riedelbauch, S.; Stens, C.: Pump to turbine transient for a pump-turbine in a model test circuit and a real size power plant, *IOP Conference Series: Earth and Environmental Science*, 240:072039. doi: 10.1088/1755-1315/240/7/072039, mar 2019 9

[98] Rodrigues, E.; Godina, R.; Santos, S.; Abebe Worke, B.; Contreras, J.; Catalão, J.: Energy storage systems supporting increased penetration of renewables in islanded systems, *Energy*, 75. doi: 10.1016/j.energy.2014.07.072, 2014 7

[99] Rood, E.P.; Telionis, D.P.: Editorial, *ASME Journal of Fluids Engineering*, 113(3):313-314. doi: 10.1115/1.2909502, 1991 35

[100] Ruchonnet, N.; Braun, O.: Reduced Scale Model Test of Pump-Turbine Transition, in: *Proceedings of 6th IAHR International Meeting of the Working Group on Cavitation and Dynamic Problems in Hydraulic Machinery and Systems*, IAHR, Ljubljana, Slovenia, 2015 9, 80, 82

[101] Ruchonnet, N.; Braun, O.: 1D simulation of pump-turbine transition, *Journal of Physics: Conference Series*, 813:012039. doi: 10.1088/1742-6596/813/1/012039, 2017 9

[102] Ruprecht, A.; Helmrich, T.; Aschenbrenner, T.; Scherer, T.: Simulation of Vortex Rope In A Turbine Draft Tube, in: *Proceedings of the Hydraulic Machinery and Systems 21st IAHR Symposium*, Lausanne, Switzerland, 2002 6

[103] Rychkov, S.I.: Reactive power control services based on a generator operating as a synchronous condenser, vol. 46, pp. 405–409. doi: 10.1007/s10749-013-0369-6, 2013 29

[104] Safwat, H.H.: *Transients in cooling water systems of thermal power plants*, Ph.D. thesis, TU Delft, 1972 3

[105] Saito, S.: The Transient Characteristics of a Pump during Start Up, *Bulletin of JSME*, 25(201):pp. 372-379. doi: 10.1299/jsme1958.25.372, 1982 3

[106] Schafer, D.; Simond, J.J.: Adjustable speed asynchronous machine in hydro power plants and its advantages for the electric grid stability., *CIGRÉ Report*, 1998 7

[107] Schlunegger, H.; Thöni, A.: 100 MW full-size converter in the Grimsel 2 pumped-storage plant, in: *Proceedings of Hydro2013*, Innsbruck, Austria, 2013 1

[108] Schmucker, H.; Flemming, F.; Coulson, S.: Two-Way Coupled Fluid Structure Interaction Simulation of a Propeller Turbine, *International Journal of Fluid Machinery and Systems*, 3:pp. 342-351. doi: 10.5293/IJFMS.2010.3.4.342, Dec 2010 10

[109] Schneider, K.: *Das Verhalten von Kreiselpumpen beim Auftreten von Druckwellen*, Ph.D. thesis, University of Stuttgart, 1986 3

[110] Schobeiri, M.: *Turbomachinery Flow Physics and Dynamic Performance*, 1st edn., Springer Berlin, Heidelberg, ISBN 978-3-642-06114-1. doi: 10.1007/b137854, 2005 16

[111] Schoenung, S.M.; Hassenzahl, W.V.: Long vs. short-term energy storage:sensitivity analysis., *Sandia National Laboratories SAND2007-4253*. doi: 10.2172/912652, Jul 2007 7

[112] Schröder, D.: *Elektrische Antriebe - Grundlagen*, vol. 6 of *Springer-Lehrbuch*, Springer Vieweg. doi: 10.1007/978-3-662-55448-7, 2017 130

[113] SEW-EURODRIVE GmbH & Co KG: *Catalog - Electric Cylinders*, 2016, 20176945/EN 106

[114] Shouse, K.C.; Clark, C.E.; Lattanzio, R.K.; Croft, G.K.; Leggett, J.A.; Miller, R.S.; Procita, K.; Westphal, M.I.; Ramseur, J.L.: U.S. Climate Change Policy, *Congressional Research Service*, r46947 VERSION 3, Dec 2021 1

[115] Siemens Flow Instruments A/S: *Magnetisch-induktive Durchflussmessgeräte - SITRANS F M MAG 5100W*, Nov 2010, A5E03376527-01 37

[116] Siemens Flow Instruments A/S: *Magnetisch-induktive Durchflussmessgeräte - SITRANS F M MAG 5000/6000*, Dec 2013, A5E02944982-002 37

[117] SIMSEN: *official Webpage*, last checked 05/10/2022. URL https://www.epfl.ch/research/facilities/hydraulic-machines-platform/ptmh/simsen/ 5

[118] Stens, C.: *Investigation of a fast transition from pump mode to generating mode in a reversible pump turbine*, Ph.D. thesis, University of Stuttgart, ISBN 978-3-9812054-5-9, 2018 6, 9, 18, 31, 82

[119] Stens, C.; Riedelbauch, S.: CFD simulation of the flow through a pump turbine during a fast transition from pump to generating mode, in: *Proceedings of 6th IAHR International Meeting of the Working Group on Cavitation and Dynamic Problems in Hydraulic Machinery and Systems*, pp. pp. 323-330, IAHR, Ljubljana, Slovenia, 2015 9

[120] Stens, C.; Riedelbauch, S.: CFD analysis of fast transition from pump mode to generating mode in a reversible pump turbine, in: *High Performance Computing in Science and Engineering '16: Transactions of the High Performance Computing Center, Stuttgart (HLRS) 2016*, ed. Nagel, W.; Kröner, D.; Resch, M., pp. pp. 487-498, Springer International Publishing, 2016

[121] Stens, C.; Riedelbauch, S.: Investigation of a fast transition from pump mode to generating mode in a model scale reversible pump turbine, *IOP Conference Series: Earth and Environmental Science*, 49:112001. doi: 10.1088/1755-1315/49/11/112001, Nov 2016

[122] Stens, C.; Riedelbauch, S.: Influence of guide vane opening on the flow phenomena in a pump turbine during a fast transition from pump mode to generating mode, *Journal of Physics: Conference Series*, 813(1):012024. doi: 10.1088/1742-6596/813/1/012024, 2017 9

[123] Tanaka, T.; Tsukamoto, H.: Transient Behavior of a Cavitating Centrifugal Pump at Rapid Change in Operating Conditions - Part 1: Transient Phenomena at Opening/Closure of Discharge Valve, *Journal of Fluids Engineering*, 121(4):pp. 841-849. doi: 10.1115/1.2823545, 1999 3

[124] Tanaka, T.; Tsukamoto, H.: Transient Behavior of a Cavitating Centrifugal Pump at Rapid Change in Operating Conditions - Part 2: Transient Phenomena at Pump Startup/Shutdown, *Journal of Fluids Engineering*, 121(4):pp. 850-856. doi: 10.1115/1.2823546, 1999

[125] Tanaka, T.; Tsukamoto, H.: Transient Behavior of a Cavitating Centrifugal Pump at Rapid Change in Operating Conditions - Part 3: Classifications of Transient Phenomena, *Journal of Fluids Engineering*, 121(4):pp. 857-865. doi: 10.1115/1.2823547, 1999 3

[126] Trivedi, C.; Cervantes, M.; Gandhi, B.: Investigation of a High Head Francis Turbine at Runaway Operating Conditions, *Energies*, 9:p. 149. doi: 10.3390/en9030149, 2016 4

[127] Trivedi, C.; Cervantes, M.J.; Bhupendrakumar, G.; Dahlhaug, O.G.: Pressure measurements on a high-head Francis turbine during load acceptance and rejection, *Journal of Hydraulic Research*, 52(2):pp. 283-297. doi: 10.1080/00221686.2013.854846, 2014 4

[128] Trivedi, C.; Cervantes, M.J.; Dahlhaug, O.G.; Gandhi, B.K.: Experimental Investigation of a High Head Francis Turbine During Spin-No-Load Operation, *Journal of Fluids Engineering*, 137(6). doi: 10.1115/1.4029729, 2015 4

[129] Trivedi, C.; Cervantes, M.J.; Gandhi, B.K.; Dahlhaug, O.G.: Transient Pressure Measurements on a High Head Model Francis Turbine During Emergency Shutdown, Total Load Rejection, and Runaway, *Journal of Fluids Engineering*, 136(12). doi: 10.1115/1.4027794, 2014 4

[130] Trivedi, C.; Cervantes, M.J.; Gandhi, B.K.; Ole, D.G.: Experimental investigations of transient pressure variations in a high head model Francis turbine during start-up and shutdown, *Journal of Hydrodynamics*, 26:pp. 277-290. doi: 10.1016/S1001-6058(14)60031-7, Apr 2014 4

[131] Truckenbrodt, E.: *Fluidmechanik - Band 1: Grundlagen und elementare Strömungsvorgänge dichtebeständiger Fluide*, 4th edn., Springer Berlin, Heidelberg, ISBN 978-3-540-79017-4. doi: 10.1007/978-3-540-79018-1, 2008 73

[132] Truckenbrodt, E.: *Fluidmechanik - Band 2: Elementare Strömungsvorgänge dichteveränderlicher Fluide sowie Potential- und Grenzschichtströmungen*, 4th edn., Springer Berlin, Heidelberg, ISBN 978-3-540-79023-5. doi: 10.1007/978-3-540-79024-2, 2008 15

[133] Tsukamoto, H.; Matsunaga, S.; Yoneda, H.; Hata, S.: Transient Characteristics of a Centrifugal Pump During Stopping Period, *Journal of Fluids Engineering*, 108(4):pp. 392-399. doi: 10.1115/1.3242594, 1986 3

[134] Tsukamoto, H.; Nishi, M.; Uno, M.; Kaku, Y.; Muto, T.; Tanaka, T.: Transient Characteristics of Cavitating Centrifugal Pump with Rapid Change in Flow Rate., *Transactions of the Japan Society of Mechanical Engineers Series B*, 60:pp. 1883-1890. doi: 10.1299/kikaib.60.1883, 1994 3

[135] Tsukamoto, H.; Ohashi, H.: Transient Characteristics of a Centrifugal Pump During Starting Period, *Journal of Fluids Engineering*, 104(1):pp. 6-13. doi: 10.1115/1.3240859, 1982 3

[136] UNFCCC: The Paris Agreement, *Paris Climate Change Conference*, COP 21, Nov 2015 1

[137] Wack, J.: *Numerical Investigation of the Full Load Instability in a Francis Turbine*, Ph.D. thesis, University of Stuttgart, ISBN 978-3-948328-03-0, 2020 6

[138] Wack, J.; Riedelbauch, S.: On the Physical Mechanisms that Cause the Full Load Instability in Francis Turbines, *IOP Conference Series: Earth and Environmental Science*, 774(1):012022. doi: 10.1088/1755-1315/774/1/012022, 2021 6

[139] WIKA Alexander Wiegand SE & Co. KG: *Datenblatt Drucksensor Für Präzisionsmessungen*, Jan 2020, PE 81.54 37, 101

[140] Wylie, E.; Streeter, V.: *Fluid Transients*, vol. 2, McGraw-Hill International Book Company, ISBN 9780070721876, 1978 22

[141] XFLEX-HYDRO: *official Webpage*, last checked 05/10/2022. URL https://xflexhydro.net xvi, 10

[142] Yasuda, Y.; Ardal, A.R.; Huertas-Hernando, D.; Carlini, E.M.; Estanqueiro, A.; Flynn, D.; Gomez-Lazaro, E.; Holttinen, H.; Kiviluoma, J.; van Hulle, F.; Kondoh, J.; Lange, B.; Menemenlis, N.; Milligan, M.; Orths, A.; Smith, C.; Söder, L.: Flexibility Chart: Evaluation on diversity of flexibility in various areas, in: *Proceedings of 12th International Workshop on Large-Scale Integration of Wind Power into Power Systems as well as on Transmission Networks for Offshore Wind Farms, WIW2013*, Energynautics GmbH, Germany, ISBN 978-3-98-13870-7-0, 2013 9

[143] Yin, C.; Yang, J.; Zeng, W.; Cheng, Y.: Simulation of the simultaneous load rejection processes of two parallel pump turbines using a 1D–3D approach, *IOP Conference Series: Earth and Environmental Science*, 240:082001. doi: 10.1088/1755-1315/240/8/082001, Mar 2019 7

A Principle of Variable Speed Technology

There are two main concepts for the variable speed operation of hydropower plants, which are explained in detail by Hildinger and Ködding [42] and shown in Figure A.1. Both concept have specific advantages and disadvantages, which fit on different applications. In both approaches, the frequency from the electrical grid is converted to a required frequency to achieve the specified rotational speed of the runner. If the power plant is equipped with synchronous electrical machine the converted frequency is directly applied to the stator of the motor generator (SMFC). If there is a double-fed induction asynchronous machine involved, the grid frequency is fed on the stator and the converted frequency specifies the excitation voltage at the rotor (DFIM).

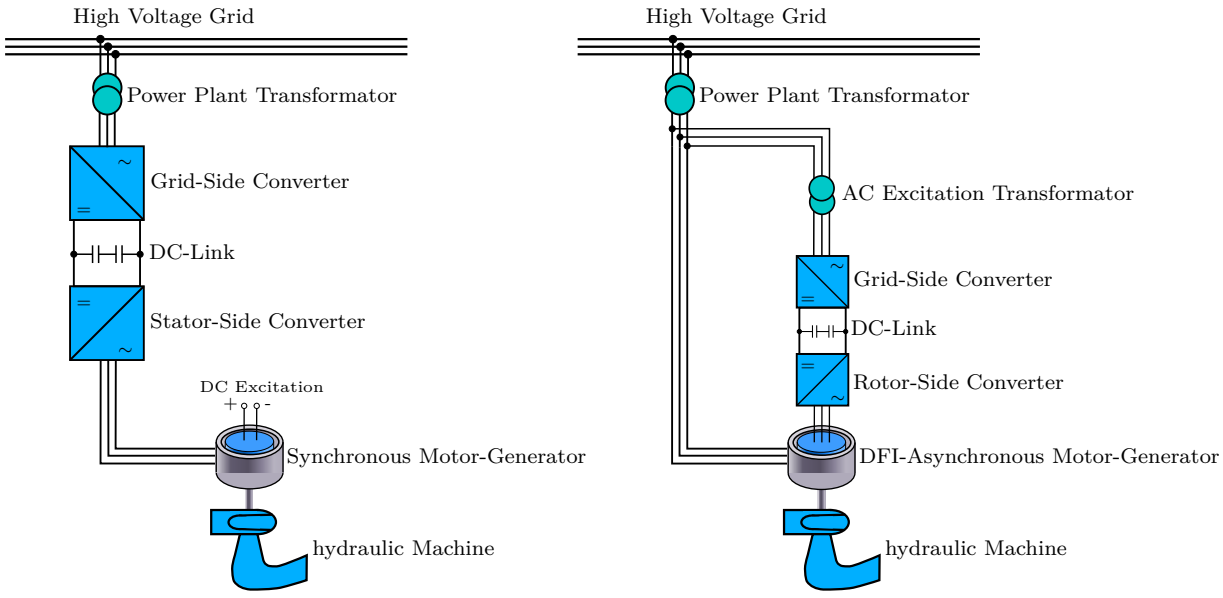

(a) SMFC concept **(b)** DFIM concept

Figure A.1: Comparison of electrical equipment for variable speed operation.

Synchronous Machine with Full Power Converter - SMFC

The SMFC concept decouples grid frequency from the stator field frequency of the electrical machine. The used converter unit consists of a grid-side converter, the

rotor-side converter and the DC link in between. The entier energy which is delivered to the grid or absorbed by the hydraulic machine passes the converter unit completely. This means that the converter must be designed for the same amount of power as the motor generator.

According to [42], the properties of this concept are:

- possibility to use standard synchronous motor generators
- converter unit can theoretically be retrofitted as bypass
- maximum flexibility in rotational speed, operating limits are only given by the hydraulic machine
- very fast acceleration with almost rated torque, also from standstill
- no time delay for synchronication
- fast active power injection in pump and turbine mode due to flywheel effect
- due to the high powers and voltages, the converter requires special design concepts which make them expensive
- high space requirement which leads to high costs, especially for underground power plants

Double-fed Induction Asynchronous Machine - DFIM

With the external-excited asynchronous machine, the stator is directly connected to the power plant transformer. Therefore stator field and electrical grid have the same frequency. The converter unit, which in principle has the same design as the SMFC concept, is connected to the rotor via a further transformer. It decouples the rotating magnetic field in the rotor from the rotation itself. Thus, a relative rotation of the rotor to the rotating stator field is enabled. The prerequisite is the transmission of electrical power from or into the rotor. Since this power transmission, which is often effected via slip rings, is limited, the flexible speed range of this machine is also limited [112]. This range of flexibility is often given as ± 10 % of the rated rotational speed [62, 83, 92].

Some of the listed properties of this concept below are described by [82]:

- certain speed range around the design speed in both rotation directions
- a smaller and less loaded converter is cheaper than full size converter, but still high investments are necessary

- first experiences with this technology have been made in new power plants
- lower efficiency drop due to lower converter losses compared to the SMFC concept
- pump start up without supplementary equipment (under the condition of closed guide vanes)
- fast active power injection in pump and turbine mode due to flywheel effect
- reactive power control with static volt-ampere reactive compensator (SVC) even when the unit is at standstill
- cannot be retrofitted, as asynchronous machines are untypical for existing hydropower plants

B Numerical Models

B.1 Power Plant Simulation Model

B.1.1 Parameters

List of pipeline elements of 1D power plant simulation model.

Table B.1: Pipeline elements of 1D power plant simulation model.

Element	L [m]	D [m]	$\lambda \cdot 10^3$ [-]	a [$\mathrm{m\,s^{-1}}$]
lt1	25.40	6.225	0.000	1100
lt2	32.01	4.150	0.014	1100
lt3	54.37	4.150	0.040	1100
lt4	435.15	4.150	2.588	1100
lt5	116.90	4.150	0.187	1100
lt6	10.22	3.525	0.001	1100
lt7	27.17	2.900	0.010	1100
lt8	3.33	2.725	0.000	1100
lt9-arma	4.750	2.550	0.000	1100
lt10-DT	21.940	3.712	0.000	800
lt11	5.92	6.600	0.000	800
lt12	39.85	6.600	0.000	800
lt13	23.01	7.450	0.000	800

B.1.2 Model Validation

Validation of 1D power plant simulation model. Comparison of measurement and simulation results of a load rejection scenario.

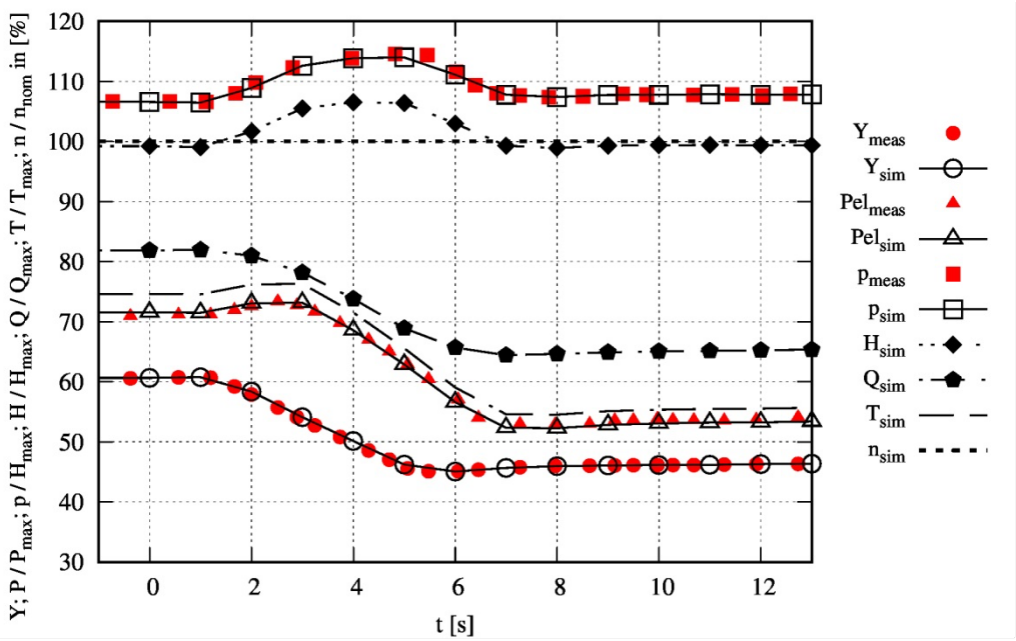

Figure B.1: Calibration of power plant simulation model with measured values [55].

B.2 Test Rig Simulation Model

List of pipeline elements of 1D test rig simulation model.

Table B.2: Pipe elements of 1D test rig model.

Element	**Branch**	L [m]	D [m]	λ [−]	a [m s^{-1}]
head water	-	-	-	-	-
lt1	-	0.010	1.000	0.0000	100
lt2	-	0.010	1.000	0.0000	100
lt3	-	0.010	1.000	0.0000	100
lt4	HWV	0.600	1.800	0.01491	1200

Continued on next page

Continued from previous page

Element	**Branch**	L [m]	D [m]	λ [−]	a [m s^{-1}]
lt5	HWV	0.800	1.800	0.01491	1200
lt6	HWV	0.800	1.800	0.01491	1200
lt7	HWV	0.675	1.800	0.01491	1200
lt8-noloss	model	1.650	0.300	0.00010	1200
lt9-noloss	model	1.122	0.300	0.00010	1200
lt10-ar115nl	model	0.750	0.300	0.00010	1200
lt11-noloss	model	4.875	0.300	0.00010	1200
lt12-noloss	model	0.775	0.300	0.00010	1200
lt13-noloss	model	0.650	0.200	0.00010	1200
lt14-sr	model	1.420	0.256	0.0000	800
lt15-uw1	model	1.00	1.000	90.000	800
lt16-uw2	model	1.00	1.000	0.01381	800
lt17	model	3.775	0.300	0.05364	800
lt18-ar116nl	model	0.270	0.300	0.00010	800
lt19	model	4.900	0.300	0.032280	800
lt20	model	1.300	0.300	0.38370	800
lt21	TWV	0.675	1.800	2764.81	800
lt22	TWV	0.800	1.800	0.01491	800
lt23	TWV	0.800	1.800	0.02982	800
lt24	TWV	0.430	1.800	0.02982	800
lt25	-	0.010	1.000	0.00000	100
lt26	-	0.010	1.000	0.00000	100
lt27	-	0.010	1.000	0.00000	100
tail water	-	-	-	-	-
lt28	HWV	1.125	1.800	2750.00	1200
lt29	pumps	0.840	0.300	0.00001	1200
lt30	pumps	1.750	0.300	0.22000	1200
lt31	pumps	1.074	0.300	0.00001	1200
lt32-2	pumps	0.435	0.300	0.00001	1200

Continued on next page

Continued from previous page

Element	**Branch**	L [m]	D [m]	λ [−]	a [m s^{-1}]
lt33-2	pumps	0.275	0.300	0.00001	1200
lt34-2	pumps	1.000	0.250	0.00001	1200
lt35-2	pumps	0.100	0.250	0.00001	1200
lt36-2	pumps	0.590	0.250	0.10000	1200
lt37-2	pumps	1.637	0.300	0.00001	800
lt38-2	pumps	1.720	0.300	0.00001	800
lt39	pumps	15.527	0.300	0.03458	800
lt40	pumps	0.715	0.300	0.26500	800
lt41	TWV	1.125	1.800	0.02982	800
lt42-2	pumps	5.498	0.275	0.00001	1200
lt43-2	pumps	0.590	0.250	0.50000	1200
lt44-2	pumps	1.182	0.300	0.00001	800
lt45-2	pumps	4.085	0.300	0.00001	800
lt46-2	pumps	1.809	0.300	0.00001	800
lt47-2	pumps	1.370	0.300	0.00001	800
ltby1	bypass	1.650	0.300	0.25000	1200
ltby2	bypass	2.895	0.300	0.06000	1200
ltby3	bypass	0.500	0.300	0.02000	800
ltby4	bypass	0.350	0.275	2.50000	800
ltby5	bypass	7.930	0.250	0.06000	800
ltby6	bypass	0.750	0.275	0.05100	800
ltby7	bypass	4.216	0.300	0.17000	800

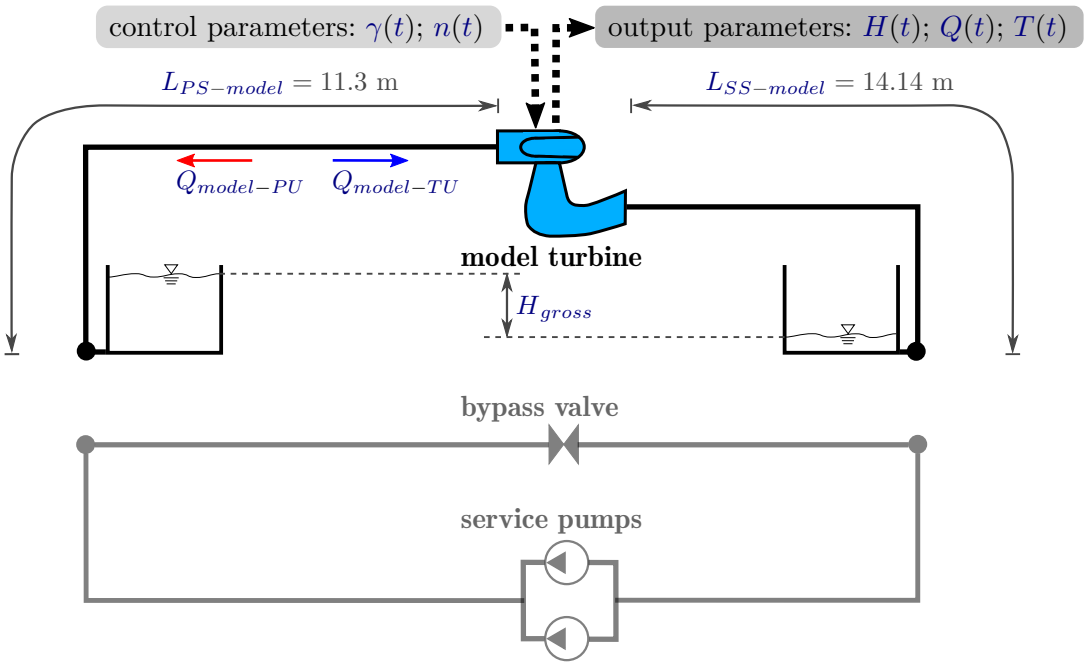

Figure B.2: Schematic of the open-loop test rig configuration with characteristic dimensions. The components of the closed-loop test rig are illustrated in transparent for comparison.

C Further Results

C.1 Further Test Case Results

Table C.1: Investigated variables for the respective pressure sensors in specific operating conditions of the model machine. p_0 and p_2 are referenced to setpoints of pressure at spiral case respectively draft tube. Others are referenced to pressure of test rig simulation results.

Mode	**PU**	**PU→TU**		**TU**	**TU→PU**	
	$(meas-ref)/ref$	e_{max}/ref_{ini}	Υ_{norm}	$(meas-ref)/ref$	e_{max}/ref_{ini}	Υ_{norm}
p_0	-0.000	0.049	0.096	-0.005	0.038	0.062
p_2	0.004	0.058	0.083	-0.006	0.032	0.053
p_3	0.004	0.060	0.070	-0.007	0.035	0.048
p_4	-0.001	0.040	0.112	0.021	0.031	0.074
p_5	0.006	0.045	0.121	0.003	0.047	0.085
p_6	0.002	0.044	0.134	-0.004	0.044	0.095
p_7	-0.004	0.057	0.145	0.003	0.021	0.101
p_8	-0.006	0.052	0.156	-0.002	0.019	0.105

Table C.2: Investigated variables of service pumps and the bypass armatur in specific operating conditions of the model machine. Variables are referenced to test rig simulation results.

Mode	PU	PU→TU		TU	TU→PU	
	$(meas-ref)/ref$	e_{max}/ref_{ini}	Υ_{norm}	$(meas-ref)/ref$	e_{max}/ref_{ini}	Υ_{norm}
n_{pumps}	-0.001	0.013	0.020	-0.002	0.003	0.055
Δp_{pump1}	0.005	0.080	0.050	0.004	0.051	0.036
Δp_{pump2}	0.004	0.050	0.057	0.002	0.029	0.043
Q_{pumps}	-0.017	0.351	0.080	-0.011	0.074	0.028
$n_{ed-pump1}$	-0.002	0.030	12.20	-0.002	0.024	10.50
$n_{ed-pump2}$	-0.004	0.008	12.51	-0.005	0.014	10.79
$Q_{ed-pump1}$	-1.991	2.308	81.86	-1.998	2.309	70.56
$Q_{ed-pump2}$	-1.972	2.309	83.93	-1.977	2.308	72.46
Q_{bypass}	0.003	0.054	0.106	-0.008	0.061	0.045
H_{bypass}	-0.012	0.050	0.020	-0.026	0.021	0.010

C.2 Fast Transition with Linear Speed Profile

Turbine operation is not achieved for $x_{t-Sr} = 3.0$ due to the speed limitation of the service pumps.

$$n_{proto}(t) = |n_{proto-rated}| \begin{cases} -1 + 2 \cdot {}^{t}/_{\Phi}, & PU \rightarrow TU \\ 1 - 2 \cdot {}^{t}/_{\Phi}, & TU \rightarrow PU \end{cases} \tag{C.1}$$

C.2.1 Results of Guide Vane Opening of $\gamma/\gamma_{max} = 0.4$

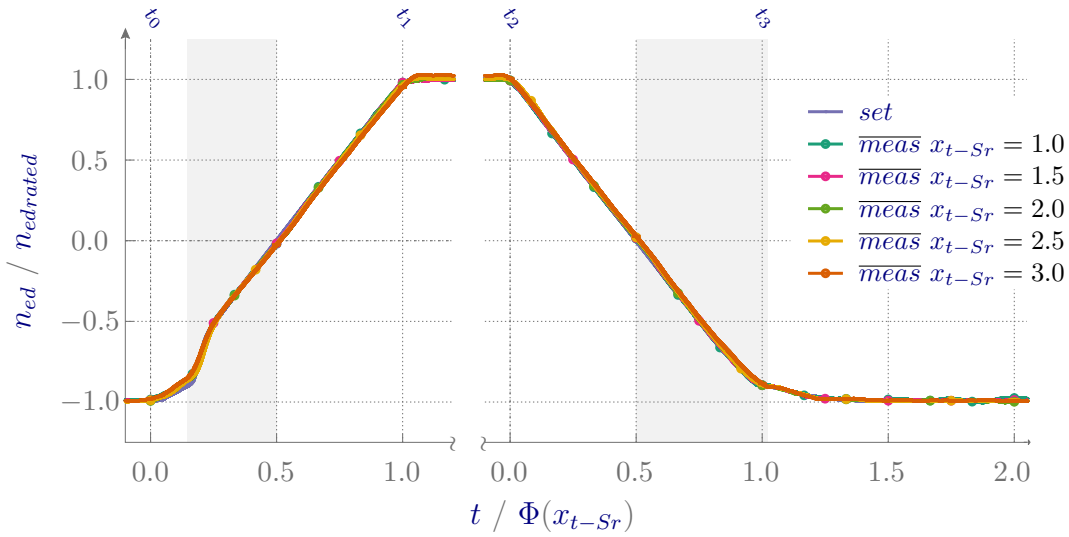

Figure C.1: Comparison of speed coefficient between setpoints and measurement results for different time scale factors of speed controlled fast transitions from pump to turbine mode (left) and vice versa (right) with linear profile and a guide vane opening of $\gamma/\gamma_{max} = 0.4$.

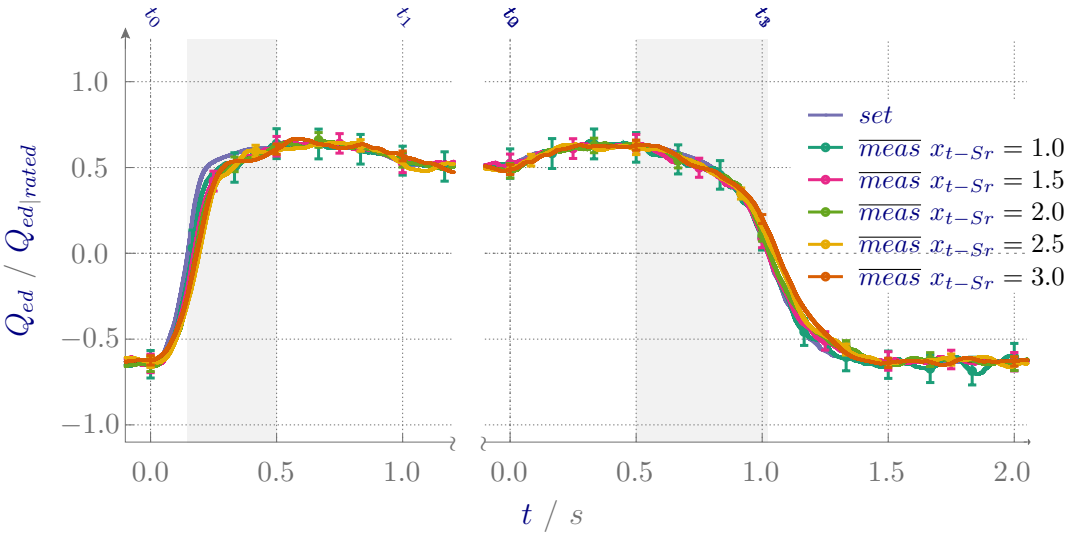

Figure C.2: Comparison of discharge coefficient between setpoints and measurement results for different time scale factors of speed controlled fast transitions from pump to turbine mode (left) and vice versa (right) with linear profile and a guide vane opening of $\gamma/\gamma_{max} = 0.4$.

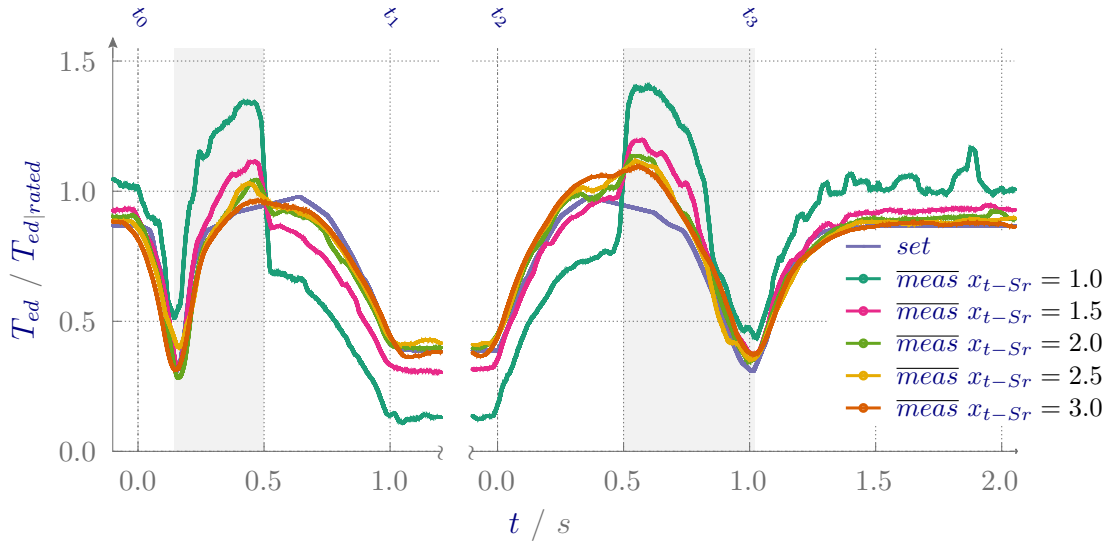

Figure C.3: Comparison of torque coefficient between setpoints and measurement results for different time scale factors of speed controlled fast transitions from pump to turbine mode (left) and vice versa (right) with linear profile and a guide vane opening of $\gamma/\gamma_{max} = 0.4$.

C.2.2 Results of Guide Vane Opening of $\gamma/\gamma_{max} = 0.6$

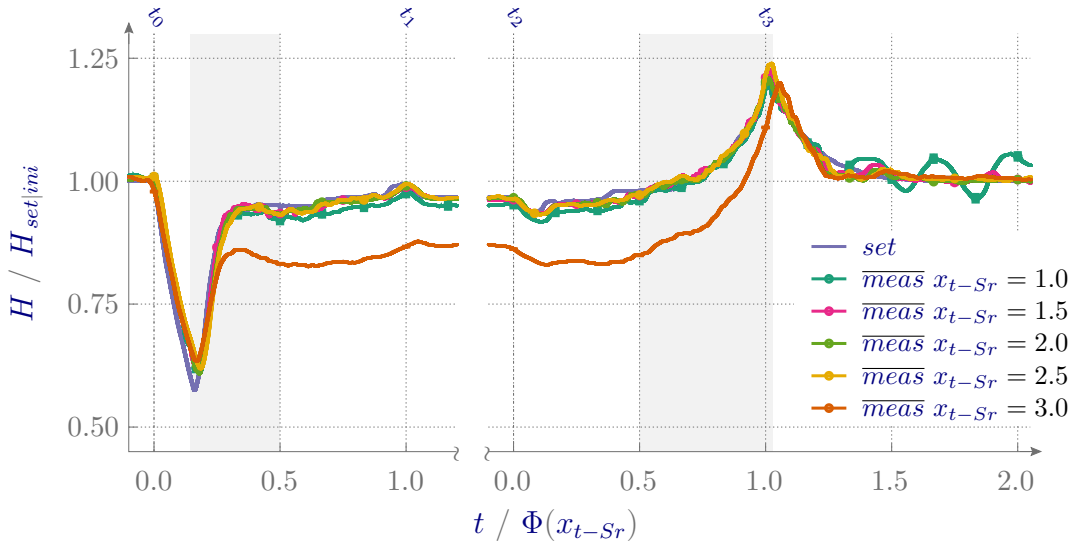

Figure C.4: Comparison of head between setpoints and measurement results for different time scale factors of speed controlled fast transitions from pump to turbine mode (left) and vice versa (right) with linear profile and a guide vane opening of $\gamma/\gamma_{max} = 0.6$.

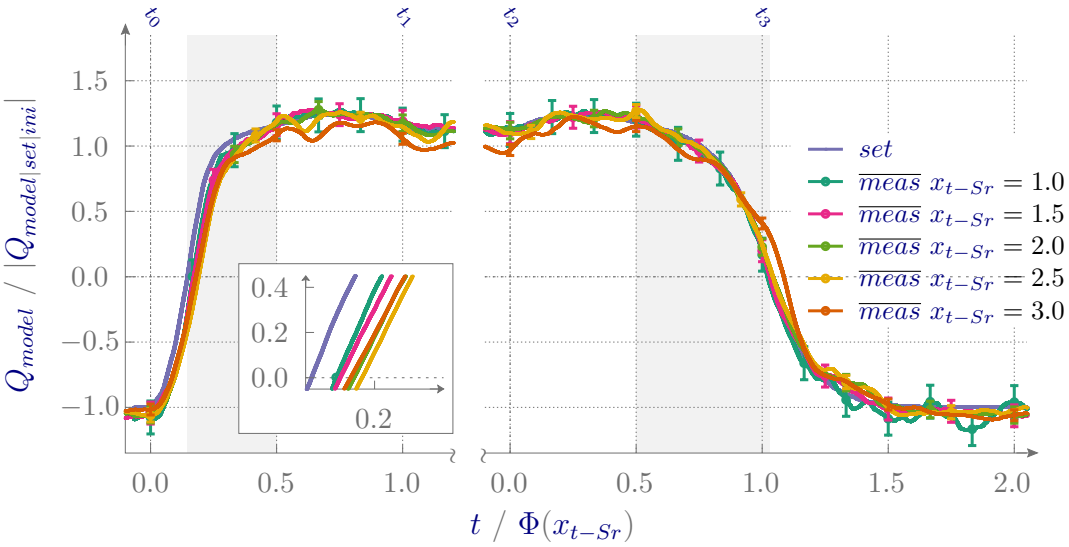

Figure C.5: Comparison of discharge between setpoints and measurement results for different time scale factors of speed controlled fast transitions from pump to turbine mode (left) and vice versa (right) with linear profile and a guide vane opening of $\gamma/\gamma_{max} = 0.6$.

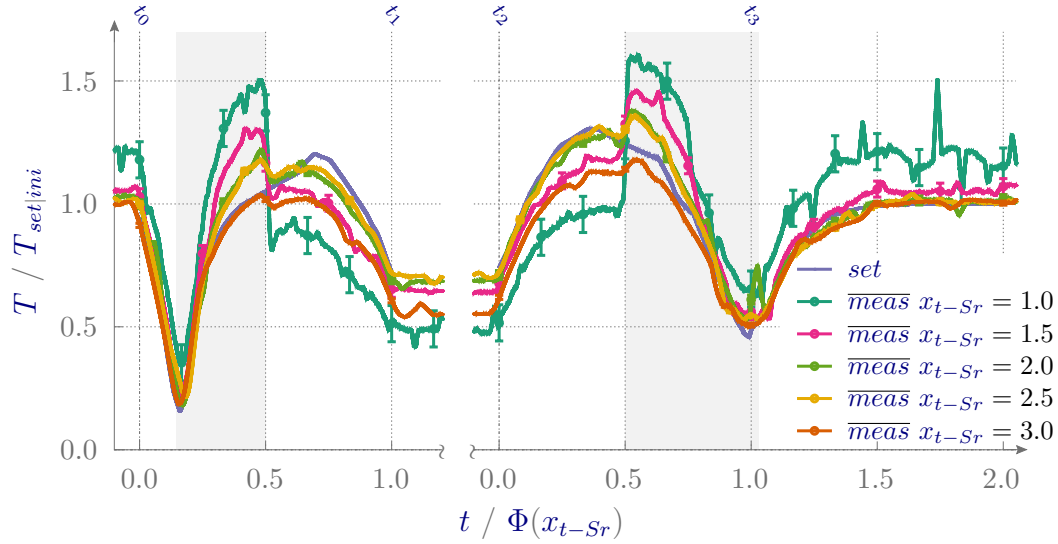

Figure C.6: Comparison of torque between setpoints and measurement results for different time scale factors of speed controlled fast transitions from pump to turbine mode (left) and vice versa (right) with linear profile and a guide vane opening of $\gamma/\gamma_{max} = 0.6$.

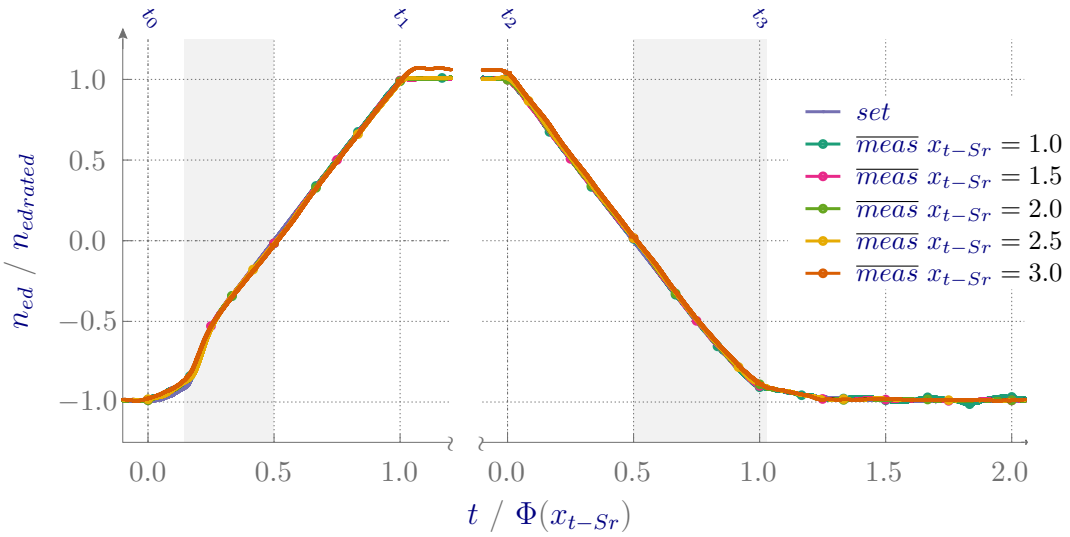

Figure C.7: Comparison of speed coefficient between setpoints and measurement results for different time scale factors of speed controlled fast transitions from pump to turbine mode (left) and vice versa (right) with linear profile and a guide vane opening of $\gamma/\gamma_{max} = 0.6$.

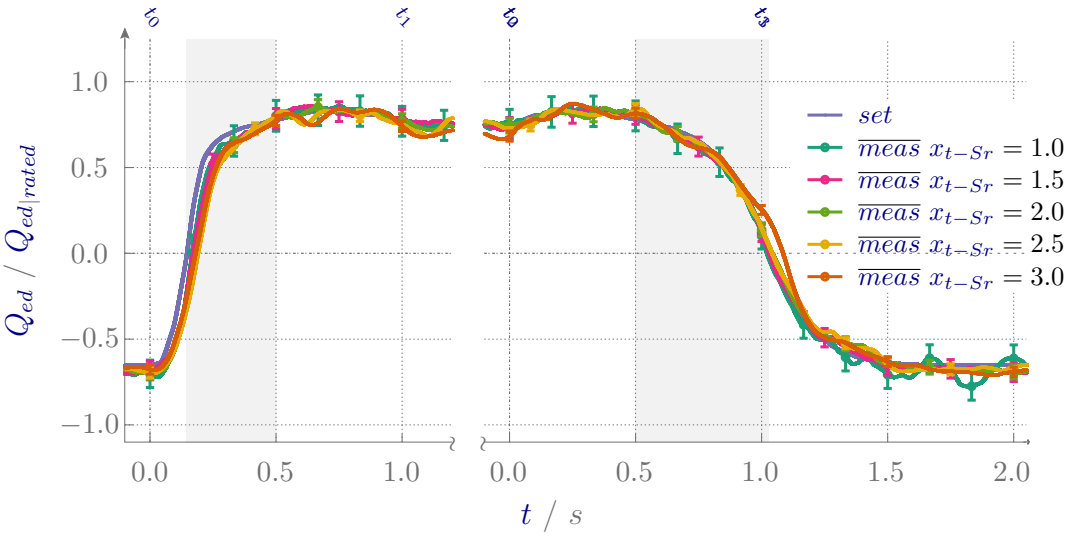

Figure C.8: Comparison of discharge coefficient between setpoints and measurement results for different time scale factors of speed controlled fast transitions from pump to turbine mode (left) and vice versa (right) with linear profile and a guide vane opening of $\gamma/\gamma_{max} = 0.6$.

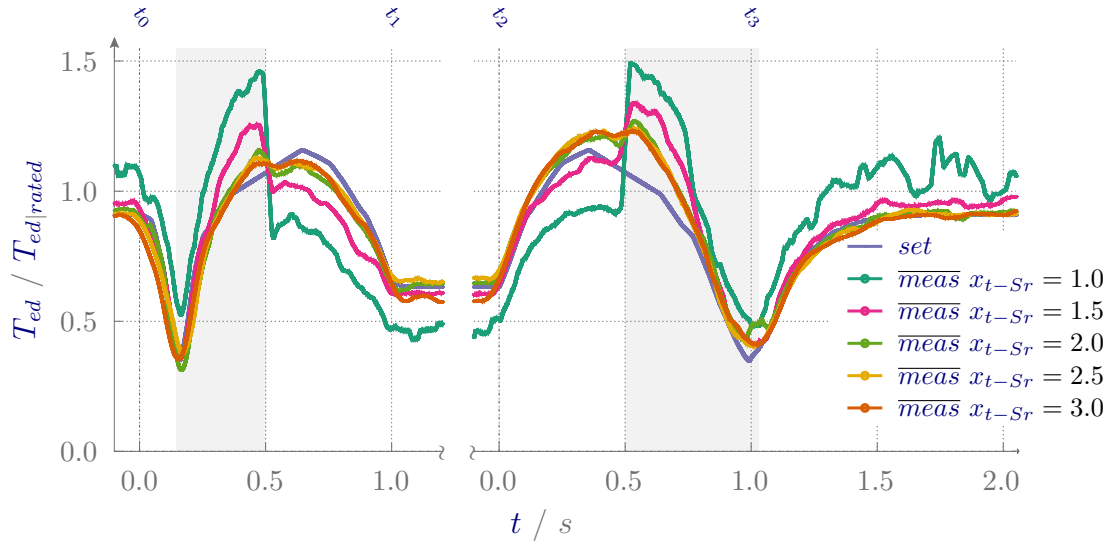

Figure C.9: Comparison of torque coefficient between setpoints and measurement results for different time scale factors of speed controlled fast transitions from pump to turbine mode (left) and vice versa (right) with linear profile and a guide vane opening of $\gamma/\gamma_{max} = 0.6$.

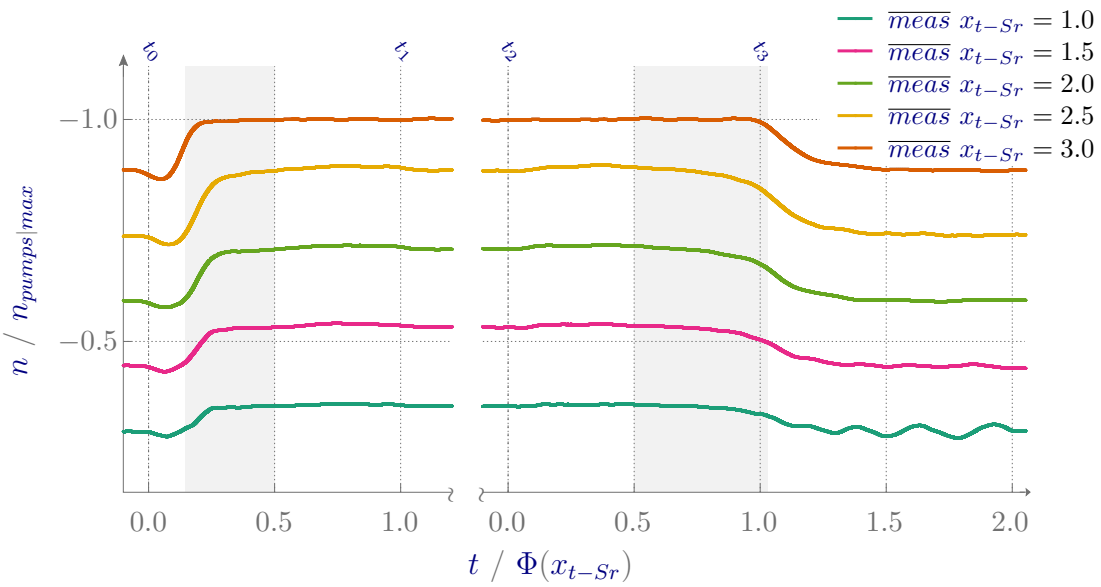

Figure C.10: Measured rotational speed of the service pumps for different time scale factors of speed controlled fast transitions from pump to turbine mode (left) and vice versa (right) with linear profile and a guide vane opening of $\gamma/\gamma_{max} = 0.6$.

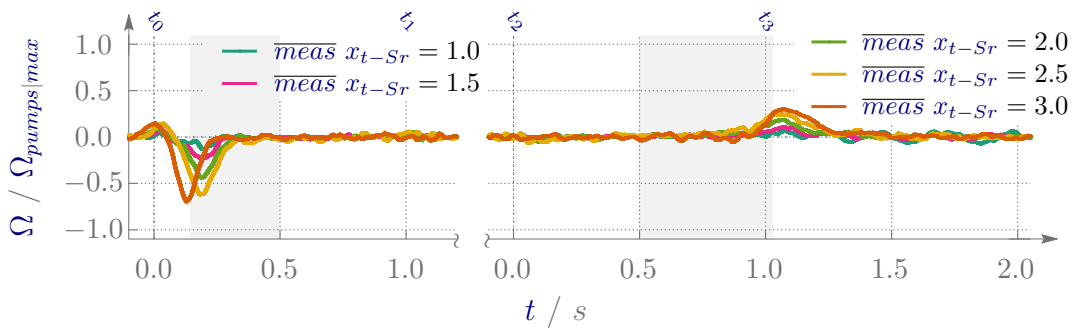

Figure C.11: Measured rotational speed acceleration of the service pumps for different time scale factors of speed controlled fast transitions from pump to turbine mode (left) and vice versa (right) with linear profile and a guide vane opening of $\gamma/\gamma_{max} = 0.6$.

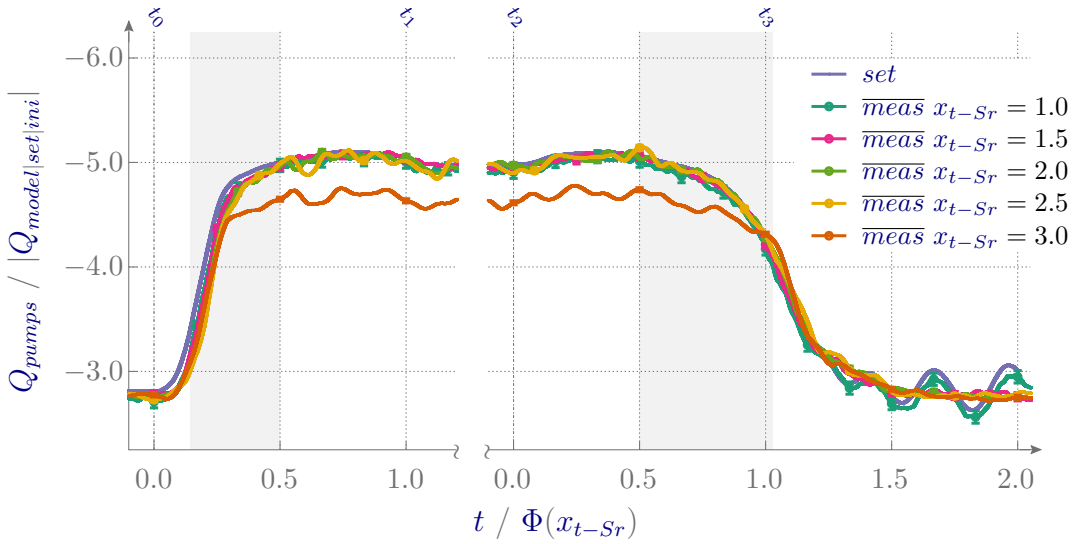

Figure C.12: Measured discharge of the service pumps for different time scale factors of speed controlled fast transitions from pump to turbine mode (left) and vice versa (right) with linear profile and a guide vane opening of $\gamma/\gamma_{max} = 0.6$.

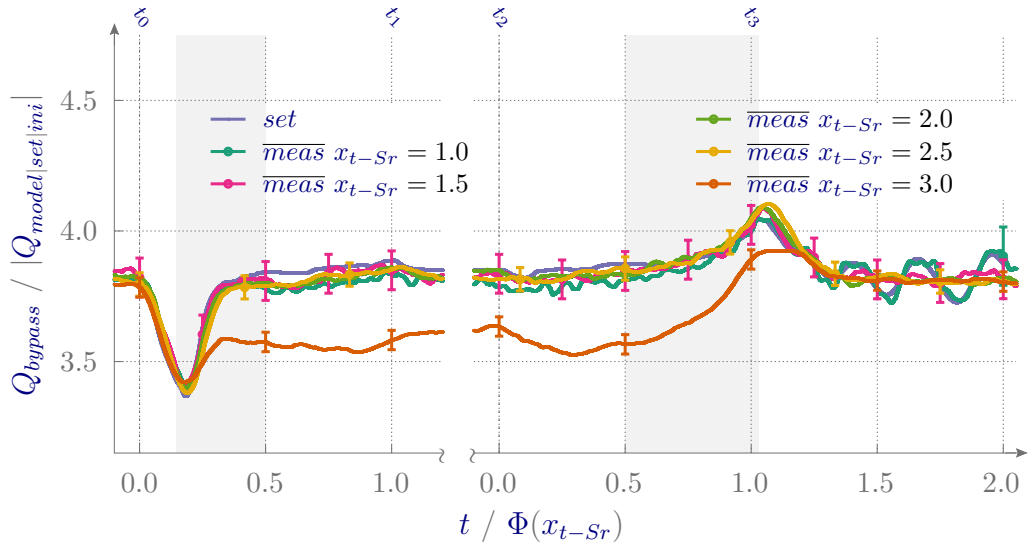

Figure C.13: Measured bypass discharge for different time scale factors of speed controlled fast transitions from pump to turbine mode (left) and vice versa (right) with linear profile and a guide vane opening of $\gamma/\gamma_{max} = 0.6$.

C.2.3 Results of Guide Vane Opening of $\gamma/\gamma_{max} = 0.8$

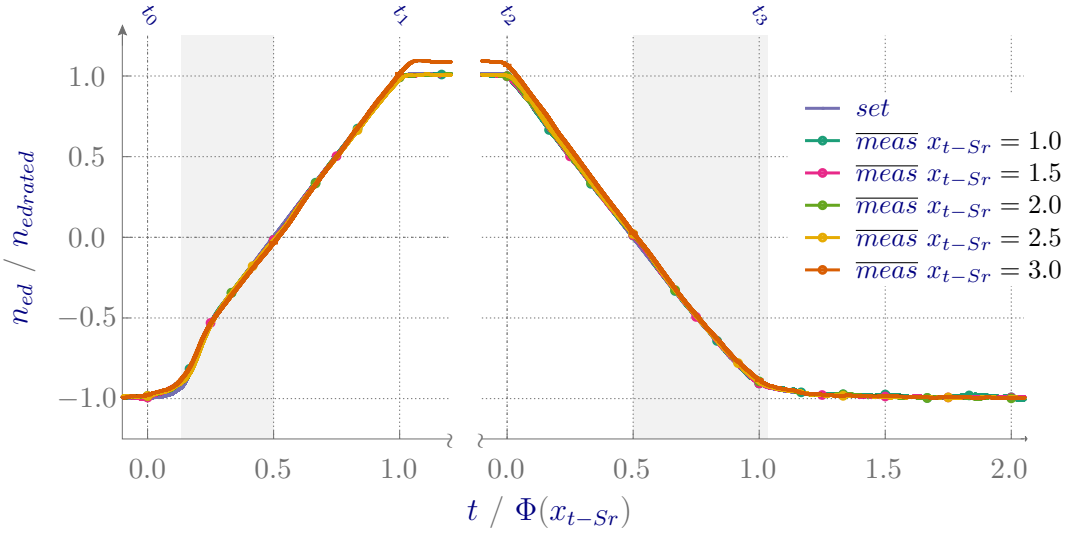

Figure C.14: Comparison of speed coefficient between setpoints and measurement results for different time scale factors of speed controlled fast transitions from pump to turbine mode (left) and vice versa (right) with linear profile and a guide vane opening of $\gamma/\gamma_{max} = 0.8$.

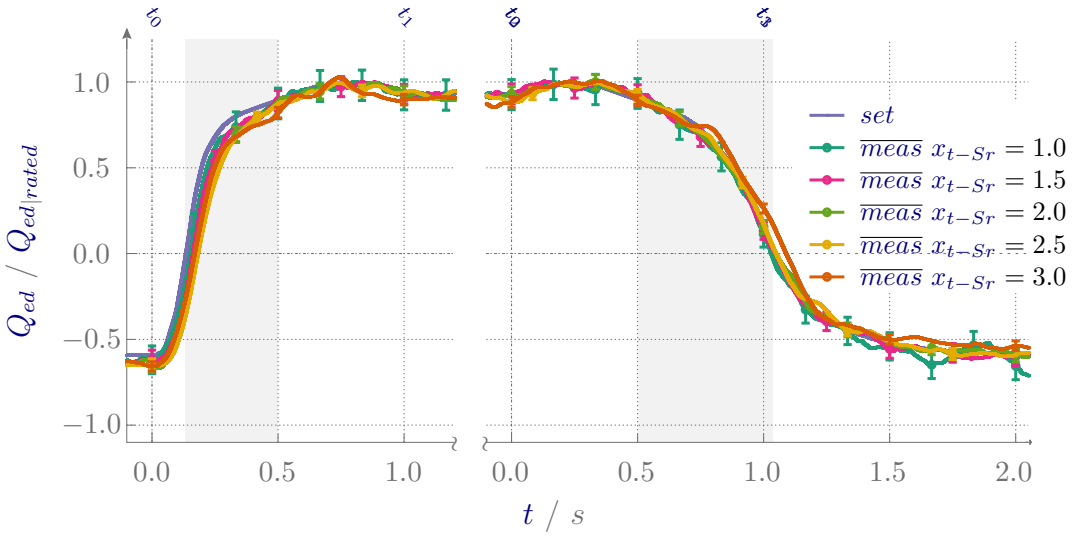

Figure C.15: Comparison of discharge coefficient between setpoints and measurement results for different time scale factors of speed controlled fast transitions from pump to turbine mode (left) and vice versa (right) with linear profile and a guide vane opening of $\gamma/\gamma_{max} = 0.8$.

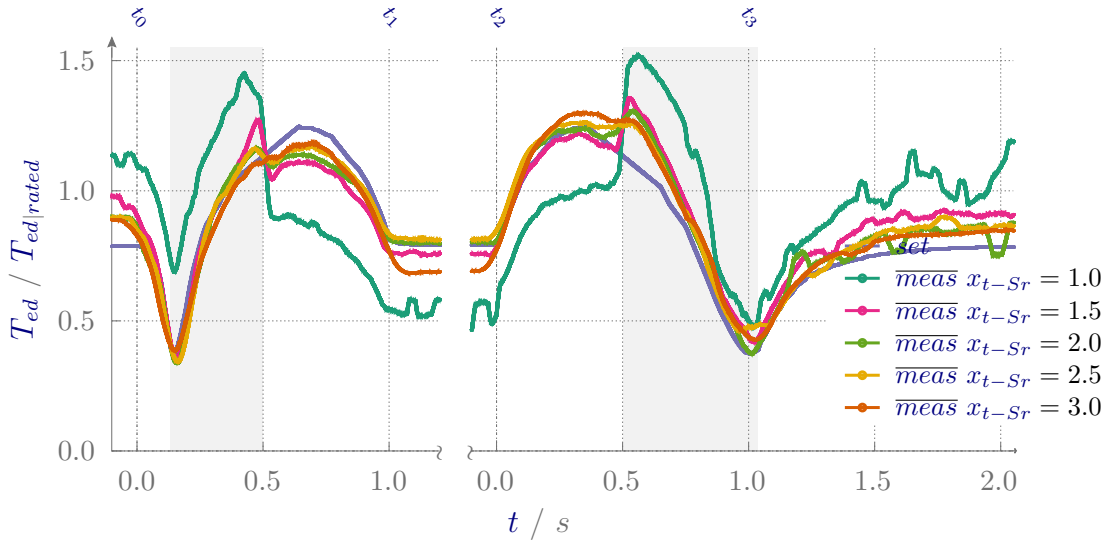

Figure C.16: Comparison of torque coefficient between setpoints and measurement results for different time scale factors of speed controlled fast transitions from pump to turbine mode (left) and vice versa (right) with linear profile and a guide vane opening of $\gamma/\gamma_{max} = 0.8$.

C.3 Fast Transition with Spline Speed Profile

C.3.1 Results of Guide Vane Opening of $\gamma/\gamma_{max} = 0.4$

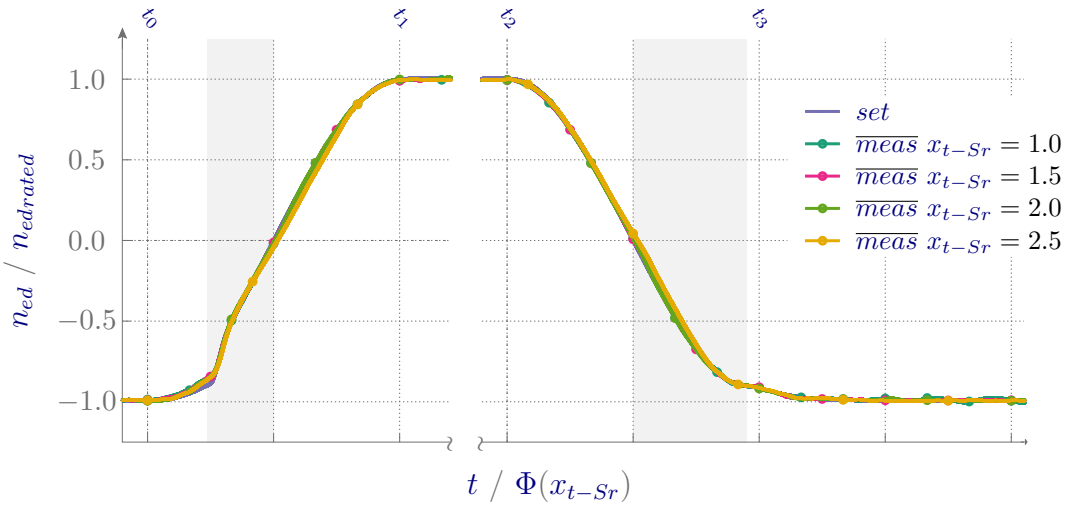

Figure C.17: Comparison of speed coefficient between setpoints and measurement results for different time scale factors of speed controlled fast transitions from pump to turbine mode (left) and vice versa (right) with spline profile and a guide vane opening of $\gamma/\gamma_{max} = 0.4$.

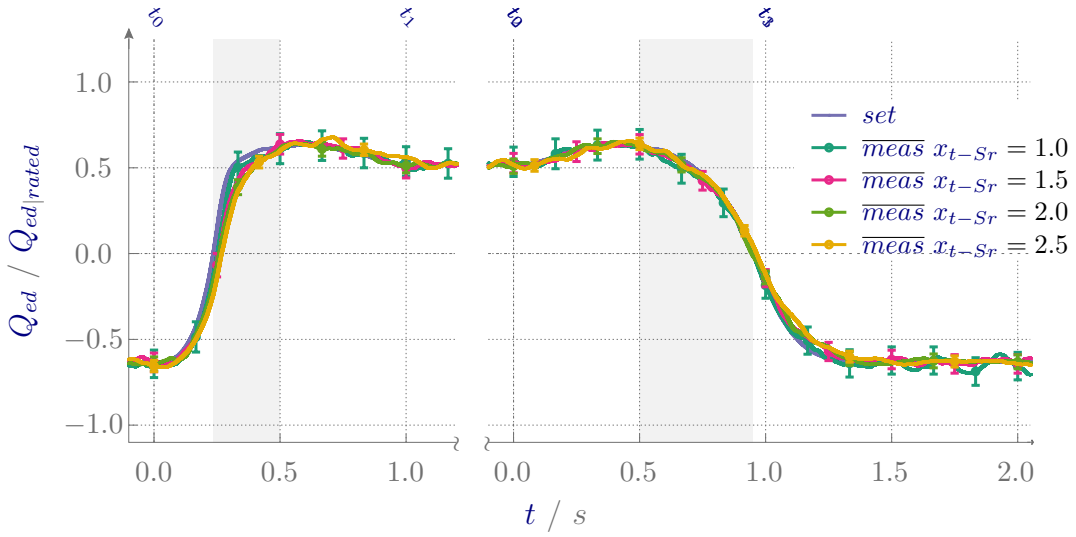

Figure C.18: Comparison of discharge coefficient between setpoints and measurement results for different time scale factors of speed controlled fast transitions from pump to turbine mode (left) and vice versa (right) with spline profile and a guide vane opening of $\gamma/\gamma_{max} = 0.4$.

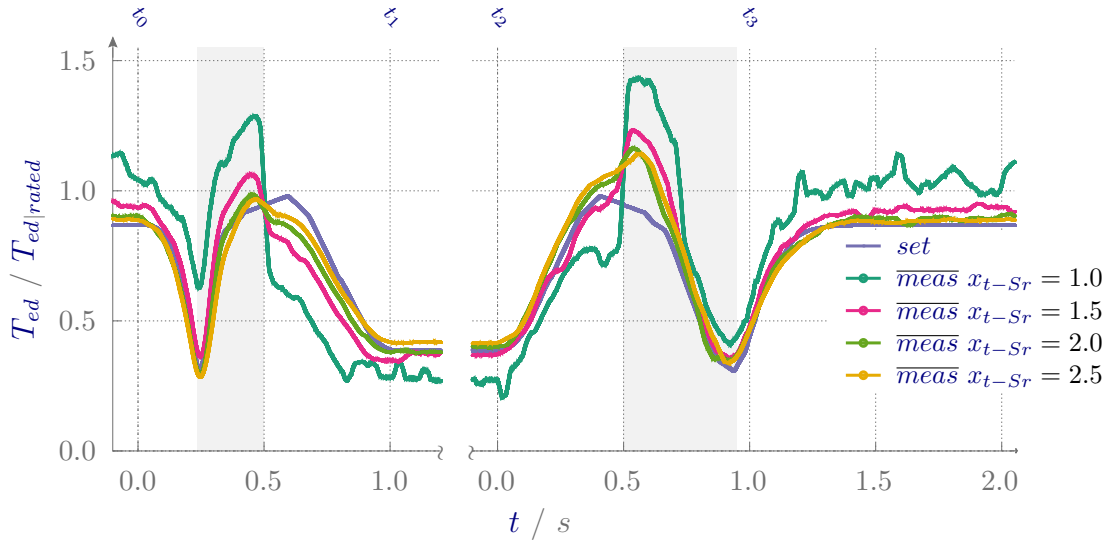

Figure C.19: Comparison of torque coefficient between setpoints and measurement results for different time scale factors of speed controlled fast transitions from pump to turbine mode (left) and vice versa (right) with spline profile and a guide vane opening of $\gamma/\gamma_{max} = 0.4$.

C.3.2 Results of Guide Vane Opening of $\gamma/\gamma_{max} = 0.6$

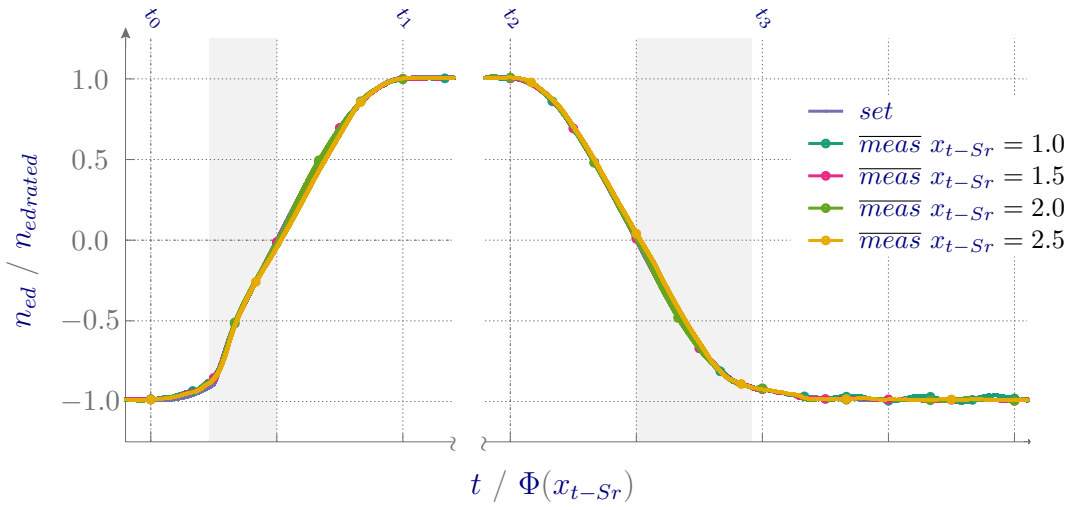

Figure C.20: Comparison of speed coefficient between setpoints and measurement results for different time scale factors of speed controlled fast transitions from pump to turbine mode (left) and vice versa (right) with spline profile and a guide vane opening of $\gamma/\gamma_{max} = 0.6$.

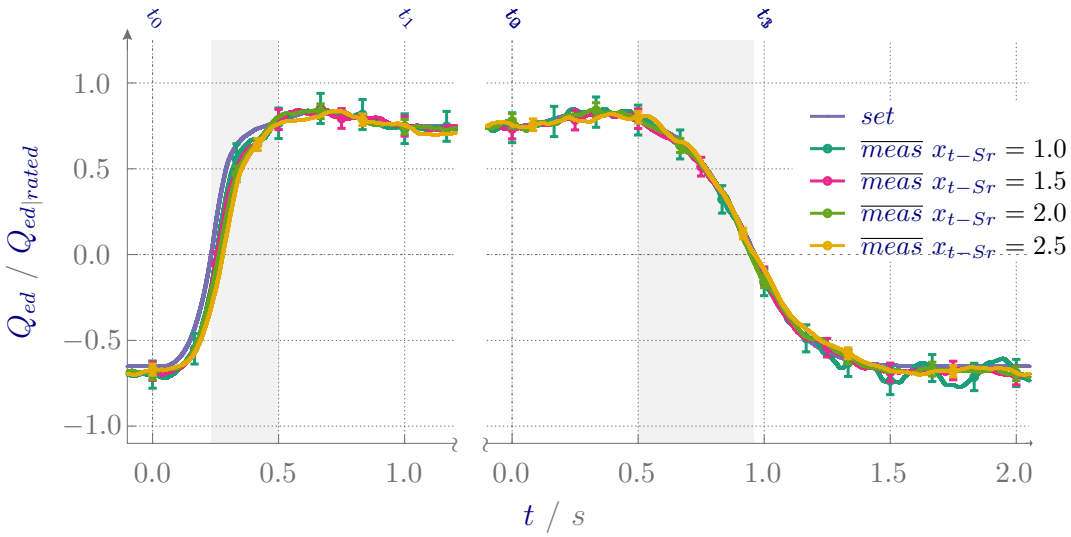

Figure C.21: Comparison of discharge coefficient between setpoints and measurement results for different time scale factors of speed controlled fast transitions from pump to turbine mode (left) and vice versa (right) with spline profile and a guide vane opening of $\gamma/\gamma_{max} = 0.6$.

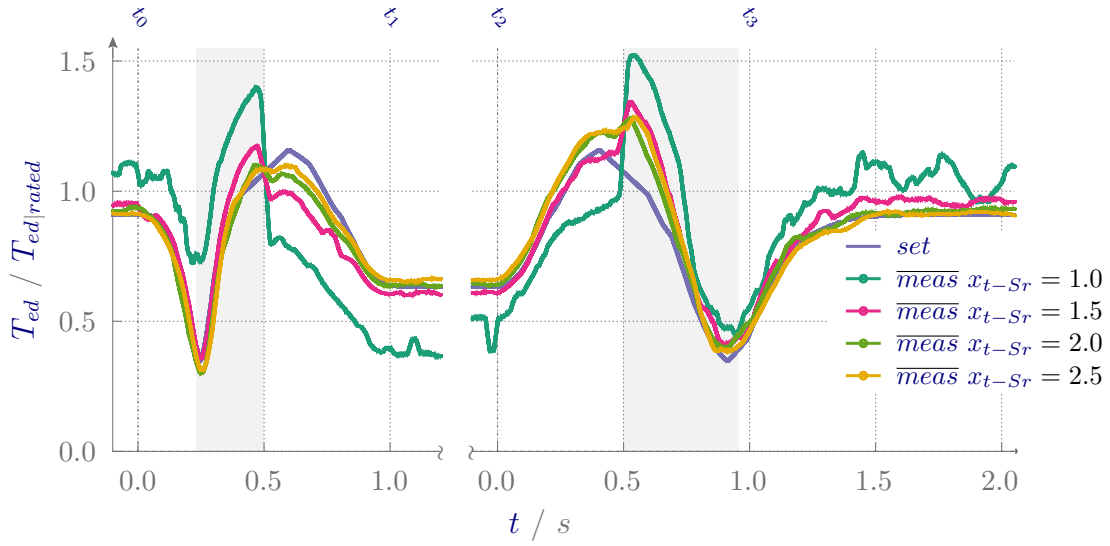

Figure C.22: Comparison of torque coefficient between setpoints and measurement results for different time scale factors of speed controlled fast transitions from pump to turbine mode (left) and vice versa (right) with spline profile and a guide vane opening of $\gamma/\gamma_{max} = 0.6$.

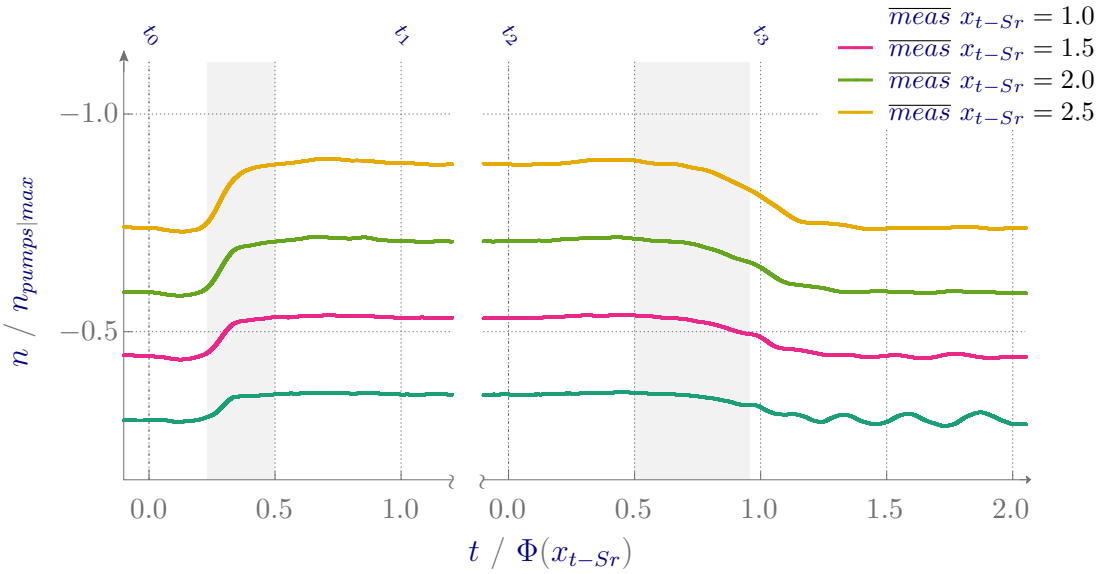

Figure C.23: Measured rotational speed of the service pumps for different time scale factors of speed controlled fast transitions from pump to turbine mode (left) and vice versa (right) with spline profile and a guide vane opening of $\gamma/\gamma_{max} = 0.6$.

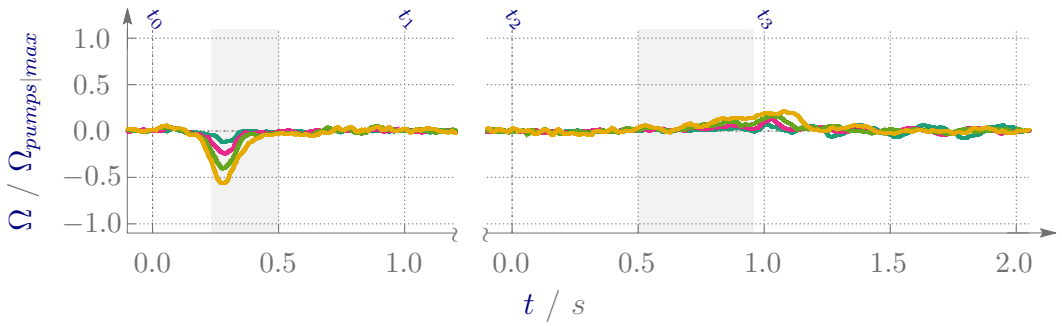

Figure C.24: Measured rotational speed acceleration of the service pumps for different time scale factors of speed controlled fast transitions from pump to turbine mode (left) and vice versa (right) with spline profile and a guide vane opening of $\gamma/\gamma_{max} = 0.6$.

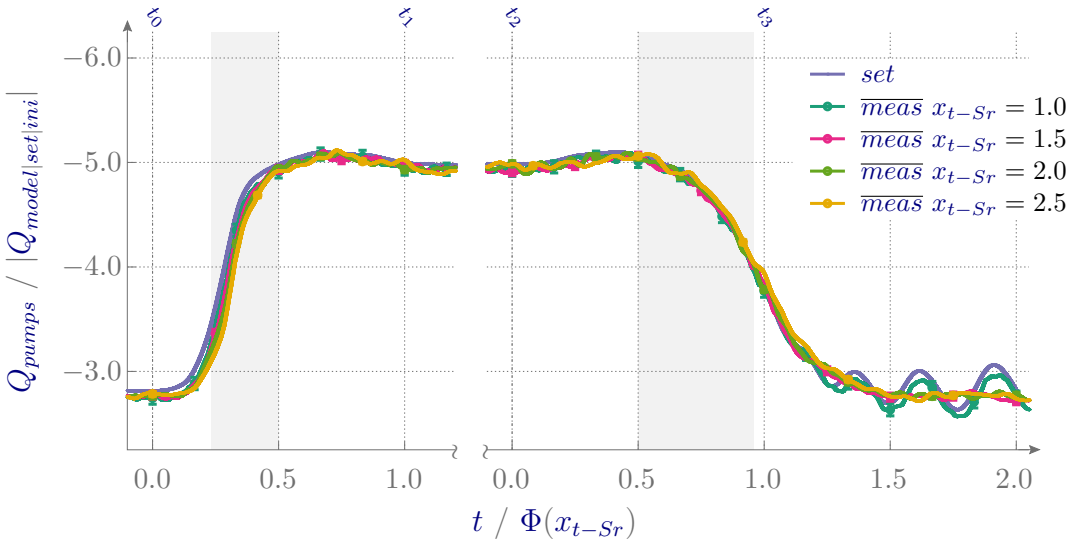

Figure C.25: Measured discharge of the service pumps for different time scale factors of speed controlled fast transitions from pump to turbine mode (left) and vice versa (right) with spline profile and a guide vane opening of $\gamma/\gamma_{max} = 0.6$.

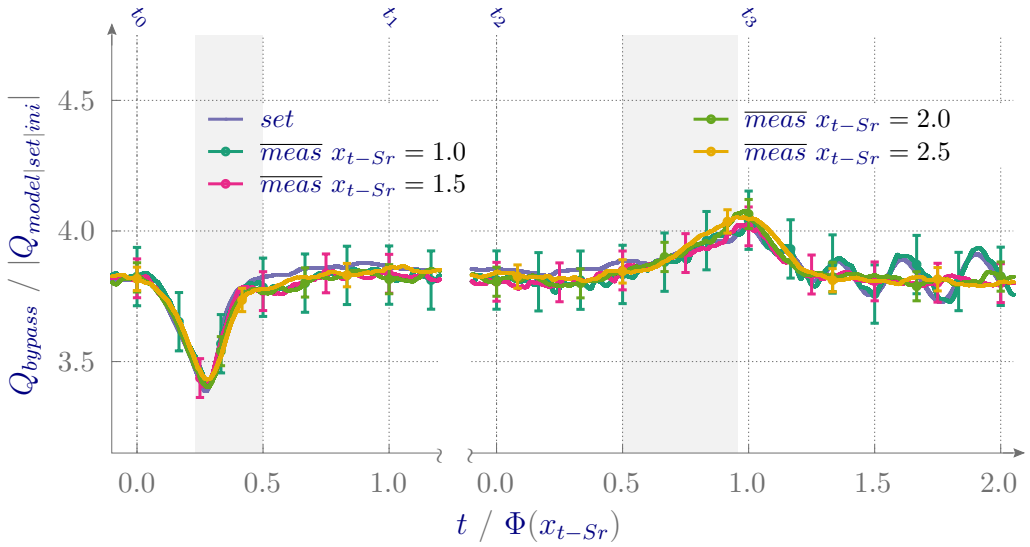

Figure C.26: Measured bypass discharge for different time scale factors of speed controlled fast transitions from pump to turbine mode (left) and vice versa (right) with spline profile and a guide vane opening of $\gamma/\gamma_{max} = 0.6$.

C.3.3 Results of Guide Vane Opening of $\gamma/\gamma_{max} = 0.8$

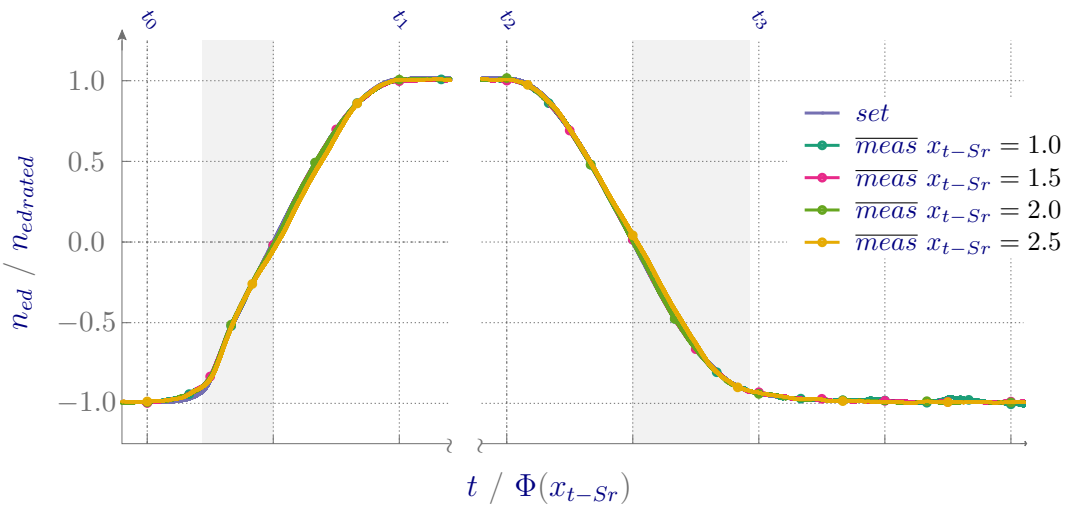

Figure C.27: Comparison of speed coefficient between setpoints and measurement results for different time scale factors of speed controlled fast transitions from pump to turbine mode (left) and vice versa (right) with spline profile and a guide vane opening of $\gamma/\gamma_{max} = 0.8$.

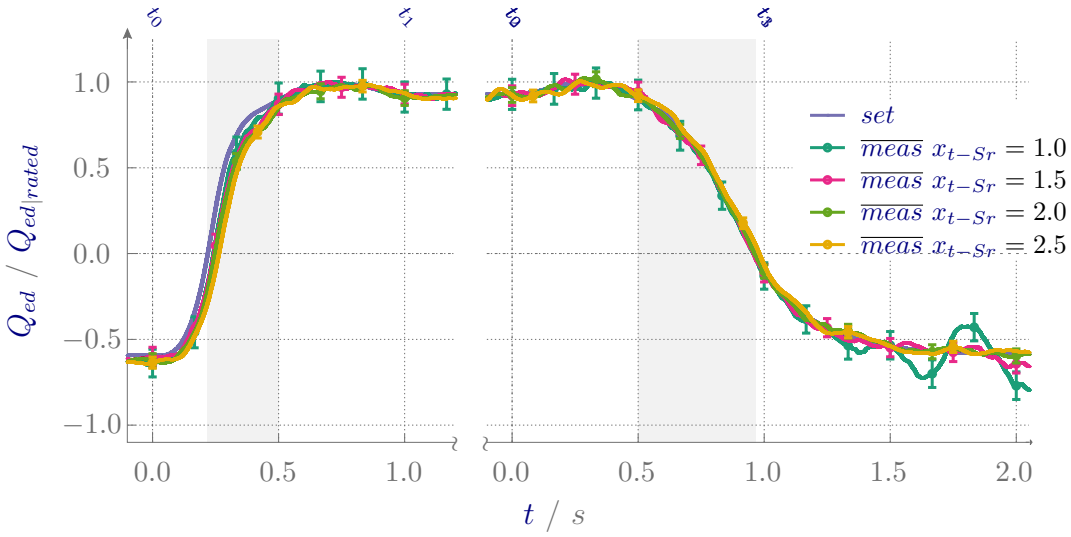

Figure C.28: Comparison of discharge coefficient between setpoints and measurement results for different time scale factors of speed controlled fast transitions from pump to turbine mode (left) and vice versa (right) with spline profile and a guide vane opening of $\gamma/\gamma_{max} = 0.8$.

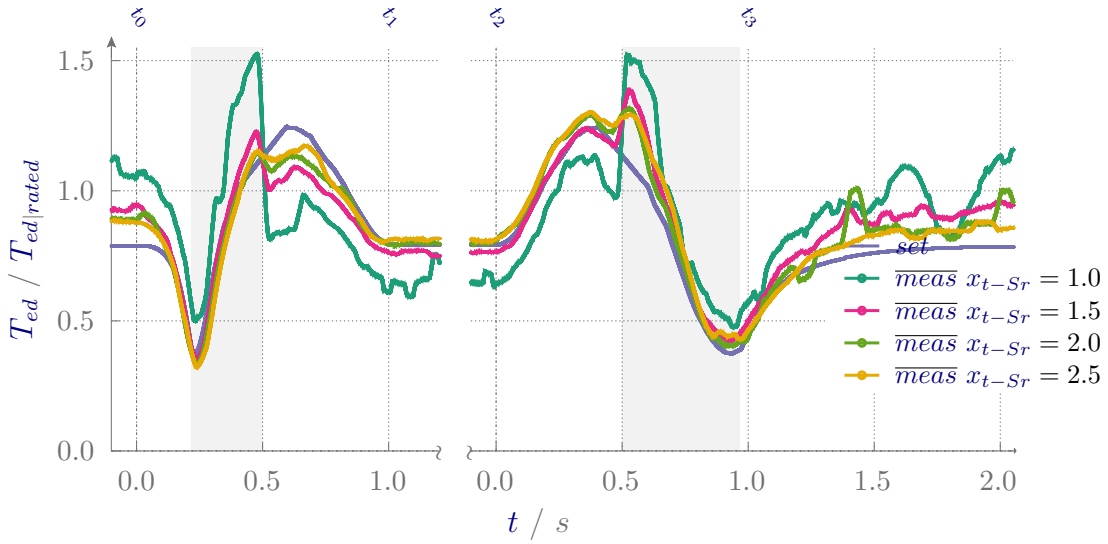

Figure C.29: Comparison of torque coefficient between setpoints and measurement results for different time scale factors of speed controlled fast transitions from pump to turbine mode (left) and vice versa (right) with spline profile and a guide vane opening of $\gamma/\gamma_{max} = 0.8$.

C.4 Fast Transition with Tangential Hyperbolic Speed Profile

$$n_{proto}(t) = |n_{proto-rated}| \begin{cases} \tanh(\pi \cdot {}^{t}/_{\Phi}) / \tanh(\pi), & PU \rightarrow TU \\ -\tanh(\pi \cdot {}^{t}/_{\Phi}) / \tanh(\pi), & TU \rightarrow PU \end{cases} \tag{C.2}$$

$$n_{proto}(t) = |n_{proto-rated}| \begin{cases} \tanh(2 \cdot \pi \cdot {}^{t}/_{\Phi}) / \tanh(2 \cdot \pi), & PU \rightarrow TU \\ -\tanh(2 \cdot \pi \cdot {}^{t}/_{\Phi}) / \tanh(2 \cdot \pi), & TU \rightarrow PU \end{cases} \tag{C.3}$$

$$n_{proto}(t) = |n_{proto-rated}| \begin{cases} \tanh(4 \cdot \pi \cdot {}^{t}/_{\Phi}) / \tanh(4 \cdot \pi), & PU \rightarrow TU \\ -\tanh(4 \cdot \pi \cdot {}^{t}/_{\Phi}) / \tanh(4 \cdot \pi), & TU \rightarrow PU \end{cases} \tag{C.4}$$

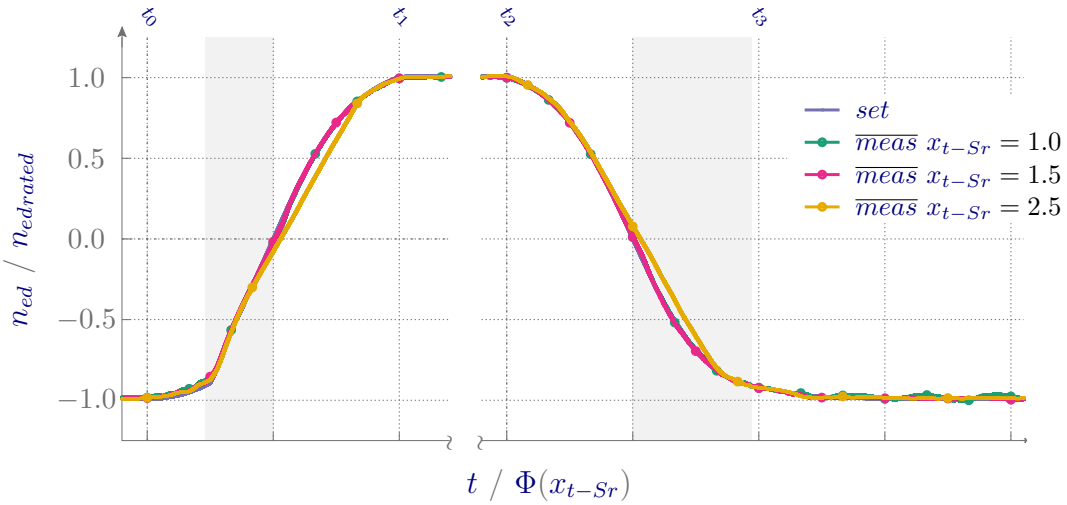

Figure C.30: Comparison of speed coefficient between setpoints and measurement results for different time scale factors of speed controlled fast transitions from pump to turbine mode (left) and vice versa (right) with hyperbolic tangent profile according to Eqn. C.2 and a guide vane opening of ${}^{\gamma}/_{\gamma_{max}} = 0.6$.

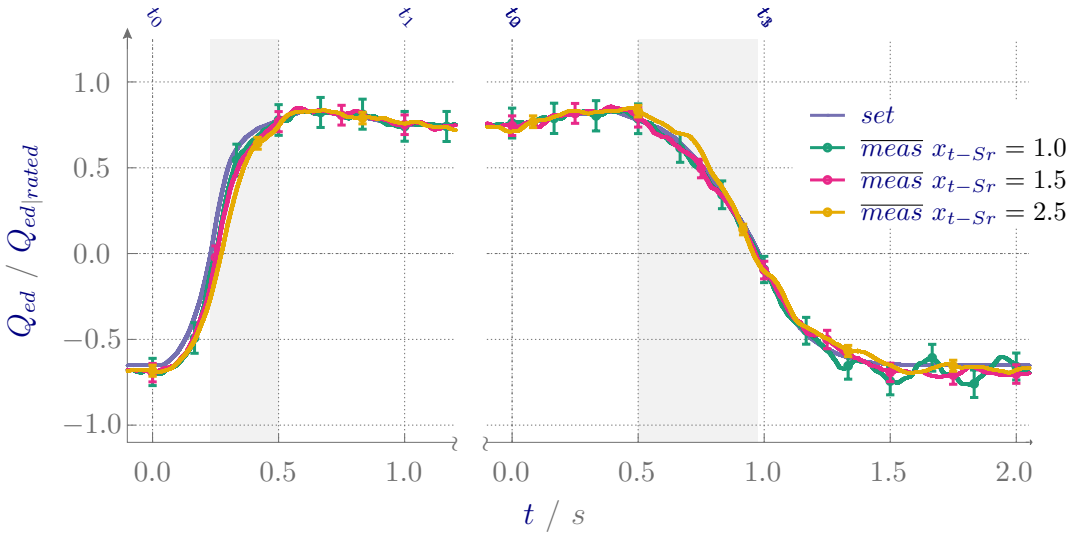

Figure C.31: Comparison of discharge coefficient between setpoints and measurement results for different time scale factors of speed controlled fast transitions from pump to turbine mode (left) and vice versa (right) with hyperbolic tangent profile according to Eqn. C.2 and a guide vane opening of $\gamma/\gamma_{max} = 0.6$.

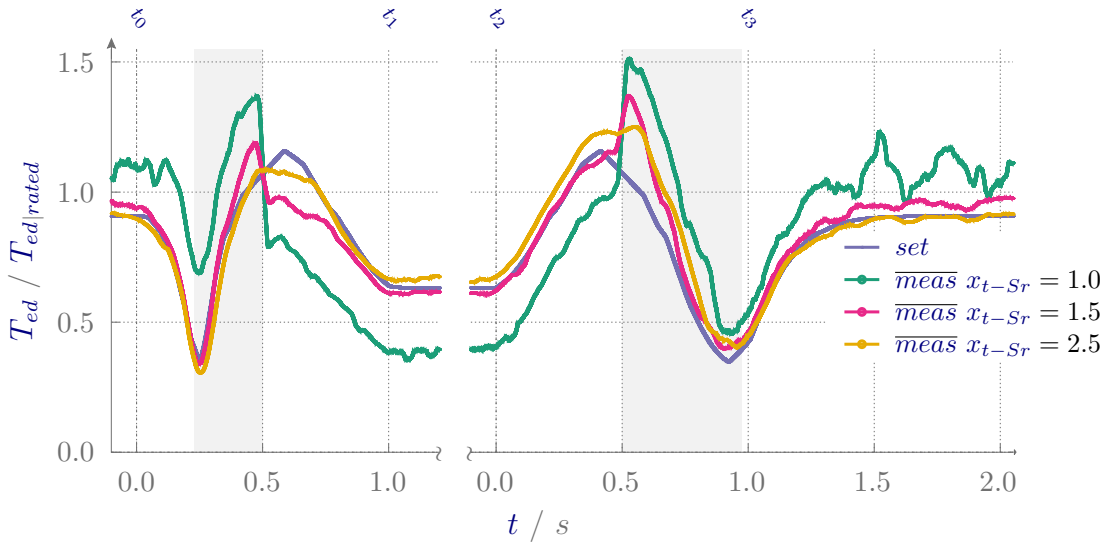

Figure C.32: Comparison of torque coefficient between setpoints and measurement results for different time scale factors of speed controlled fast transitions from pump to turbine mode (left) and vice versa (right) with hyperbolic tangent profile according to Eqn. C.2 and a guide vane opening of $\gamma/\gamma_{max} = 0.6$.

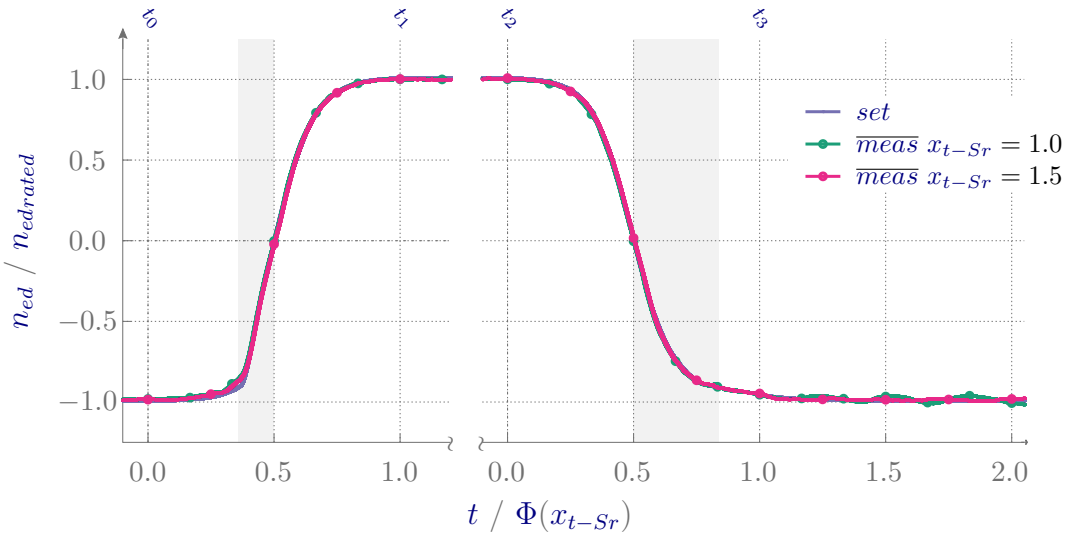

Figure C.33: Comparison of speed coefficient between setpoints and measurement results for different time scale factors of speed controlled fast transitions from pump to turbine mode (left) and vice versa (right) with hyperbolic tangent profile according to Eqn. C.3 and a guide vane opening of $\gamma/\gamma_{max} = 0.6$.

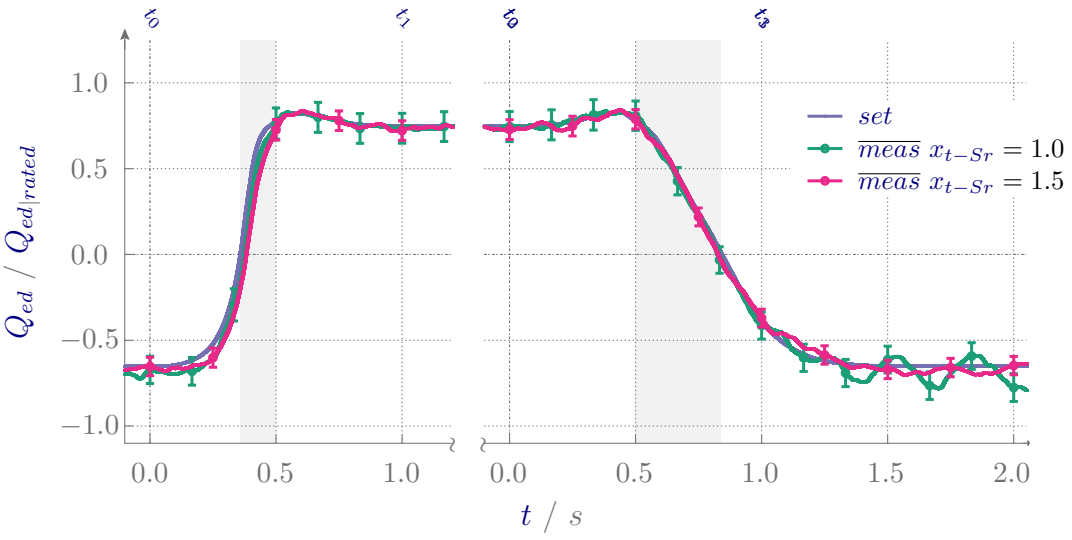

Figure C.34: Comparison of discharge coefficient between setpoints and measurement results for different time scale factors of speed controlled fast transitions from pump to turbine mode (left) and vice versa (right) with hyperbolic tangent profile according to Eqn. C.3 and a guide vane opening of $\gamma/\gamma_{max} = 0.6$.

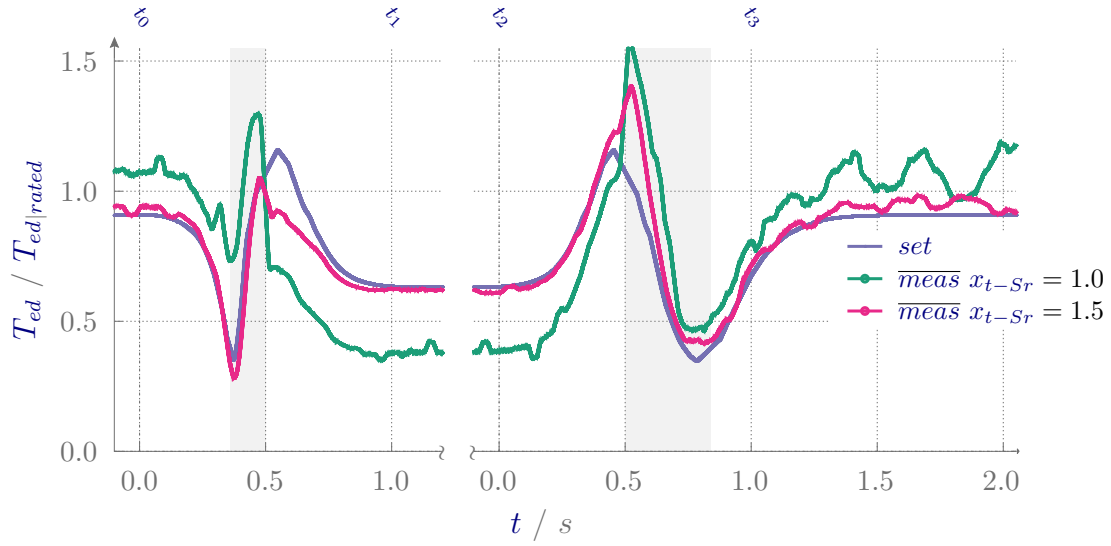

Figure C.35: Comparison of torque coefficient between setpoints and measurement results for different time scale factors of speed controlled fast transitions from pump to turbine mode (left) and vice versa (right) with hyperbolic tangent profile according to Eqn. C.3 and a guide vane opening of $\gamma/\gamma_{max} = 0.6$.

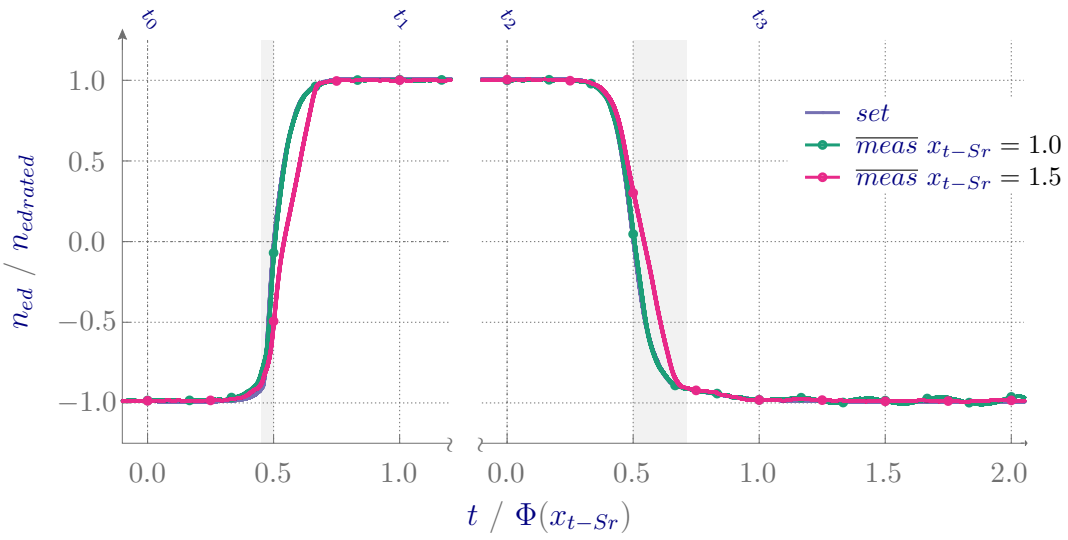

Figure C.36: Comparison of speed coefficient between setpoints and measurement results for different time scale factors of speed controlled fast transitions from pump to turbine mode (left) and vice versa (right) with hyperbolic tangent profile according to Eqn. C.4 and a guide vane opening of $\gamma/\gamma_{max} = 0.6$.

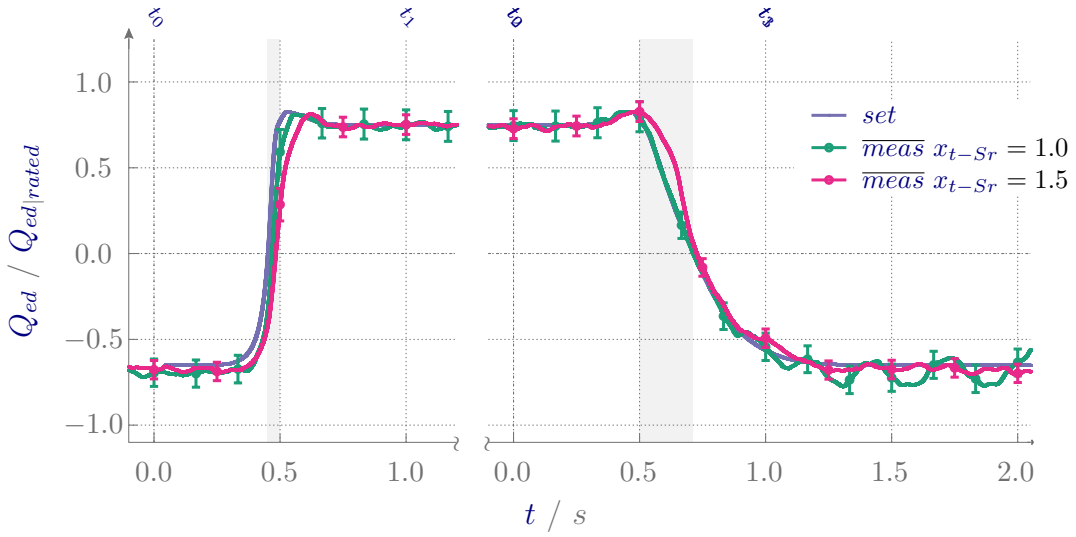

Figure C.37: Comparison of discharge coefficient between setpoints and measurement results for different time scale factors of speed controlled fast transitions from pump to turbine mode (left) and vice versa (right) with hyperbolic tangent profile according to Eqn. C.4 and a guide vane opening of $\gamma/\gamma_{max} = 0.6$.

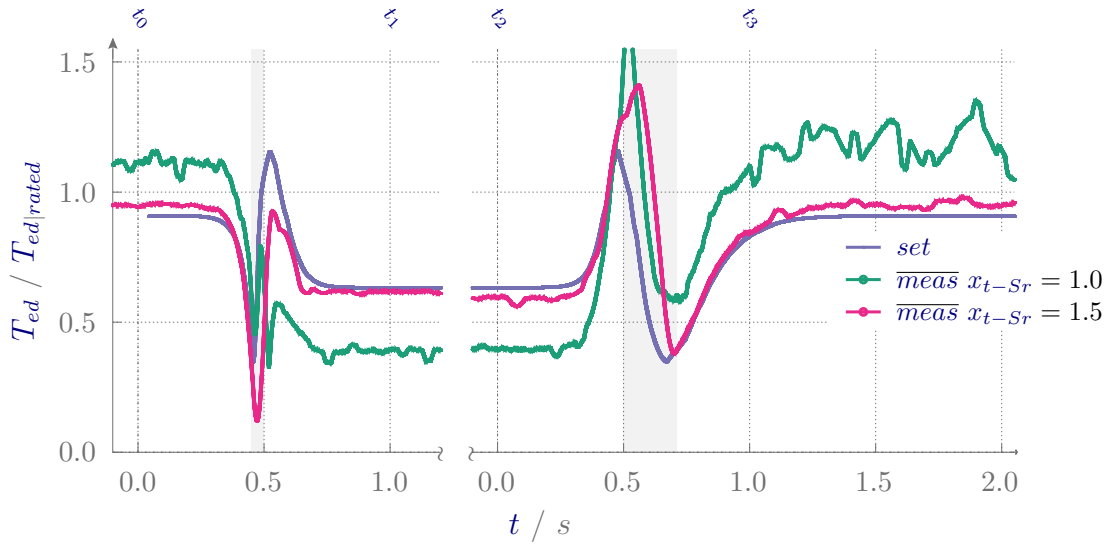

Figure C.38: Comparison of torque coefficient between setpoints and measurement results for different time scale factors of speed controlled fast transitions from pump to turbine mode (left) and vice versa (right) with hyperbolic tangent profile according to Eqn. C.4 and a guide vane opening of $\gamma/\gamma_{max} = 0.6$.

C.5 Power Control via Guide Vane Adjustment

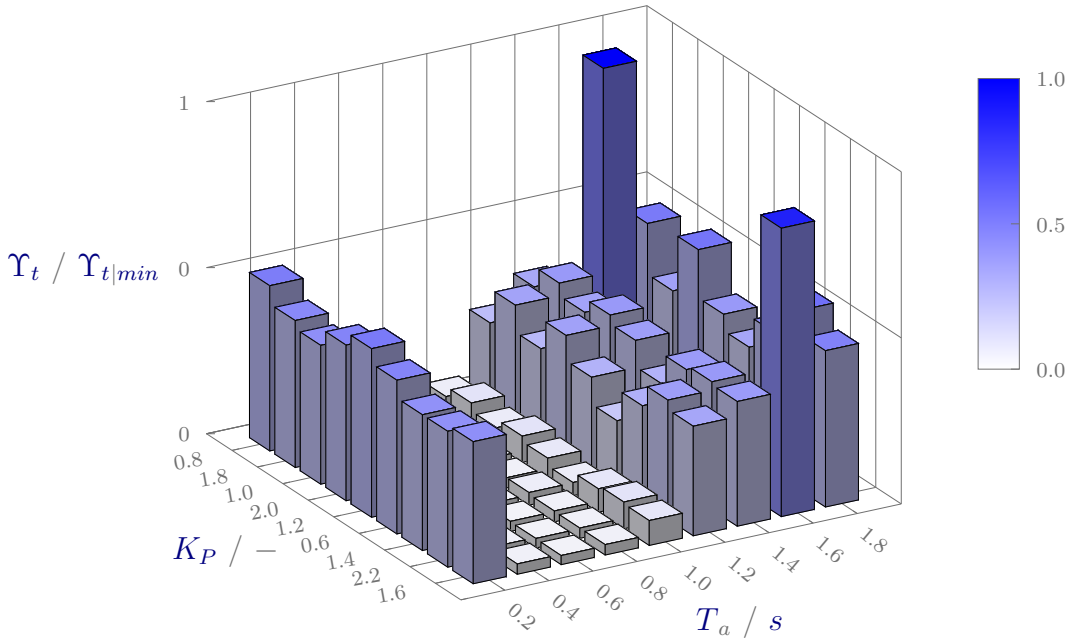

Figure C.39: Parameter study for optimizer parameters for load cases with power control via guide vane adjustment.

D Calibration of Test Rig Measurement Sensors

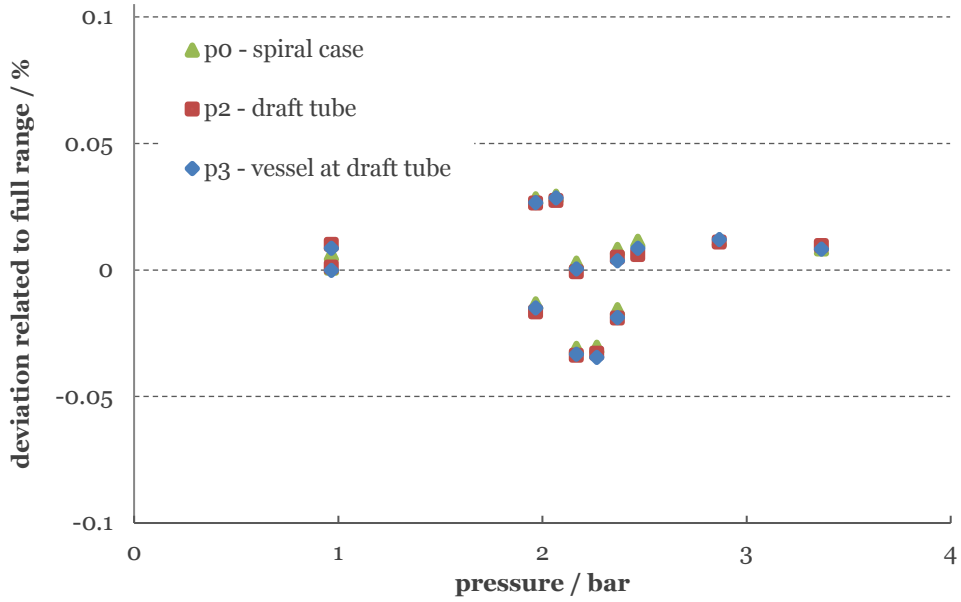

Figure D.1: Calibration result of absolute pressure sensors mounted at model machine.

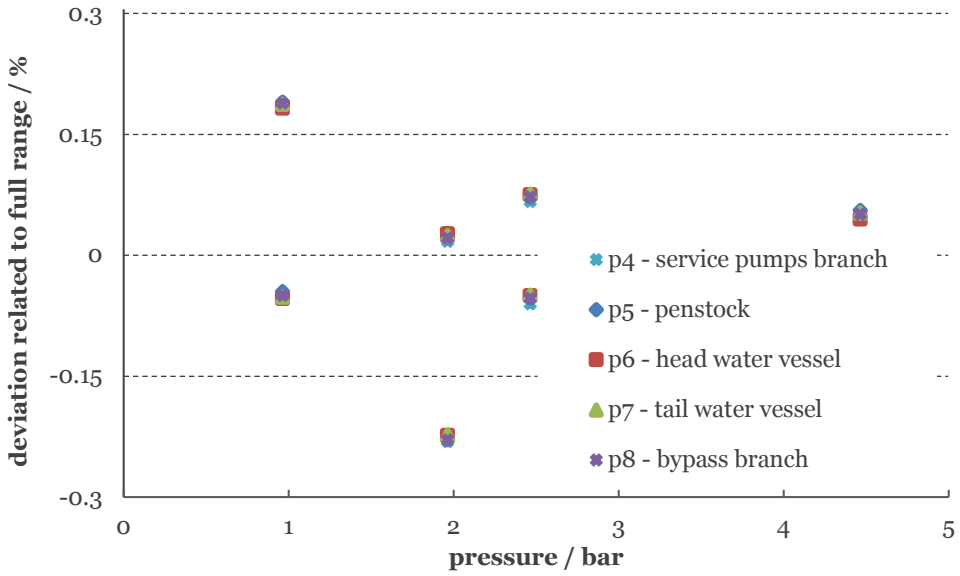

Figure D.2: Calibration result of absolute pressure sensors distributed in the test rig.

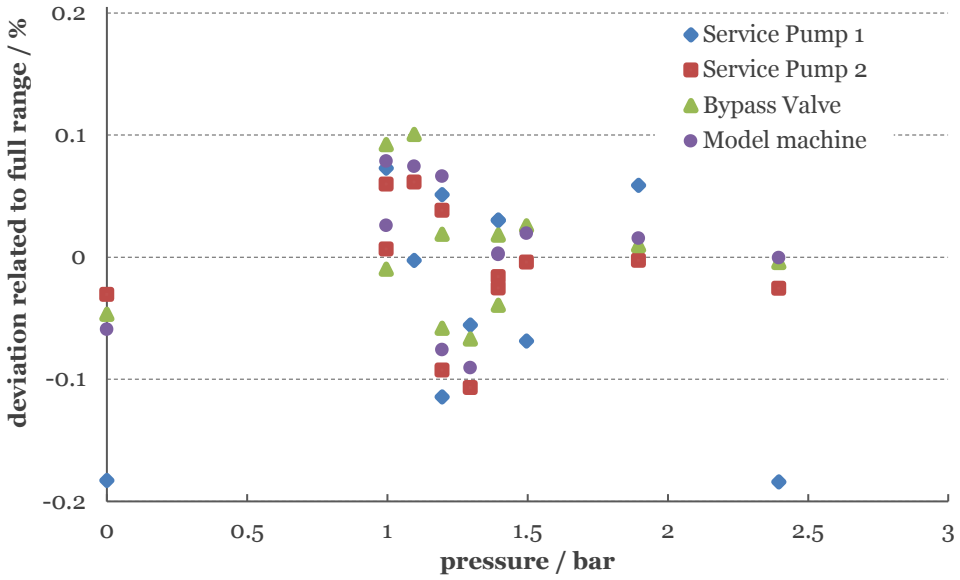

Figure D.3: Calibration result of differential pressure sensors.

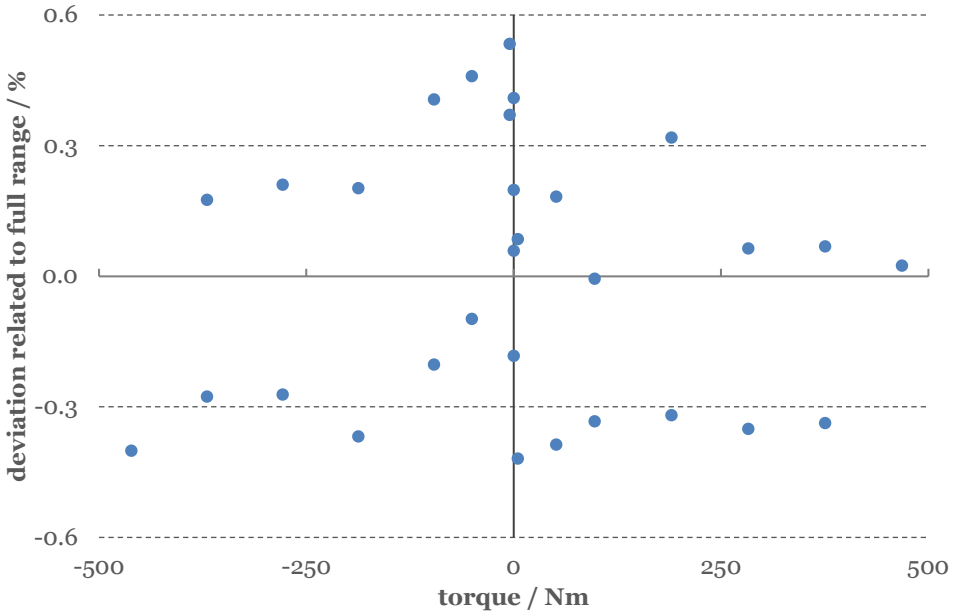

Figure D.4: Calibration result of torque sensors.

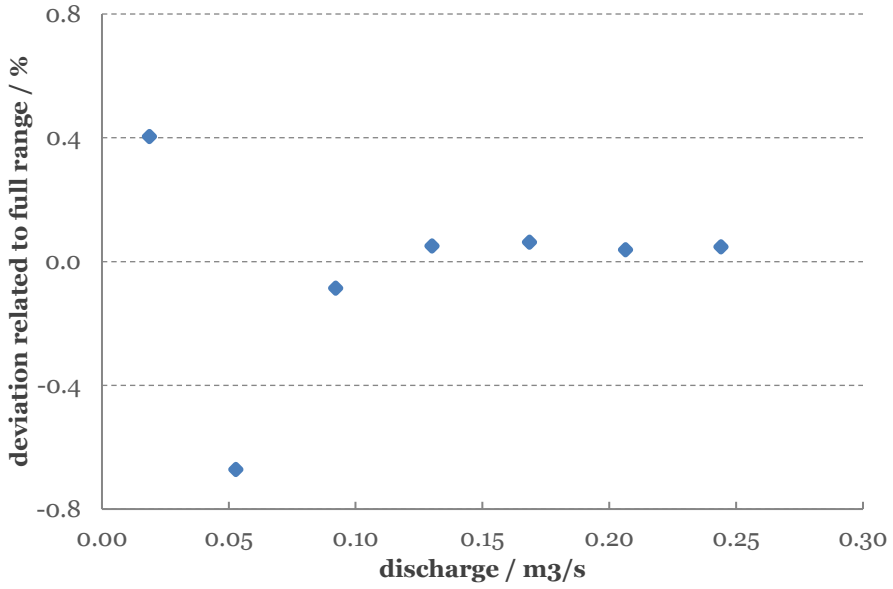

Figure D.5: Calibration result of discharge measurement sensor in the bypass.

Liste der bisher erschienenen IHS-Mitteilungen

Nr.	Jahr	Verfasser	Titel
1	1986		Beitrag zur 14. Sitzung des VDEW-Arbeitsausschusses „Meßmethoden in Wasserkraftanlagen”. ISBN 3-9802130-0-5
2	1989	Schneider, K. Eichinger, P.	Das Verhalten von Sicherheits-Drosselklappen. Modifikation des Standardcharakteristikenverfahrens zur Berechnung zeitlich zurückliegender Druckverläufe. ISBN 3-9802130-1-3
3	1989	Ruprecht, A.	Finite Elemente zur Berechnung dreidimensionaler, turbulenter Strömungen in komplexen Geometrien. ISBN 3-9802130-2-1
4	1990	Maurer, W.	Drehzahlregelung von Wasserturbinen mit Zustandsreglern. ISBN 3-9802130-3-X
5	1990	Acosta Del Carpio, H.	Das dynamische Verhalten von Kreiselpumpen niedriger spezifischer Drehzahl bei raschen Drehzahländerungen. ISBN 3-9802130-4-8
6	1990	Gronenberg, R.	Untersuchung des dynamischen Verhalten von Rückflußverhinderern unterschiedlicher Bauart. ISBN 3-9802130-5-6
7	1992	Eichinger, P.	Untersuchung des Reibungsverhaltens bei instationären Strömungsvorgängen in Rohrleitungen. ISBN 3-9802130-6-4
8	1993	Chihab, W. S.	Experimentelle und theoretische Untersuchung des Saugrohrs einer Kaplanturbine. ISBN 3-9802130-7-2
9	1994		Aktuelle Forschungsarbeiten des Instituts. ISBN 3-9802130-8-0
10	1994	Feyrer, R.	Kontinuierliche On-Line Berechnung der zulässigen Leistungsänderung in einem Pumpspeicherwerk. ISBN 3-9802130-9-9
11	1996	Zhang, Y.	Finite Elemente zur Berechnung instationärer Strömungen mit bewegten Wänden. ISBN 3-9804376-0-4

Nr.	Jahr	Verfasser	Titel
12	1997	Ginter, F.	Berechnung der instationären, turbulenten Strömung in hydraulischen Strömungsmaschinen. ISBN 3-9804376-1-2
13	1997		Beiträge zum Seminar „Kleinwasserkraft", Stuttgart, 10.10.97 ISBN 3-9804376-2-0
14	1998	Welzel, B.	Numerische Optimierung einer Axialturbine. ISBN 3-9804376-3-9
15	1999	Harbort, T.	Entwicklung eines echtzeitfähigen Simulationsprogramms zur Untersuchung instationärer Vorgänge in Wasserkraftwerken. ISBN 3-9804376-4-7
16	1999		Beiträge zum 2. Seminar „Kleinwasserkraft", Stuttgart, 01.10.99 ISBN 3-9804376-5-5
17	2000	Gentner, Ch.	Experimentelle und numerische Untersuchung der instationären Strömung in einer Axialturbine. ISBN 3-9804376-6-3
18	2000	Steibler, P.	Finite Element Methode zur numerischen Strömungsberechnung mit beliebigen Elementen. ISBN 3-9804376-7-1
19	2000	Lin, J.-C.	Überwachung von Wasserschlössern in Wasserkraftwerken mit Fuzzy-Control. ISBN 3-9804376-8-X
20	2000	Ott, Ch.	Entwurf und Simulation einer Staustufenregelung. ISBN 3-9804376-9-8
21	2001	Bauer, Ch.	Instationäre Berechnung einer hydraulischen Axialturbine unter Berücksichtigung der Interaktion zwischen Leit- und Laufrad. ISBN 3-9807322-0-7
22	2001	Liu, W.	Modeling of Swirling Turbulent Flows. ISBN 3-9807322-1-5
23	2002		Beiträge zum 3. Seminar „Kleinwasserkraft", Stuttgart, 05.10.01 ISBN 3-9807322-2-3

Nr.	Jahr	Verfasser	Titel
24	2001	Janetzky, B.	Ein Verfahren zur Berechnung instationärer Strömungen mit freier Oberfläche. ISBN 3-9807322-3-1
25	2002	Anz, R.	Systemidentifikation und Reglerselbsteinstellung in Wasserkraftanlagen. ISBN 3-9807322-4-X
26	2002	Maihöfer, M.	Effiziente Verfahren zur Berechnung dreidimensionaler Strömungen mit nichtpassenden Gittern. ISBN 3-9807322-5-8
27	2003		Beiträge zum 4. Seminar „Kleinwasserkraft“, Stuttgart, 19.09.03 ISBN 3-9807322-6-6
28	2003	Batrekhy, S.	Numerische und experimentelle Strömungsuntersuchungen an Rechen von Wasserkraftanlagen. ISBN 3-9807322-7-4
29	2005		Beiträge zum 5. Seminar „Kleinwasserkraft“, Stuttgart, 14.10.05 ISBN 3-9807322-8-2
30	2007	Helmrich, T.	Simulation instationärer Wirbelstrukturen in hydraulischen Maschinen. ISBN 978-3-9807322-9-1
31	2010	Lippold, F.	Zur Simulation von Fluid-Struktur-Wechselwirkungen mit flexiblen Kopplungsverfahren. ISBN 978-3-9812054-0-4
32	2011	Kirschner, O.	Experimentelle Untersuchung des Wirbelzopfes im geraden Saugrohr einer Modell-Pumpturbine. ISBN 978-3-9812054-1-1
33	2016	Ruopp, A.	Optimierung von symmetrischen Gezeitenströmungsturbinen und deren Analyse in großräumigen Gezeitenströmungsgebieten. ISBN 978-3-9812054-2-8
34	2016	Wang, H.	Very large eddy simulation for prediction of flow instabilities in turbomachinery. ISBN 978-3-9812054-3-5

Nr.	Jahr	Verfasser	Titel
35	2017	Neipp, A.	Ein- und zweistufige axiale Entspannungsturbine zur Energierückgewinnung. ISBN 978-3-9812054-4-2
36	2018	Stens, C.	Investigation of a fast transition from pump mode to generating mode in a reversible pump turbine. ISBN 978-3-9812054-5-9
37	2018	Krappel, T.	Turbulenzauflösende Strömungssimulation einer Francisturbine in Teillast. ISBN 978-3-9812054-6-6
38	2019	Schmidt, H.	Entwicklung eines Analyseverfahrens zur Kavitationsdetektion und Lokalisierung in hydraulischen Strömungsmaschinen. ISBN 978-3-9812054-7-3
39	2019	Schlipf, M.	Automatisierte Mehrzieloptimierung hydraulischer axialer Strömungsmaschinen. ISBN 978-3-9812054-8-0
40	2019	Brost, V.	Wiederaufbau des Stromnetzes mit einem Inselverbund aus Wasserkraftanlagen. ISBN 978-3-9812054-9-7
41	2019	Mössinger, P.	Numerische Untersuchung der Strömung bei transienten und instabilen Betriebszuständen von Francis-Turbinen. ISBN 978-3-9812054-00-9
42	2020	Tismer, A.	Entwicklung einer Softwareumgebung zur automatischen Auslegung von hydraulischen Maschinen mit dem Inselmodell. ISBN 978-3-948328-01-6
43	2020	Frey, A.	Untersuchung von periodischen und turbulenten Strömungsfluktuationen einer Francis-Turbine im Teillastbetrieb mit Laser-Doppler-Anemometrie. ISBN 978-3-948328-02-3
44	2020	Wack, J.	Numerical Investigation of the Full Load Instability in a Francis Turbine. ISBN 978-3-948328-03-0

Nr.	Jahr	Verfasser	Titel
45	2021	Hankeln, F.	Zur numerischen Berechnung des Betriebsverhaltens von Kreiselpumpen bei hydroabrasiver Erosion ISBN 978-3-948328-04-7
46	2022	Junginger, B.	Untersuchungen zum Einfluss des Laufradspalts einer schnellläufigen Axialturbine unter Verwendung skalenauflösender Turbulenzmodelle. ISBN 978-3-948328-05-4


9 783948 328061